



PhD thesis

UNIVERSITE DE LILLE 1 - SCIENCES ET TECHNOLOGIES
Ecole doctorale Sciences de la Matière, du Rayonnement et de l'Environnement
UFR de Chimie

To obtain the grade of
DOCTOR
in Materials Sciences

by
Claire SCHAYES
Graduate Engineer of
Ecole Nationale Supérieure de Chimie de Lille

Low cycle fatigue of the Fe-3Si steel: damage mechanisms and strain localisation by EBSD

PhD defended in Villeneuve d'Ascq on January 14, 2016 in front of the following dissertation committee:

Mirentxu DUBAR	Professor, University of Valenciennes and Hainaut-Cambresis, France	Examinator
Leo KESTENS	Professor, University of Gent, Belgium	Rewiever
Thierry PALIN-LUC	Professor, ENSAM, Bordeaux, France	Rewiever
Eric HUG	Professor, University of Normandie, Caen, France	Examinator
Frédéric PALLESCHI	CAD Manager, VALEO, Créteil, France	Guest
Jean-Bernard VOGT	Professor, ENSCL, Lille, France	PhD director
Jérémie BOUQUEREL	Associate Professor, ENSCL, Lille, France	PhD supervisor

Unité Matériaux Et Transformations UMET

CNRS UMR 8207 – Université Lille 1



Thèse de Doctorat

Présentée à
L'UNIVERSITE DE LILLE 1 - SCIENCES ET TECHNOLOGIES
Ecole doctorale Sciences de la Matière, du Rayonnement et de l'Environnement
UFR de Chimie

Pour obtenir le titre de
DOCTEUR
Spécialité Sciences des Matériaux

Par
Claire SCHAYES
Ingénieur diplômée de
L'Ecole Nationale Supérieure de Chimie de Lille

Fatigue oligocyclique de l'acier Fe-3Si: mécanismes d'endommagement et localisation de la déformation par EBSD

Soutenue à Villeneuve d'Ascq, le 14 Janvier 2016 devant la commission d'examen :

Mirentxu DUBAR	Professeur, Université de Valenciennes et du Hainaut-Cambresis, France	Président
Leo KESTENS	Professeur, Université de Gand, Belgique	Rapporteur
Thierry PALIN-LUC	Professeur, ENSAM, Bordeaux, France	Rapporteur
Eric HUG	Professeur, Université de Normandie, Caen, France	Examineur
Frédéric PALLESCHI	CAD Manager, VALEO, Créteil, France	Invité
Jean-Bernard VOGT	Professeur, ENSCL, Lille, France	Directeur de thèse
Jérémie BOUQUEREL	Maître de conférence, ENSCL, Lille, France	Encadrant de thèse

Unité Matériaux Et Transformations UMET

CNRS UMR 8207 – Université Lille 1

Remerciements

Je m'exprime ici dans ma langue natale car je ne saurais trouver les mots justes autrement.

Je souhaite remercier Alexandre LEGRIS, directeur du laboratoire UMET pour m'avoir accueillie au sein de ses locaux et l'entreprise VALEO pour m'avoir embauchée afin de mener cette thèse et pour son soutien financier. Je remercie également l'Agence Nationale Recherche Technologie pour le financement de ce projet de recherche dans le cadre du dispositif CIFRE – Conventions Industrielles de Formation par la Recherche.

Je souhaite exprimer toute ma gratitude envers mon directeur de thèse, Jean-Bernard VOGT sans qui tout ceci n'aurait été possible. Je tiens à le remercier pour son accompagnement de l'école d'ingénieur à aujourd'hui, ses nombreux conseils et pour la confiance qu'il m'a accordée. J'espère que l'on sera encore amené à travailler ensemble par la suite.

Merci également à mon encadrant de thèse, Jérémie BOUQUEREL, pour sa confiance et ses nombreux encouragements.

Je tiens à remercier mes encadrants industriels Jean-Claude MIPO et Frédéric PALLESCHI grâce à qui j'ai pu m'intégrer rapidement à l'équipe et comprendre rapidement les problématiques industrielles et les modélisations mécaniques.

Je remercie Mirentxu Dubar qui a accepté de présider mon jury de thèse. Je tiens également à la remercier pour les nombreux accès au microscope JEOL 7100 au laboratoire LAMIH qu'elle m'a octroyé. Je souhaite également exprimer ma reconnaissance envers Leo KESTENS et Thierry PALLIN-LUC pour m'avoir fait l'honneur d'examiner ma thèse en profondeur et envers Erig HUG pour avoir participé à mon Jury de thèse.

Je souhaite remercier le professeur Stephan ZAEFFERER pour avoir accepté de collaborer avec notre équipe et pour m'avoir accueilli dans son laboratoire afin que je me forme à l'ECI. Merci à mes collègues Jérôme LEGRANGER et Radu FRATILA pour les calculs électrotechniques chez VALEO.

Je tiens également à remercier chaleureusement toute l'équipe MPGM et plus particulièrement Jocelyn GOLEK pour son aide avec les différentes machines de fatigue et Damien CRETON alias « Le vieux » pour son aide technique et la bonne ambiance qu'il apporte à l'équipe. Merci aussi à Ahmed ADDAD pour son aide et son expertise avec les microscopes et pour sa bonne humeur.

Merci également à tous les doctorants, post-doctorants et stagiaires qui m'ont accompagné pendant ces trois années et à qui je souhaite beaucoup de succès dans leurs projets.

Merci à tous ceux que j'ai côtoyés dans le bureau 227 : Changqing YE, Hassine KACEM, Caio RESENDE, Fatima ALARAB, Floriane LEAUX et plus particulièrement merci à ceux avec qui j'ai partagé le bureau ces 3 années : Carla CARLE et Gulzar SEIDAMETOVA, j'ai voyagé à travers vous et beaucoup appris de vos pays d'origine que j'espère visiter un jour. Un merci tout particulier à Maxime DELBOVE pour nos discussions de travail qui ont contribué à la réussite de ma thèse et les nombreux moments de complicité. Je te souhaite bon courage pour la fin et je suis certaine que ta thèse sera de grande qualité!

Merci également aux différents occupants du bureau 226 : Rudy PATARD, Romain CANDELA, Devadas BHAT, Kaoutar NAJI - seule femme et expérimentatrice du bureau, bon courage !, Marc-Antoine LOUCHEZ (évite les biberons, c'est mauvais pour la santé) et merci aussi à toi, Jérôme DEQUEKER, le faux méchant du bureau!

Et merci à tous les doctorants que j'ai appris à connaître, notamment grâce à l'organisation du barbecue ! Juliette DEFEBVIN-MARRANT, Nils GARVIK, Guillaume BELLINO, François HOUSAER, Antoine KRAYCH et Saadia OUCHIAR (gentille grande gueule).

Un merci particulier à mes 2 acolytes : Bertrand GIRARDIN et Benjamin PRIEUR, je vous promets que vous allez encore me supporter longtemps les amis ;-)

Un énorme merci à Laure ARBENZ. Grâce à toi les déplacements à Créteil se sont transformés en séjour de luxe, les 4* vont me manquer ! Bonne chance à Besançon et à très vite...

Merci à tous les copains et amis de l'école maternelle, de l'école primaire, du collège, du lycée, de la prépa, de l'école d'ingénieur et de l'escalade. C'est aussi grâce à vous que je suis qui je suis et que je suis arrivée au bout de cette thèse !

J'ai du mal à trouver les mots justes pour exprimer toute la gratitude que j'ai envers ma famille. Je ferais comme vous le dites toujours du « Claire », court et direct : MERCI ! (en étoffant un peu ça donne ça : merci d'être là et de m'avoir rendue indépendante mais surtout merci pour votre amour indéfectible).

Finalement, je souhaite remercier celui qui est à mes côtés depuis des années déjà et je l'espère pour longtemps encore. Il m'a toujours soutenu dans mes choix et mes projets et je lui en suis infiniment reconnaissante. Merci Clément Coquelle.

Table of contents

Remerciements	5
Table of contents.....	7
Symbols and abbreviations	11
Introduction.....	15
• Context of the PhD study	15
• Problematic	16
• Objectives and solving approach.....	17
1 Literature Review	23
1.1 Introduction.....	23
1.2 Iron-Silicon steel	23
1.2.1 Crystalline structure	23
1.2.2 Physical, mechanical and magnetic properties of iron-silicon steel	26
1.2.3 Effect of impurities	28
1.2.4 Influence of the rolling process	30
1.3 Fatigue phenomena.....	31
1.3.1 Fatigue test.....	31
1.3.2 Microstructural evolution	39
1.3.3 Iron-silicon steels.....	42
1.3.4 Conclusion	49
1.4 Fatigue damage characterisation	49
1.4.1 Topographic analysis of surface damage	50
1.4.2 Crystallographic based analyses.....	53
1.4.3 Conclusion	62
1.5 Conclusion	62
2 Material and experimental procedures	65
2.1 Composition and origin of the steel	65
2.2 Microstructure.....	65
2.3 Mechanical properties.....	66
2.3.1 Hardness.....	66
2.3.2 Tensile test	67

2.3.3	Cyclic stress-strain curve (CSSC)	68
2.4	Fatigue tests	70
2.5	Analysis techniques	72
2.5.1	Scanning Electron Microscope (SEM) observations	72
2.5.2	Transmission Electron Microscope (TEM) Observations.....	73
2.5.3	Controlled Electron Contrast Channelling Imaging (cECCI) observations	73
2.5.4	Electron Back-Scattered Diffraction (EBSD) measurements	73
2.6	Digital Image Correlation (DIC).....	75
2.7	Conclusion	78
3	Low cycle fatigue behaviour.....	83
3.1	Reference tests.....	83
3.1.1	Stress response to strain cycling	83
3.1.2	Work hardening.....	85
3.1.3	Fatigue resistance.....	86
3.1.4	Conclusion	87
3.2	Influence of testing parameters	88
3.2.1	Experimental protocol.....	88
3.2.2	Results	91
3.3	Conclusion	98
4	Fatigue damage mechanisms	101
4.1	Fracture surface observations.....	101
4.2	Crack initiation.....	102
4.3	Evolution of dislocation structures with $\Delta\varepsilon_t$	102
4.4	Discussion	104
4.5	Conclusion	110
5	Quantitative strain evaluation.....	115
5.1	Image Quality (IQ) and Line Segment Method (LSM)	115
5.2	Misorientation based analysis.....	119
5.2.1	Kernel based approach.....	120
5.2.2	Grain based approach	123
5.2.3	Summary of the results	124

5.3	Discussion	125
5.3.1	Dislocation structures and EBSD analyses.....	125
5.3.2	Strain estimation by EBSD analyses	129
5.3.3	Dislocation density for low strain variation estimation	135
5.4	Conclusion	137
6	Rotor design optimisation	141
6.1	Introduction.....	141
6.1.1	Context	141
6.1.2	Methodology	141
6.2	Choice of material model	143
6.2.1	Cyclic accommodation regimes.....	144
6.2.2	Work-hardening laws	144
6.2.3	Material model choice.....	149
6.3	Validation of the model.....	157
6.3.1	Fatigue lives estimation and comparison with the experiments	160
6.3.2	Strain distribution validation.....	161
6.4	Application to rotor sizing	162
6.4.1	Introduction.....	162
6.4.2	Refinement of the thickness of the leakage path (TLP)	164
6.4.3	Conclusion	169
6.5	Conclusion	171
	Conclusions and perspectives	175
	Conclusions.....	175
	Perspectives.....	177
	References.....	181
	Annexes	191
	Annex 1: EBSD – acquisition step choice.....	191
	Annex 2: Digital Image Correlation (DIC).....	194
	Annex 3: Rotor Tip Thickness (TT) refinement	200
	Annex 4: Summary of fatigue tests	205

Abstract	208
Résumé.....	208

Symbols and abbreviations

- Symbols

Symbol	Definition	Symbol	Definition
A	Elongation to fracture	K_{pw}	Fatigue resistance coefficient of the Pseudo-Wöhler relation
A_u	Uniform elongation	K_{wp}	Energy coefficient
b	Burger vector	λ	Magnetostriction
C_e	Fatigue resistance exponent of the Basquin relation	n	monotonic work-hardening exponent
C_i, γ_i	Chaboche material parameters	N	Number of cycle
C_p	Fatigue resistance exponent of the Manson-Coffin relation	N_f	Number of cycles to failure
C_{pw}	Fatigue resistance exponent of the Pseudo-Wöhler relation	N_f^{FEA}	Estimated number of cycles to failure by FEA
C_{wp}	Energy exponent	p	Cumulative plastic strain
Δε_e	Elastic strain variation	ρ	dislocation density
Δε_{ea}	Stabilised elastic strain variation	R	Isotropic hardening
Δε_p	Plastic strain variation	R_∞	Saturation value of the isotropic hardening
Δε_p/2	Plastic strain amplitude	R_ε	Strain ratio
Δε_{pa}	Stabilised plastic strain variation	σ	Stress
Δε_t	Total strain variation	S	Element size
Δσ	Stress variation	σ*	Effective stress
Δσ/2	Stress amplitude	σ_a	Stabilised stress amplitude
ε	Strain	σ_{a0}	Stress amplitude at 1/4 cycle
ε̇	Strain rate	σ_{fat}	Fatigue limit
E	Young modulus	σ_G	Internal stress
ε_{ea}	Stabilised elastic strain amplitude	σ_m	Mean stress
ε_p	Plastic strain	T	Temperature
ε̇_p	Plastic strain rate	T₀	Transition temperature
ε_{pa}	Stabilised plastic strain amplitude	T_C	Curie temperature
ε_{pa0}	Plastic strain amplitude at 1/4 cycle	τ_{relax}	Relaxation rate
ε_{xy}	Shear strain	UTS	Ultimate Tensile Strength
ε_y	Longitudinal strain	W_e	Elastic energy per cycle
HV	Vickers Hardness	W_p	Plastic energy per cycle
K	Monotonic work-hardening coefficient	X	Kinematic hardening
k	Stabilised yield stress	X_∞	Saturation value of the kinematic hardening
K_e	Fatigue resistance coefficient of the Basquin relation	YS	Yield Strength
K_p	Fatigue resistance coefficient of the Manson-Coffin relation		

- **Abbreviations**

Abbreviation	Definition
AFM	Atomic Force Microscopy
BCC	Body Centered Cubic
cECCI	controlled Electron Contrast Channelling Imaging
DIC	Digital Image Correlation
EBSD	Electron Back-Scatter Diffraction
ECCI	Electron Contrast Channelling Imaging
FCC	Face Centered Cubic
FEA	Finite Element Analysis
FWMH	Full Width at Half Maximum
GND	Geometrically Necessary Dislocation
GNO	Grain Non-Oriented
GO	Grain Oriented
GOS	Grain Orientation Spread
GROD	Grain Reference Orientation Deviation
HAGB	High Angle Grain Boundary
HCP	Hexagonal Close Packed
IPF	Inverse Pole Figure
IQ	Image Quality
KAM	Kernel Average Misorientation
LAGB	Low Angle Grain Boundary
LCF	Low Cycle Fatigue
LSM	Line Segment Method
ND	Normal Direction
OM	Optical Microscopy
PSB	Persistent Slip Bands
PSM	Persistent Slip Mark
RD	Rolling Direction
SEM	Scanning Electron Microscope
SRO	Short Range Order
SSD	Statistically Stored Dislocation
TD	Transversal Direction
TEM	Transmission Electron Microscope
TLP	Thickness of leakage path
TT	Tip thickness
XRD	X-Ray Diffraction

Introduction

Introduction

- **Context of the PhD study**

This PhD work is financially supported by the company Valeo, a French car supplier company, in the frame of a CIFRE agreement (Conventions Industrielles de Formation par la REcherche - Industrial Agreements for Training through Research) and was conducted both in the laboratory UMET (Unité Matériaux Et Transformations) located in Lille in France and Valeo Research center located in Créteil in France.

Since the regulation n°443/2009 of the European Parliament [CE09] establishing standards in terms of CO₂ emissions in lightweight vehicles, car suppliers and car makers are actively working both on vehicle mass reduction and motor efficiency. These aspects are essential to reach the goal of 95 grams of CO₂ per kilometre for the new light vehicles in 2020 [CE09]. In this frame Valeo has chosen to develop new electrical system solutions. Indeed, in 2004 Valeo proposed the machine “StARS” (Starter-Alternator Reversible System) which replaces the conventional starter and alternator with a single component. It is built on the basis of an alternator which can work reversibly in motor mode to start the engine with the power it exerts over the front belt on the crankshaft (Figure - 1). These machines are particularly useful in city driving, where vehicles are stationary about 35% of their time, with the unnecessarily running of the engine. The stop&start function enables to turn off the engine when the vehicle is stationary and restart it immediately and silently when the drivers manifest intention to leave. A reduction of fuel consumption and emissions of about 10% can be reached [VAL04].

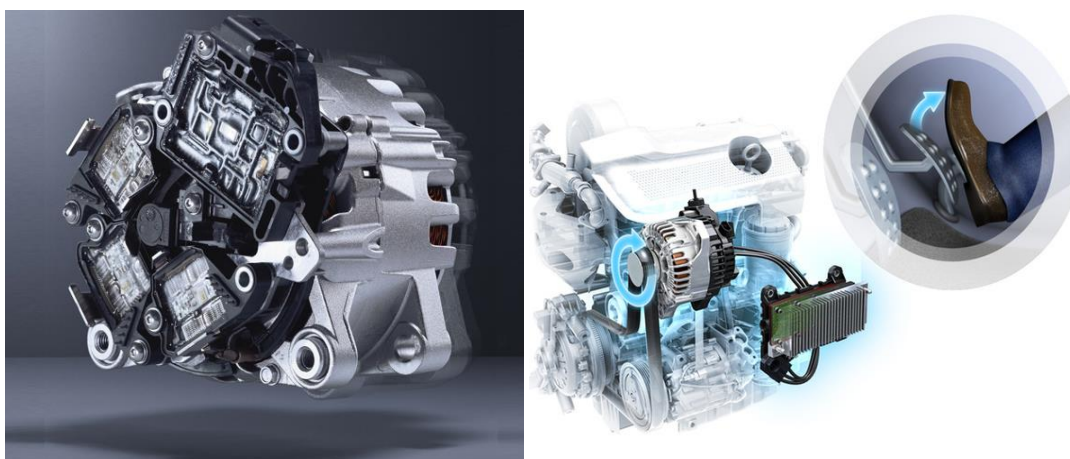


Figure - 1: The StARS system mounted on engine [VAL15]

Hence, the development of reversible machines within Valeo is constantly ongoing. In the present case, one of the new solutions adopted by Valeo is the development of cylindrical reversible machines composed of a rotor made of a stack of thin sheets of Fe-3Si non-oriented electrical steel.

This rotor consists in the repetition of several pair of poles between which magnets are placed, as shown in Figure - 4 and the rotation of the rotor induces an electric field in the stator windings of the alternator.

Due to the stop&start function which induces cyclic loading and the complex geometry of the rotor (Figure - 4) which induces the presence of stress concentrators, low cycle fatigue is suspected to occur. The considered cyclic loadings does not result from the cyclic rotation of the rotor in the stationary regime but from the transitory regime due to the complete arrest and the subsequent restart of the alternator.

- **Problematic**

The design of the rotor is based on the Haigh diagram construction [VAN12]. The latter is used in order to validate component design subjected to cyclic loading from the mechanical point of view. This diagram is based on the Goodman relation (equation 1) where σ_{al} is the alternating stress (equation 2), σ_m is the mean stress (equation 3), σ_{fat} , the fatigue limit for completely reversed loading and UTS, the Ultimate Tensile Strength of the material.

$$\sigma_{al} = \sigma_{fat} \times \left(1 - \frac{\sigma_m}{UTS}\right) \quad (1)$$

$$\sigma_{al} = \left(\frac{\sigma_{max} - \sigma_{min}}{2}\right) \quad (2)$$

$$\sigma_m = \left(\frac{\sigma_{max} + \sigma_{min}}{2}\right) \quad (3)$$

This relation is used to evaluate the interaction between mean stress and alternating stress on the fatigue life of the considered material [HER97]. The trend is that increasing the mean stress (σ_m) for a given alternating stress (σ_a) decreases the fatigue life. This relation is plotted in a graph (Figure - 2) where σ_a is plotted versus σ_m with UTS placed on the abscissa axis and σ_{fat} placed on the ordinate axis. If the coordinates given by the mean stress and the alternating stress of a component lies below the line formed by the UTS and σ_{fat} , the component will handle the loading without breaking. On the other hand, if σ_a and σ_m lie above the line, the part will fail for the given cyclic load.

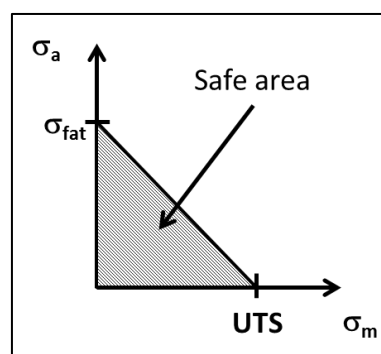


Figure - 2: Construction of the Haigh diagram

Up to now, no failure of the rotor of the starter-alternator mock-ups has been encountered, probably due to oversizing. Nevertheless the improvement of the electro-technical properties of the reversible machine suggests promoting small controlled cyclic plastic deformation in localised zones of the rotor.

It has been shown that monotonic plastic straining of Fe-3Si steel decreased its magnetic properties [IOR04] and a recent study [ALA15] showed that cyclic loadings also decrease magnetic materials properties even in the elastic regime (Figure - 3). But if controlled, the modification of the material magnetic properties can be beneficial. Indeed, if magnetic saturation is reached in zone 1 and 2 of the rotor (Figure - 4), current loss can be reduced and thus increase the machine performances. This can be reached by plastic straining induce by low cycle fatigue in these zones.

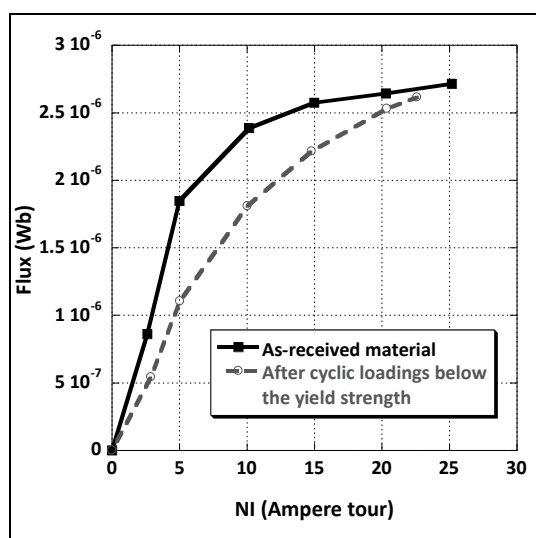


Figure - 3: Deterioration of the Fe-3Si magnetic properties after cyclic loadings below the yield strength [ALA15]

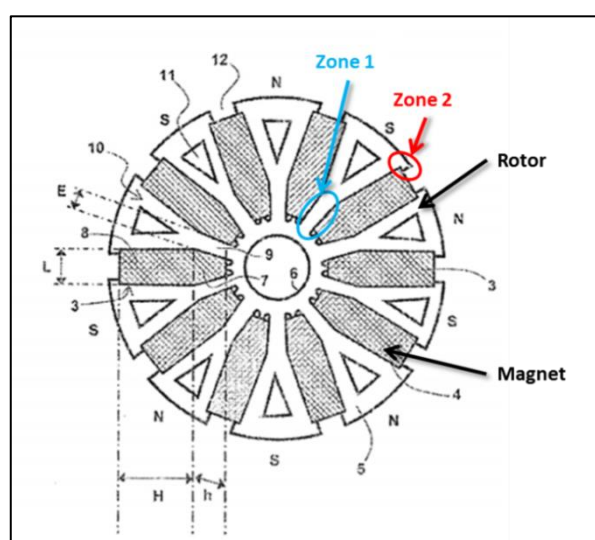


Figure - 4: Example of the complex geometry of a rotor [LEG11]

Therefore, it is proposed in the frame of the PhD thesis to optimise the sizing of the rotor while preventing mechanical rupture during use and also to improve electro-technical properties. For that purpose, the fatigue behaviour of the Fe-3Si steel, which is the rotor constituent material, is studied in detail in order to be able to answer the following questions:

1. What is the behaviour of the Fe-3Si thin steel sheet subjected to low cycle fatigue and the damage mechanisms leading to rupture?
2. How to localise and evaluate the fatigue damage at a mesoscopic scale in order to localise in a component probable crack initiation sites?
3. How to include the fatigue data in the rotor design in order to improve the machine performances while remaining mechanically reliable?

- **Objectives and solving approach**

The main objectives of this work are:

1. The understanding of cyclic plasticity and damage mechanisms of the Fe-3Si steel.
2. The development of a method to assess local cyclic strain and measurement of plasticity levels at a mesoscopic scale.
3. The improvement of the electromagnetic properties of the starter-alternator by taking into account fatigue properties of the material in the rotor sizing by a numerical approach.

To reach these goals, a study of the material is first conducted which consists in fatigue testing and microstructural investigations to understand cyclic damage accommodation mechanisms. Secondly, a method to quantitatively evaluate the strain is proposed. Finally, a numerical study is conducted which consists in defining a valid material behaviour law and in the modification of the rotor geometry in order to obtain improved machine performances.

This manuscript presents the results of this study and is divided in six chapters.

- The first chapter is a literature review. The iron-silicon steels and their properties are first presented followed by general aspects about low cycle fatigue testing. A synthesis of damage mechanisms in iron and iron-silicon steel is then given. Finally, fatigue damage characterisation techniques of metals are reviewed.
- The second chapter introduces the chemical composition, microstructure and monotonic mechanical properties of the material of the study. Then, the different experimental techniques are detailed. Fatigue testing is performed on flat specimen with control of the total strain variation and a zero strain ratio with the maximum strain between 0.3% and 1%.
- In the third chapter, the low cycle fatigue study of the material is presented. The mechanical behaviour of the material is obtained. The influence of several testing parameters, such as strain rate, strain ratio or specimen surface finishing, is also investigated.
- The chapter four is dedicated to the study of the damage mechanisms. The crack initiation sites and crack propagation are shown but the main investigation consists in the study of the evolution of the dislocation structures with the total strain variation by Transmission Electron Microscope (TEM) and controlled Electron Channelling Contrast Imaging (cECCI). An interpretation of this evolution is given based on the evolution of effective and internal stresses. It showed a transition between high and low temperature regime based on the total strain variation.
- As the damage mechanisms were identified, a quantitative evaluation of the strain by the EBSD method at a mesoscopic scale is studied in the fifth chapter. EBSD based analyses are performed on fatigued samples at different total strain variations and different EBSD criteria

are studied. A method for strain estimation is proposed and validated in the case of a complex shape analysis.

- The chapter six is dedicated to the numerical study. A material law is defined based on experimental study. Then, after model validation, slight modification of the rotor design is performed by finite element modelling.

<p style="text-align: center;"><u>Problematic</u></p> <ol style="list-style-type: none">1. What is the behaviour of the Fe-3Si steel in the form of thin sheet subjected to low cycle fatigue and the damage mechanisms leading to the rupture of the component?2. How to localise and evaluate the fatigue damage at a mesoscopic scale?3. How to integrate the fatigue data in the rotor design in order to improve the machine performances while remaining mechanically reliable?
<p style="text-align: center;"><u>Objectives</u></p> <ol style="list-style-type: none">1. Development of a method to localise and measure plasticity at a mesoscopic scale2. Improvement of the properties of the starter-alternator by taking into account fatigue properties of the material in the rotor sizing
<p style="text-align: center;"><u>Chapter 1: Literature review</u></p> <ol style="list-style-type: none">1. Presentation of iron-silicon steels2. Fatigue testing and fatigue behaviour of iron and silicon-iron steels3. Fatigue damage characterisation methods
<p style="text-align: center;"><u>Chapter 2: Material and experimental procedures</u></p> <ol style="list-style-type: none">1. Presentation of the material. Chemical composition and origin of the steel, microstructure and monotonic mechanical properties2. Presentation of the analysis techniques
<p style="text-align: center;"><u>Chapter 3: Low cycle fatigue behaviour</u></p> <ol style="list-style-type: none">1. Mechanical behaviour of the material obtained from the reference test2. Study of the influence of testing parameters
<p style="text-align: center;"><u>Chapter 4: Fatigue damage mechanisms</u></p> <ol style="list-style-type: none">1. Fracture and crack initiation observations2. Study of the evolution of dislocation structures
<p style="text-align: center;"><u>Chapter 5: Quantitative strain evaluation</u></p> <ol style="list-style-type: none">1. EBSD analyses on deformed samples2. Strain estimation in the case of strain localisation in a notched sample
<p style="text-align: center;"><u>Chapter 6: Rotor design</u></p> <ol style="list-style-type: none">1. Material law definition and material model validation2. Rotor sizing modifications and increased performances of the machine

Chapter I:

Literature review

1. Introduction
2. Iron-Silicon steel
3. Fatigue phenomena
4. Fatigue damage characterisation
5. Conclusion

1 Literature Review

1.1 Introduction

The iron-silicon steels are also known as « electrical steel ». They are produced to obtain particular magnetic properties such as magnetic permeability and small hysteresis surfaces of the magnetic curves. These steels are soft magnetic materials and more precisely ferromagnetic materials. They are easily magnetised under an external magnetic field. Their principal interest is that their magnetisation is an economically acceptable magnetic induction source [BAV92].

The iron-silicon steels sheets are produced by a rolling process. According to the process parameters [MOS90], iron-silicon steel sheets can be:

- grain oriented, for static equipment such as transformers
- non grain-oriented, for the construction of rotating machines such as generators, alternators, engines

The present study is devoted to the understanding of the low fatigue behaviour of non-oriented silicon iron steel used in car starter-alternator. Therefore, the literature review focuses, first, on the iron-silicon steels, their crystalline structure and their properties, the role of the impurities and finally the influence of the rolling process on the texture. Then, low cycle fatigue is presented with special attention to BCC metals and more particularly α -iron. A state of the art regarding plasticity mechanisms in the Fe-3Si steel is given afterward. Finally, the general tools employed to characterise cyclic damage are considered.

1.2 Iron-Silicon steel

Steel is an iron-based material with carbon content usually below 2% in weight and other alloying elements added voluntary, such as silicon for its electrical properties, or present as casting impurities.

The iron and iron-carbon structure are presented to better understand the iron-silicon steel microstructure and its specificity.

1.2.1 Crystalline structure

1.2.1.1 Iron and iron-carbon diagram

The crystalline structure of iron is modified as a function of the temperature. Indeed, iron undergoes two allotropic transformations (two modifications of its network lattice, Figure 1-1).

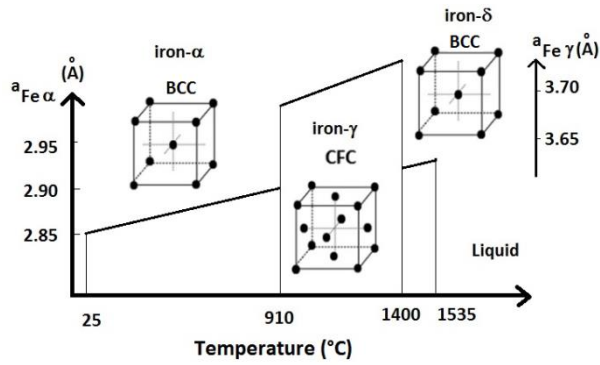


Figure 1-1 : Crystalline structure of iron

The pure α -iron is magnetic up to 768°C corresponding to the Curie temperature (T_C). Below T_C , iron is ferromagnetic, it keeps a residual magnetisation even when not subjected to an external excitation field. Above T_C , iron becomes paramagnetic and is magnetised under the influence of an external magnetic field, but if the field is switched off the magnetisation disappears. The industry is interested by the ferromagnetic property of the iron-silicon steels which enables cost efficient magnetisation process.

When carbon is added to iron, different phases can be formed depending on the carbon content, the presence of alloying elements and the cooling rate. In the case of carbon as alloying element, the metastable Fe-Fe₃C equilibrium diagram can be drawn (Figure 1-2). Fe₃C is metastable, indeed, if cooling rate is slow enough, it decomposes in α -ferrite and graphite.

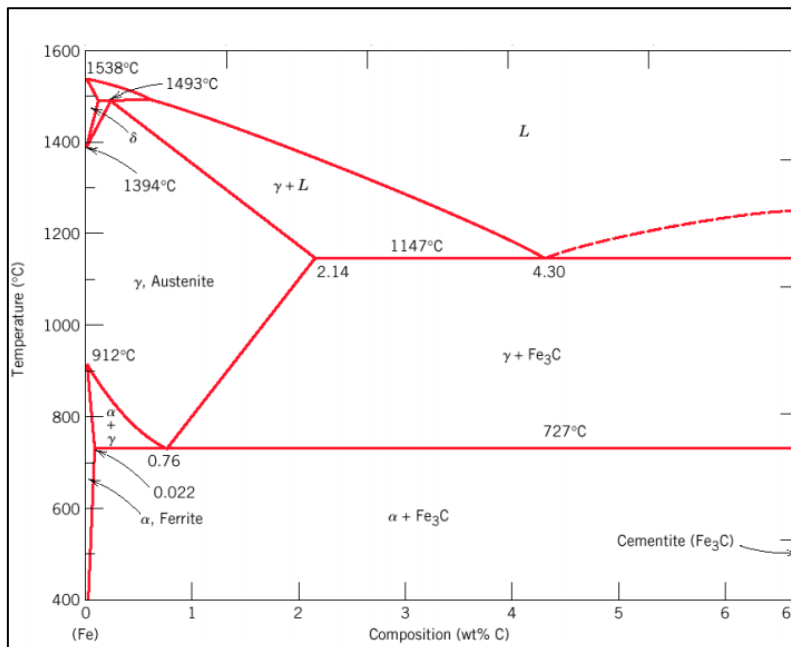


Figure 1-2 : Metastable diagram Fe-Fe₃C [CAL07]

Alloys with carbon content lower or up to 2.14 wt.% C are called steels and those whose carbon content is above 2.14% C are called cast iron. This limit is the maximum solubility of carbon in

austenite. Unalloyed steels are classified according to their carbon content: mild steels (wt.% C<0.3), medium-hard steel (0.3<wt.% C<0.6) and hard steels (wt.% C>0.6). The increase of the carbon content increases the mechanical properties (hardness, elastic limit ...) but decreases the ductility, the elongation to fracture, impact resistance and weldability.

1.2.1.2 Iron-silicon diagram

The binary iron-silicon diagram is given in Figure 1-3. Compared to iron-cementite diagram, when the Si content increases, the temperature of the $\alpha \rightarrow \gamma$ transformation is increased and the temperature of the $\gamma \rightarrow \delta$ transformation is decreased. The austenitic domain is narrow and the crystal structure of alloy containing more than 2.5 wt.% Si is that of α -iron (Body-Centered Cubic) at all temperatures up to its melting temperature.

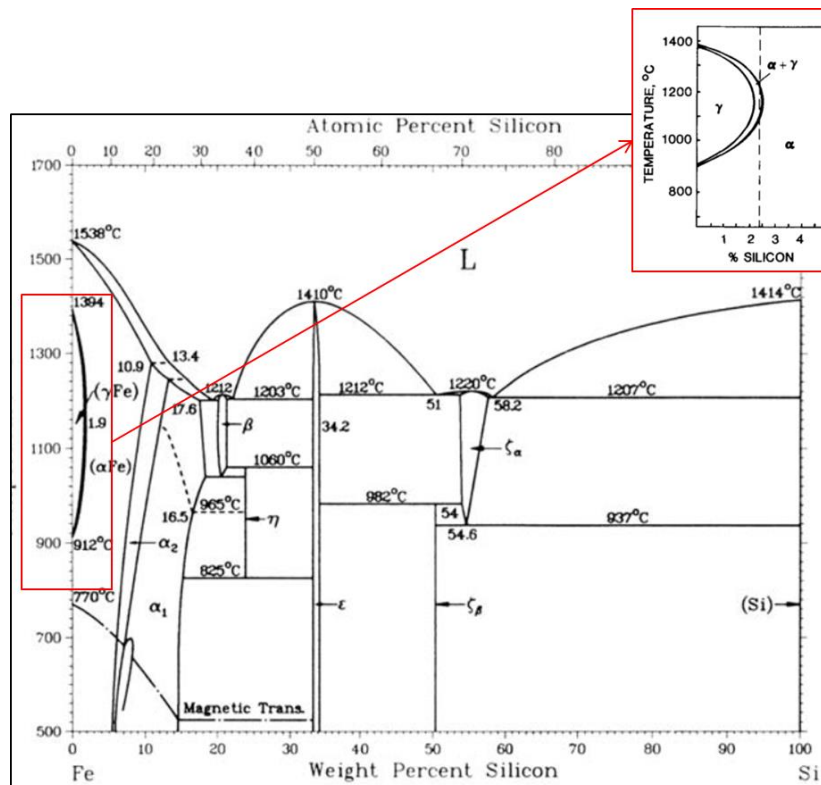


Figure 1-3: Iron-silicon binary diagram [PET10]

The domains α_1 and α_2 correspond to more ordered structures compared to the α domain. Indeed, the α domain corresponds to a solid solution of Fe-Si with the BCC structure while the domain α_2 corresponds to a B2 type structure and the domain α_1 to a D0₃-type structure, as illustrated in Figure 1-4 [GON13].

The presence of carbon in these alloys expands the region ($\alpha+\gamma$) and only 0.07% C shifts the nose of the γ domain up to 6% Si but in practice the carbon content in the electrical steel is less than 0.01% C [VIA72] to stay in the domain α .

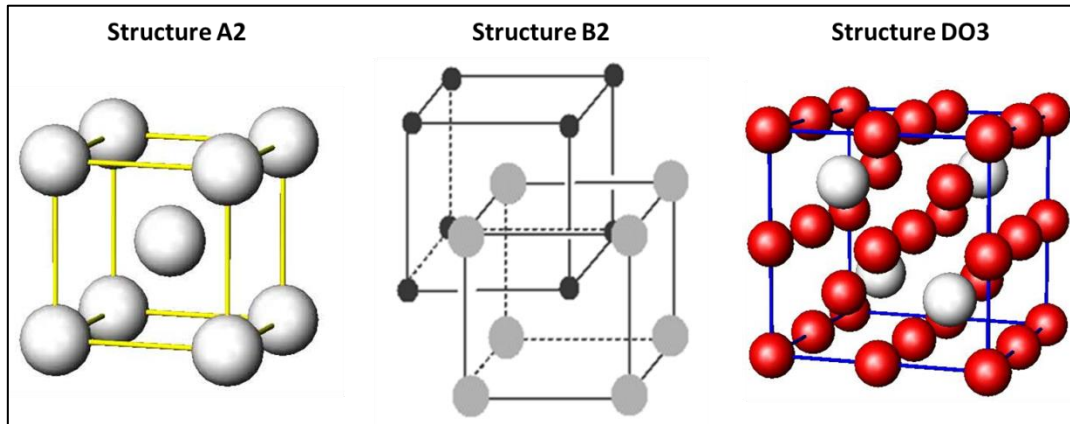


Figure 1-4: Crystalline structures obtained for iron-silicon alloys with $2.5 < \text{wt.\% Si} < 15$

1.2.2 Physical, mechanical and magnetic properties of iron-silicon steel

Silicon modifies several properties of iron, its effect can be either beneficial either detrimental [VIA72].

- The **density**, d , of iron-silicon alloys is affected according to equation (1-1) at 25°C.

$$d = 7830 - 67x\%Si \text{ (kg.m}^{-3}\text{)} \quad (1-1)$$

- The **yield strength** increases with the amount of silicon up to 4.5%wt Si.
- The **elongation to fracture** at ambient temperature decreases above 2.5%wt Si, at 5%wt Si the steel sheet is brittle.

The evolution of magnetic properties of Fe-Si with Si content is summarised in Figure 1-5.

- The **resistivity** increases up to 11%wt Si. A higher resistivity reduces eddy current losses.
- The **saturation induction**, B_s , is the state reached when an increase in the applied external magnetic field H cannot increase the magnetization of the material further. It evolves in a linear way according to equation (1-2) [MAT84].

$$B_s = 2.16 - 0.48x\%Si \text{ (T)} \quad (1-2)$$

- Magnetostriction** is a property of ferromagnetic materials that causes them to change their shape or dimensions during the process of magnetisation. The variation of materials' magnetisation due to the applied magnetic field changes the magnetostrictive strain until reaching its saturation value, λ .
- Magnetocrystalline anisotropy**, K_1 , is encountered in ferromagnetic material when it takes more energy to magnetise it in certain directions than in others, these directions are usually

related to the principal axes of its crystal lattice. Its evolution follows the equation (1-3) [MAT84].

$$K_1 = 12 + 11x\%Si \text{ (}\mu\Omega\cdot\text{cm)} \quad (1-3)$$

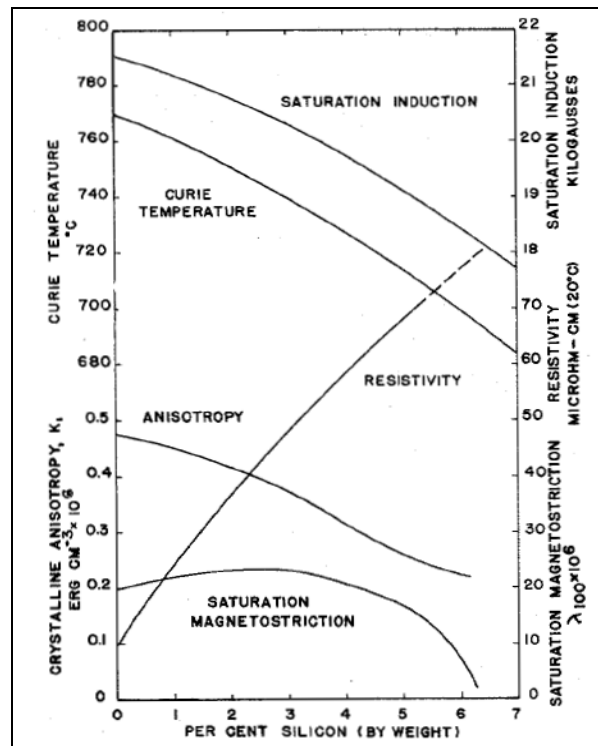


Figure 1-5: Important properties of iron-silicon alloys according to the composition [LIT71]

- **Grain orientation.** The easy magnetisation direction is [001] (Figure 1-6), it corresponds to the energetically favourable direction of spontaneous magnetisation.

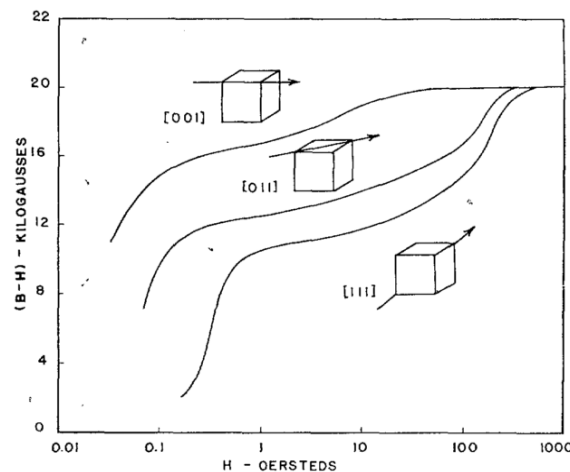


Figure 1-6: Effect of crystalline orientation on magnetization of a Fe-Si crystal [LIT71]

- **Grain size.** Above 1 mm in diameter, there is a reverse effect of the grain size on ferromagnetic losses (Figure 1-7); there is an increase in total losses due to eddy currents generated by the movement of the walls [SHI89].

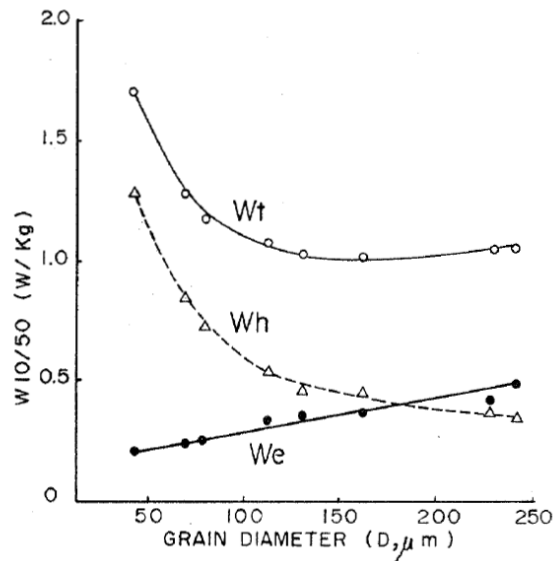


Figure 1-7: Effect of grain diameter on hysteresis loss W_h , Eddy current loss W_e and core loss W_t [MAT84]

- **Thickness**, the finest sheets tend to experience greater hysteresis losses, probably because of the greater magnetostatic energy associated with crystals having a favourable orientation not parallel to the surface.
- **Stress and strain**, the tensile stress eases the process of magnetisation and reduces hysteresis loss. Conversely, the compressive stresses interfere with the magnetisation. The effect depends on the crystal orientation and therefore varies according to the direction of the sheet.
- The **temperature** increases the resistivity and reduced hysteresis loss, thereby improving the magnetic properties. However, the saturation magnetisation is also reduced.

1.2.3 Effect of impurities

Impurities are present due to the industrial process. The harmful effect of interstitials (C, N, and O) is detailed hereafter. Interest will be also given to aluminium which is another interesting element as it improves the sheet characteristics.

- **Carbon**

The presence of carbon in Fe-Si increases the γ domain and, as mentioned in §1.2.1.2, only 0.07% C shifts the nose of the γ domain up to 6% Si [VIA72]. This silicon amount is too high in regard to ductility. The limitation of carbon is obtained by a decarburisation annealing or vacuum degassing during the process. Thus, the obtained amount of carbon can be less than 0.005% [SHI82].

- **Oxygen and nitrogen**

O and N are present as interstitials and seem to decrease electrical resistivity [ARA84]. To minimise the N content, aluminium is added to form nitride AlN that are not detrimental particles. The amount of oxygen is also decreased by the deoxidiser property of aluminium. The oxygen quantity can be

reduced by half with Al content comprised between 0.009 and 0.45wt.% because of the formation of Al_2O_3 particles [ARA84].

- **Sulfur**

Sulfur is a grain growth inhibitor due to the formation of fine MnS precipitates [MAT84]. The optimum grain size which is $150\mu m$ is obtained with 10ppm of S (Figure 1-8).

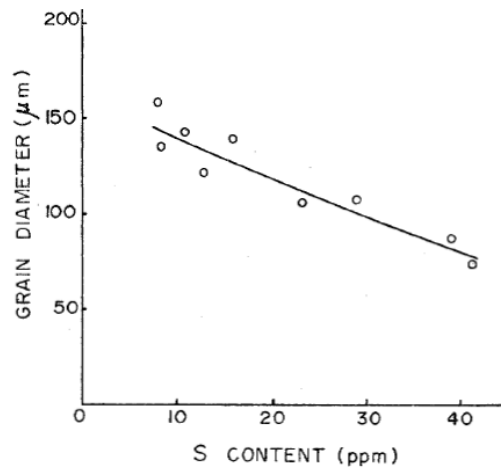


Figure 1-8: Effect of S content on grain diameter [MAT84]

- **Aluminium**

In addition to the use of aluminium to form AlN nitrides and Al_2O_3 oxides, it is of common use to add aluminium to Fe-Si alloy and form ternary compound FeSiAl. The Si + Al content remains always below 4.5% because of brittleness. The addition of aluminium has beneficial effect on the core loss (Figure 1-9).

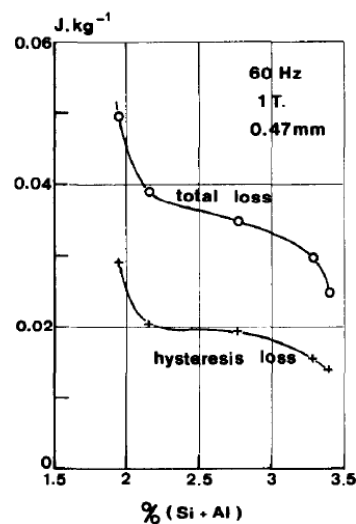


Figure 1-9: Total and hysteresis losses in NO sheets versus Si+ Al composition [BRI80]

1.2.4 Influence of the rolling process

As mentioned in the introduction, iron-silicon sheets can be grain-oriented (GO) or grain non-oriented (GNO) depending on the applied rolling process.

- Grain oriented sheets are employed in the construction of transformers in which their magnetic properties in the rolling direction can be exploited at best. Its production route is detailed in Figure 1-10. The obtained sheets have a Goss texture $[100]\{110\}$.
- Non-oriented sheets are used in rotating machine for which isotropic properties are needed. The process to obtain these sheets is detailed in Figure 1-11. The ideal texture for these steels is $(100)\langle 0vw \rangle$.

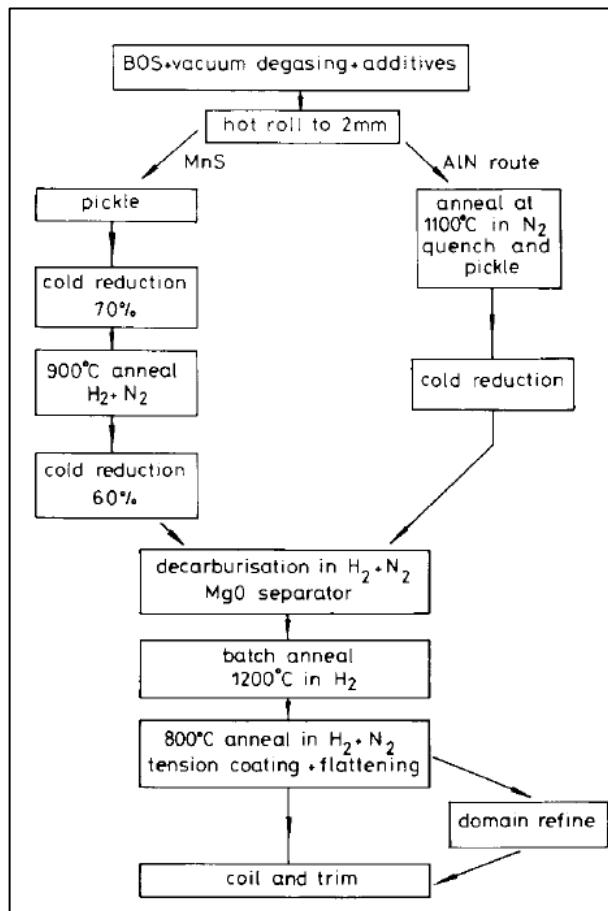


Figure 1-10: Production route of conventional (via MnS route) and high permeability (via AlN route) GO Fe-Si [MOS90]

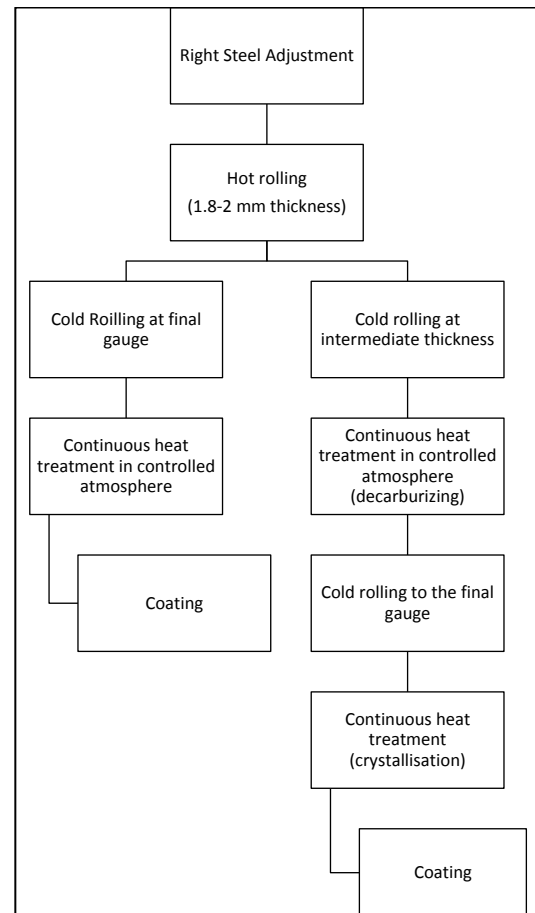


Figure 1-11: Production route of NO Fe-Si sheet [BRI80]

The Fe-3% Si steel of the study is a BCC ferritic steel and non-oriented, it is used for its magnetic properties in car starter-alternator. The purpose of the thesis is the study of its fatigue behaviour that is to say its behaviour under cyclic loadings.

1.3 Fatigue phenomena

Fatigue is the progressive and localised structural damage that occurs when a material is subjected to cyclic loading which can lead to the rupture of the component. For a smooth specimen or component, fatigue failure occurs in three steps:

- The initiation of crack(s) at the surface of the material with a length of a grain size
- The growth and coalescence of short cracks at the surface to form macrocrack
- The propagation into the bulk of the macrocrack

This is studied with specific tests: the two first steps with fatigue test on smooth specimen and the third step with fatigue-propagation test on pre-notched specimen. In the present work, only fatigue test for crack initiation investigation is considered.

1.3.1 Fatigue test

1.3.1.1 Introduction

A smooth sample is subjected to a cyclic stress amplitude $\Delta\sigma/2$ until rupture. The number of cycles to failure is related to the applied stress amplitude and by repeating the test at different stress amplitudes, it is possible to draw the Wöhler S-N curve presented in Figure 1-12.

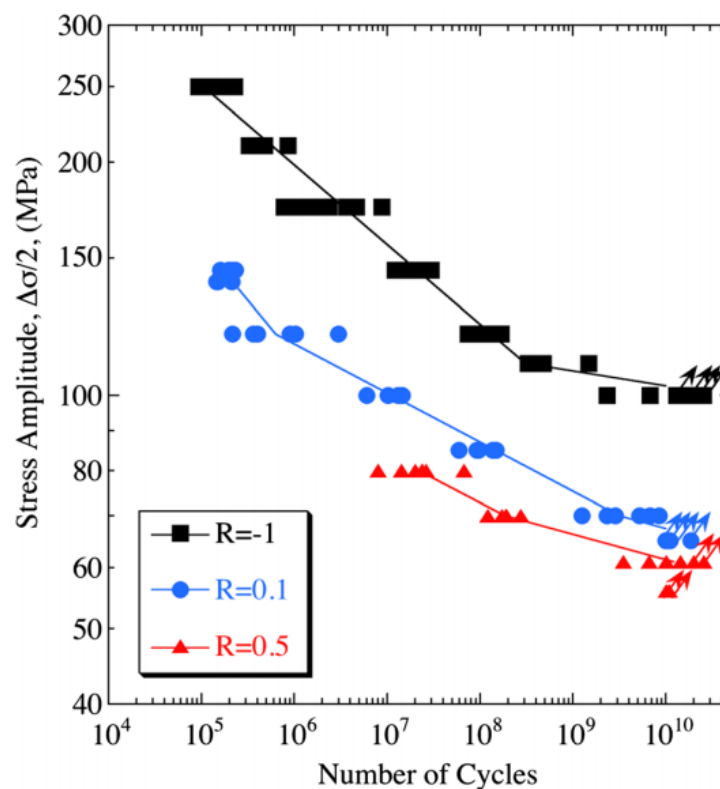


Figure 1-12: S-N curve and schematics of stable hysteresis loops at various fatigue lives [MAY16]

On S-N curves curve, different zones, corresponding to different fatigue regimes, are considered:

- Up to $N_f = 10^5$ cycles, the stress is sufficiently high to induce macroscopic plastic strain of the specimen. It corresponds to the low cycle fatigue (LCF) regime
- For $10^5 < N_f < 10^7$, the material is globally in the elastic regime, it corresponds to the high cycle fatigue (HCF) regime

Up to late 90's, it was thought that there existed a fatigue limit under which fatigue life was unlimited. It is known now that is not true and that even for $N_f > 10^7$ the material finally fails. In this case, the material is loaded in the gigacycle fatigue regime [BAT99;FUR02;MAY16]

In the present work, only LCF with plastic straining is considered.

1.3.1.2 Low Cycle Fatigue (LCF)

In LCF test, the specimen is subjected to a maximum stress exceeding the yield strength of the material involving a plastic deformation of the specimen. In LCF tests the control mode is generally the total strain and hysteresis loop (σ - ε) are periodically recorded as well as the number of cycles to failure.

1.3.1.2.1 Fatigue accommodation

From a hysteresis loop representing the evolution of the stress with the strain for each cycle, the stress amplitude $\Delta\sigma/2$, the total strain variation $\Delta\varepsilon_t$, plastic strain variation $\Delta\varepsilon_p$ and elastic strain variation $\Delta\varepsilon_e$ are obtained as shown in Figure 1-13. Then the evolution of the stress during cycling is recorded. The cyclic response is characterised by three steps:

- **Cyclic accommodation:** the stress amplitude evolves with cycling, hysteresis loops are open. If the stress amplitude increases, the material hardens and if it decreases, the material softens. Both situations can occur during the same cycling. The accommodation period is shorter or longer depending on the test conditions (type of material, strain amplitude, temperature...)
- **Stabilisation:** the stress stabilised and the hysteresis loops are closing. This period represents generally the major part of the life and is representative of the material's behaviour. Consequently, it is on these hysteresis loops that characteristic properties are taken.
- **Cracking:** the stress decreases strongly, indicating the propagation in volume of a macroscopic crack. The specimen breaks rapidly.

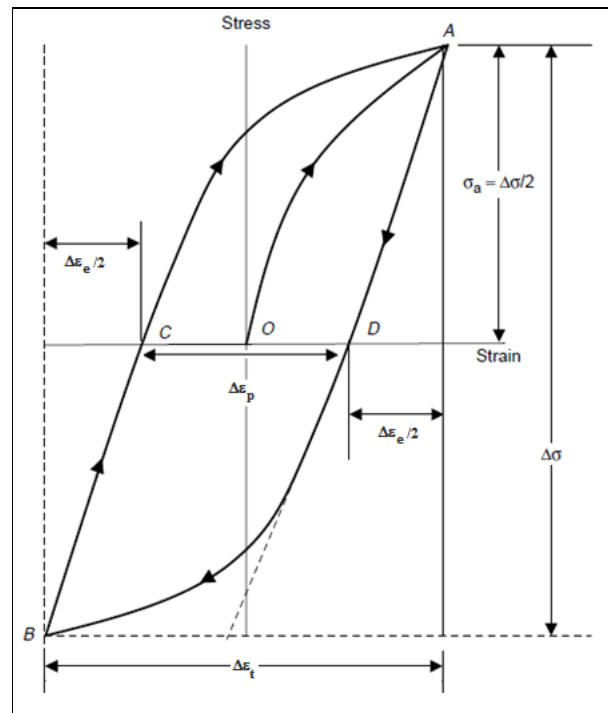


Figure 1-13: Hysteresis curve of the stress versus the strain

To compare different tests, or show the different phases, the stress amplitude is plotted against the number of cycles or versus the percentage of lifetime (Figure 1-14 (a) and (b) respectively). The first diagram is generally drawn with a logarithmic abscissa axis to better assess the changings at the beginning of the cycling.

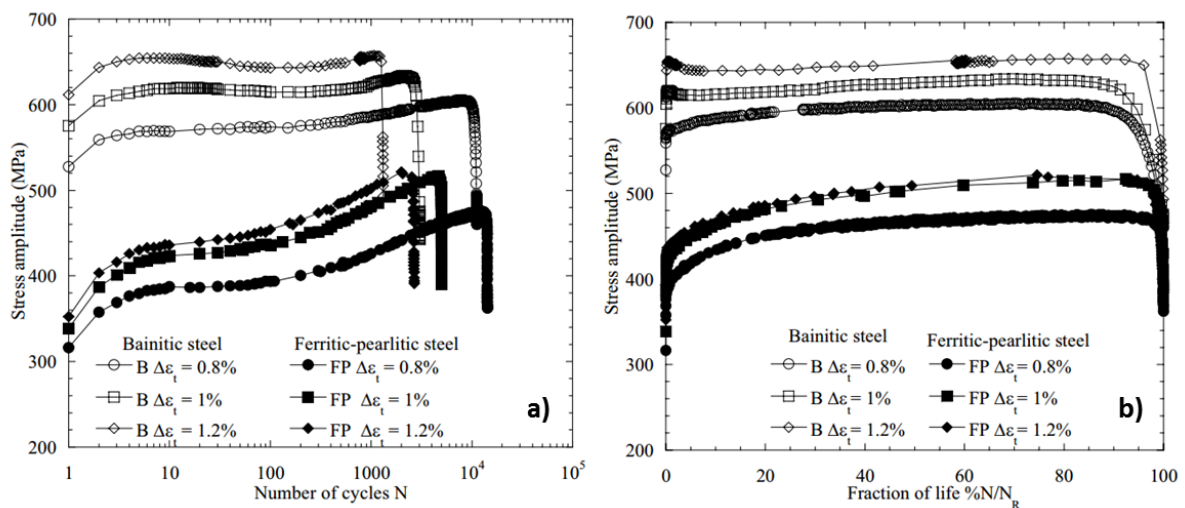


Figure 1-14: Example of the evolution of the stress with the number of cycles (a) and with the percentage of lifetime (b) for bainitic and ferritic-bainitic steel [BUL10]

1.3.1.2.2 Work-hardening

The evolution of the material during the cyclic loadings is different whether there is cyclic softening or cyclic hardening. It is possible to compare monotonic and cyclic properties of the material by plotting the stress amplitude versus the plastic strain amplitude as show in Figure 1-15. The

hysteresis curve representative of the stabilised phase is used for the cyclic curve and the tensile curve or the first quarter of the first cycle of the fatigue test is considered for the monotonic curve.

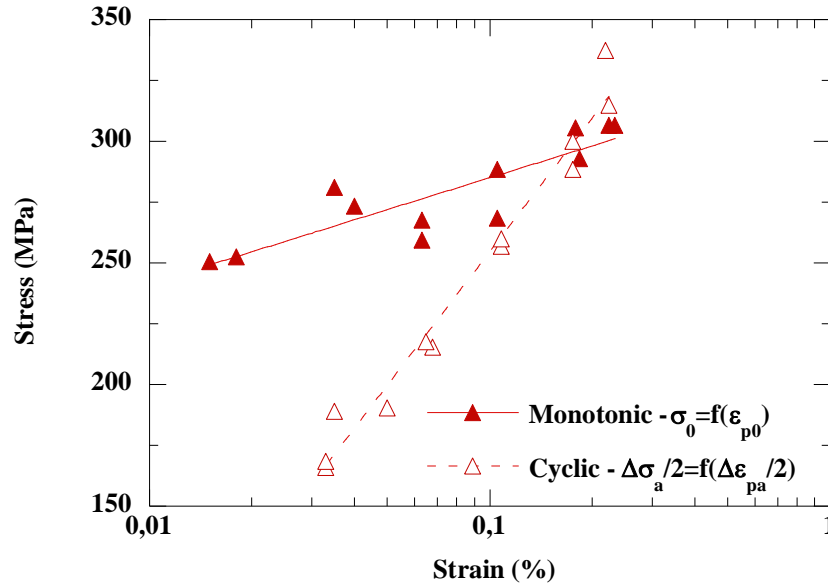


Figure 1-15 : Example of the cyclic and monotonic stress-strain curves for a polycrystalline ferritic steel [LEA11]

Monotonic work-hardening is defined by the equation (1-4).

$$\sigma_0 = K(\varepsilon_{p0})^n \quad (1-4)$$

With σ_0 , the maximum stress at the $\frac{1}{4}$ cycle, ε_{p0} the plastic strain at the $\frac{1}{4}$ cycle, n the monotonic work-hardening exponent and K the the monotonic work-hardening coefficient.

Cyclic work-hardening is defined by the equation (1-5).

$$\frac{\Delta\sigma_a}{2} = K' \left(\frac{\Delta\varepsilon_{pa}}{2} \right)^{n'} \quad (1-5)$$

With $\Delta\sigma_a/2$, the stress amplitude at stabilised state, $\Delta\varepsilon_{pa}/2$ the plastic strain amplitude at stabilised state, n' the cyclic work-hardening exponent and K' the cyclic work-hardening coefficient.

1.3.1.2.3 Fatigue resistance

- Manson-Coffin and Basquin laws

The Manson-Coffin curve represents the evolution of the plastic strain variation with the number of cycles to failure (circles in Figure 1-16). It follows a power function in accordance with Manson-Coffin law defined in equation (1-6).

$$\Delta\varepsilon_{pa} = K_p (N_f)^{C_p} \quad (1-6)$$

With $\Delta\varepsilon_{pa}$ the plastic strain variation at the stabilised stage, K_p the fatigue resistance coefficient and C_p the fatigue resistance exponent.

This relation is completed by the Basquin law defined in equation (1-7) and represented with the triangles in Figure 1-16.

$$\Delta\varepsilon_{ea} = K_e(N_f)^{C_e} \quad (1-7)$$

With $\Delta\varepsilon_{ea}$ the elastic strain variation at the stabilised stage, K_e the fatigue resistance coefficient and C_e the fatigue resistance exponent.

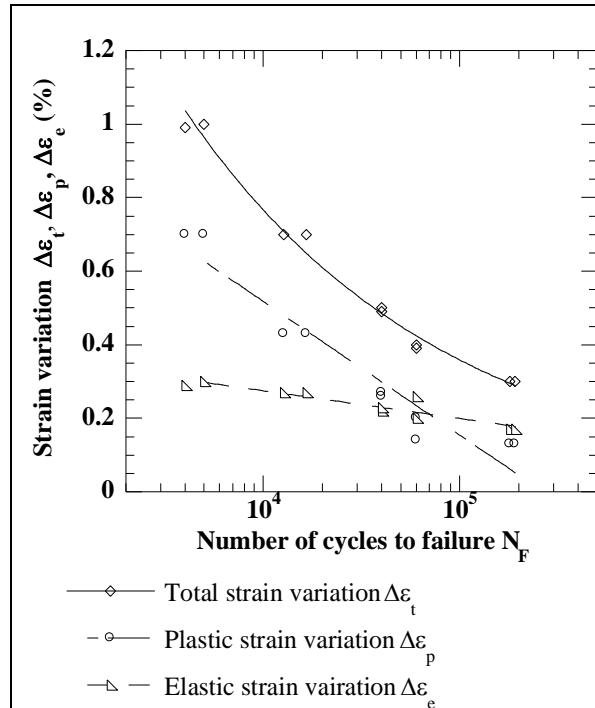


Figure 1-16: Example of the Manson-Coffin and Basquin curves for a polycrystalline ferritic steel [LEA11]

- Pseudo-Wöhler

Figure 1-17 represents the stress amplitude with the number of cycles to failure. It follows generally the power law of the pseudo-Wöhler relation (equation 1-8).

$$\sigma_a = K_{PW}(N_f)^{C_{PW}} \quad (1-8)$$

With σ_a , the stabilised stress amplitude, K_{PW} pseudo-Wöhler coefficient and C_{PW} pseudo-Wöhler exponent.

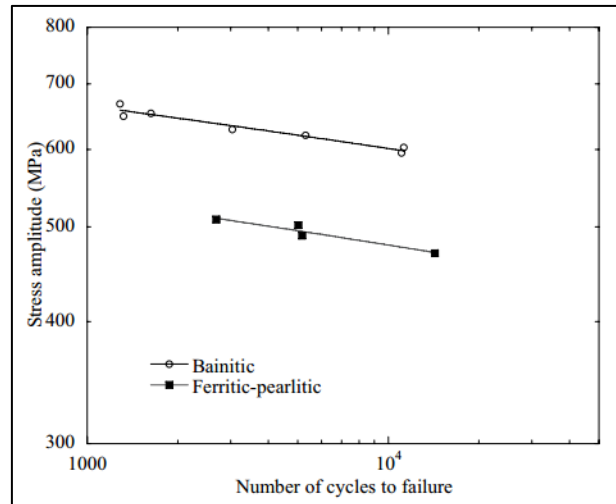


Figure 1-17: Example of the Pseudo-Wöhler curve for bainitic and ferritic-bainitic steels [BUL10]

- Criterion based on the energy density of cyclic deformation

The dissipated energy by mechanical hysteresis is related to the damage undergone by fatigue. In LCF, the plastic energy per cycle W_p can be plotted versus the lifetime (Figure 1-18) because plastic strain is important. For longer lifetimes (lower straining), the elastic energy W_e and total energy W_t of the stabilised cycle should be considered (equation 1-9 and 1-10).

$$W_t = W_e + W_p \quad (1-9)$$

$$\Delta W_p = A \sigma_a \cdot \Delta \varepsilon_{pa} = K_{Wp} (N_R)^{C_{Wp}} \quad (1-10)$$

with A , a constant of the material, σ_a the stress amplitude at the stabilised state and $\Delta \varepsilon_{pa}$ the plastic strain amplitude at the stabilised state and K_{Wp} the energy coefficient and C_{Wp} the energy exponent.

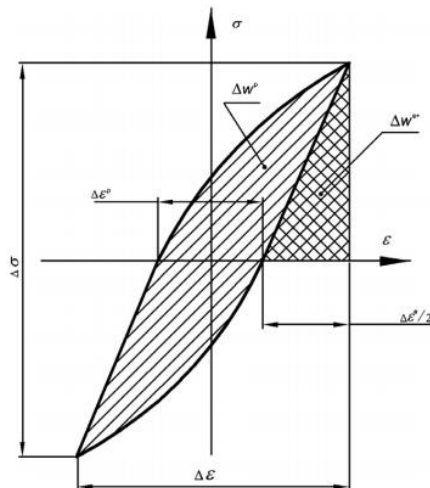


Figure 1-18 : Elastic and plastic energy in a hysteresis curve [MAG82]

The general aspects of fatigue accommodation in term of cyclic stress evolution have been presented here as well as work hardening and fatigue resistance laws. Now, it is proposed to focus on the signature of fatigue phenomena in α -iron.

1.3.1.3 LCF of α -iron

Since the 1960's, the LCF behaviour of BCC metals and more particularly of α -iron has been investigated [LOW59] [GRI66][MAG79][MUG76][MUG81][ROV91][SOM98].

The cyclic hardening curve of α -iron single crystals at room temperature is presented in Figure 1-19 [MUG81]. For plastic strain variation of $\Delta\varepsilon_p=10^{-4}$, no cyclic hardening is detected and at higher strain variation, cyclic hardening is initially rapid followed by a saturation of the peak stress. Sometimes a cumulative plastic strains up to 100 is required to reach saturation.

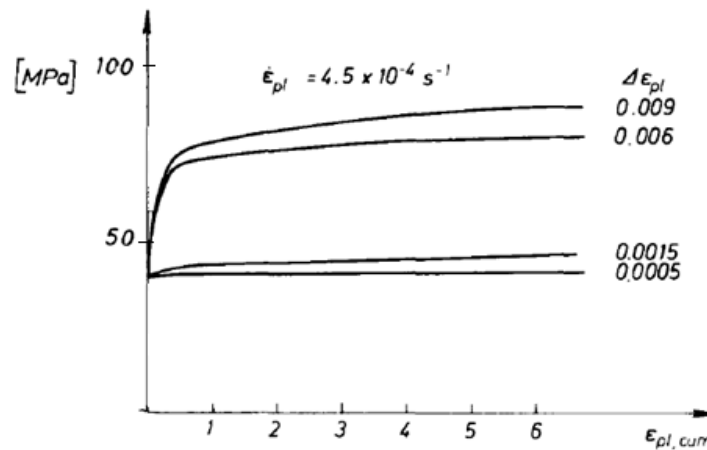


Figure 1-19 : Cyclic-hardening curves of decarburised α -iron single crystals at room temperature [MUG81]

The behaviour of polycrystalline α -iron is presented in Figure 1-20 for different temperature tests. At room temperature ($T=291\text{K}$), the behaviour of polycrystalline is similar to single crystal with rapid hardening followed by saturation.

When decreasing the temperature below $T=291\text{K}$, the stress amplitudes increase while above 291K a weak dependence on temperature is observed and the number of cycles to failure is nearly constant. At 573K , no signs of failure were observed at $\varepsilon_{pl, cum} = 400$. The influence of the temperature can be linked to the mobility of screw dislocations which is dependent on the temperature as will be explained in §1.3.2.4.

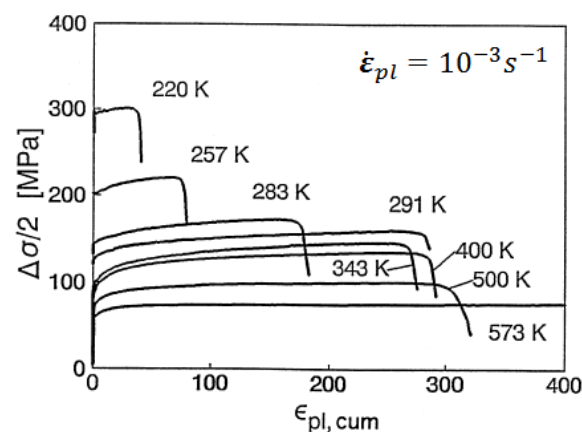


Figure 1-20: Cyclic deformation behaviour of decarburised α -iron at $\Delta\varepsilon_{pl}=2\times 10^{-3}$ at different temperatures [SOM98]

The influence of small carbon content in α -iron polycrystals were also studied by Sommer *et al.* [SOM98] for different temperatures as shown in Figure 1-21. Different behaviours are observed according to the temperature.

- At low temperature (Figure 1-21(a)), the presence of carbon decreases the stress amplitude after a short transition state which leads to an increase of the fatigue life.
- At intermediate temperature (Figure 1-21(b)), the decarburised sample hardens continuously whereas the sample with 74 ppm C softens after a short initial hardening state. The sample with 13 ppm C shows an intermediate behaviour.
- Finally at the highest temperature (Figure 1-21(c)), the presence of carbon leads to an increase of the cyclic stress amplitude and a reduction of fatigue life.

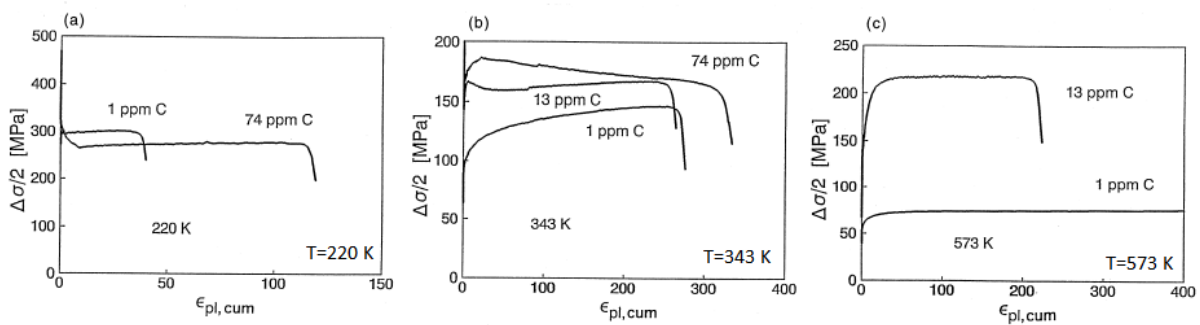


Figure 1-21: Cyclic hardening/softening curves of decarburised and carburised α -iron at $\Delta\epsilon_{pi}=2 \times 10^{-3}$ (a) 220K, (b) 343K, (c) 573K [SOM98]

In their study, Sommer *et al.* summarise the effect of carbon according to the temperature as follow:

- At low temperature, softening is linked to solid solution softening effect (elastic interaction between solute atoms and kink pairs during their formation and separation stage [KIR12]).
- At intermediate temperature, strengthening is due to carbon precipitates and softening to strain localisation in specific dislocation structures. The strengthening effect decreases with increasing the temperature because of the coarsening of the carbides and their dissolution.
- At high temperature, dynamic strain ageing occurs when carbon is present. Dynamic strain ageing arises from the competition between the pinning of the dislocation by the diffusing solutes and the release of the dislocation from this arrest [ABB02].

1.3.1.4 Conclusion

The different laws developed in the above paragraphs are useful to describe the mechanical behaviour of the material which can be implemented afterwards in the mechanical modelling software. The fatigue resistance laws are also useful for fatigue failure prediction.

Moreover, cyclic accommodation curves and work-hardening curves are useful to describe the evolution of the properties of the material during cycling. The influence of temperature and of

carbon content on the cyclic evolution of α -iron has been studied and it shows that these evolutions arise from microstructural changes. Therefore to really understand the cyclic accommodation phenomena, it is necessary to understand the damage mechanisms and the plasticity mechanisms that are described hereafter.

1.3.2 Microstructural evolution

1.3.2.4 Plasticity mechanisms in BCC

In BCC steels, a characteristic feature is the dependence of the flow stress with the temperature and with the plastic strain rate. This behaviour can be described according to the Seeger theory [SEE54]. According to this theory the flow stress can be decomposed in two terms: an athermal component σ_G and a thermal component σ^* (equation 1-11).

$$\sigma = \sigma_G + \sigma^*(\dot{\epsilon}_p, T) \quad (1-11)$$

σ_G is also called the internal stress and is related to long range interactions (for instance the stress required to bow out and to overcome the elastic interaction with other dislocations). Consequently, σ_G is related to dislocation density, ρ , and their arrangement. This relation is often expressed as defined in equation (1-12) for single crystal and in equation (1-13) for a polycrystalline alloy.

$$\sigma_G = \alpha G b \sqrt{\rho} \quad (1-12)$$

$$\sigma_G = \alpha M G b \sqrt{\rho} \quad (1-13)$$

With b the Burgers vector, G the shear modulus and α a constant which takes into account the arrangement of the dislocations and M the Taylor factor. It is usual for BCC metals to distinguish two regimes which depend on the temperature relative to a transition temperature T_0 .

In the low temperature regime ($T < T_0$), the stress level is governed by the effective stress σ^* which is required in addition to σ_G to enable the thermally activated dislocation glide, it is related to short range interaction such as lattice friction and pinning effect. Above the temperature transition T_0 , σ^* becomes negligible. This behaviour is illustrated in Figure 1-22, the transition temperature is dependent on the material, the strain rate and atmosphere.

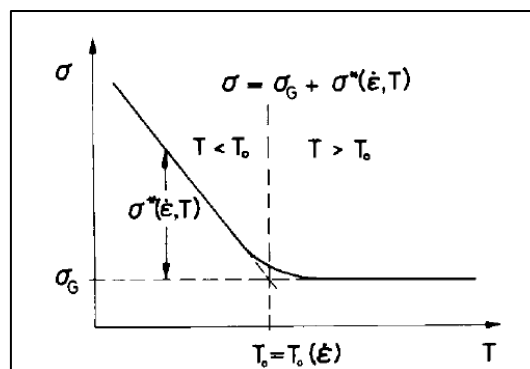


Figure 1-22: Schematic of the dependence of flow stress with temperature [MUG81]

In the low temperature regime, the mobility of screw dislocation is weak compared to the mobility of edge dislocations. Thus, long screw dislocations are observed. Above the transition temperature, the difference in mobility of edge and screw dislocations is reduced by thermal activation. The dislocations movement is isotropic. This difference in glide mode is represented in Figure 1-23.

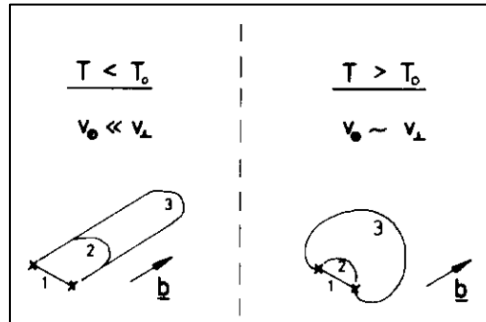


Figure 1-23: Glide mode of the dislocation as a function of the temperature [MUG81]

1.3.2.5 Cyclic accommodation in BCC

As explained in the previous paragraph, in BCC metals, the flow stress is dependent on temperature. Therefore, the cyclic accommodation of a BCC metal is here described as a function of the temperature regime.

In the “high temperature” regime ($T > T_0$), the screw and edge dislocations mobility is similar. The evolution of the microstructure is then dependent on the strain level:

- At low strain level, activation of a single slip system enables the accommodation of the deformation. A dipole structure is formed which consists of channels with low density of mobile screw dislocations and veins of high density of edge dislocations (Figure 1-24 (a)). The deformation is possible by the quasi-reversible movement of screw dislocations between the channels
- When the strain increases, the dislocation structure will turn into walls by densification of the veins (Figure 1-24 (b)). When a second glide system is activated, a labyrinth structure is formed (Figure 1-24 (c)).
- At high strain level, the material activates several glide systems. Gliding becomes multiple and dislocations cells are formed (Figure 1-24 (d)). Cells accommodate deformation by dislocation glide from one cell wall to the other.

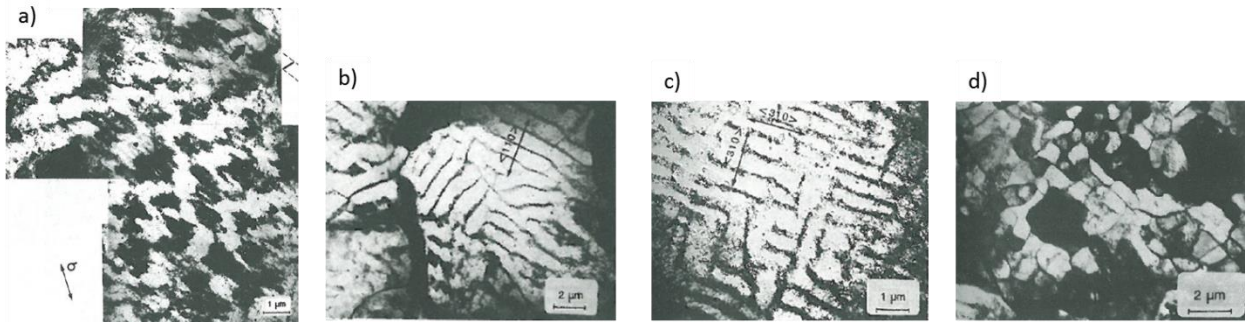


Figure 1-24 : Microstructure evolution of a low-alloyed ferritic polycrystalline steel subjected to cyclic loading in the high temperature regime (a) matrix structure (b) walls (c) labyrinth (d) cells [ROV91]

In the “low temperature” regime ($T < T_0$), the screw dislocations mobility is weak when compared to the edge dislocations mobility.

- At low strain level, the dislocation density remains low during cycling even if the cumulative plastic strain is high. The edge dislocation featuring quasi-reversible movement enables deformation while the presence of long screw dislocation segments underline their difficult mobility.
- At higher strain level ($\Delta\epsilon_p > 10^{-3}$), dislocation arrangement is different. During the first cycles, screw dislocations interact with each other and their density increases. Edge dipoles appear through cross-slip annihilation, they tangle and form multipole. Then, debris are created by interaction of small dislocation loops and lead to the formation of dislocations clusters constituted of multipoles and debris (Figure 1-25 (a)). Between the clusters, screw dislocations accommodate the strain and their density tends to decrease. To cross the cluster, screw dislocation must do double cross-slip which induces the formation of debris. This leads to the increase in flow stress and thickening of the clusters and their transformation into walls and finally cells (Figure 1-25 (b)).

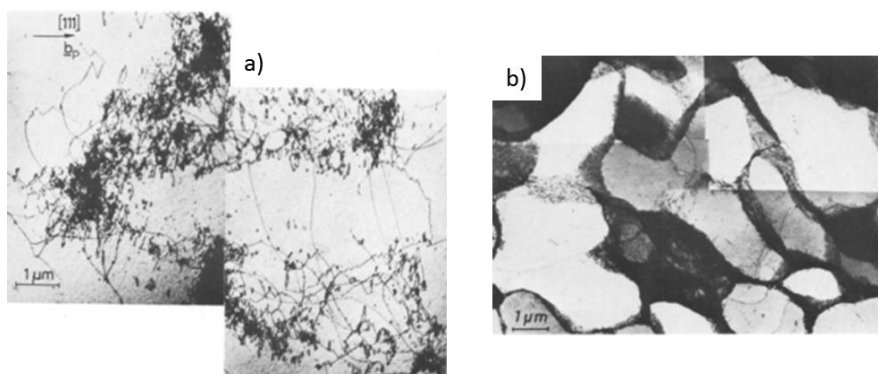


Figure 1-25: Microstructure evolution of a-iron single crystal in the low temperature regime (a) dislocation debris (b) dislocation cells [MUG81]

As shown in the previous chapter (§1.3.1.6) different behaviours are observed according to the temperature when small amount of carbon is added to α -iron polycrystals. This is transcribed also in

the dislocation structure evolution [SOM98]. At low temperature, cell structure is developed with long screw dislocation in the cell interior (Figure 1-26 (a) and (b)). At intermediate temperatures, small carbon content leads to strain localisation in persistent slip band (PSB) (in connection with cyclic softening) (Figure 1-26 (c)). In the high temperature regime, wall and labyrinth structures are observed (Figure 1-26 (d)).

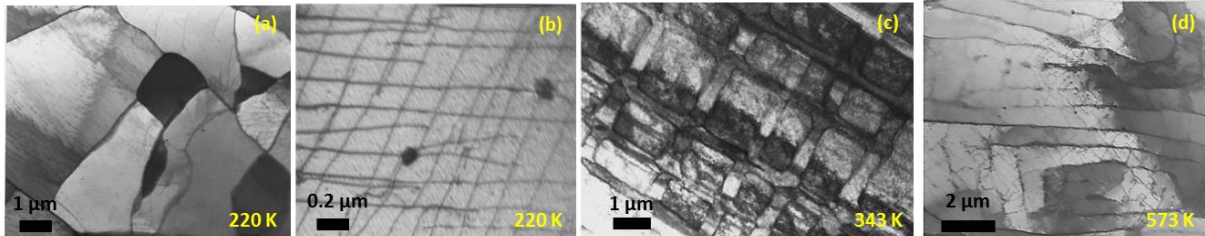


Figure 1-26 : Evolution of the dislocation structures in carburised α -iron with cyclic loading according to the temperature (a) cell structure and (b) long screw dislocations in the cell interior (c) PSB (d) wall and labyrinth structures [SOM98]

1.3.3 Iron-silicon steels

The cyclic properties of iron-silicon steels are of major interest in the present work. Therefore, the studies of strain accommodation mechanisms for monotonic loading are first presented. Secondly, the works on strain accommodation mechanisms induced by cyclic loadings are considered.

- Monotonic strain accommodation

Since the 60's, the deformation mechanisms of iron-silicon alloys have been studied. Griffiths and Riley [GRI66] have studied the evolution of the dislocation structures of an iron-3%silicon steel during a tensile test which curve is presented in Figure 1-27. They have shown that at 2% of deformation, many dislocations are present in all the grains (Figure 1-28 (a)). From 5% of deformation, dislocations gather and form clusters separated by zones of lower dislocation density (Figure 1-28 (b)). When increasing deformation, cells are formed. The cells diameter decrease with increasing the deformation (Figure 1-28 (c)).

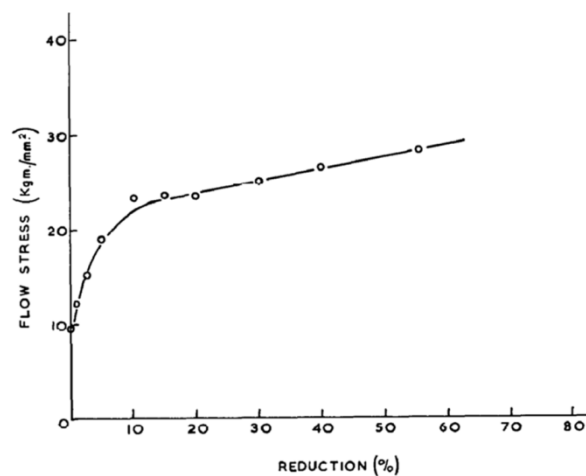


Figure 1-27: The variation of flow stress of cold-rolled 3% silicon-iron sheet with amount of reduction [GRI66]

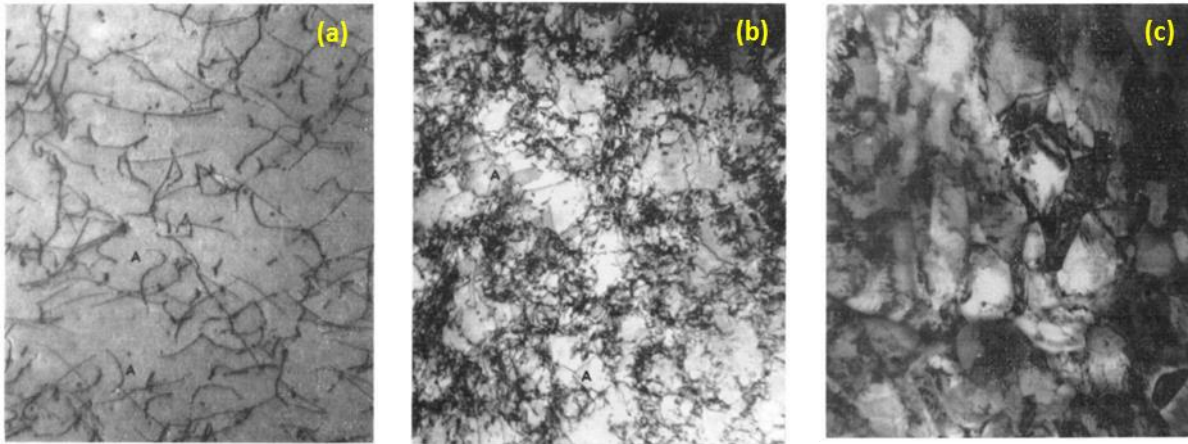


Figure 1-28: Dislocation structure after (a) 2%, (b) 10% and (c) 50% of deformation. Magnification: X 30 000 [GRI66]

E. Hug [HUG93], O. Hubert [HUB98] and E. Iordache [IOR03] have worked on polycrystalline Fe-3%Si. Their studies focused on the evolution of the magnetic properties with the plastic deformation of the iron-silicon steel. Their studies showed that the monotonic mechanical behaviour in tensile test of the Fe-3%Si corresponds to standard mild steel behaviour with the presence of an upper and lower yield point and the presence of a Lüders plateau (L_p) as illustrated in Figure 1-29.

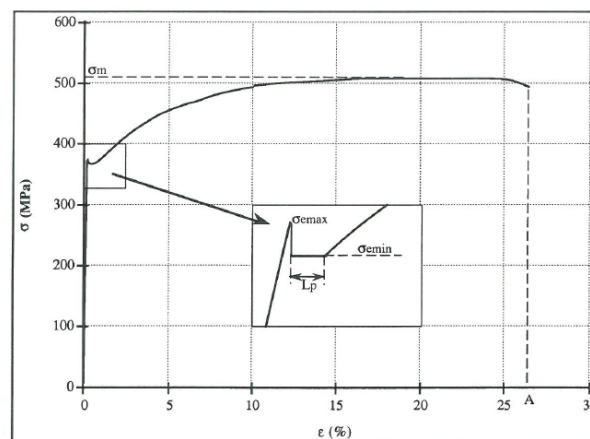


Figure 1-29: Conventional traction curve of a Fe-3%Si steel in the rolling direction at ambient temperature and $\dot{\epsilon} = 6.67 \times 10^{-4} \text{s}^{-1}$ [HUG93]

The occurrence of the Lüders plateau is the consequence of the rapid increase of mobile dislocation density within the specimen at the beginning of the plastic deformation [HAH62]. It is often associated with dislocations locking concept. Indeed, according to Cottrell [COT49], dislocations are anchored by segregates or precipitates in the undeformed material. Then, when the upper yield stress is reached, dislocations are teared off their pinning points, and a lower stress is needed for their glide resulting in the Lüders plateau.

The microstructural study (Figure 1-30) during the tensile test of the iron-silicon steel shows that:

- On the Lüders plateau (L_p): screw dislocations parallel to each other or forming an angle of 45° are observed. Locally, groups in the form of walls of low density are visible.
On the sample surface, fine parallel slip lines in grains distributed throughout the volume appear.
- Between 1 to 10% of plastic strain, dislocation clusters of low density are formed progressively, between these clusters, isolated dislocations are present (Figure 1-30(b) and (c)). The slip lines gradually fade.
- From 10% of plastic strain, dislocation walls separated by channels of low dislocation density are formed (Figure 1-30(d)). These walls then transform into dislocation cells (Figure 1-30(e)).
Thick and wavy slip bands appear in the most deformed grains and then concentrate at grain boundaries.

These observations are consistent with the study of Griffiths and Riley.

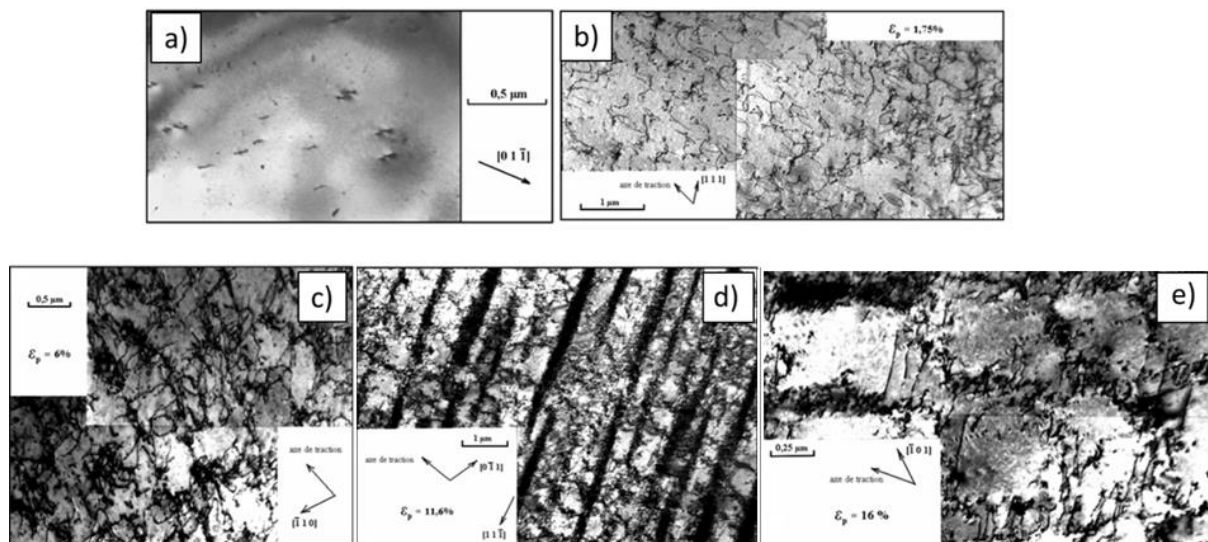


Figure 1-30: TEM micrographs of Fe-3%Si subjected to a monotonic loading (a) undeformed state (b) $\epsilon_p=1.75\%$ (c) $\epsilon_p=6\%$ (d) $\epsilon_p=11.6\%$ | $\epsilon_p=18.5\%$ [IOR03] (e) $\epsilon_p=16\%$

In addition to these studies which focuses on the deformation of Fe-3%Si in traction, other studies focus on the behaviour of Fe-3%Si steel in compression. Indeed, Low and Turkalo [LOW62] have studied the deformation mechanisms of single crystals of Fe-3%Si subjected to 1% of compression at ambient temperature. After deformation, they observed screw dislocation in direction $[\bar{1}\bar{1}1]$ and edge dislocation along the $[2\bar{1}1]$ direction and many debris. They rely on the model developed by Johnston and Gilman based on the observation of deformed crystal of LiF [GIL62] to interpret their results. Indeed, jogs are formed when screw dislocations are subjected to cross-slip (Figure 1-31), the applied stress enables the glide of screw dislocations but not of the jogs. When the original screw dislocation continues its slip, a "path" is created behind the dislocation. This path consists in a dotted

line of interstitials or of two edge dislocations of opposite sign in plane separated with the same distance than the height of the jog (Figure 1-32). Also, in iron-silicon steel, screw dislocations are able to move in any direction of the crystal without regard to specific slip planes, their motion is rather governed by the direction of the local shear stress [LOW62]. Therefore, jogs of screw dislocations might appear when the planes of the maximal shear stress are different to the slip planes. These phenomena could explain the low velocity of the screw dislocation compared to edge dislocation in Fe-3%Si as pointed out by Low and Guard [LOW59].

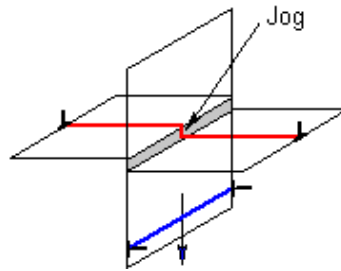


Figure 1-31: Schematic representation of jog formation by dislocation cross-slip

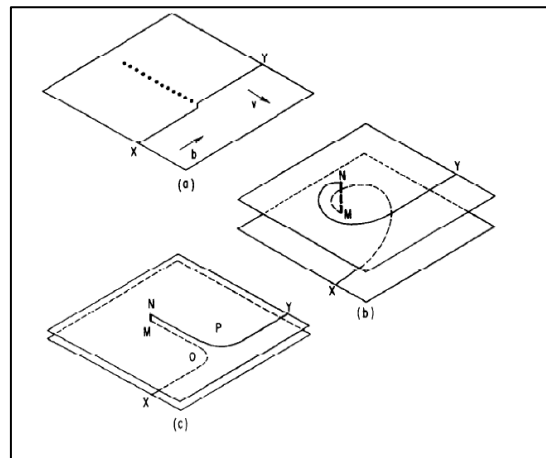


Figure 1-32: Behaviour of screw jogs of different height [LOW62] (a) low height jogs creating punctual defects while the dislocation glide (b) high height jogs, the dislocation NY and MX glide independently (c) intermediate jog height, dislocation NP and MO interact and cannot cross [GIL62]

Lakso and Marcinkowski [LAK74] have studied the compressive stress-strain behaviour of polycrystalline Fe-Si alloys with Si content between 0 and 25 at.% with special focus on the effect of atomic order. This study showed that in alloy containing less than 10 at.% Si, only short range order is encountered and this short range order increases the yield strength (Figure 1-33).

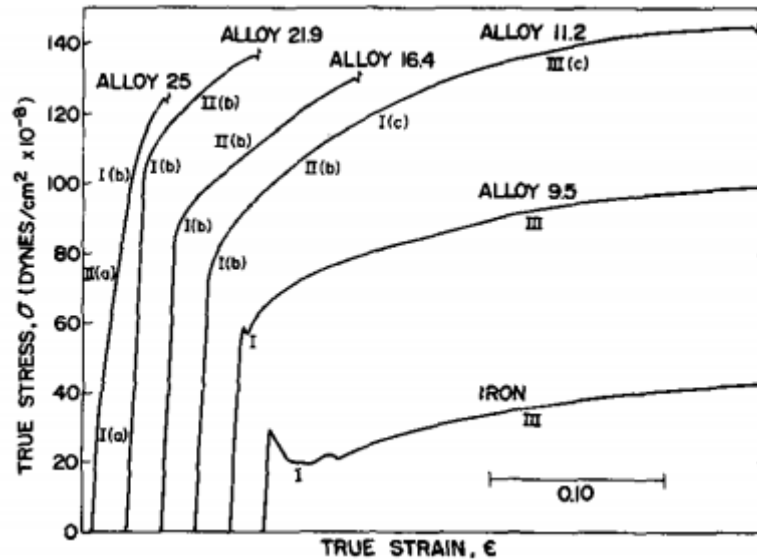


Figure 1-33: Effect of composition on the room temperature (298K) compressive stress-strain curves of different Fe-Si alloys [LAK74]

- Cyclic strain accommodation

In addition to monotonic loading studies of iron-silicon steels, Mori *et al.* [MOR79] and Sestak *et al.* [SES88] have studied the cyclic damage mechanism of iron silicon single crystals. The influence of silicon content on the cyclic hardening curves is presented in Figure 1-34.

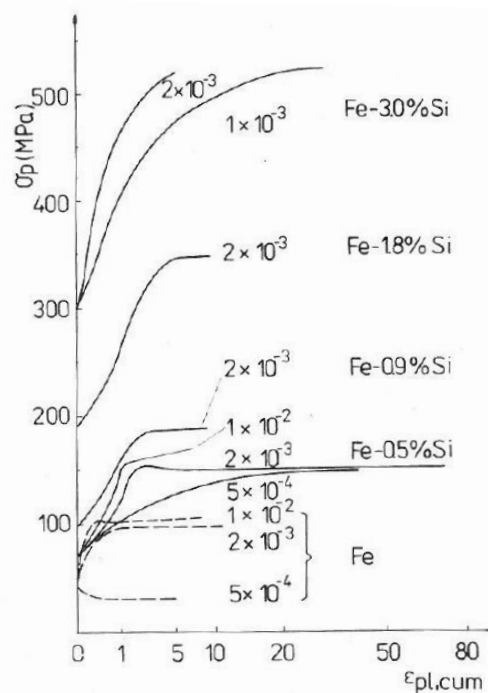


Figure 1-34: Cyclic hardening curves obtained at $\dot{\epsilon}=1.6 \cdot 10^{-3} \text{ s}^{-1}$ and $T=295\text{K}$ for several Si content [SES88]

All the curves start with a rapid hardening stage followed by a saturation stress. It can be noticed that with increasing the silicon amount:

- the difference of stress value between saturation and the first cycle increases

- the saturation stress is reached more slowly

During the rapid hardening stage, the vein and channel structure is observed (Figure 1-35) and veins spacing is dependent on silicon amount (Figure 1-36). The cyclic hardening stage is the result of the increase of dislocations density within veins. Shortly before the saturation stage, veins turn into walls for Fe-0.5%Si (Figure 1-38) and during the saturation stage, secondary slip is activated and thus promotes the formation of the cell structure in Fe-0.9%Si (Figure 1-38).

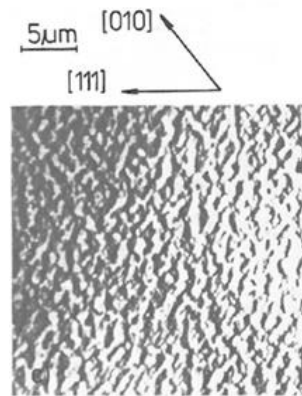


Figure 1-35: Veins and channels dislocation structure in a Fe-3%Si at $\Delta\epsilon_{pl}=10^{-2}$ and $\epsilon_{pl,cum}=2,3$ [SES88]

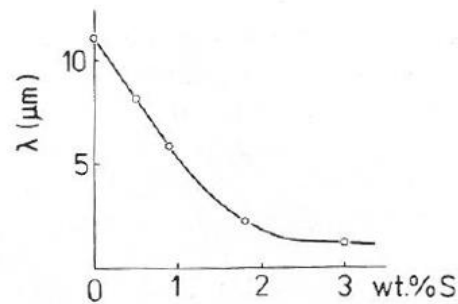


Figure 1-36: Average distance between veins as a function of silicon content [SES88]

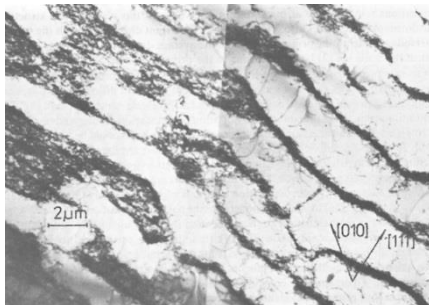


Figure 1-37: Evolution of veins into walls for Fe-0.5%Si at $\Delta\epsilon_{pl}=2.10^{-3}$, $\epsilon_{pl,cum}=0,48$ and $T=295\text{K}$ [SES88]

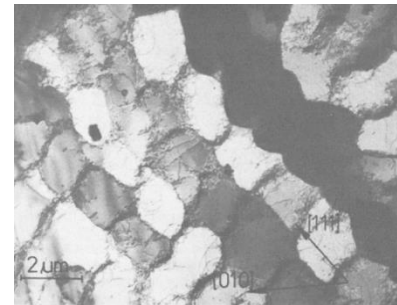


Figure 1-38 : Cell dislocation structure in Fe-0.9%Si [SES88]

On the sample surface, slip bands parallel to the primary glide system can be seen during the first cycles (Figure 1-39), then these bands fades due to their enlargement (Figure 1-40).

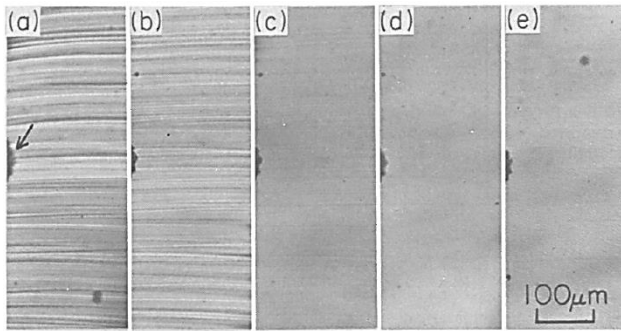


Figure 1-39: Optical microscope observations pointing out the evolution of the slip lines during cycling (a) ½ cycle, (b) 1 cycle, (c) 10 cycles, (d) 50 cycles and (e) 90 cycles at $\Delta\epsilon_p=0.02$ [MOR79]

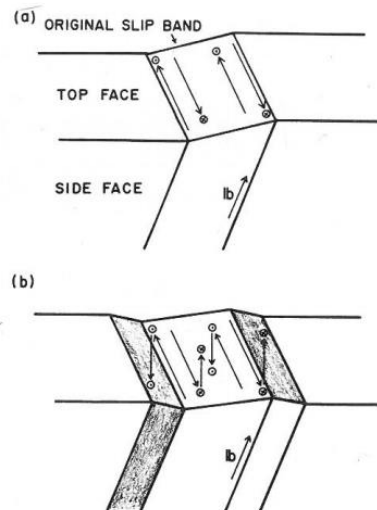


Figure 1-40: Enlargement process of the slip bands (a) after ½ cycle and (b) after 1 cycle [MOR79]

In polycrystalline Fe-0.5%Si and Fe-1%Si subjected to cyclic bending the dislocation cell was never observed, the veins and channels dislocation structure enables the strain accommodation [USH09]. The study shows also that crack propagation is intergranular for Fe-1%Si (Figure 1-41).

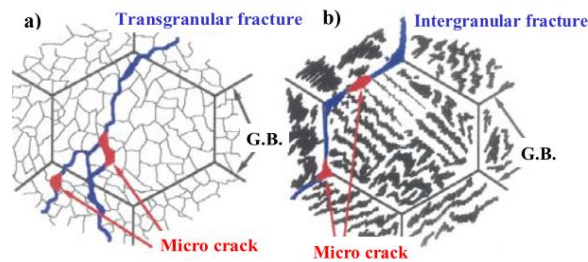


Figure 1-41: Schematic illustration of fatigue fracture of (a) Si free sample with the cell dislocation structure and (b) Fe-1%Si with the vein dislocation structure [USH09]

Magnin and Driver have studied the influence of the strain rate on the crack initiation mode of Fe-3%Si polycrystals under cyclic deformation at a total strain variation of $\Delta\epsilon_t=0.6\%$ [MAG79]. They revealed three behaviours:

- At high strain rate, $\dot{\epsilon}_t \geq 2 \times 10^{-4} s^{-1}$, crack initiation mode is intergranular.
- At low strain rate, $\dot{\epsilon}_t \leq 2 \times 10^{-6} s^{-1}$, crack initiation is transgranular and fatigue lives are lower than in the case of the high strain rate
- At intermediate strain rate, $2 \times 10^{-6} < \dot{\epsilon}_t < 2 \times 10^{-4} s^{-1}$, both crack initiation mode are present.

The crack propagation is then transgranular with cleavage facet in Fe-3%Si [YU84] and intergranular in Fe-4%Si [CHA05a]. Fatigue behaviour studies on a similar Fe-3%Si than the one studied in the present work have been made in the high-cycle regime [HOE13][BOD16]. In both studies, crack propagation is characterised by cleavage facets, signs of rapid and brittle crack propagation.

1.3.4 Conclusion

According to the Seeger theory, the flow stress is dependent on temperature and strain rate in BCC materials. There exist two regimes depending on whether the material is deformed below or above the transition temperature.

In the low temperature regime, cyclic deformation is accommodated by edge dislocation glide at low plastic strain variation. When plastic strain is increased, screw dislocations are involved, glide becomes multipole and dislocation cells are formed, it results in cyclic hardening and saturation of the material.

In the high temperature regime, the dislocation structure evolves with the plastic strain variation from the veins and channels structure to the cell structure; it results in limited strain hardening.

The study of iron-silicon steels shows that silicon addition to iron results in hardening of the material. In fatigue at ambient temperature, it induces more pronounced cyclic hardening when compared to iron. The vein and channel dislocation structure is first formed, followed by dislocation walls. In Fe-0.9%Si, dislocation cells were formed due to cyclic loading but it has never been observed in Fe-3Si. Also, Si addition in iron promotes intergranular fatigue fracture.

1.4 Fatigue damage characterisation

Crack initiation and crack propagation are the two steps leading to the final rupture of a component subjected to fatigue. In LCF, the mechanisms leading to crack initiation are studied by mean of surface observation or dislocation structure evolution. For that purpose, several techniques are used. The most classically techniques used for fatigue characterisation such as Optical Microscopy (OM), Scanning Electron Microscopy (SEM), Transmission Electron Microscopy (TEM), X-Ray Diffraction (XRD) and Atomic Force Microscopy (AFM), are detailed in Figure 1-42.

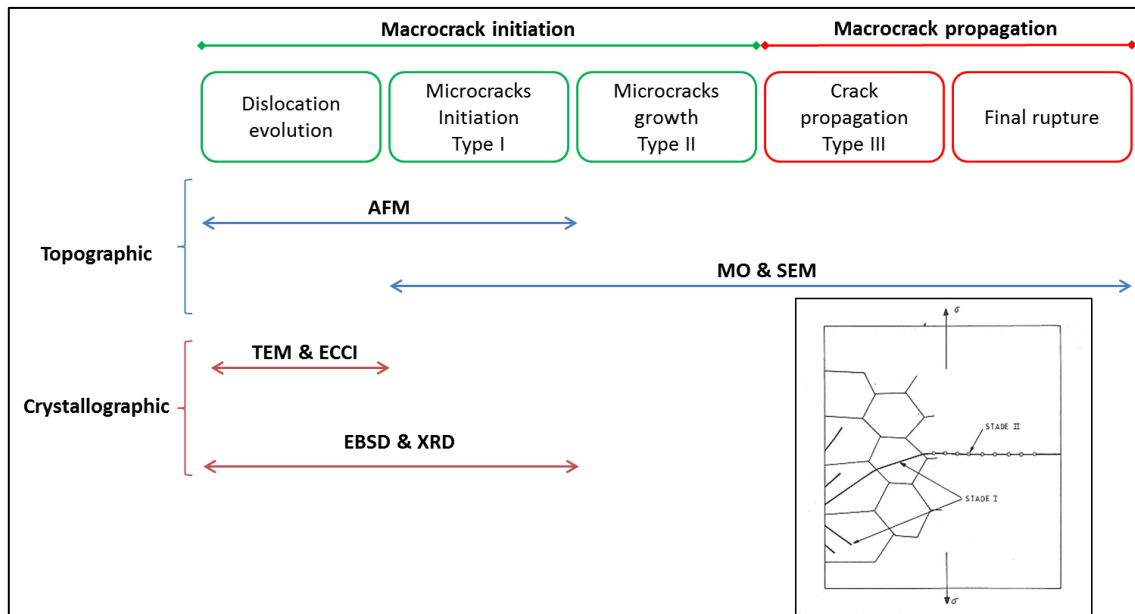


Figure 1-42: Fatigue damage characterisation methods and microcrack definition according to J. Polak [POL91] and J.L. Chaboche [CHA82]

Optical Microscopy (OM) and Scanning Electron Microscope (SEM) are qualitative techniques, they enables the observation of slip bands, micro-cracks, crack propagation paths and fracture surfaces. The Atomic Force Microscopy (AFM) enables quantitative analysis by the measure of surface profiles of slip bands. In addition to these three techniques based on topographic analyses, there are crystallographic based techniques:

- X-Ray Diffraction (XRD) enables the detection of microstrain and can measure residual stress.
- Transmission Electron Microscope (TEM) provides images of dislocation structures and crystallographic description of these structures.
- Controlled Electron Channeling Contrast Imaging (cECCI) also provides images of dislocation structures associated with the diffraction vector. It is implemented in a Scanning Electron Microscope.
- Electron-BackScattering Diffraction (EBSD) which provides information on the crystalline orientation of each grain and within the grains, quantitative information can be obtained by these techniques provided that a correct post-treatment of the data is performed.

1.4.1 Topographic analysis of surface damage

In fatigue, cracks generally initiate at the surface of the specimen and propagate in the bulk, the reasons of this are: 1) at the surface, the grains are less constrained than the grain in the interior, 2) the free surface enables the formation of the surface relief 3) the stress and strain concentration around a defect or an inclusion is highest on the free surface [POL03].

Indeed, cyclic plasticity is accommodated by dislocations (nucleation, glide and structure formation) in the bulk of the specimen and it results in the evolution of the surface roughness. First, slip bands appear at the surface, and then irreversibility of slip may lead to the formation of intrusions and extrusions (Figure 1-43) which act as stress concentrator where crack may initiate.

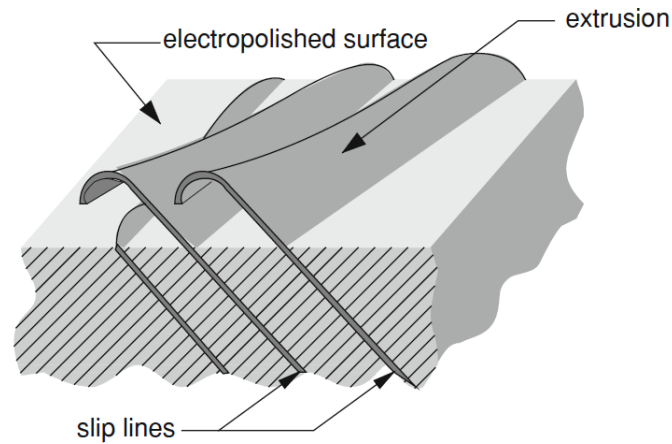


Figure 1-43: Intrusion-extrusion formation in a specimen subjected to cyclic loading [MIL13]

Thus, slip marks at the surface of the specimen are signs of cyclic damage and their analysis can lead to an estimation of damage. Relief intensity depends on the stress level, the microstructure and the number of cycles. The generation of extrusion/intrusion is generally associated with dislocation cross-slip and persistent slip bands (PSB) which appears on the surface as persistent slip markings (PSM). It is shown by Mughrabi [MUG81] and Sommer [SOM98] in ferrite. Nevertheless, surface relief has also been encountered when no PSB are present in the material. Indeed, the relief can be considered as extruded material at the surface without any link with the dislocation structure [VOG88]. Such surface relief has been observed while reversible planar dislocation structure [VOG01], [HEI01] or dislocations cell structure [POL85] were formed in the material.

Mughrabi [MUG78] has studied the slip marks on the surface of copper single crystals subjected to fatigue. Mughrabi plotted the volume fraction occupied by persistent slip markings, f , versus the resolved plastic shear strain, γ_{pl} , (Figure 1-44). It results in a power relation between f and γ_{pl} . With a similar purpose, Karuskevich *et al.* studied the slip marks on the surface of an aluminium alloy subjected to fatigue. Their study showed that slip lines density, k , could be correlated to the number of cycles [KAR12] (Figure 1-45).

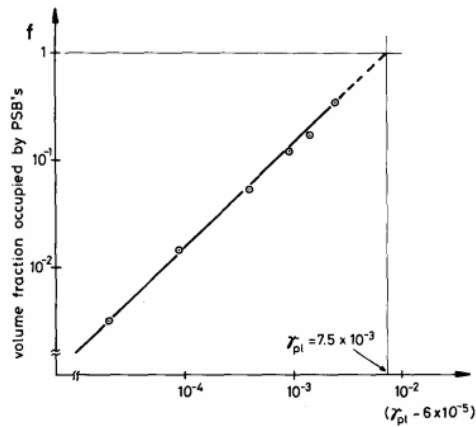


Figure 1-44: Plot of volume fraction, f , of persistent slip bands as a function of γ_{pl} [MUG78]

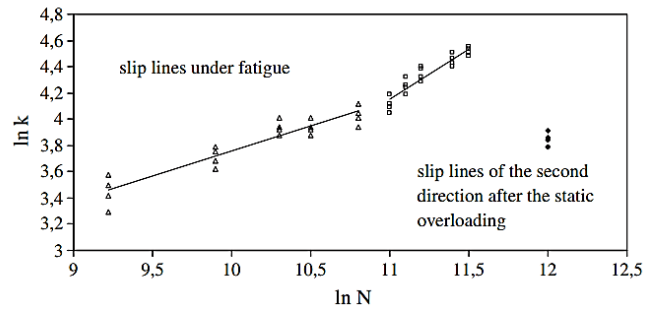


Figure 1-45: Relationship between the slip lines density (k) and the number of cycles, N [KAR12]

Both studies rely on 2D surface observation by OM or SEM and provide valuable quantitative information that enables an estimation of the load undergone by the material by counting the slip marks on the surface. However, it provides only two-dimensions information of three-dimension phenomena.

The Atomic Force Microscopy (AFM) presents the advantage of providing quantitative information concerning the slip marks geometry such as their height and their width and with a better resolution than SEM. Indeed, Man *et al.* [MAN03] showed the real benefit of the AFM technique. They have studied the relief evolution in a fatigued 316L. They showed that the appearance of the first persistent slip marks (PSM) can be correlated with the cyclic hardening/softening curve. Moreover, they showed that the height of the slip lines increases continuously during the life of the material. The initial growth rate of the slip marks is fast and then decreases to reach a constant growth rate until rupture of the material (Figure 1-46).

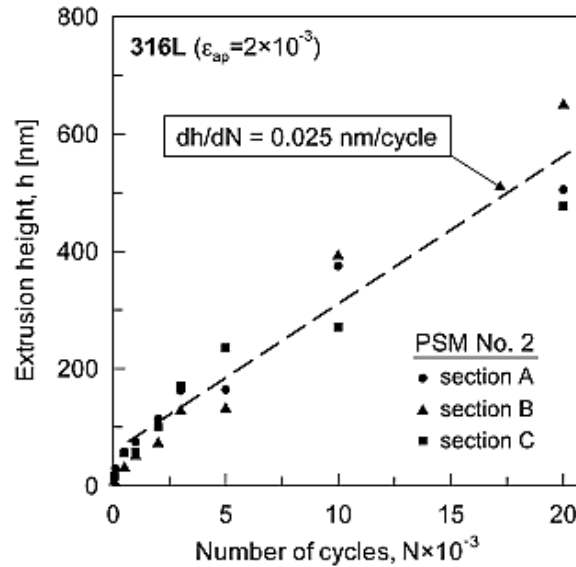


Figure 1-46: Extrusion height h versus the number of cycles, N [MAN03]

AFM was also used to characterise the fatigue damage and interpret cyclic plasticity mechanisms of duplex steel (50% austenite and 50% ferrite) [SAL08]. The study showed that even at low strain amplitude, the two phases are involved in the accommodation of the cyclic plasticity with a predominant contribution of the austenite phase. But AFM mainly enabled the cartography of the Duplex steel and allowed the identification of different slip marks especially in ferrite (Figure 1-47).

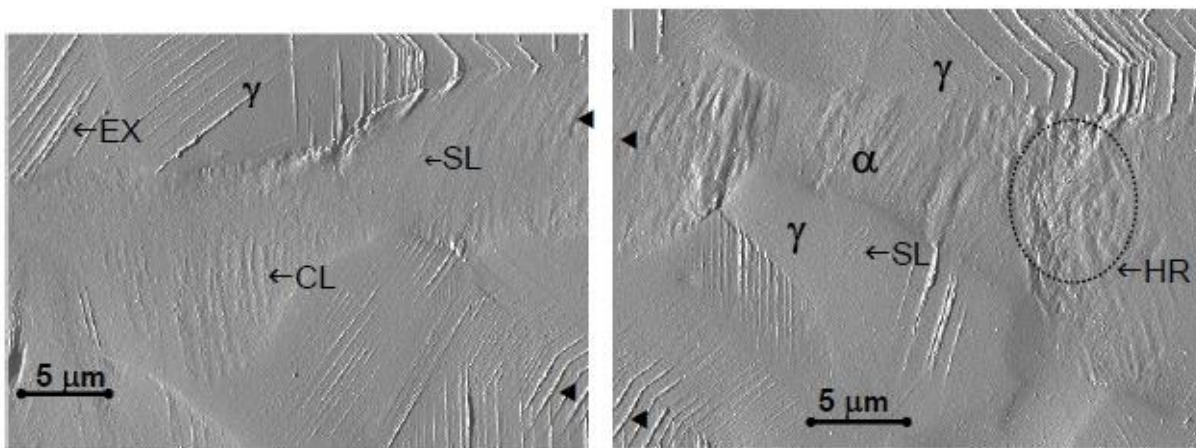


Figure 1-47: AFM (signal error) micrographs with almost all kinds of slip markings. SL: slip line, CL: cord like extrusion, EX: ribbon like extrusion, HR: highly rugged area (◄: images overlap at this symbol) [VOG13b]

1.4.2 Crystallographic based analyses

1.4.2.1 X-ray diffraction (XRD)

The deformation of a crystal lattice has different effects on XRD profiles:

- In the case of uniform macrostress, e.g. a uniform deformation of several grains (of a few hundred microns) leading to a deformation of the interreticular distance $\varepsilon = \Delta d/d_0$ inferior to

$\varepsilon < 0,2\%$, the XRD peaks are shifted to a higher or lower angular position according to Bragg's law (Figure 1-48 (a)).

- For microstress, that is to say local non-uniform deformation, a broadening of the XRD peak is observed due to changes in dislocation density (Figure 1-48 (b)).

A simple parameter is used: the Full Width at Half Maximum (FWHM) (Figure 1-47). In fatigue, the evolution of FWHM during cycling provides qualitative information on microstructural changes, residual microstress, dislocation density or the amount of plastic strain.

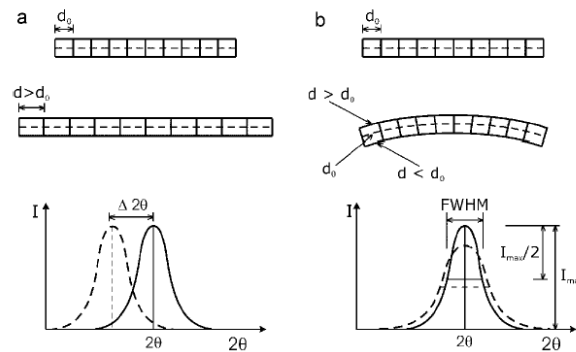


Figure 1-48: Influence of the macroscopic stress (uniform deformation) (a) and of microstress (nonuniform deformation) (b) on the diffraction peak [PIN12]

For example, an increase in the FWHM associated with cyclic work hardening, is observed for aluminium alloy AA6110 [JUI11] while a decrease of FWHM was observed by Dalei *et al.* during cyclic deformation of a shot peened micro-alloyed steel [DAL11]. Pinheiro *et al.* [PIN12] used the XRD technique in order to study the microstructural changes associated with the fatigue damage in steel tubes. They showed an evolution in 3 stages of the FWHM during the lifetime of the material (Figure 1-49):

- A rapid decline of the FWHM is observed during the first stage (up to N_1); this is linked to dislocation glide and multiplication and strain localisation
- The second stage (between N_1 and N_2) is characterised by a moderate decrease of FWHM and corresponds to the major part of the life of the material. It corresponds to microcracks initiation and propagation
- The third stage (after N_3) is depicted by a rapid drop of FWHM before break. The lower FWHM is related to the relaxation of microstress by the initiation and propagation of macrocrack

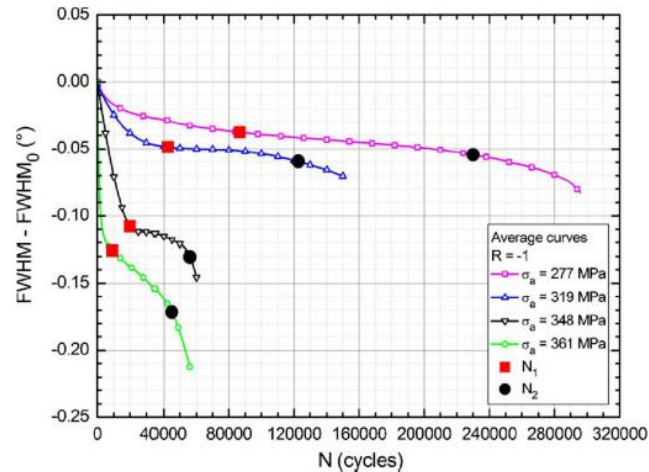


Figure 1-49: Evolution in 3 stages of FWHM during fatigue testing of a ferrite-pearlitic steel at many different stress amplitudes. N1 characterises the end of the first stage and N2 characterises the beginning of the third stage [PIN12]

As XRD method is non-destructive, the technique is used for the assessment of damage in industrial installations. However, XRD has a spatial resolution often greater than the grain size. Thus evaluation of local plastic deformation is not possible. Nevertheless, it is possible to estimate the dislocation density by the X-ray line broadening analysis. The technique has been applied to study dislocation structures in plastically deformed materials. Indeed, Groma showed that the analysis of the tail of the line profile enables the evaluation of three parameters of the dislocation distribution: the average dislocation density, the average dislocation fluctuation and formal dislocation polarization [GRO98]. The mathematical theory is described in [GRO98].

The procedure has been applied to the evaluation of dislocation densities of plastically deformed Cu single crystal by uniaxial compression in the [100] direction at constant strain rate of $2 \times 10^{-4} \text{ s}^{-1}$. The evolution of dislocation density $\langle \rho \rangle$ is presented in Figure 1-50, the evolution of the dislocation polarization characterised by the measured parameter $\langle s^2 \rangle$ is shown in Figure 1-51 and the evolution of the relative fluctuations ($\langle \sigma^2 \rangle = \langle \rho^2 \rangle - \langle \rho \rangle^2 / \langle \rho \rangle^2$) is presented in Figure 1-52. Dipole notation ($\langle \cdot \rangle$) is adopted according to [GRO13] and is relative to terms calculated from the XRD profile.

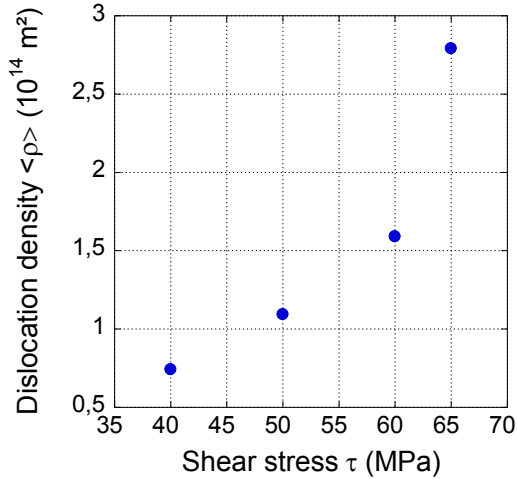


Figure 1-50 : Evolution of the measured dislocation density with increasing the resolved shear stress [GRO00]

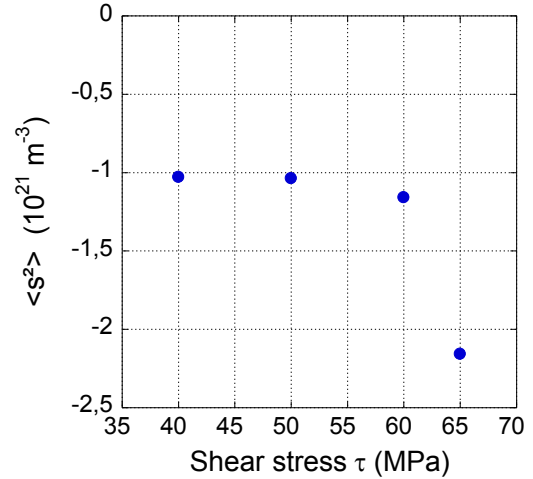


Figure 1-51 : Evolution of the measured $\langle s^2 \rangle$ parameters (formal dislocation polarization) with increasing the resolved shear stress [GRO00]

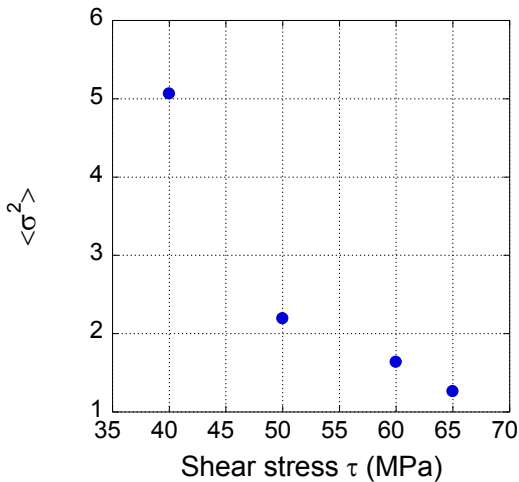


Figure 1-52 : Evolution of the relative fluctuation $\langle \sigma^2 \rangle$ with increasing the resolved shear stress [GRO00]

The fact that dislocation density increases while the relative fluctuation decreases with deformation reveals that the dislocation arrangement tends to homogenisation.

Therefore, this technique offers valuable information about dislocations evolution during deformation.

1.4.2.2 Transmission Electron Microscopy (TEM)

Since the invention of transmission electron microscopy in 1931 by Max Knoll and Ernst Ruska, a lot of progress has been made in terms of resolution (spatial resolution up to 0.08nm). TEM is the reference technique for the study of dislocation structure evolution induced by fatigue. Indeed, the link between dislocation structure and cyclic stress amplitude is known for BCC, FCC and HCP materials [MAG79][MUG78]. And as shown in the previous paragraph, TEM has been used to study

the cyclic accommodation of Fe-3Si steels [SES88][USH09]. TEM provides images of these dislocation structures (imaging mode) but it can also provide a crystallographic description of the structures (disorientation dipolar walls, between dislocations cells ...). TEM can be used for the analysis of industrial component subjected to fatigue. Vogt *et al.* evaluated the value of deformation of a power plant component by comparison with laboratory tests [VOG00]. Indeed, the study on smooth samples showed that fatigue loadings induce the formation of dislocation cells and that misorientation between these cells could be linked to a strain amplitude and thus be a damage indicator (Figure 1-53). By evaluation of the cell misorientation in the in-use component, the strain variation that it has undergone could be evaluated (Figure 1-53).

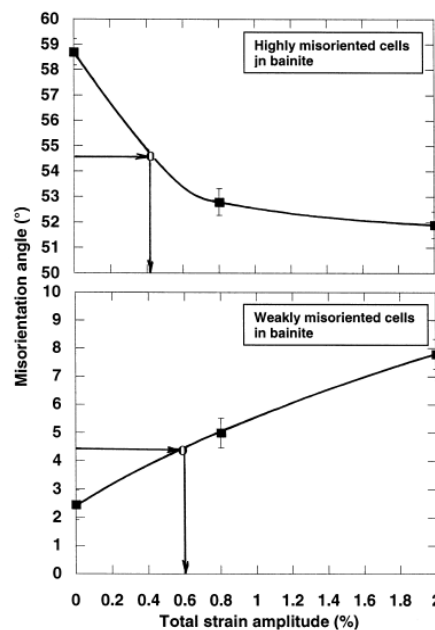


Figure 1-53: Determination of strain amplitude in service of a component (○) from the average cells misorientation measured by TEM (■) [VOG00]

Despite the good spatial and angular resolution of TEM, it presents several limitations due to the destructive sample preparation and the analyses areas which are limited to a few micrometres making the technique difficult to implement a statistical approach. But, the same methodology can be applied with a better statistical approach by the use of Electron Back-Scattered Diffraction (EBSD).

1.4.2.3 Electron BackScattered Diffraction (EBSD)

In 1928, S. Nishikawa and S Kikuchi discovered electron diffraction, they obtained diffraction pattern from a crystal of calcite with apparent lines [MAI06]. These lines correspond to the so-called Kikuchi lines. For each measured point, the backscattered electrons are detected and the corresponding diffraction pattern is obtained. The use of the Hough transform in 1992 enabled the determination of the crystal orientation. Since the 1980-1990, with the development of computed technologies, the indexation of the diffraction patterns has been automated and orientation map was possible.

EBSD was first used for the identification of crystalline phases in complex cases [PET07] [SMA01] or during recrystallization [BAU07] [SIN03] but also for the study of textures [PET07][WRI07][HUM01]. The idea of using EBSD technique to evaluate strain within material has appeared in the late 90s. Indeed, Buchanan *et al.* showed a link between image quality (IQ) and the plastic deformation in 1997 [BUC97]. They measured the decrease of the image quality of the analyses on 316 stainless steel subjected to different strain variations. A calibration curve which linked the image quality to the strain variation was then established and enabled the evaluation of the plastic strain of a sample taken from a welded component. However, IQ method depends on several factors such as: the energy of the electron beam, the emission current, the surface of the sample state and sometimes also the orientation crystal and results should be interpreted carefully.

Therefore, Lehockey *et al.* preferred to focus on the local changes of the crystal orientation [LEH00]. Their study on steels deformed by monotonic traction allowed them to develop a criterion of misorientation angle density (for disorientation angles less than 5 °) called IMD (Integrated angular Misorientation Density) defined in equation (1-22).

$$IMD_{\phi} = \frac{\sum_{\phi_0}^{\phi_{max}} \phi \cdot MD(\phi)}{N} \quad (1-14)$$

With ϕ_0 : minimum deviation angle (usually 1), ϕ_{max} : maximum angular deviation ($\phi \leq 5^\circ$ or $\phi \leq 15^\circ$), N: the number of pixels pairs in the scan area, MD(ϕ): the number of distribution of misorientations of angular deviation ϕ , ϕ : magnitude of the angular deviation, in radians.

A linear relationship is established between the IMD and the known plastic deformation of the analysed samples. This correlation is then used to evaluate the plastic deformation of a steam generator tube of a nuclear plant. Since, misorientation angles are measured as an absolute value, the measurement error is accumulated when calculating the IMD. Therefore IMD is function of the number of data points in studied maps.

Kamaya *et al.* adopted a similar approach in order to establish a relationship between the misorientation of the crystal and the deformation of the material [KAM05]. They studied a 304 austenitic stainless steel deformed by monotonic traction and deformation of the crystal is assessed by comparing the misorientation between a “central” point of the grain and other points of it. This parameter is correlated with the plastic deformation of the material and does not depend on the density of data in the map. However, this technique does not enable the assessment of strain localisation phenomenon.

Jedrychowski *et al.* studied the relationship between microstructure, as local misorientation, grain orientation and mechanical processing (compression) of their material: hexagonal zirconium oxide

Zr₇O_{2α} [JED13]. The EBSD maps showed that orientation deviations appear with increasing deformation because of the formation of intragranular dislocation substructure. They used two parameters to describe the misorientation: KAM (Kernel Average Misorientation) which measures the misorientation between the considered pixel and its neighbours and GOS (Grain Orientation Spread) criteria which measures the misorientation between a reference pixel of the grain and other pixels of the grain (detailed information about these criteria is given in §5.2. It turns out that KAM is particularly suitable for the description of areas where there are strong interactions between dislocations and where the density of sub-boundaries increases. The GOS criterion is suitable for the description of deformation when it is accompanied by a moderate increase in the dislocation density and a significant shift in a grain.

In addition to the evaluation of strain in material subjected to monotonic loading, many studies were performed in order to measure plasticity induced by LCF. Kamaya studied the damage due to LCF in a 316 stainless steel [KAM09]. He studied the distribution of local misorientation (KAM criterion) and the degree of plastic deformation defined by a parameter averaging the misorientations over a mapped area (MCD or GROD criterion) (details regarding the definition of these criteria are given in the next chapter).

Both parameters are used to distinguish a monotonic loading from a cyclic one (Figure 1-54).

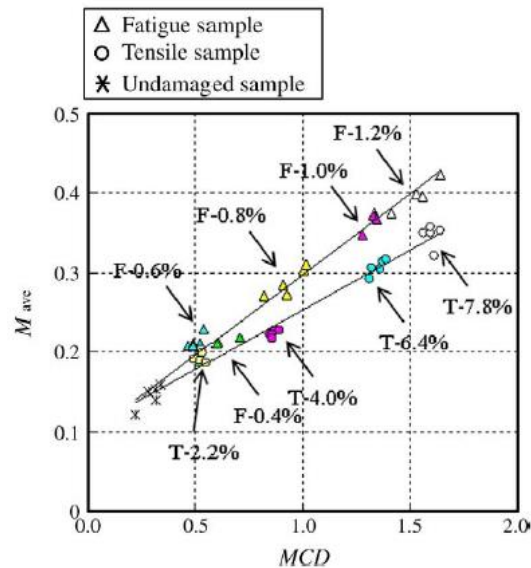


Figure 1-54: Relation between KAM parameter (M_{ave}) and GROD (MCD) for sample subjected to monotonic and cyclic loading [KAM09]

MCD (Modified Crystal Deformation) is the averaged misorientation from a specific orientation referred to as the central orientation assigned to each grain [KAM09]. It is not dependent on the acquisition step and therefore does not take into account local misorientation unlike the KAM. The two parameters are thus complementary.

Also, it is possible to link local misorientation parameter to the fraction of lifetime by establishing first a calibration curve which then enables the evaluation of damage in a similar material [KAM11].

In 2012, F. Léaux did a cross study EBSD/TEM of the LCF of a ferritic steel. The study showed that the evolution of the mean KAM criteria with plastic strain was not linear (Figure 1-55). Explanation for this came from the analyses of the dislocation structures by TEM. Indeed, dislocation cells are formed during cycling and the cells diameter is dependent on the plastic strain variation. The increase of KAM up to a plastic strain variation of 0.5% was linked to the decrease of cells diameter, the following decrease of mean KAM was attributed to a subsequent increase of the cells diameter. This work was then used to estimate the lifetime of a real component by evaluation of the average KAM.

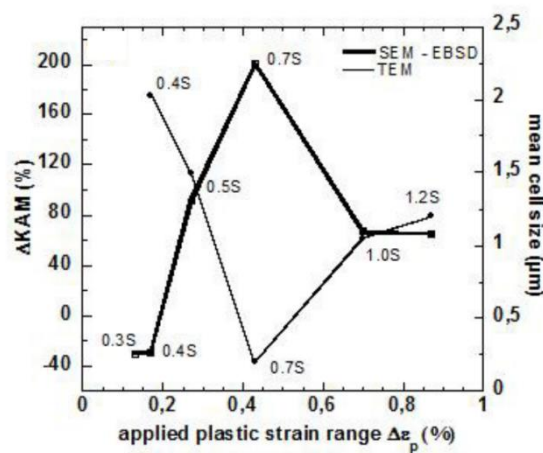


Figure 1-55: Variation of ΔKAM and evolution of mean cell size as a function of the plastic strain range obtained on lab specimens [VOG13a]

1.4.2.4 Electron Contrast Channeling Imaging (ECCI)

The ECCI technique enables the study of dislocation near the surface of bulk specimens and on a large area in a SEM [WIL97]. ECCI is a SEM technique based on the fact that the intensity of backscattered electrons strongly depends on the orientation of the incident beam relative to the crystal plane. Slight local distortions in the crystal lattice due to dislocations cause a modulation of the backscattered electron intensity, allowing the defects to be imaged and optimal contrast (i.e. optimised channelling) is obtained at diffraction angles slightly larger than the Bragg angle [ZAE14]. Though electron channelling is known since the late 60's [COA69], applications were limited until the last decade because of the limitation of microscope performances [resolution and computational limitations]. Figure 1-56 shows dislocation cells obtained from the study of the deformation of TWIP steel on the same area by ECCI (Figure 1-56(a)) and TEM (Figure 1-56(b)) [GUT09]. It shows that ECCI produces detailed images and formation walls was also observed [AHM97][KAN05a], which confirms

the ability of the technique for the observation of dislocation structure even with low misorientation with respect to the matrix.

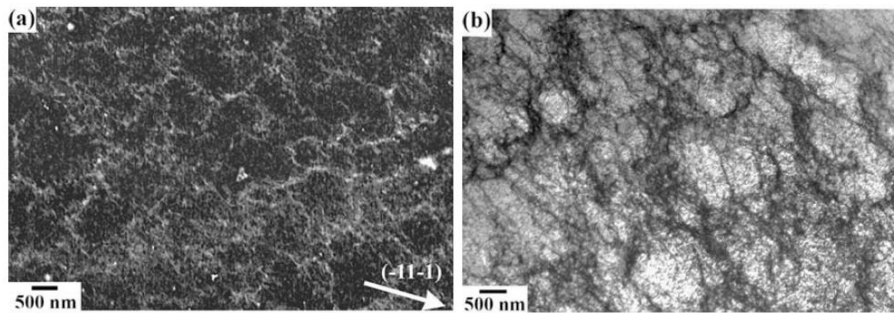


Figure 1-56: Dislocation cells of the same zone of a TWIP steel (Twinning-InducedPlasticity) Fe-22Mn-0.6C after monotonic loading observed by (a) ECCI and (b) TEM [GUT09]

Therefore, the ECCI is an interesting technique employed to characterise deformed materials as sample preparation is less destructive when compared to TEM and the analysis surface is larger. It has thus been employed in fatigue studies on copper [AHM99][AHM01], austenitic steel 316L [DLU13], and on single crystal of ferritic stainless steel [TAN09]. In the study of Ahmed *et al.* [AHM06], a statistical study could be made by ECCI. They focused on the evolution of the crack and the dislocation structures in monocrystalline copper. They could link the width of the PSB to the length of the associated type I crack. PSBs are located at the crack tip. Buque *et al.* used the ECCI technique combined with EBSD to study the microstructure developed in a polycrystalline nickel subjected to cyclic loading [BUQ01]. The study showed that 4 close dislocation structures are formed and that they are dependent on grain orientation (Figure 1-57).

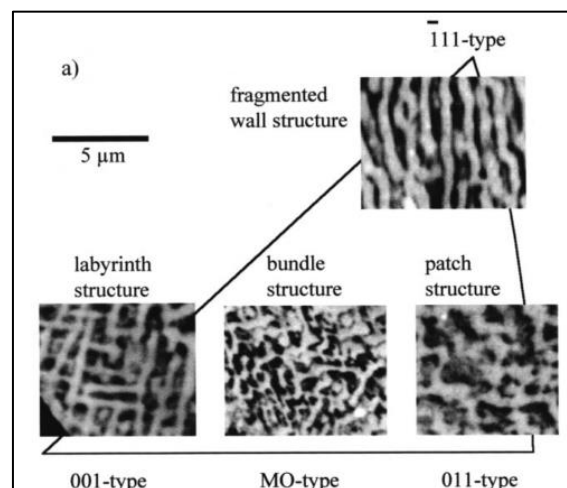


Figure 1-57: Dislocation structures associated with grain orientation (MO-type : Multi-oriented) à $\epsilon_{pcum}=5.10^{-4}$ [BUQ01] Additionally, the cECCI technique developed by Zaefferer [ZAE14] associates the crystal orientation to the observation of the dislocation in order to achieve the two-beam conditions for crystal observations. It is a strong concurrent to TEM as dislocation observation can be associated to the diffraction vector \mathbf{g} and grain orientation [NEL15]. With this technique called cECCI, dislocation

density could be evaluated in a Fe-3%Si steel with Goss texture deformed by tensile test up to $\sigma=500\text{MPa}$. The dislocation density measured by ECCI was similar to the density by TEM [GUT12].

1.4.3 Conclusion

Slip marks induced by cyclic loading can be observed by topographic observation techniques: OM, SEM and AFM. OM and SEM gives qualitative information about the roughness whereas it is possible to measure slip mark height width and angle with AFM. The dislocation structures developed during LCF that may induce the formation of these surface roughness can be observed by TEM and cECCI. XRD technique can be used for fast and statistical study of internal stress state of deformed crystalline material. EBSD can provide information about damage localisation provided that careful data post-processing is performed.

1.5 Conclusion

The Fe-3%Si of the study is a BCC ferritic steel and non-oriented. It is used in car startor-alternator for its magnetic properties. Under monotonic loading, **Fe-3Si steels exhibit higher stress level than α -iron. Only few studies exist on the low cycle-fatigue behaviour of iron-silicon steels** and none on the Fe-3Si of this study. The studies show that **Fe-Si steels containing about 3% of silicon reach saturation stress slower than α -iron.** The dislocation structure evolution is also different; the cell dislocation structure is not expected to form.

To characterise the fatigue damage, several microscopic techniques are available and in this study, **dislocation structure evolution** with fatigue life and plastic strain evolution will be studied by **TEM and cECCI**. Then, **quantitative strain evaluation by EBSD** will be carried out. **MO and SEM are used for surface relief analyses.**

Chapter II: Material and experimental procedures

1. Composition and origin of the steel
2. Microstructure
3. Mechanical properties
4. Fatigue tests
5. Analysis techniques
6. Digital Image correlation
7. Conclusion

2 Material and experimental procedures

2.1 Composition and origin of the steel

The rotors of the starter-alternators are produced by stamping of iron-silicon steel sheets. The steel was provided by ArcelorMittal located in Saint Chély d'Apcher in France. It was obtained by a rolling process which details are unknown. The grade used in this study is the M330-35A according to the EN10106 classification (or graded as 36F185 according to ASTM A677). The chemical composition of the sheets received as foils of 1030x1000mm, are detailed in Table 2-1.

Table 2-1: Chemical composition of M330-35A – ArcelorMittal datas

Elements	C	Mn	P	Si	S	Al	Fe
wt%	0.003	0.109	0.011	2.884	0.004	0.448	Bal.

2.2 Microstructure

The investigated M330-35A exhibits a ferritic structure (Figure 2-1) with a wide grain size distribution (Figure 2-2). The average grain size determined by the intercept method is 75 μm . The final sheet thickness, which is $t=350\mu\text{m}$, corresponds to a thickness of 4-5 grains.

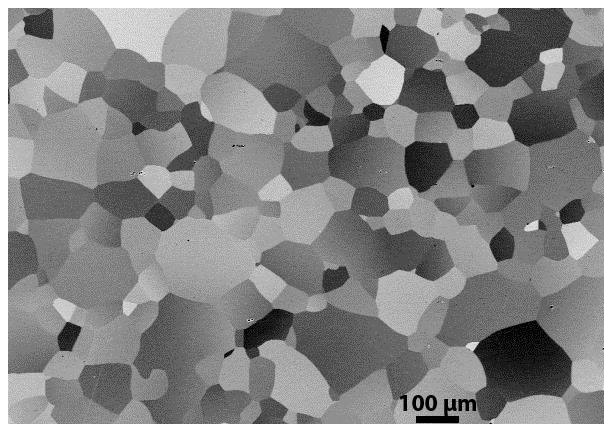


Figure 2-1: Microstructure of the M330-35A

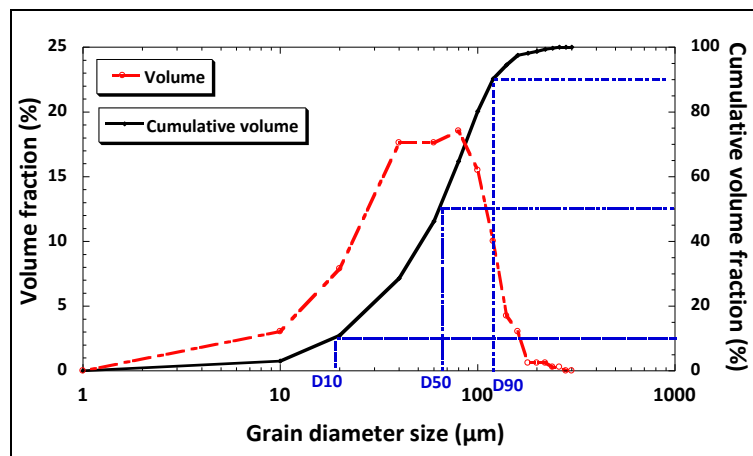


Figure 2-2: Grain size distribution of the M330-35A by 2D analysis

The ideal texture for non-oriented silicon steel is (001) [uv0] where each grain has two $\langle 100 \rangle$ directions in the sheet plane, and the properties are nearly isotropic but no industrial process has been developed to obtain this ideal structure yet [CUN08]. To evaluate the texture of M330-35A, two EBSD maps were realised on as received M330-35A (Figure 2-3).

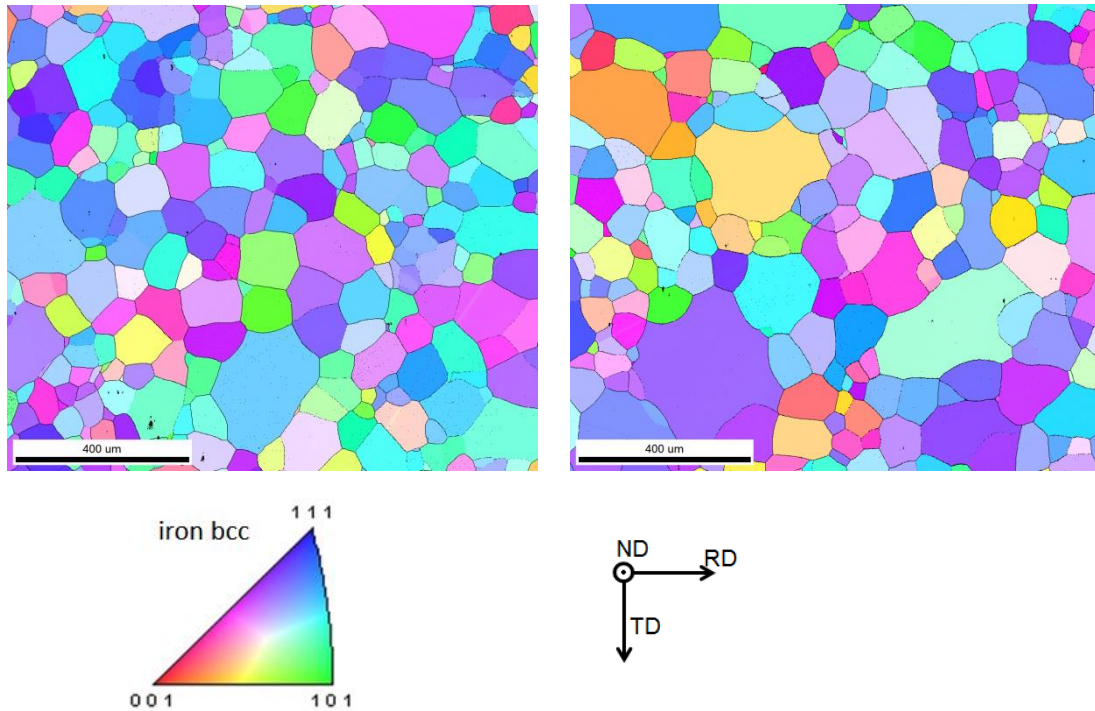


Figure 2-3: Orientation maps of two zones of M330-35A in the normal direction

It reveals that M330-35A has a slight texture due to the recrystallization and it is $[1\ 1\ 1] // ND$ fibres (Figure 2-4), which is consistent with other iron-silicon steels [CAM04a][CAM04b].

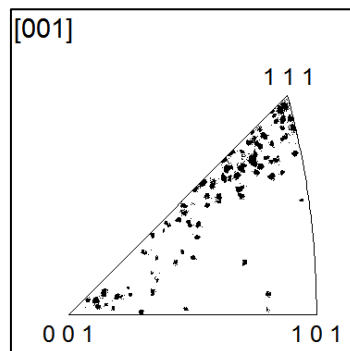


Figure 2-4: Inverse pole figure // ND of M330-35A as received

2.3 Mechanical properties

2.3.1 Hardness

The hardness of M330-35A was evaluated by a Mitutoyo hardness tester, model AVK-C1. A load of 500g was used and the indentation time is 10s, the results are presented in Table 2-2.

Table 2-2: Vickers hardness of M330-35A

Number of measures	25
Maximum hardness (HV)	198
Minimu hardness (HV)	158
Average (HV)	180
Standard deviation	9

2.3.2 Tensile test

Monotonic tensile properties of M330-35A were evaluated by tensile test on a MTS servo-controlled hydraulic fatigue machine with a capacity of 25kN. Tests were performed under displacement control to obtain an average strain rate of 4.10^{-3} s^{-1} . From the tensile test, the yield strength (YS), the ultimate tensile strength (UTS), the uniform elongation (Au) and the elongation to fracture (A) can be determined. The extensometer was not used in this test therefore, the Young modulus I cannot be determined from the tensile curve (due to a lack of precision on the measure at the beginning of the test). However, it can be determined from the first quarter of the first cycle of fatigue tests. The tensile curve of M330-35 is presented in Figure 2-5 and Table 2-3 gives the characteristics values.

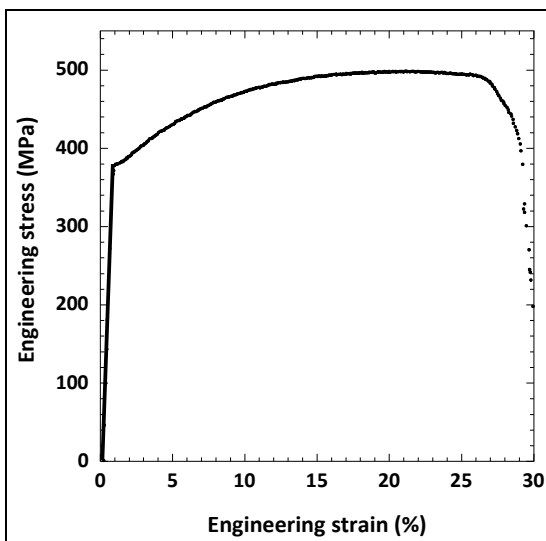


Figure 2-5: Tensile test of M330-35A

Table 2-3: Mechanical monotonic properties of M330-35A

Young modulus E (Gpa)	Yield	
	strength YS (MPa)	YS _{0,2%} (MPa)
195	367	380
Ultimate tensile strength UTS (MPa)	Uniform deformation Au (%)	Elongation to fracture A (%)
499	20	28

M330-35A is a ductile material. The fracture surface of the material (Figure 2-6) exhibits a mixed rupture mode with the presence of dimples typical of a ductile fracture and the presence of transgranular brittle cleavage. These observations suggest that, at the necking point, crack initiation started from the classical mechanism of microvoid nucleation and coalescence but once the internal crack reached a given length, it propagates in a brittle manner pointing out a low fracture toughness of the material.

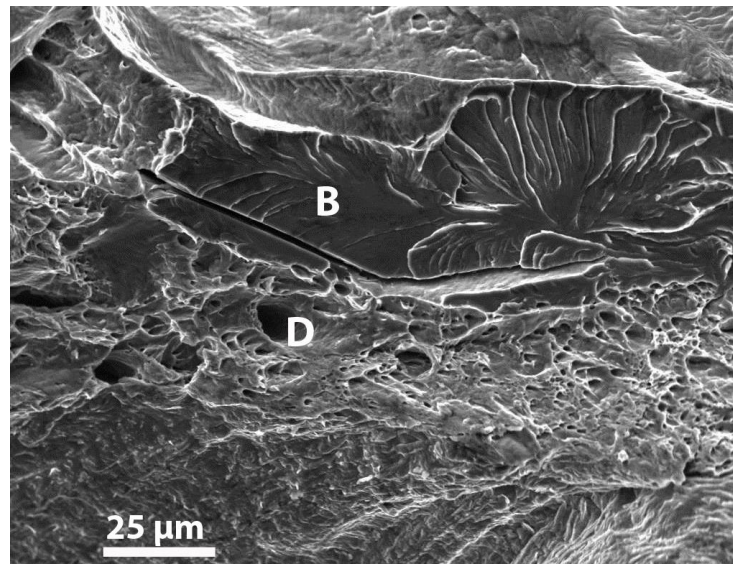


Figure 2-6: Fracture surface of the tensile sample showing sign of ductility (D) and of brittleness (B)

This mixed rupture mode has also been observed by Bode *et al.* [BOD16] on a non-oriented electrical steel similar to the one studied in the present work (Figure 2-7). They showed that ductile failure occurs by grain necking of large grains.

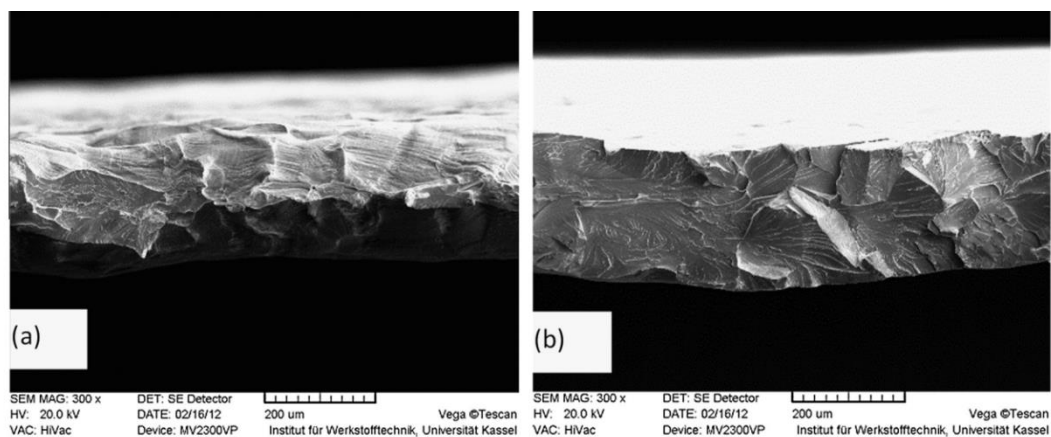


Figure 2-7: Fracture surfaces of specimens after tensile test, (a) area of local necking, (b) cleavage facets [BOD16]

2.3.3 Cyclic stress-strain curve (CSSC)

To obtain first information regarding fatigue behaviour of the material (hardening or softening), the incremental step test method was employed. This test is performed under load control mode and the strain is measured by an extensometer. Once the strain is stabilised, the step is finished and the load is increased for the following loading step. The advantage of this test is that it needs only one sample. However it is important to specify a parameter for the end of a step which is characterised by a stabilisation of the deformation during cycling. It is considered that the stabilisation is reached when the difference between two cycles is inferior or equal to $10^{-4}\%$ as it is shown in Figure 2-8. Table 2-4 summarises the results.

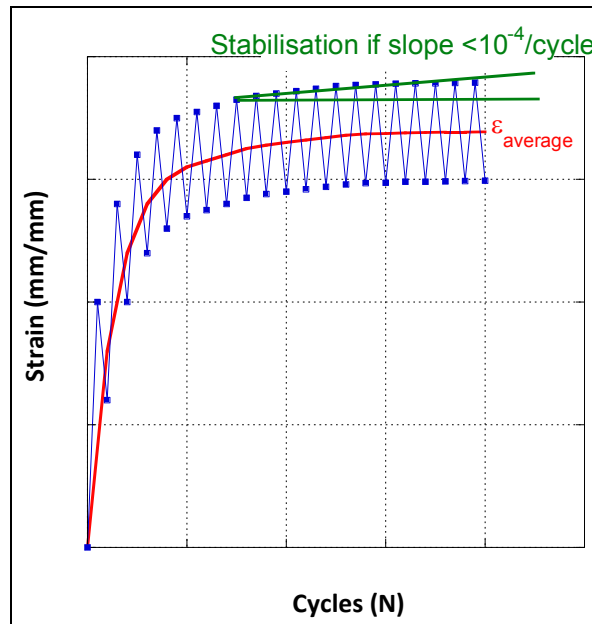


Figure 2-8: Stabilisation criteria of a step

Table 2-4: Summary of the fatigue test by steps

Identification	Step number	σ_{max}	Young modulus		Material response			Deformation (stabilised regime)			Number of cycles to reach the stabilisation criteria	
			Load (Gpa)	Unload (Gpa)	σ_{max} (MPa)	σ_{min} (MPa)	σ_a (MPa)	ϵ_{max} (%)	ϵ_{min} (%)	$\Delta\epsilon_t$ (%)		
M13-68	1	0.7Re	208	210	253	4.4	129.02	0.126	0.008	0.118	Approximately equal to	100
M13-68	2	0.8Re	210	206	292	3.6	148	0.146	0.008	0.138		100
M13-68	3	0.9Re	208	206	330	2	166.42	0.175	0.018	0.158		200
M13-68	4	Re	207	209	364	3.2	138.62	0.622	0.46	0.162		4000
M13-68	5	1.1Re	195	193	403	1.2	202.22	1.89	1.69	0.2		4000
M13-68	6	1.2Re	197	186	437	4.8	221.03	3.83	3.59	0.24		5000
M13-68	7	1.3Re	179	169	495	29.6	262.4	9.31	9.02	0.29		500
M13-68	8	1.4Re	171	164	508	7.2	257.83	15	14.7	0.34	Non stabilised	-

The cyclic stress-strain curve obtained by the incremental step test method of the material M330-35A is represented in Figure 2-9 and compared with the monotonic tensile curve. The diagrams point out a cyclic hardening of M330-35A. Thus, if only monotonic properties of the material in the design of the rotor are considered, it results in oversizing. Indeed, for a same stress, the strain is more important in monotonic loading than in cyclic loading. Therefore, with fatigue characterisation of the material an optimisation of the rotor design is possible while maintaining good reliability.

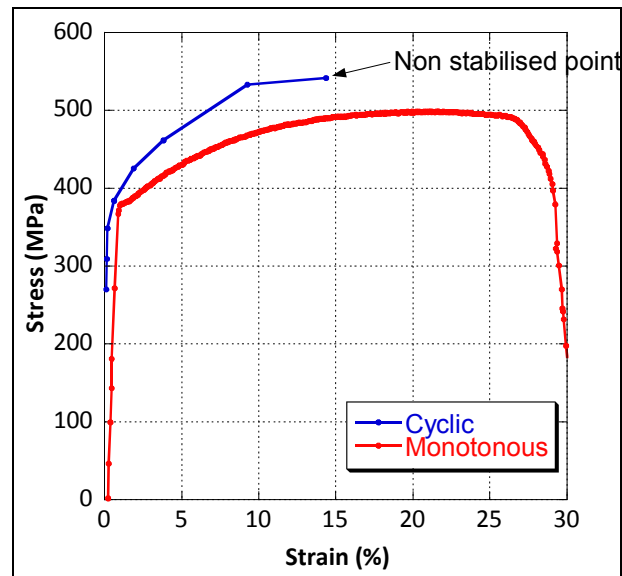


Figure 2-9: Cyclic and monotonic stress-strain curve of M330-35A

2.4 Fatigue tests

LCF tests were performed on a MTS servo-hydraulic machine with a load capacity of 25kN. This machine was chosen for its ability to perform push-pull test at a frequency up to 25Hz. LCF tests were performed under total axial strain control $\Delta\varepsilon_t$ ranging from 0.3 % to 1 %. A push-pull mode ($R_\varepsilon=0$), a triangular wave form, and a constant strain rate of $1 \cdot 10^{-2} \text{ s}^{-1}$ were employed (Figure 2-10). Strain was measured by means of an extensometer of 8 mm gauge length. Specimen surfaces were finely electro-polished before testing. Due to the sheet thickness ($t=350\mu\text{m}$), the geometry of the specimen cannot follow the dimensions imposed by the norm ISO 12106:2003 [ISO03]. Indeed, to prevent bending and performing strain-controlled test (use of an extensometer), the specimen was redesigned to minimise the size (Figure 2-12). The use of an anti-buckling system (Figure 2-11) in which the samples is inserted appeared unavoidable. Samples are collected from the steel sheets by electro-erosion.

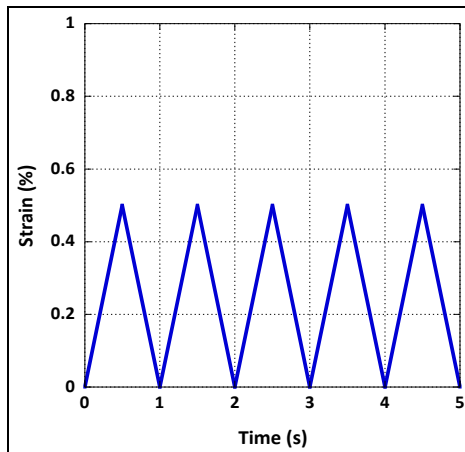


Figure 2-10: Load signal of the reference test

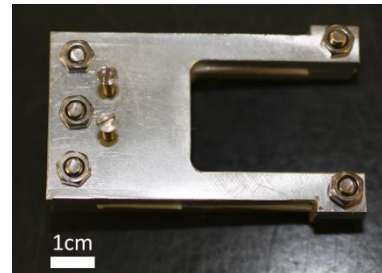


Figure 2-11: Anti-buckling system

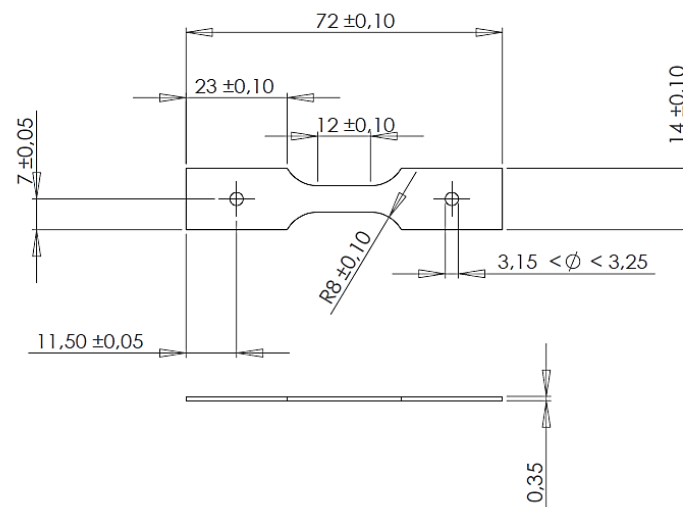


Figure 2-12: Specimen geometry for LCF tests

The tests were conducted with strain controlled mode. For every total strain variation, a minimum of two fatigue tests were conducted. Maximum and minimum stresses were recorded for each cycle. Stress-strain hysteresis loops were recorded for the first ten cycles and then at a logarithmic manner. From the hysteresis loops, stress variation, $\Delta\sigma$, plastic strain variation, $\Delta\varepsilon_p$, and total strain variation, $\Delta\varepsilon_t$, are obtained (Figure 2-13). Elastic strain variation $\Delta\varepsilon_e$ corresponds to the total strain variation minus the plastic strain variation.

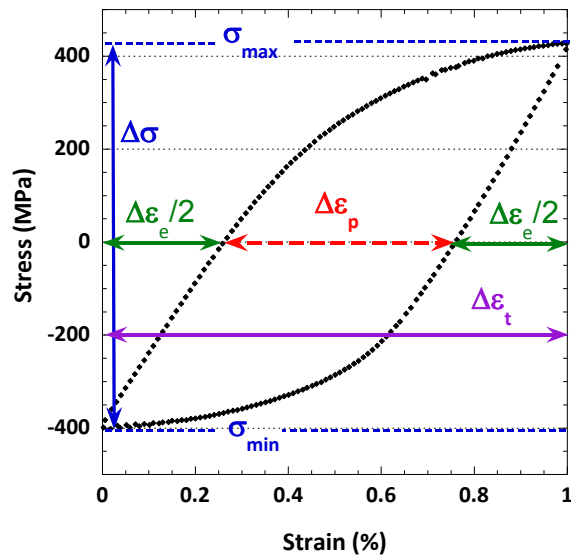


Figure 2-13: Example of hysteresis loop

The fatigue life is defined as the number of cycles leading to a drop of 25% of the tensile stress thereby taking the mid-life pseudo stabilised hysteresis loop as reference.

The parameters of the reference tests are summarised in Table 2-5. A summary of the fatigue tests is given in Annex 4.

Table 2-5: Parameters of the reference tests

Machine	MTS 25kN					
Surface sample state	Polished					
Control signal	Triangular					
Strain rate	$\dot{\epsilon} = 1.10^{-2} s^{-1}$					
Total strain variation, $\Delta\epsilon_t$ (%)	0.3	0.4	0.5	0.7	0.9	1
Strain ratio, $\epsilon_{min}/\epsilon_{max}$	$R_\epsilon = 0^+$					

2.5 Analysis techniques

In order to characterise the material damage subjected to fatigue loading, several techniques have been employed in the present work, they are detailed here.

2.5.1 Scanning Electron Microscope (SEM) observations

Qualitative observations can be obtained through SEM observations such as initiation crack mode, propagation crack mode (fracture observations) and plasticity marks. All samples were at least mechanically polished to $\frac{1}{4}\mu m$ before the fatigue tests. Observations were made on a FEI Quanta 400 microscope.

2.5.2 Transmission Electron Microscope (TEM) Observations

Thin foils were prepared and examined using a Philips CM30 transmission electron microscope. Discs with a diameter of 3 mm were extracted from the specimen gages previously thinned up 100 μm by mechanical polishing. Finally, the foils were electrochemically polished to perforation using the twin-jet technique in a solution of 10 vol% perchloric acid and 90 vol% ethanol.

2.5.3 Controlled Electron Contrast Channelling Imaging (cECCI) observations

In addition to TEM, the electron channelling contrast imaging (ECCI) technique was employed for the dislocations arrangement identification. By contrast with standard ECCI, cECCI requires the knowledge of grain orientations to place the sample in two-beam diffraction conditions which is obtained through standard Electron Back Scattered Diffraction (EBSD) analysis. Therefore, Orientation Imaging Mapping was first performed and the resulting data were entered as input in the TOCA software [ZAE02] which provides a simulated electron channelling pattern (ECP). Afterwards, the program was used to determine tilt and rotation of the microscope stage needed to obtain the two-beam diffraction conditions for the defined set of lattice planes.

The ECCI technique is extremely sensitive to the surface condition [ZAE14] and sample preparation remains a critical step. The samples were ground to 1200 grit paper, followed by mechanical polishing with 9, 3 and $\frac{1}{4}$ μm diamond pastes. An intermediate chemical polishing with 10% HF and 90% H_2O_2 was applied to remove the deformation layer caused by mechanical preparation. The final mechanical polishing consisted of prolonged mechanical polishing with colloidal silica, which removed the oxide layer produced on the surface by the chemical polishing step [ZAE14].

EBSD measurements were obtained with an EDAX/TSL system, with a Hikari camera and with the TSL OIM Data collection software. cECCI acquisitions were carried out on a Zeiss Merlin instrument and on a JEOL JSM-7100F microscope.

2.5.4 Electron Back-Scattered Diffraction (EBSD) measurements

EBSD analyses were carried out on a FEI Quanta 400 electron microscope fitted with an Oxford Instruments EDS/EBSD system. The purpose is to obtain EBSD pattern which processing provide localisation of the strain at a mesoscopic scale.

EBSD specimens were prepared by grinding, polishing and a final electrochemical polishing in a solution of 10 vol% perchloric acid and 90 vol% ethanol. A Nordlys CCD camera was used for pattern acquisition. Data were recorded at 1 μm step size using Oxford Instruments Aztec software. The analyses were carried out using both Oxford Instruments Channel 5 and TSL OIM 7 commercial software. By choosing the highest possible image resolution for pattern processing and by optimizing the Hough transform parameters, an angular resolution of about 0.3° has been measured. The step size for acquisition is chosen according to Chen *et al* optimisation method [CHE12](see ANNEX 1). The

observations were made in the centre of the useful area of the fatigue samples, with surfaces oriented at an angle of 70° to the horizontal and the acquisition parameters are detailed in Table 2-6.

Table 2-6: EBSD acquisition parameters

Working distance	Step size	Bining	Scan size
15 mm	$1\mu\text{m}$	$2*2$	$800\mu\text{m}*450\mu\text{m}$

The local strain levels of the Fe-3Si steel were considered through the Image Quality (IQ) of the pattern, the line segment method (LSM) as well as the study of local misorientation. These latter aspects are studied by means of the KAM, GROD and GOS criteria (define hereafter).

The schematic illustration showing a grain composed of pixels in the EBSD measurement is presented in Figure 2-14. The thick lines represent grain boundaries determined as boundaries which have misorientation larger than 15° . A square grid is used for the mapping, thus each pixel i has eight neighbouring pixels.

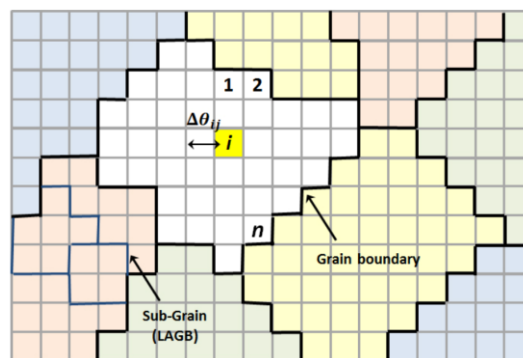


Figure 2-14: Schematic illustration showing a grain composed of pixels in a square grid based EBSD measurement [BOU15]

2.5.4.4 Line Segment Method

When considering the line segment method (LSM) [JED13], the grain boundary traces are represented by line segments separating adjacent EBSD points associated to a specific misorientation. Indeed, whereas conventional metallography considers a grain boundary as a line separating two grains, OIM grain boundary refers to a line segment separating two measurement points in a scan. The High Angle Grain Boundaries, with misorientations usually higher than 15° , correspond to the metallographic grain boundaries. The Low Angle Grain Boundaries (LAGB) are associated with misorientations between 2 and 15° and generally correspond to subgrains.

2.5.4.5 Image Quality

In the Image Quality maps (IQ), each mapping point corresponds to the quality of an electron backscatter diffraction pattern. Therefore, image quality is affected by the non-indexable areas

related to the presence of defects, grain boundaries and deformation. Hence, lower IQ patterns correspond to a lattice distortion that can be related to structures such as grain boundaries and dislocation sub-structures [WRI11][PET10]. Indeed, deformation within the material induces the formation of two types of dislocation: the Statistically Stored Dislocations (SSD) and the Geometrically Necessary Dislocations (GND) (Figure 2-15). In the SSD regions, the global burger's vector is close to zero on the contrary to the GND regions where there is a change in the crystallographic orientation. This can lead to the formation of subgrain boundaries. In this case, the diffraction pattern of the volume is the superposition of the images of the two subgrains resulting in a shift of the Kikuchi lines (Figure 2-16). GND may also come from the distortion of the network induced by a phase change.

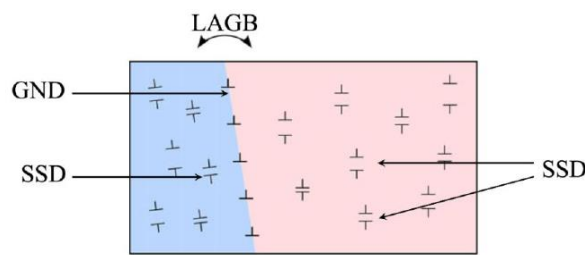


Figure 2-15: Schematic representation of Statistically Stored Dislocations (SSD) and Geometrically Necessary Dislocations (GND) [WRI11]

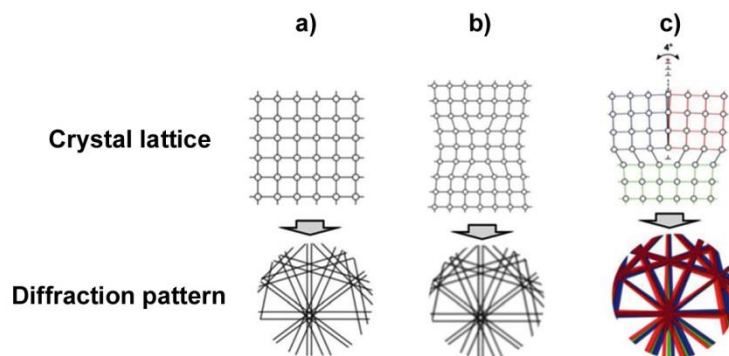


Figure 2-16: Schematic representation of the influence of network changes on the diffraction pattern a) non-deformed, b) with a zero global Burger's vector, c) in the case of a LAGB [WRI11]

2.6 Digital Image Correlation (DIC)

DIC method consists in the image acquisition of a specimen surface having a grey level distribution before and after deformation. Then, displacement vectors distribution is obtained by image correlation. More details regarding the principles of the technique are given in annex 2.

In the present study, the use of the DIC technique has been considered to evaluate the strain in a notched specimen subjected to cyclic loading with a force control mode for two reasons:

- 1) Validate the strain estimation based on the EBSD analyses (§5.3.2)

2) Validate the strain distribution evaluated by finite element analysis (§6)

DIC is performed with Aramis application system constituted of CCD camera and Aramis v6.3 software developed by GOM. The camera, equipped with a 100mm lens, has a resolution of 2448*2050 pixels and a maximum frame rate of 15Hz.

To conduct the DIC analyses, the notch specimen is first mechanically polished up to $3\mu\text{m}$. Then, to obtain a speckle surface, a white antireflection paint is applied uniformly on the surface. Once it is dry, a graphite-based spray is applied in order to obtain correct grey distribution from the random repartition of black dots on the surface (Figure 2-17 (a)). The sample is then put into the fatigue testing machine and the camera is placed in front of the specimen at 90° to its surface (Figure 2-17 (b)).

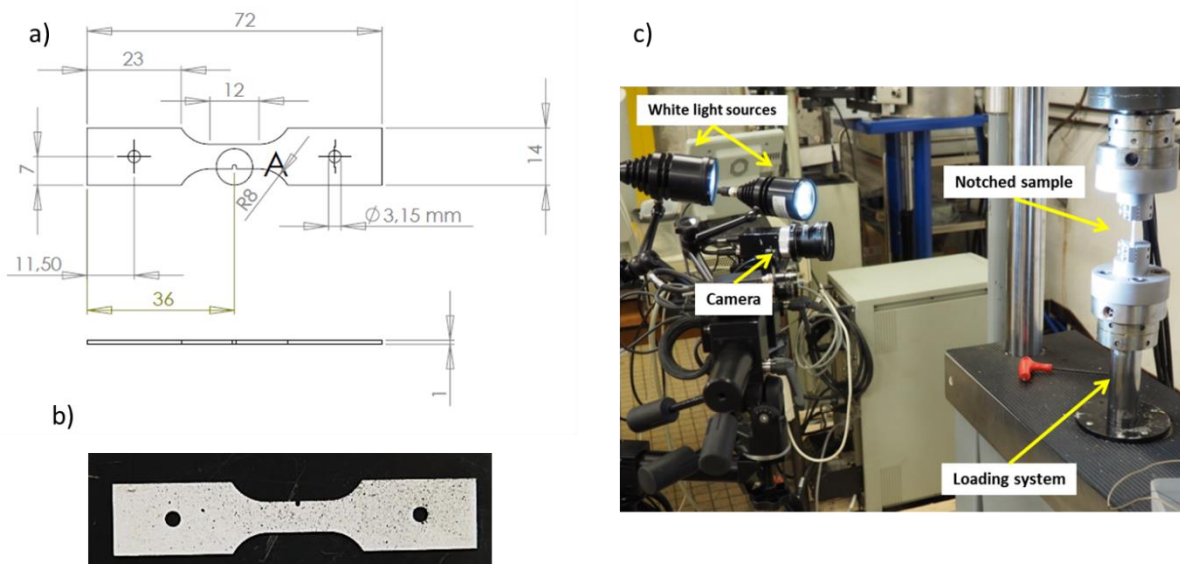


Figure 2-17: (a) Dimensions of the notched sample, (b) Speckle surface of a notched sample and (c) experimental set-up

The sample is subjected to cyclic loading under load control mode as shown in Figure 2-18. Image acquisition is performed before the fatigue test and during the cycles number $N=1, 10, 11, 50, 100, 500, 1000$ and 2000 cycles.

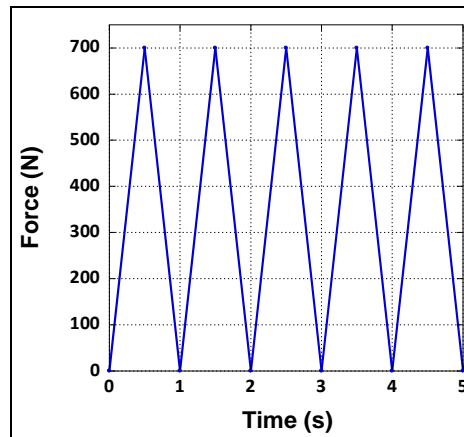


Figure 2-18: Cyclic loading with force control, $F_{\max}=700\text{N}$ and $F_{\min}=0\text{N}$

The displacement field in the deformed image is calculated with the Aramis software by comparison with the initial image of the undeformed state. The strain along the Y axis, ε_y , and shear strain, ε_{xy} are then calculated at each stage. The strain distributions at F_{\max} are shown in Figure 2-19 as a function of the number of cycles. Strain is measured with an error of 0.1%.

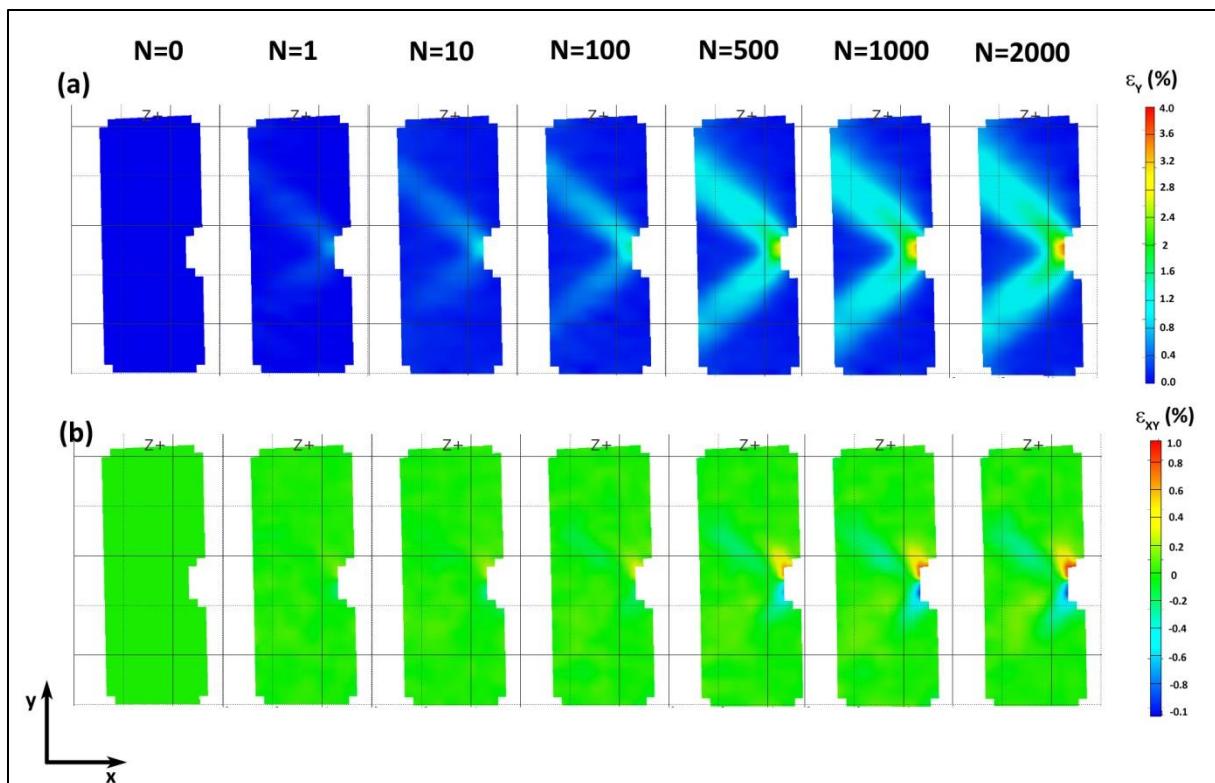


Figure 2-19: (a) Longitudinal strain, ε_y , and (b) shear strain, ε_{xy} , distribution estimation by DIC of a notched sample subjected to cyclic loading at F_{\max} for $N=0, 1, 10, 100, 500, 1000$ and 2000 cycles

These results highlight the longitudinal strain localisation in the notch root and the shear bands and the shear strain in the shear bands. Due to the subset size (9 pixels), the strain distribution in the exact vicinity of the notch cannot be evaluated. The evolution of the longitudinal strain ε_y at the point where the strain is the maximum at the notch root is evaluated Figure 2-20 (a) and (b).

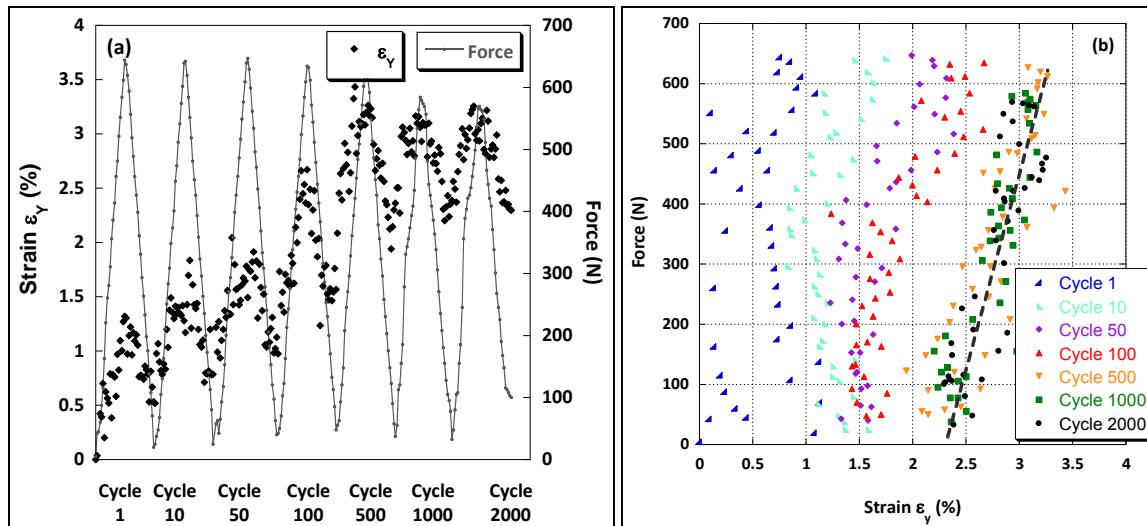


Figure 2-20: (a) Evolution of the longitudinal strain ε_y at the notch root and (b) hysteresis curves as a function of the cycle number

The Figure 2-20 (a) shows that the cyclic evolution of the longitudinal strain is in agreement with the cyclic load, the strain increases when the force increases. Moreover, the maximum strain increases with the number of cycle up to $N=500$ cycles. From this number of cycles, the strain evolution is in a stabilised regime where no more plastic straining occurs as shown in the hysteresis curves (Figure 2-20 (b)).

2.7 Conclusion

In the as-received condition, the **non-oriented M330-35A steel** exhibits a **large ductility to plastic deformation**. However, the **mixed rupture mode** with the presence of dimples and presence of transgranular brittle cleavage suggest a **low fracture toughness** of the material.

The incremental step test method performed under load control shows that the **M330-35A hardens under cyclic loading**.

Fatigue tests are conducted under **strain control mode at $2 \cdot 10^{-3} \text{ s}^{-1}$ and a strain ratio $R_\varepsilon=0$** . The **total strain variation ($\Delta\varepsilon_t$)** is comprised between **0.3% and 1%**. Due to the thickness of the specimen, an **anti-buckling system** is used.

Different analysis techniques are used to characterise the fatigue damage:

- **SEM** is used to determine **crack nucleation** and **propagation modes**.
- **TEM** and **cECI** enables **dislocation structures observations**
- **EBS**D measurements are made to obtain a **correlation between EBSD signature and the applied strain** and to **localise the strain at a mesoscopic scale**

Finally, **DIC technique** is considered to **evaluate the strain in a notched specimen** subjected to cyclic loading with a force control mode. These results will be used to validate strain estimation based on EBSD analyses and strain distribution given by finite element analysis.

The fatigue properties of the material and the influence of several parameters on its behaviour are studied in the chapter III. Then, the fatigue damage mechanisms are studied at different scales. Indeed, macroscopic damage is studied by the observation of fracture surfaces and crack initiation sites observations and microscopic damage is studied by the evolution of dislocation structure in the material. EBSD is then used for quantitative damage evaluation. Finally, DIC results are used to validate the results of the finite element analysis.

Chapter III:

Low Cycle fatigue behaviour

1. Reference test
2. Influence of parameters
3. Conclusion

3 Low cycle fatigue behaviour

As presented in the first chapter, only few studies have been devoted to the cyclic behaviour of iron-silicon steels and in the case of the present material M330-35A, only high-cycle fatigue has been considered [HOE13]. However, the LCF study is needed in order to:

- 1) Understand the damage mechanisms of the material leading to the rupture
- 2) Establish a procedure to localise strain induced by the cyclic loadings in a component
- 3) Describe the material behaviour under cyclic loading in order to define a material law that can be implemented in the numerical modelling to improve the rotor design

The fatigue behaviour of a material is related to complex phenomena and involves many parameters. However, in the frame of laboratory which aims at understanding physical phenomenon, sample geometry and loading conditions are adapted to the experimental setup and to allow further metallurgical investigation. To be as close as possible to the real loading conditions of a component, a separated study on the influence of several loading parameters is conducted.

Thus, the work is separated in two parts:

- The reference tests which characterises the general behaviour of the material. These tests are strain controlled with an asymmetric signal.
- The study of the influence of several parameters which are detailed hereafter.

3.1 Reference tests

3.1.1 Stress response to strain cycling

The cyclic behaviour of M330-35A with the number of cycles and with the fatigue life fraction for different total strain variations, $\Delta\varepsilon_t=0.3\%$ to $\Delta\varepsilon_t=1\%$, are shown in Figure 3-1 (a) and (b) respectively.

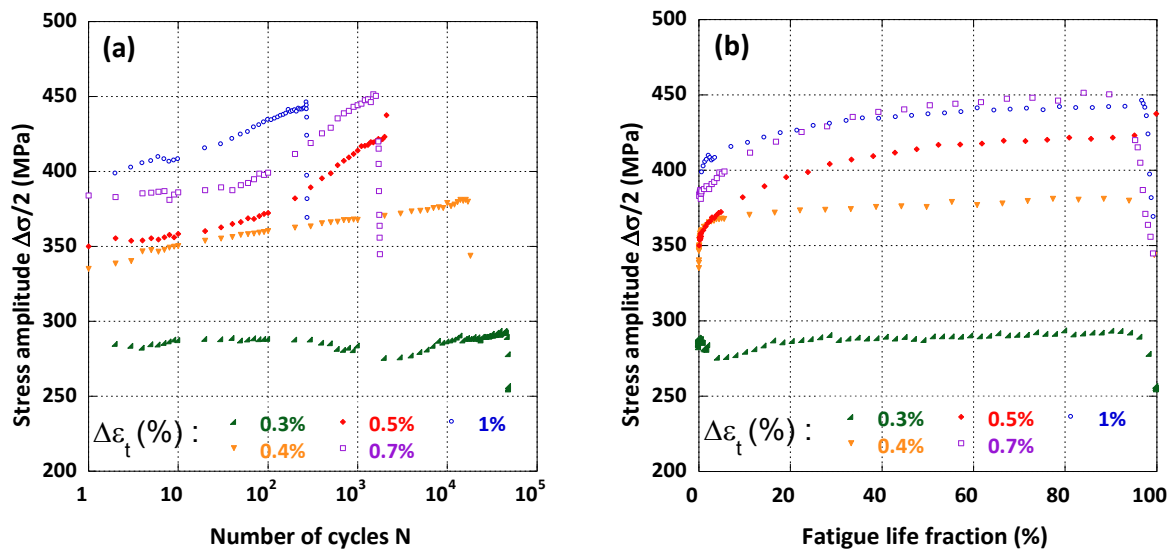


Figure 3-1: Evolution of the stress amplitude of the M330-35A steel with the number of cycles (a) and of the fraction of lifetime (b)

Different behaviours are observed according to the total strain variation. For total strain variations superior to $\Delta\varepsilon_t=0.3\%$, a short period of about 10 cycles with almost constant stress amplitude is observed. Then, a rapid hardening stage occurs followed by a moderate hardening stage. For $\Delta\varepsilon_t=0.5\%$, the transition between the high and low hardening rate periods represents about 30% of the fatigue life. At $\Delta\varepsilon_t=0.4\%$, the rapid hardening stage corresponds to about 10% of the fatigue life. Figure 3-1 (b) shows that the hardening is very strong at the beginning of the fatigue life and then lessens for the major part of the life. The saturation stress amplitude is the same for total strain variations superior to $\Delta\varepsilon_t \geq 0.7\%$ and is 450MPa.

For the test performed at $\Delta\varepsilon_t=0.3\%$, the evolution is almost constant with a stress value lower than the yield stress. In this case the material is loaded in a quasi-elastic regime.

The Fe-3Si steel of the present study being single phase ferritic steel, it is interesting to compare its behaviour to that of α -iron single crystal. Indeed, in the case of α -iron single crystal, Mughrabi *et al.* [MUG81] have also shown that above a given plastic deformation, cyclic hardening occurs (Figure 1-19). Compared to α -iron, the present Fe-3Si exhibits higher stress amplitudes. This is consistent with the previous studies on the cyclic behaviour of Fe-Si steel with various amount of silicon by Sestak *et al.* [SES88] and it is attributed to solid solution strengthening by Si atoms.

Linear stress amplitude for the first cycles followed by cyclic hardening was also observed in the case of Cu-Al [ABE79].

Moreover, M330-35A reaches similar stress amplitudes for total strain variation superior to $\Delta\varepsilon_t=0.7\%$ which suggests that strain localise in specific dislocation structure at these strain level. This will be verified by the study of the damage mechanisms in the next chapter.

3.1.2 Work hardening

The evolution of the material during the cyclic loadings is different whether there is cyclic softening or cyclic hardening. Thus, the cyclic work hardening curve corresponding to the stabilised stress amplitude versus the plastic strain amplitude is compared to the monotonic hardening curve.

The first quarter of the first cycle of the fatigue test is considered for the monotonic stress-strain curve whereas the stabilised hysteresis curve is considered for the cyclic stress-strain curve. In the present study, as there is no complete stabilisation, hysteresis curves from the quasi-stabilised state are considered. More precisely, it has been arbitrarily decided to consider hysteresis curves taken at 70% of the fatigue life as stabilised.

These curves are represented in Figure 3-2. The cyclic curve does not follow the power law defined in equation (1-5) which links the stabilised stress amplitude to the stabilised strain amplitude. Indeed the cyclic hardening curve presents a discontinuity: at low plastic strain amplitudes, the stress amplitude remains low. Then, between $\Delta\varepsilon_p/2 = 0.005\%$ and $\Delta\varepsilon_p/2 = 0.01\%$, the stress amplitude increases and finally stabilises at about 425MPa above $\Delta\varepsilon_p/2 = 0.01\%$. This discontinuity in the cyclic stress-strain curve was expected from cyclic accommodation curves as 1) M330-35A does not harden at very low plastic strain ($\Delta\varepsilon_t = 0.3\%$ in Figure 3-1 (a) and (b)) and 2) similar stress amplitudes are reached above $\Delta\varepsilon_t = 0.7\%$.

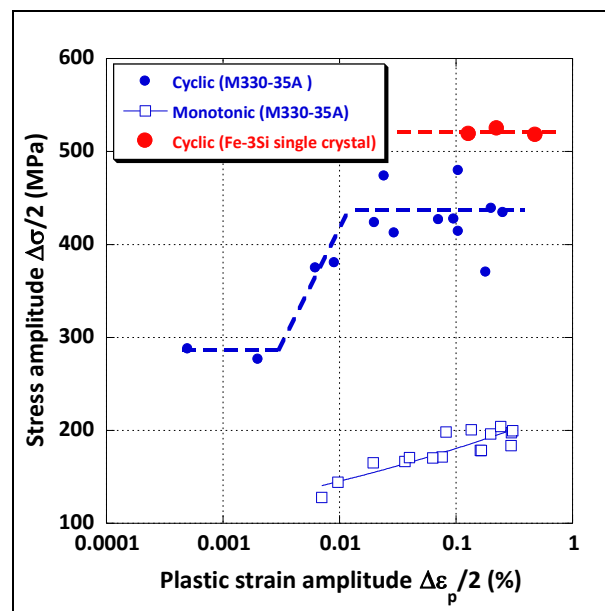


Figure 3-2: Cyclic stress-strain curve and monotonic hardening curve of M330-35A and cyclic stress-strain curve of Fe-3Si single crystal oriented for single slip on $(\bar{1}01)$ plane [SES88]

At low strain variations, similar absence of hardening has been reported for niobium [ANG79] [MEI92], pure iron single crystal [MUG76] and in Fe-3Si single crystals (at $\dot{\varepsilon} = 2 \cdot 10^{-3} s^{-1}$, $\Delta\varepsilon_p \leq 6 \cdot 10^{-4}$) [MAG82]. Mughrabi *et al.* attributed this to the limited dislocation multiplication in this regime and a

strain accommodation by quasi-reversible back and forth motion of the more mobile edge dislocations [MUG76]. Similar stabilised stress amplitude were also observed in the cyclic stress-strain curve of Fe-3Si single crystal above $\Delta\varepsilon_p/2=0.1\%$ by Sestak *et al.* [SES88].

3.1.3 Fatigue resistance

As mentioned in §1.3.1.2.3, the fatigue resistance of a material is estimated through the Manson-Coffin and Basquin relations, the Pseudo-Wöhler relation, and on the evolution of the energy density with fatigue life.

3.1.3.1 Manson-Coffin and Basquin relations

The Manson-Coffin curve shows the evolution of the plastic deformation with the number of cycles to failure, it is represented in blue round symbols in Figure 3-3. The Basquin curve relates the elastic deformation to the number of cycles to failure; it is plotted in red triangle symbols in Figure 3-3. These curves follow the power laws that are defined in equation (1-6) and (1-7), their coefficients are detailed in Table 3-1. Manson-Coffin law is thus adapted for fatigue life prediction.

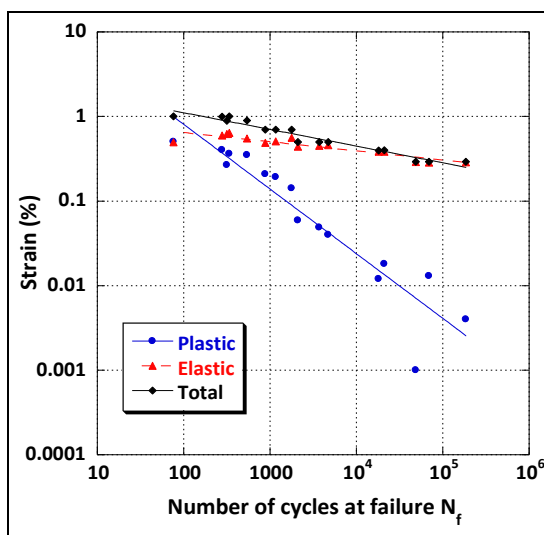


Figure 3-3: Stabilised plastic, elastic and total strains versus the number of cycles to failure for M330-35A

Table 3-1: Basquin and Manson-Coffin coefficients for M330-35A

Basquin relation	
$\Delta\varepsilon_{ea}=K_e(N_f)^{C_e}$	
K_e	C_e
1.0407	-0.1070
Manson-Coffin relation	
$\Delta\varepsilon_{pa}=K_p(N_f)^{C_p}$	
K_p	C_p
27.311	-0.7673

3.1.3.2 Pseudo-Wöhler relation

The stress amplitude evolution with the number of cycles to failure is plotted in Figure 3-4. The stress amplitude does not follow the power law defined in (1-8). It is due to the absence of hardening at low strain amplitudes and similar stabilised stress amplitude at strain variation superior to $\Delta\varepsilon_t=0.7\%$. This is in agreement with the cyclic stress-strain curve in Figure 3-2.

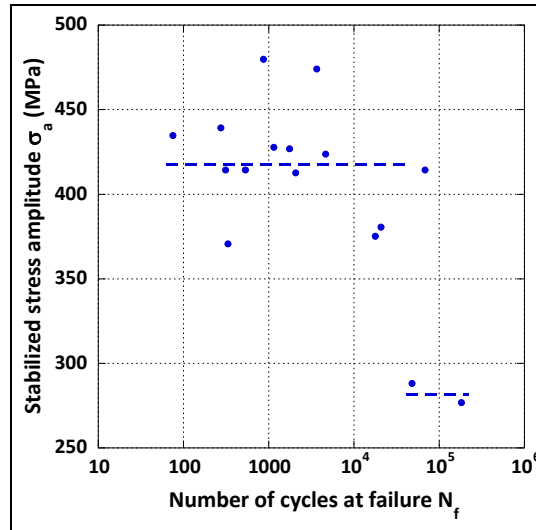


Figure 3-4: Stabilised stress amplitude versus the number of cycles to failure for M330-35A

3.1.3.3 Relationship based on the energy density of cyclic strain

The Figure 3-5 describes the evolution of the hysteresis curve area taken at 70% of the fatigue life as a function of the number of cycles to failure. The curve fits well the power law defined in equation (1-10) and its coefficients are presented in Table 3-2. The relation is based on the dissipated energy during cycling. As deformation and stress are taken into account in this curve, the discontinuity in the evolution of stress amplitude with the number of cycles to failure is less visible.

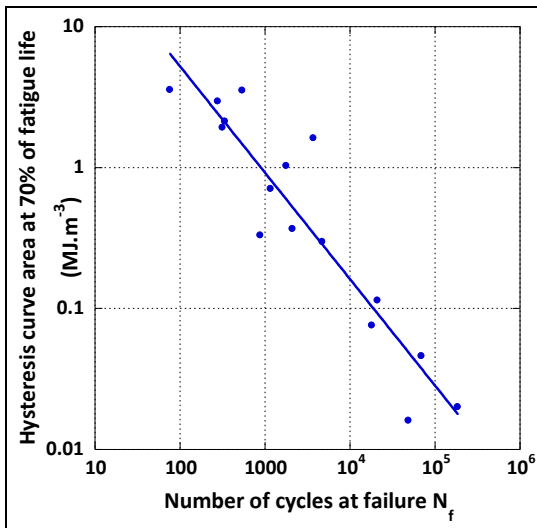


Table 3-2: Coefficient of the power law defining fatigue resistance curve based on energy density for M330-35A

$$\Delta W_p = K_{Wp} (N_R)^{C_{Wp}}$$

K_{Wp}	C_{Wp}
31.577	-0.62402

Figure 3-5: Area of the stabilised hysteresis curve versus the number of cycles to failure for M330-35A

3.1.4 Conclusion

The M330-35A exhibits two types of stress response to cyclic straining: a strong hardening followed by a moderate but continuous hardening at high strain range and rather stable response at low strain range. It leads to discontinuities in the cyclic hardening curve. Thus, the use of fatigue resistance law based on cyclic stress amplitude (Pseudo-Wöhler curve) is not encouraged. Indeed, in chapter six

concerning numerical modelling, fatigue life prediction from mechanical analyses will be needed and from the present work the Manson-Coffin relation based on the evolution of plastic strain variation is the most adapted for the M330-35A steel.

3.2 Influence of testing parameters

The influence of different parameters on the fatigue behaviour of M330-35A was studied. Some parameters are related to the definition of the specimen state: surface finishing and direction of the loading axis of the specimen to the rolling direction, other parameters are related to the test procedure: strain ratio, strain rate, holding time, prior-cycling.

3.2.1 Experimental protocol

3.2.1.4 Influence of specimen state

In order to study the influence of the specimen state, the fatigue tests were conducted with the same protocol than for the reference test (Table 2-5) for three different strain variations, $\Delta\varepsilon_t=0.5\%$, 0.7% and 1%. For the as-received specimen, no polishing was performed in order to study the influence of the surface coating. It consists in a pigmented varnish made with 88etal88l-stable resins, mineral products and pigments. It is applied on the steel sheet in order to provide inter-laminar insulation and corrosion protection. In addition, the influence of the rolling direction was studied by collecting specimen at 90° to the rolling direction (Figure 3-6). If the material exhibits isotropic properties no effect should be observed.

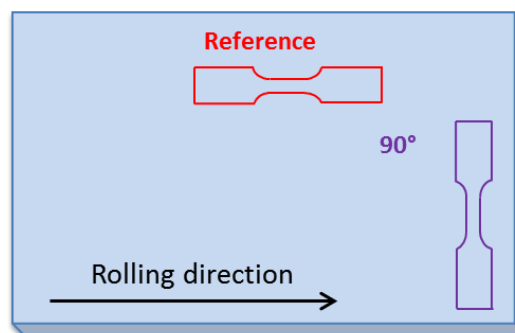


Figure 3-6: Direction of specimen collection in regard to the rolling direction

3.2.1.5 Influence of the testing protocol

Different parameters were changed with regard to the reference test protocol. Only one parameter is changed at a time everything else staying equal. Thus, the strain ratio and the strain rate influences are studied. Then, relaxation phenomenon and load history are also considered.

- The influence of the mean strain is studied by fatigue tests with a load signal corresponding to $R_\varepsilon=-1$ as shown in Figure 3-7.

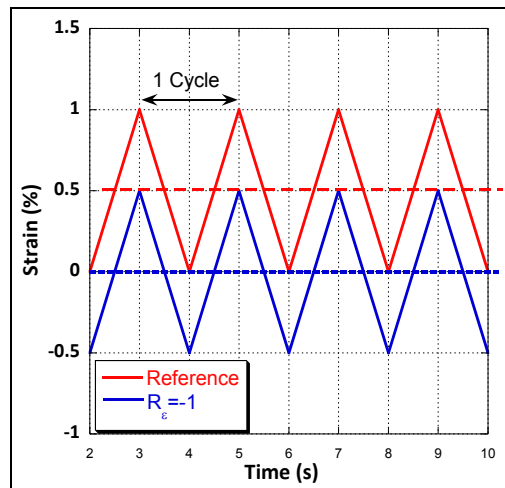


Figure 3-7: Load signal at $R_\epsilon=-1$

- The strain rate of the reference test is $\dot{\epsilon} = 1.10^{-2} s^{-1}$. As this strain rate, the test frequency is close to 1Hz which reduces the test duration in comparison with classical strain rate of $\dot{\epsilon} = 4.10^{-3} s^{-1}$ or $\dot{\epsilon} = 1.10^{-3} s^{-1}$. To study, the material behaviour at medium strain rate, tests were conducted at $\dot{\epsilon} = 1.10^{-3} s^{-1}$, ten times lower than the reference test speed.
- Relaxation phenomenon are usually linked to high temperature test, however the influence of a holding time on the material behaviour was studied here. These tests are related to fatigue-relaxation tests. It consists in a cyclic load at ambient temperature at $\dot{\epsilon} = 1.10^{-2} s^{-1}$ with a holding time at ϵ_{max} as shown in (Figure 3-8). The holding time was chosen in order to obtain complete relaxation. Therefore, the relaxation time is different according to the strain variation, holding times are reported in Table 3-3.

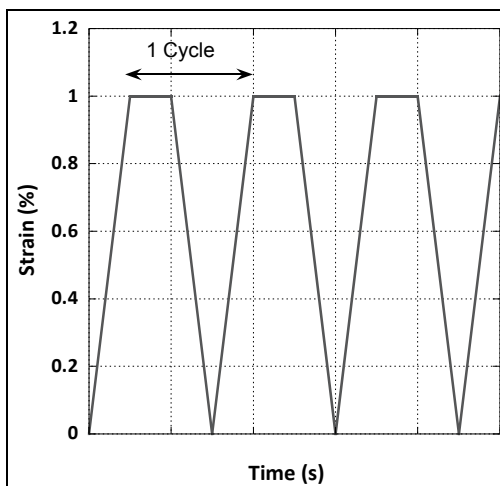


Figure 3-8: Load signal to study the influence of an holding time

Table 3-3: Holding time according to the total strain variation

$\Delta\epsilon_t$ (%)	0.5	0.7	1
Holding time (s)	90	90	10

- To study the influence of the loading history, two successive blocks of variable amplitude are applied to the specimen, 5 cycles at $\Delta\epsilon_t=1\%$ were applied followed by a cycling at a lower

strain variation until rupture (Figure 3-9). This load sequence would be similar to an overload cycling of the rotor in the alternator.

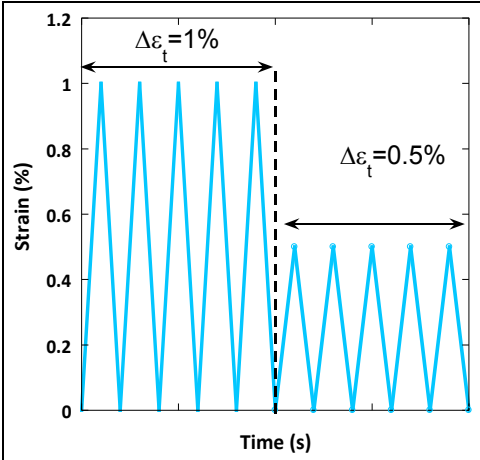


Figure 3-9: Load signal of the two-steps test

A summary of the different parameters and protocol is presented in Table 3-4.

Table 3-4: Summary of the studied parameters

	Reference	90°	As received	$R_\varepsilon=-1$	10^{-3}	Relaxation	Two-steps
Direction to rolling	0°	90°	0°	0°	0°	0°	0°
Surface state	Polished	Polished	As received	Polished	Polished	Polished	Polished
Strain ratio $R_\varepsilon = \frac{\varepsilon_{min}}{\varepsilon_{max}}$	0 ⁺	0 ⁺	0 ⁺	-1	0 ⁺	0 ⁺	0 ⁺
Strain rate (s ⁻¹)	10 ⁻²	10 ⁻²	10 ⁻²	10 ⁻²	10 ⁻³	10 ⁻²	10 ⁻²
Holding time	No	No	No	No	No	Yes	No
Prior cycling	No	No	No	No	No	No	Yes
Colour code							

3.2.2 Results

3.2.2.1 Cyclic accommodation

The cyclic accommodation curves corresponding to samples collected perpendicular to rolling direction and samples tested as received are plotted in Figure 3-10 (a) and (b) respectively and the cyclic accommodation curves corresponding to symmetric tests at $R_\varepsilon=-1$ and tests at a strain rate of $\dot{\varepsilon} = 1.10^{-3}s^{-1}$ are plotted in Figure 3-10 (c) and (d) respectively. Cyclic accommodation curves corresponding to relaxation tests and the influence of prior-cycling are shown in Figure 3-10 (e) and (f) respectively.

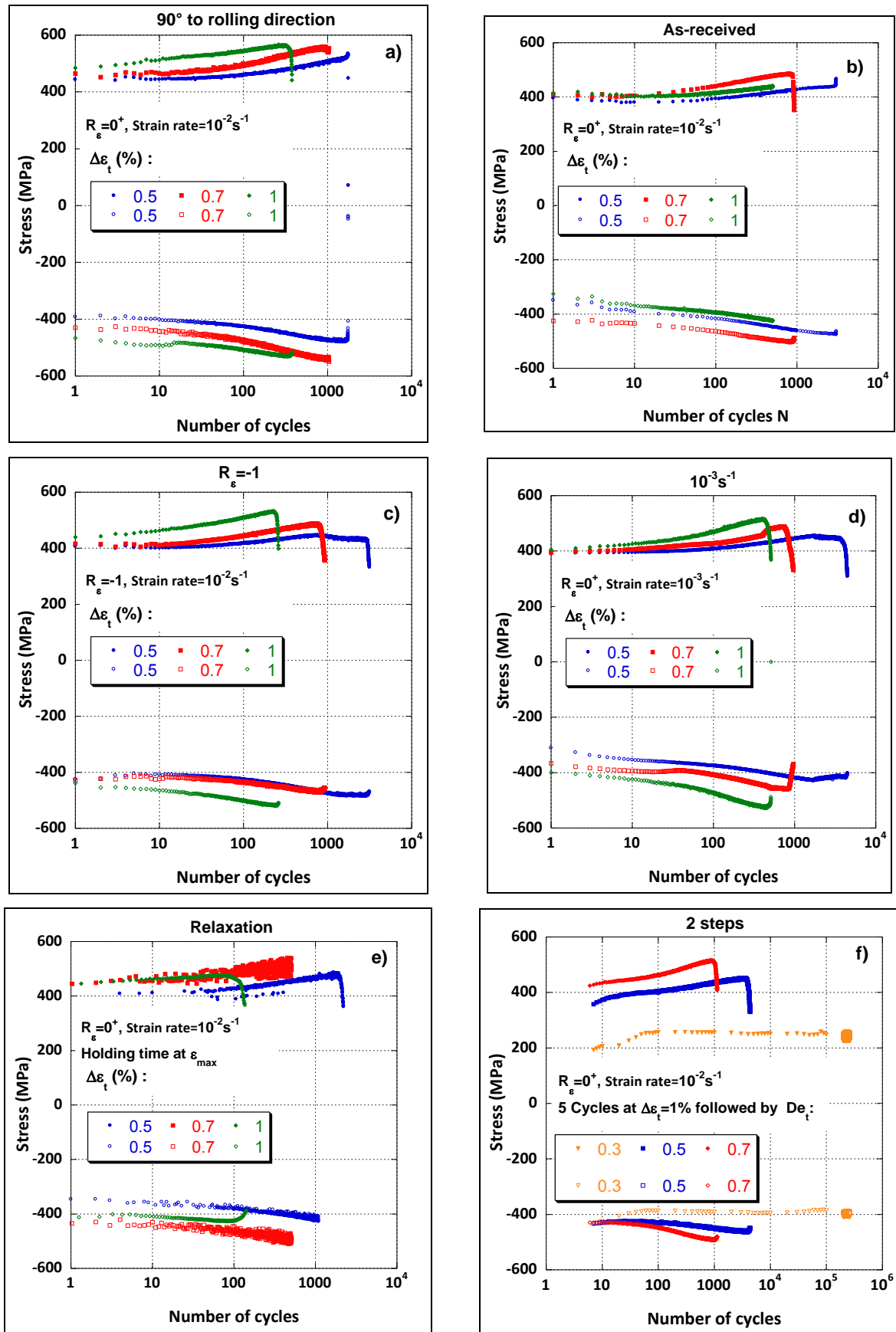


Figure 3-10: Cyclic accommodation of M330-35A (a) specimen taken at 90° to the rolling direction, (b) as received specimen, (c) tests at $R_\epsilon = -1$, (d) tests at 10^{-3} s^{-1} , (e) relaxation tests and (f) 2 steps tests

Cyclic accommodation curves show that the same behaviour is obtained for every condition and is the same than for the reference test with rather stable stress amplitude evolution for about 10 cycles followed by cyclic hardening.

The cyclic accommodation curves corresponding to the as-received material (Figure 3-10 (b)) are similar to those of the reference test. This means that the removal of the coating does not influence the results. Also it shows that there is no noticeable residual stress resulting from the rolling process at the surface of the sample in the as-received material which would have induced different results than the reference test for which the specimen surfaces are polished.

In the following for purpose of comparison, the as-received curve (Figure 3-10 (b)) can be assumed to represent the reference test (Figure 3-1).

In the case of isotropic properties of the material, the cyclic accommodation curves corresponding to samples collected perpendicular to the rolling direction (Figure 3-10 (a)) should be similar to the reference test. Here, the samples collected perpendicular to the rolling direction reach slightly higher stresses than those collected in the rolling direction (Figure 3-10 (b)). This effect reflects probably the slight texture pointed out in the as received material. When samples are collected perpendicular to the rolling direction, the orientations of the grain for dislocation slip activity is less favourable and thus, higher stress is needed to activate dislocation slip and accommodate the strain.

The cyclic accommodation curves corresponding to symmetric tests, $R_\epsilon = -1$ (Figure 3-10 I) is similar to the reference tests; no influence of the strain ratio is observable here. The cyclic accommodation curves corresponding to the tests performed at $\dot{\epsilon} = 10^{-3} \text{s}^{-1}$ are also similar to those corresponding to the reference tests.

The cyclic accommodation curves corresponding to samples subjected to cyclic loading with a holding time at ϵ_{\max} is presented in Figure 3-10 (d). Whereas relaxation phenomena are usually encountered at high temperature (above $0.3T_M$), it appears that the material at room temperature presents a relaxation of the stress in tension (ϵ_{\max}) (Figure 3-11). This relaxation is characterised by the relaxation rate, τ_{relax} , as defined in the equation (3-1), with σ_{peak} corresponding to the maximum stress and σ_{relax} corresponding to the relaxed stress as defined in Figure 3-11.

$$\tau_{\text{relax}} = \frac{\sigma_{\text{peak}} - \sigma_{\text{relax}}}{\frac{1}{2}(\sigma_{\text{peak}} + \sigma_{\text{relax}})} \quad (3-1)$$

The relaxation is approximately 20% (Table 3-5). Moreover, the material behaviour (peak stress evolution and number of cycles to failure) is identical to the reference test for the three strain amplitudes (Figure 3-10 I). The stress amplitude is stable for the 10 first cycles then the material hardens. Hysteresis curves could not be recorded for these tests.

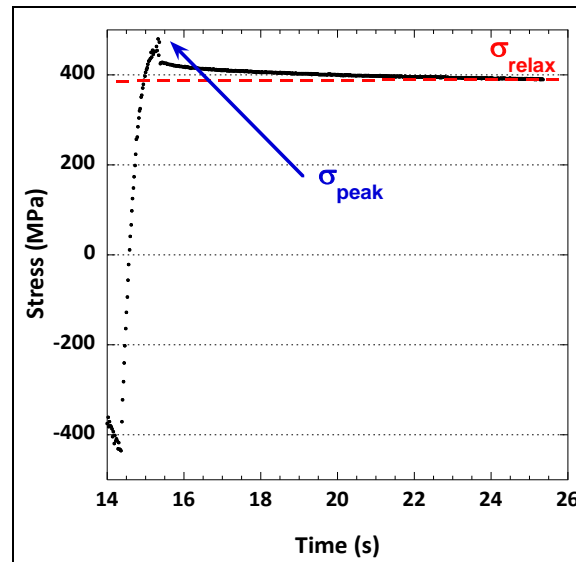


Figure 3-11: Stress answer to the loading with a holding time

Table 3-6: Relaxation rate for the different strain amplitude

$\Delta\varepsilon_t$ (%)	0.5	0.7	1
Relaxation τ_{relax} (%)	15	22	20

Finally, the cyclic accommodation curves corresponding to the two-steps tests are considered. For these tests, the samples are initially cycled at $\Delta\varepsilon_t=1\%$ for 5 cycles followed by cyclic loadings at $\Delta\varepsilon_t=0.3\%$, $\Delta\varepsilon_t=0.5\%$ or $\Delta\varepsilon_t=0.7\%$ (Figure 3-10 (f)).

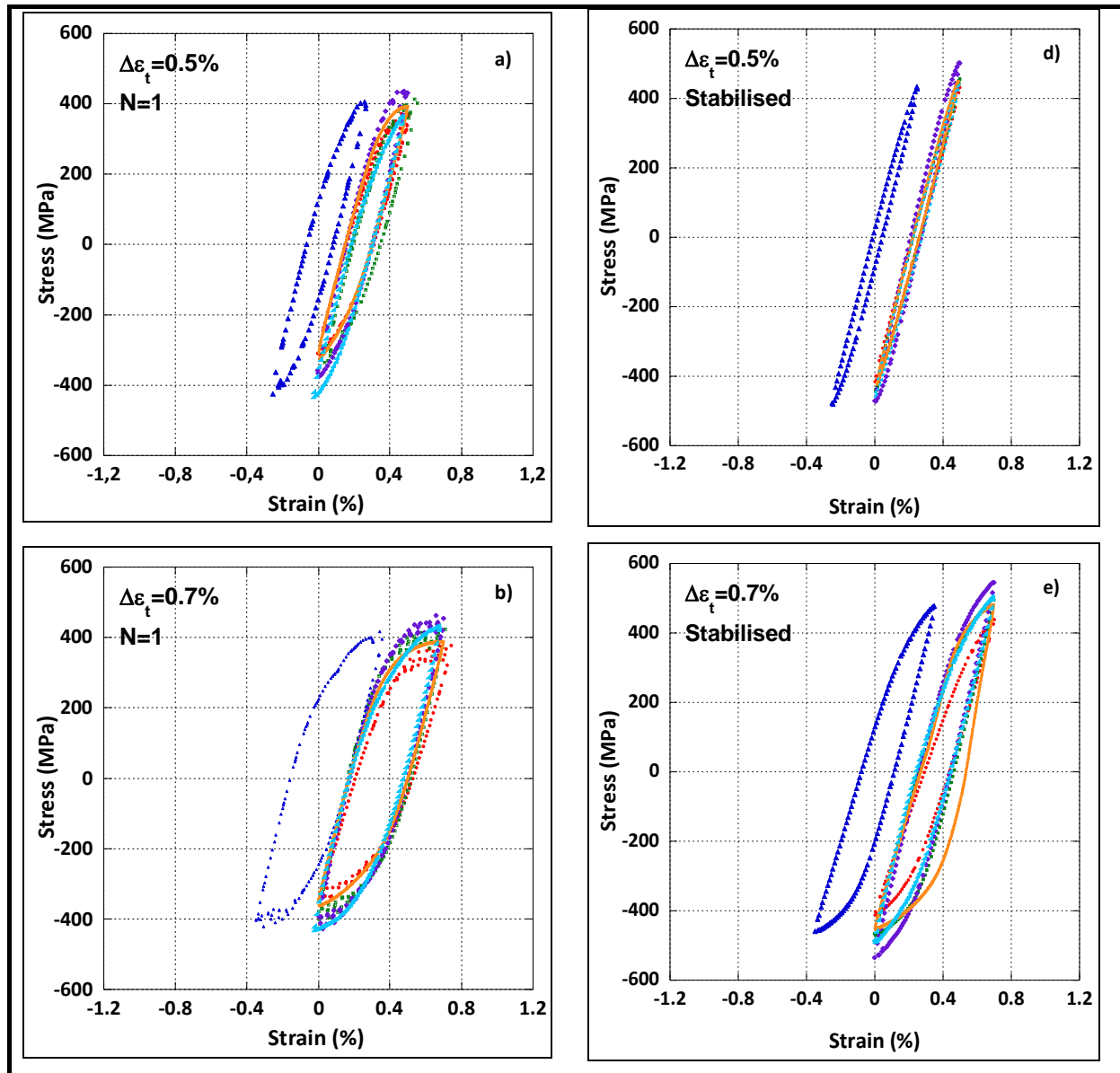
After the prior-cycling at $\Delta\varepsilon_t=1\%$, the material starts directly hardening and for $\Delta\varepsilon_t=0.5\%$ and $\Delta\varepsilon_t=0.7\%$, the material behaviour is the same than for the reference test. Plastic strain amplitudes of the first cycle after prior-cycling and at the stabilised state are the same than for the reference test.

However, the behaviour is different at $\Delta\varepsilon_t=0.3\%$, the material hardens for the first hundred cycles and then stabilised, the stabilised plastic strain amplitude $\varepsilon_{pa} = 0.05\%$ is ten times superior to the reference test. Also, the stress becomes asymmetric after the prior-cycling. This asymmetric behaviour is related to a memory effect of the material. It has been shown by Chopra *et al.* that in α -iron subjected to two-step tests with first cycles at an initial high strain range followed by cycles at a lower strain range, the stress amplitude decreases rapidly but the modification in the substructure is very slow [CHO74]. Such phenomenon may occur in the present M330-35A material, the dislocation structure created during the first cycles may induce slip asymmetry of the dislocation. Only the study of dislocation structure evolution and damage mechanisms of the material can verify this assumption.

3.2.2.2 Hysteresis curves

The evolution of the hysteresis curves for the different conditions is plotted in Figure 3-12.

All the hysteresis curves present the same shape than the reference test. The stress amplitudes and the plastic strain ranges remain similar to the reference test condition. Only the specimen taken perpendicular to the rolling direction exhibits slightly higher stress value than the reference test which might be a consequence of the texture observed in the as-received material.



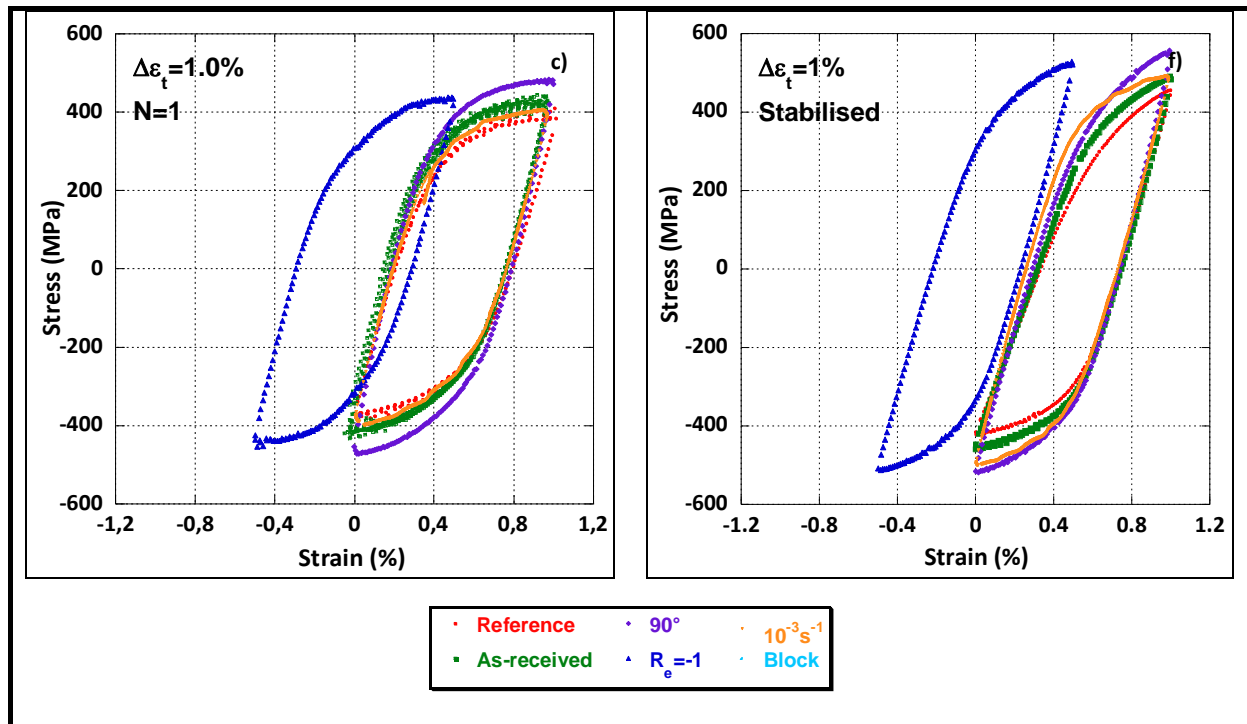


Figure 3-12: Hysteresis curve for the reference test (in red), the as received specimen (in green) and 90° specimens (in purple) of the first cycle (a) $\Delta\epsilon_t=0.5\%$ (b) $\Delta\epsilon_t=0.7\%$ (c) $\Delta\epsilon_t=1\%$, and the pseudo-stabilised cycle (taken at 70% of the fatigue life) (d) $\Delta\epsilon_t=0.5\%$ | $\Delta\epsilon_t=0.7\%$ (f) $\Delta\epsilon_t=1\%$

3.2.2.3 Cyclic hardening curve

Cyclic hardening curves for all conditions are plotted in Figure 3-13. As noticed from the stabilised hysteresis curve, stress amplitude is higher for samples taken perpendicular to the rolling direction. Also, it seems that the stress amplitudes for the reference tests are lower than for the other conditions. However, this comment should be taken carefully due to the non-negligible scattering of the results. This scatter can arise from the mechanical fatigue testing conditions but, in the present case, the major contributor to this scatter is most probably due to the thickness of the specimen. Indeed, the sheet thickness is 350 μm which represent only 4 to 5 grains. Thus, few grains participate to the cyclic accommodation and according to metallurgic factor such as the grain size, grain orientation, grains response to cyclic load can be different and induce uncontrolled scatter. Nevertheless, the tendency is that similar stress amplitudes are reached for stabilised plastic strain ϵ_{pa} , superior to 0.1%.

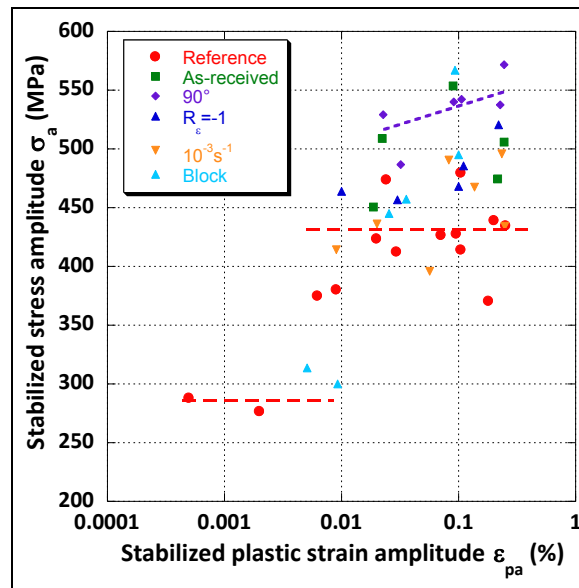


Figure 3-13: Cyclic hardening curves for different conditions

3.2.2.4 Resistance to fatigue

The study of the material response to cyclic loading (in the reference condition) revealed that Manson-Coffin relation (equation 1-7) and energy based law (equation 1-10) were adapted for fatigue life prediction of the present material.

Thus the Manson-Coffin curves for all conditions are plotted in Figure 3-14. It shows that the Manson-Coffin relation stays valid for all the testing conditions. However, regarding the energy based law (Figure 3-15), there are differences between the reference condition and the other conditions. Indeed, the reference curve is lower than for the other conditions in the high strain range. This is due to the difference in the stress amplitudes related in Figure 3-13.

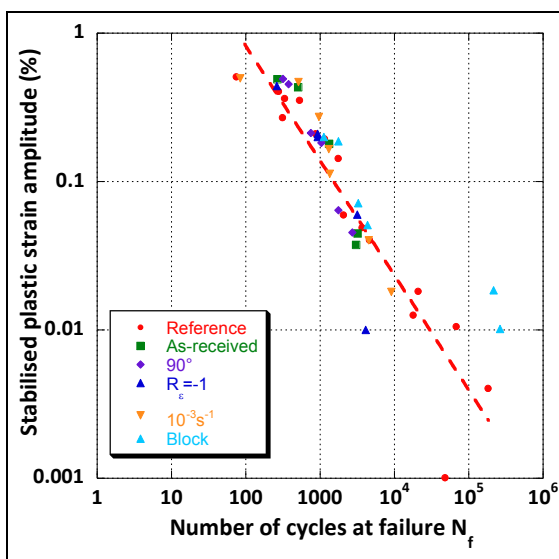


Figure 3-14: Stabilised plastic strain amplitude versus the number of cycles to failure for different conditions

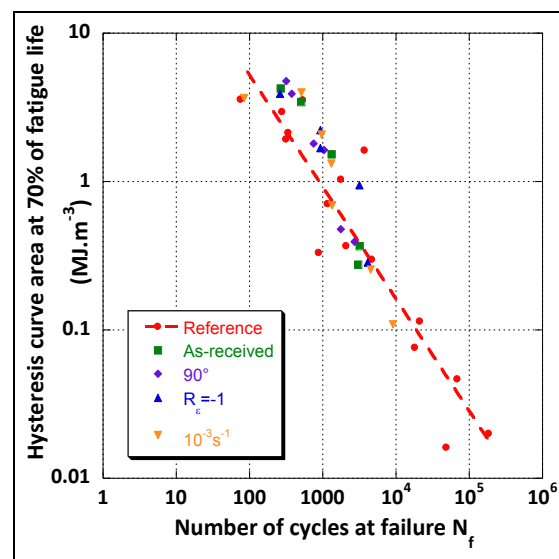


Figure 3-15: Area of the stabilised hysteresis curve versus the number of cycles to failure for different conditions

Consequently, the Manson-Coffin relation established for the reference condition is the most adapted to fatigue life prediction of this material. Therefore, this relation will be used for fatigue life prediction of numerical modelled component.

3.3 Conclusion

Under cyclic loading at $R_e=0$ and strain rate of 2.10^{-3} s^{-1} , M330-35A exhibits different cyclic accommodation behaviours according to the total strain variation.

At $\Delta\varepsilon_t=0.3\%$, the stress amplitude evolution is almost constant, the material is loaded in a quasi-elastic regime.

For $\Delta\varepsilon_t>0.3\%$, a short period of about 10 cycles with almost constant stress amplitude is observed followed by a rapid hardening stage and finally a moderate hardening stage.

This LCF study shows also that the **Manson-Coffin law is well suited for the prediction of fatigue lives** of this material.

The study of different testing conditions related to the specimen (surface state and direction toward rolling) and related to the test procedure (choice of strain ratio, strain rate, holding time, prior cycling) shows that they can modify the fatigue response. Especially, when **cycling perpendicular to the rolling direction, M330-35A exhibits higher stress amplitude** than when loaded in the parallel direction.

Under fatigue-relaxation, **stress relaxation of about 20%** occurs but it has no consequence on the cyclic accommodation and fatigue life of the material.

Finally, the two-step tests with first cycles at $\Delta\varepsilon_t=1\%$ followed by cycles at $\Delta\varepsilon_t=0.3\%$ induce **stress asymmetry which arise from a memory effect of the material** from the dislocation structures created during the first cycles.

The Manson-Coffin relation established from the reference test stays valid for all conditions as well as the relation based on the energy density of cyclic strain. This is useful, because one law can be applied to many conditions, therefore, **these relations can be used for fatigue life prediction of numerical modelled component.**

Chapter IV:

Fatigue damage mechanisms

1. Fracture surface observations
2. Crack initiation
3. Evolution of dislocation structures
with $\Delta\varepsilon_t$
4. Discussion

4 Fatigue damage mechanisms

LCF study of the M330-35A steel revealed two behaviours depending on total strain variations. There is no cyclic hardening at low strain variations, with almost constant stress amplitude. At higher strain range, rapid hardening occurs after a short transient period of about 10 cycles followed by moderate hardening. In order to understand the mechanism leading to the failure of the specimen microstructural observations are made at different scales.

First, analyses of the fracture surface of samples loaded until rupture were made. Secondly, observations of the evolution of slip marks on the surface of the samples were carried out. Both observations were performed by SEM. Finally, the evolution of the dislocation structures as a function of the total strain variation is studied by TEM on ruptured samples and by cECCL on samples subjected to interrupted tests. All these observations lead to a discussion and interpretation of the cyclic strain accommodation mechanisms leading to the rupture of the material.

4.1 Fracture surface observations

After the fatigue tests, the fracture surfaces of the samples were observed by SEM. The general appearance of the fracture surfaces suggests a brittle fracture. Some grains exhibit a pure transgranular cleavage fracture with the presence of rivers (Figure 4-1). Other grains are also flat, decorated with rivers but with largely spaced striations typical of cyclic cleavage (Figure 4-2). It can be considered that the main crack did not propagate by fatigue.

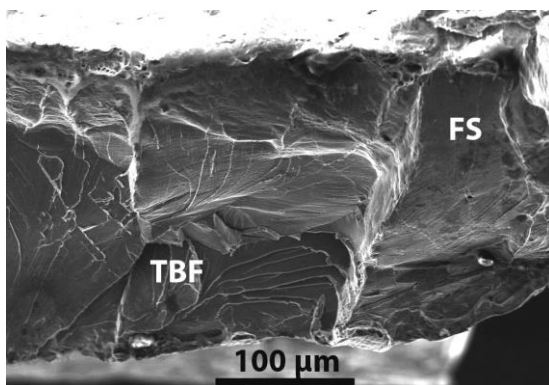


Figure 4-1: Fracture surface of a sample fatigued at $\Delta\epsilon_i=0.5\%$ ($N_f=2422$ cycles) showing transgranular brittle fracture (TBF) cleavage fracture and fatigue striations (FS)

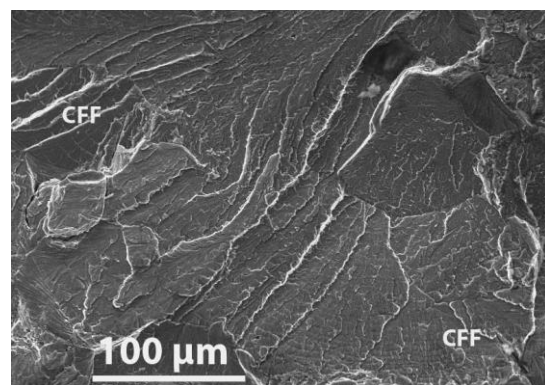


Figure 4-2: Fracture surface of a sample fatigued at $\Delta\epsilon_i=1\%$ ($N_f=279$ cycles) showing cyclic cleavage fracture (CFF)

Such fragile aspects of a fatigue fracture surface are rather unusual for a material that exhibits a macroscopic ductile behaviour. However, it confirms previous observations made on Fe-3Si steels by Van Hoecke *et al.* [HOE13], Shimojo *et al.* [SHI99], Chakravarthula *et al.* [CHA05a] and Bode *et al.*

[BOD16]. Shimojo *et al.* tried to establish a crystallographic orientation criterion for striation formation in Fe-3Si steel, but their conclusion was that striations occurred provided that the fatigue crack plane is perpendicular to the loading direction without crystallographic relationship [SHI99].

4.2 Crack initiation

The observations of the surface of the polished fatigue samples revealed an effect of the strain variation on crack initiation sites. Indeed, below $\Delta\varepsilon_t=0.7\%$, slip marks are visible and crack initiation is mainly transgranular (Figure 4-3), whereas above $\Delta\varepsilon_t=0.7\%$, few slip marks were observed and crack initiation is intergranular (Figure 4-4). At $\Delta\varepsilon_t=0.7\%$, mixed crack initiation mode is observed.

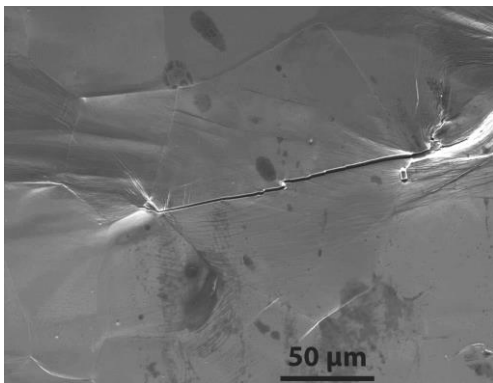


Figure 4-3: SEM image of a sample after fatigue failure at $\Delta\varepsilon_t=0.5\%$ ($N_f=4709$ cycles) showing transgranular crack initiation

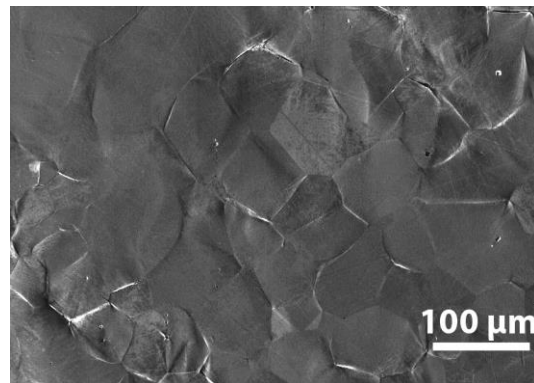


Figure 4-4: SEM image of a sample after fatigue failure at $\Delta\varepsilon_t=1\%$ ($N_f=200$ cycles) showing intergranular crack initiation

Transgranular crack nucleation results from localisation of plastic deformation in adapted dislocations structures. There are several causes for crack initiation at grain boundaries. Strain accumulation at grain boundaries leads to high stress which may be relaxed by crack nucleation and propagation. Whether a crack forms at grain boundary depends on the applied strain level, on the grain boundary character (low or high angle boundary, special or random boundary) or on strain incompatibility between neighbouring grains for example.

4.3 Evolution of dislocation structures with $\Delta\varepsilon_t$

Dislocations structures are observed by TEM investigations, thin foils are extracted from ruptured samples but far from the main crack loaded at different total strain variations.

The as-received material (Figure 4-5 (a)) exhibits a low dislocation density. After the test performed at $\Delta\varepsilon_t=0.4\%$ (Figure 4-5 (b)), some dislocations are visible but they appear as rather short, isolated and serrated segments. At $\Delta\varepsilon_t=0.5\%$ (Figure 4-5 (c)), the dislocation density increases and two slip systems were activated. By comparison with the dislocation structure found after the test, at $\Delta\varepsilon_t=0.4\%$, they are more elongated in the form of elliptical shape. They also tend to entangle and to bundle especially at the intersecting glide planes. At $\Delta\varepsilon_t=0.7\%$ (Figure 4-5 (d)), the vein and channel

structure is formed within the grain, it is characterised by veins of high dislocation density and channel of low dislocation density. Dislocation walls are formed near the triple point. This suggests a higher strain localised in this region. Finally, at $\Delta\varepsilon_t=1\%$ (Figure 4-5 I), the wall structure is observed near grain boundaries as well as in the grain interior but the walls appeared more frequently condensed and the channels contained a very high dislocation density and a large number of debris and small loops.

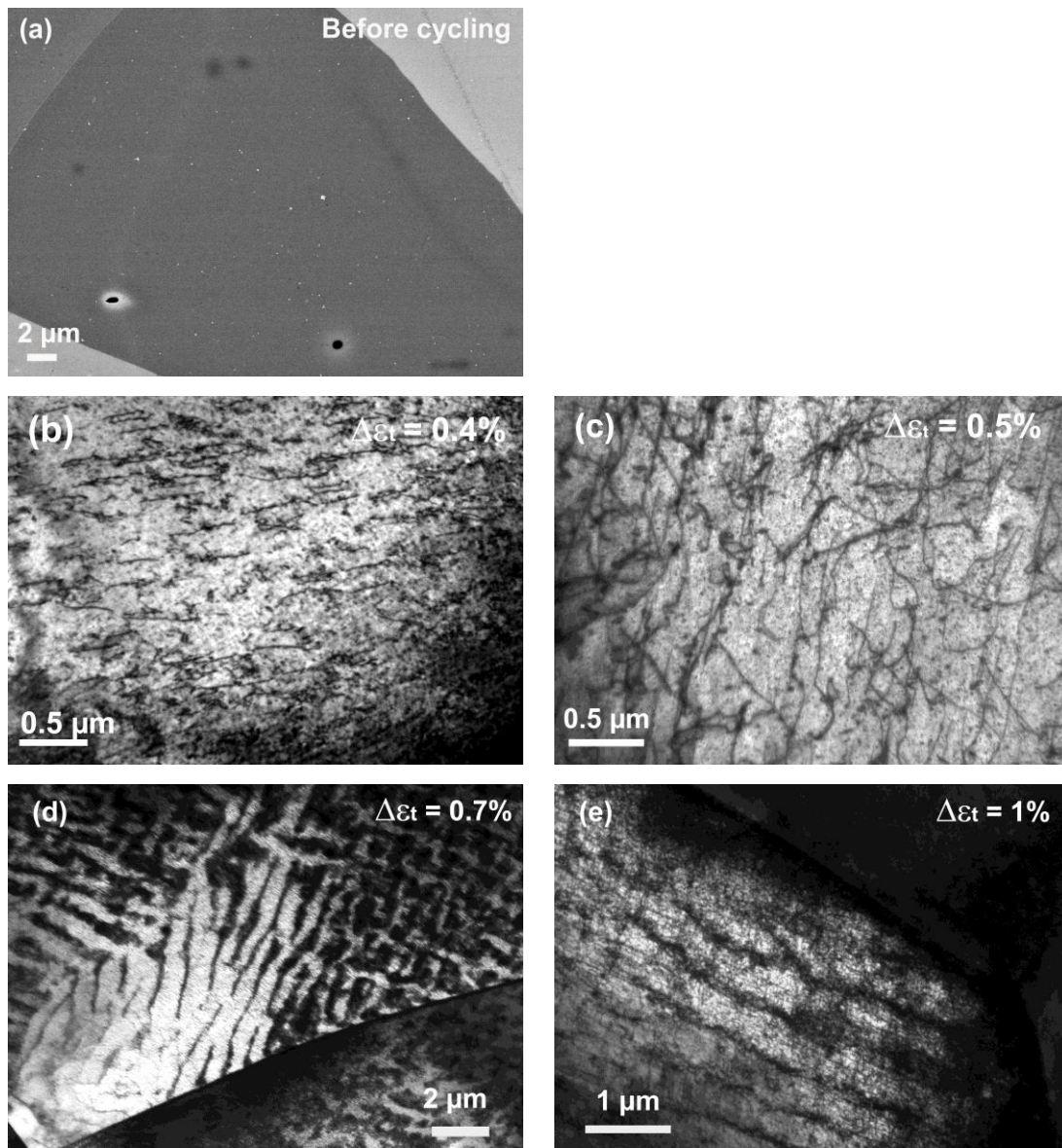


Figure 4-5: cECCL image of raw material (a) and TEM images of ruptured samples after cyclic straining at $\Delta\varepsilon_t=0.4\%$ - $N_f=21075$ cycles (b), $\Delta\varepsilon_t=0.5\%$ - $N_f=4705$ cycles (c), $\Delta\varepsilon_t=0.7\%$ - $N_f=1785$ cycles (d) and $\Delta\varepsilon_t=1\%$ - $N_f=338$ cycles I

From these observations, it can be concluded that the dislocation mobility is difficult and that the formation of stable dislocation arrangement is very slow. The formation of dislocation structures, as

$\Delta\varepsilon_t$ increases, proceeds gradually to form an organised wall structure without ever forming a cell structure as it could be expected for ferritic steels ([SES88], [USH99]). At low strain variation, plastic strain is most probably accommodated by the back and forth motion of edge dislocations. Thus, the dislocations lines that appear in Figure 4-5 (b) correspond to the screw dislocations which motion is difficult. Increasing the strain increases the dislocation density and activates a second glide system which induces the creation of bundles. Further increase of the strain promotes the formation of veins of high dislocation density and channels of low dislocation density. Then, stress incompatibilities appear in the vicinity of grain boundaries where condensed dislocation walls are created.

4.4 Discussion

From those observations, it appears that crack initiation mode and dislocation structure is strongly dependent on the applied strain variation. The total strain variation of $\Delta\varepsilon_t=0.7\%$ seems to be a transition strain at which crack initiation mode changes and dislocation structures start to form. Seeking an explanation to this phenomenon, the evolution of internal and effective stresses with fatigue life and total strain variation were analysed by hysteresis loop analysis. The Handfield-Dickson's method was chosen [DIC84] in order to decompose the macroscopic stress into the effective stress (thermal component) and the internal stress (athermal component). It enables the determination of the effective stress from analysis of hysteresis loops recorded during fatigue (Figure 4-6) and without interruption of the fatigue test which is an advantage in comparison to relaxation tests.

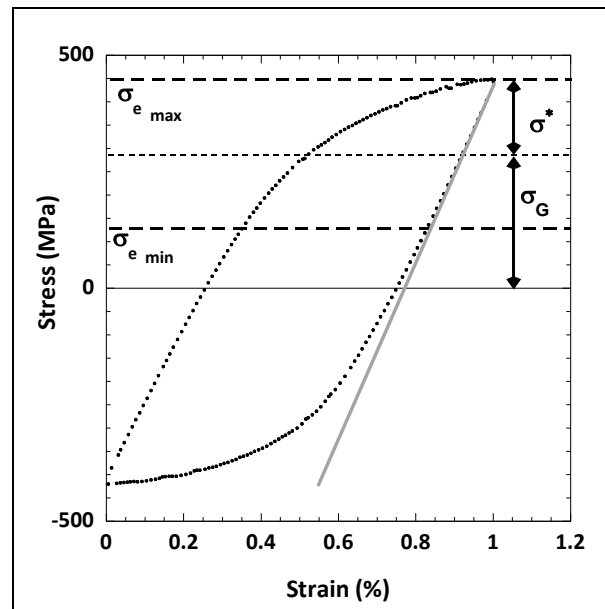


Figure 4-6: Dickson's method for hysteresis loop analysis

The advantage of this method is that it can be made without interruption of the fatigue test as a relaxation test would have required. The effective stress, σ^* , related to short range interactions and

internal stress, σ_G , related to long range interactions are calculated from the elastic domain delimited by the two frontiers: $\sigma_{e_{max}}$ and $\sigma_{e_{min}}$ and it is considered that $\sigma_{e_{min}}$ is reached when $(\sigma_{hysteresis} - \sigma_{Young})^2 > 150$. The effective stress is then obtained by the equation (4-1) and the internal stress by equation (4-2).

$$\sigma^* = \frac{\sigma_{e_{max}} - \sigma_{e_{min}}}{2} \quad (4-1)$$

$$\sigma_G = \frac{\sigma_{e_{max}} + \sigma_{e_{min}}}{2} \quad (4-2)$$

Finally, the stress components σ^* and σ_G of the macroscopic stress amplitude are plotted against the cumulative plastic strain for different total strain ranges (Figure 4-7).

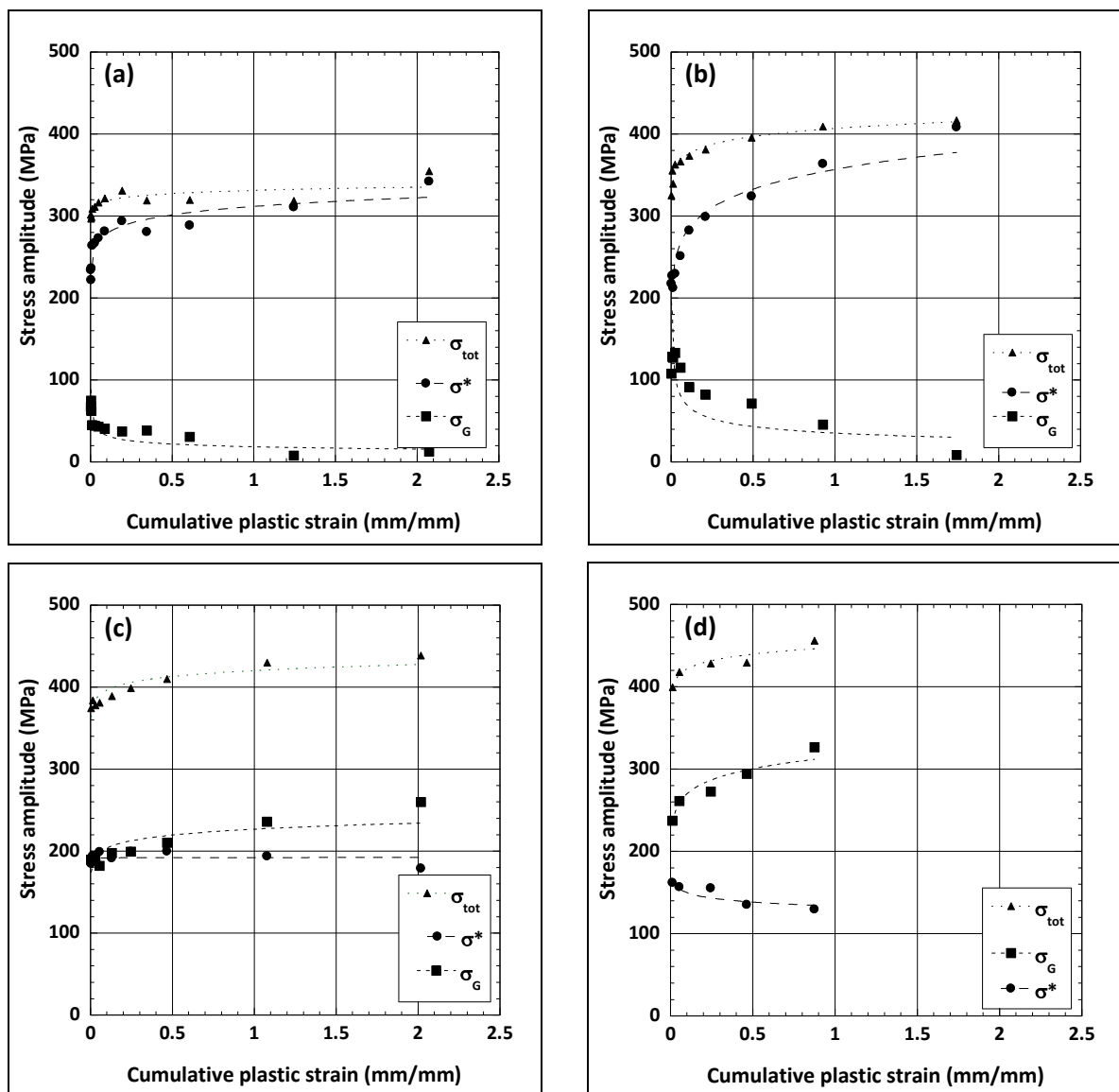


Figure 4-7: Internal and effective stress evolution vs cumulative plastic strain of the M330-35A steel for tests performed at $\Delta\varepsilon_t =$ a) 0.4%, b) 0.5%, c) 0.7%, and d) 1%

These graphs indicate different situations depending on whether $\Delta\varepsilon_t$ is below or above 0.7% and confirms the transition in cyclic strain accommodation mechanisms at this strain variation. Indeed,

below $\Delta\varepsilon_t=0.7\%$ the effective stress σ^* is much greater than the internal stress σ_G and the shape of the stress amplitude curve is reflected by that of the effective stress. The situation is opposite above $\Delta\varepsilon_t=0.7\%$ which appears as a transition strain. Indeed, at $\Delta\varepsilon_t=0.7\%$, the effective and internal stresses have similar values up to a cumulative plastic strain value of 0.3. Then, the internal stress exceeds the effective stress and starts to increase with increasing cumulative plastic strain, as does the macroscopic stress amplitude.

According to the Seeger theory (equation 1-11) [SEE54], at low strain amplitudes, the high values of the effective stress, higher than the internal stress suggest that M330-35A is deformed in the low temperature regime. As suggested by Mughrabi *et al.* [MUG76], the accommodation of low strain amplitudes is possible by the quasi reversible motion of the more mobile edge dislocations and requires only little motion of the less mobile screw dislocations. At higher strain, the opposite situation prevails: the internal stress is higher than the effective stress and the wall structure is present. This suggests that the material is fatigued in the high temperature regime. The internal stress is linked to interactions with long range obstacles such as dislocation walls and grain boundaries [MUG83]. When the test temperature is kept constant, the transition from the low to the high temperature regime is usually reported as a function of the strain rate.

In Figure 4-8, the evolutions of stabilised internal and effective stresses in pure α -iron and in M330-35A are plotted versus the stabilised plastic strain variation. It shows that both materials present a transition in the evolution of internal and effective stresses at a plastic strain variation of approximately $\Delta\varepsilon_{pa}=0.25\%$. Also, a large gap between effective stress and internal stress characterises the present Fe-3Si steel (Figure 4-8).

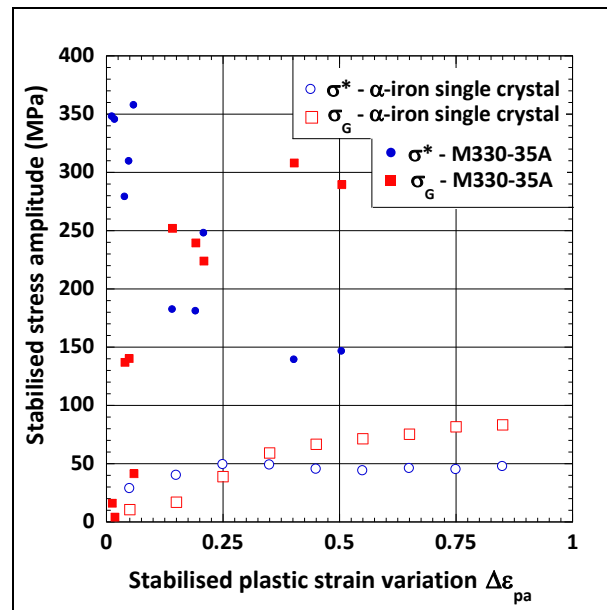


Figure 4-8: Comparison between M330-35A and α -iron single crystals of internal and effective stresses evolutions

[MUG76]

The increase in cyclic effective stress caused by the presence of Si atoms has already been pointed out in 12Cr martensitic steels [VOG94].

Two reasons can be brought forward for the observed transition:

- The first reason is the mobility of Si atoms during cycling straining. By using Mössbauer spectroscopy, Ruiz *et al* [RUJ05] showed a certain amount of ordering after thermomechanical process in Fe-Si alloy with Si content up to 7.6 wt%; however, cold deformation removed the order. Lakso *et al* [LAK74] have shown that short range order is present in Fe-Si alloy containing less than 10 at.% Si and that the yield strength is increased by increasing the Si content. Moreover, in ordered solid solution materials, even when only short range ordering occurs, the effective stresses are high [VOG94]. Therefore, in the present Fe-3Si alloy, the reduction of effective stresses by fatigue might arise from disordering. In fatigue, disordering can occur in the present alloy if both, a critical value of the plastic strain amplitude and a critical amount of cumulative plastic deformation, are reached. For the tests at the lowest total strain, none of these two conditions is satisfied especially the plastic deformation at each cycle is too low. Therefore, the effective stress remains high and constant or slightly increases during the test. For the tests at the highest strain, the amount of plastic deformation allows disordering the Fe-Si atoms clusters within few cycles. Here a decrease of the effective stress is observed because dislocations can glide more freely and randomly than in the (short-range) ordered materials.

- The second reason for the transition from the low to the high temperature regime is related to the role of grain boundaries. This generates high localised stress values which triggered high localised plastic activity (which is underlined in the next chapter with the EBSD analyses). Moreover, the presence, in the vicinity of grain boundary, of dislocation wall structures typical of higher cyclic strain confirms this situation.

In order to support the existence of strain gradients from grain boundaries to grain interiors, the evolution of the dislocation structures was studied by cECCI on samples fatigued at $\Delta\varepsilon_t=0.5\%$ and $\Delta\varepsilon_t=1\%$ for different life fractions. Examples of the results are presented in Figure 4-9 ($\Delta\varepsilon_t=0.5\%$) and Figure 4-10 ($\Delta\varepsilon_t=1\%$).

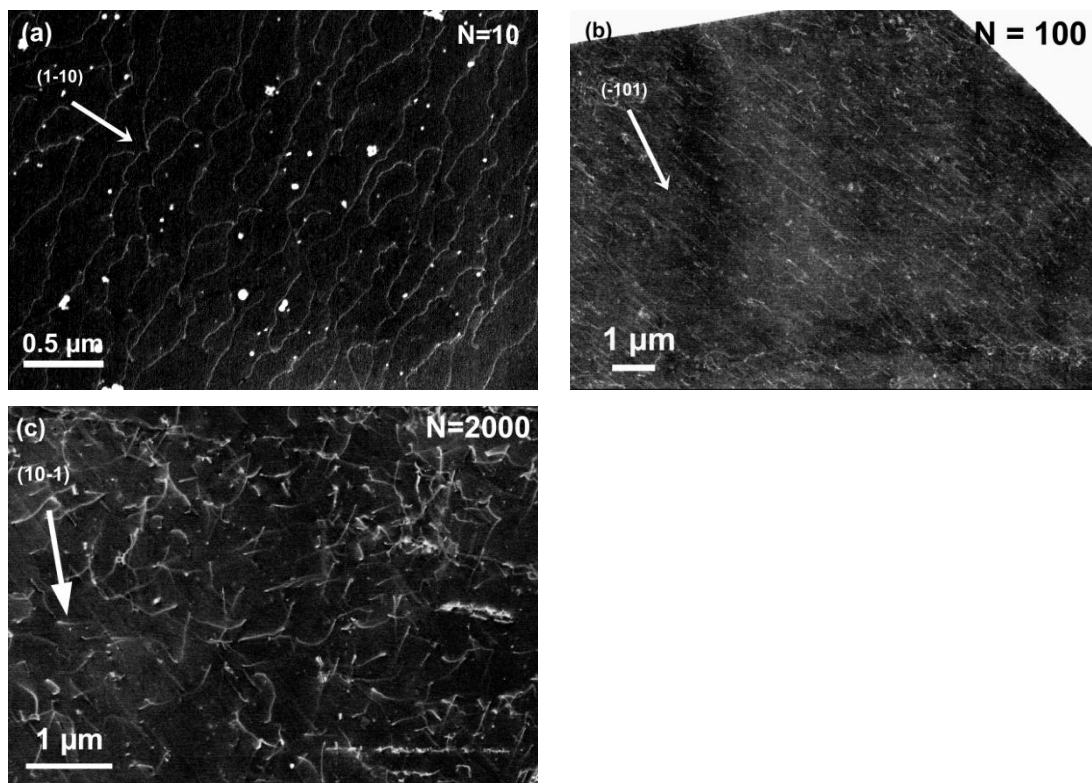


Figure 4-9: SEM-cECCI images of M330-35A steel cycled at $\Delta\varepsilon_t=0.5\%$ for different numbers of cycles showing dislocation structure (loading axis is horizontal in these images), (a) $N=10$ cycles, (b) $N=100$ cycles and (c) $N=2000$ cycles

At $\Delta\varepsilon_t=0.5\%$ and at $N=10$ cycles (0.4% lifetime) elongated jogged dislocations are found within the grain with only one slip system activated (Figure 4-9 (a)). The same configuration is observed at $N=100$ cycles (4% lifetime) as shown in Figure 4-9 (b). At $N=2000$ cycles, (80% lifetime), shorter jogged dislocations are visible and 2 slip systems are activated (Figure 4-9 (c)). No dislocation structures are observed, at this strain level, the strain is accommodated by quasi-reversible motion of dislocations.

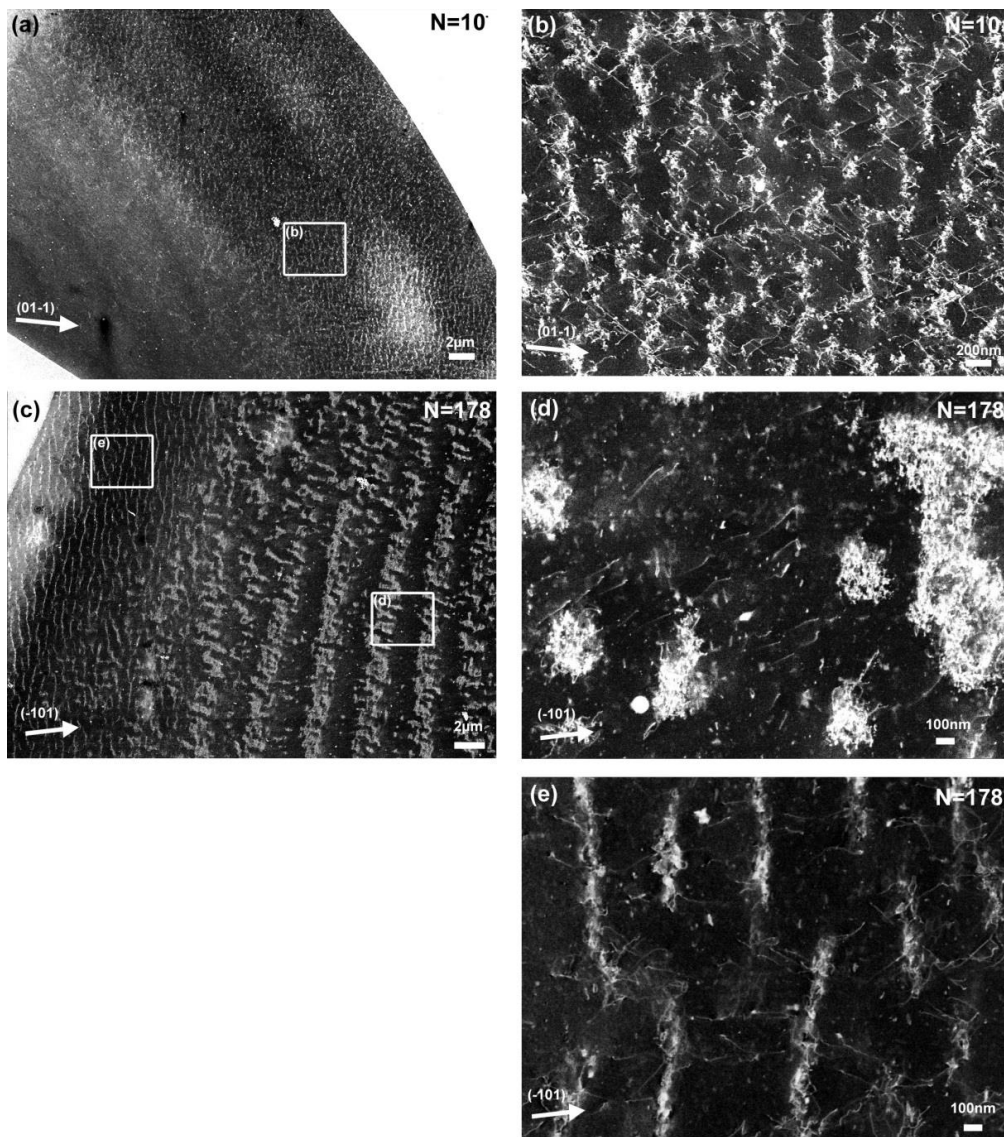


Figure 4-10: SEM-cECCI images of M330-35A steel cycled at $\Delta\epsilon_t=1\%$ for different numbers of cycles showing dislocation structure (loading axis is horizontal in these images), N=10cycles (a) and higher magnification of the square area in (b) and N=178cycles (c) and higher magnification of the square areas in (d) and (e)

At $\Delta\epsilon_t=1\%$, it appears that dislocation structure formation has already started after 10 cycles: dislocations bundles and condensed walls can be observed but they are located near the grain boundaries while the grain interior contained fewer dislocations (Figure 4-10 (a,b)). Moreover, there is double glide of screw dislocations in the channels between the walls. Slip activity and dislocation structuration are not homogeneous within the grain. The observations on other grains showed that dislocation structuration is not homogeneous within the sample. After 178 cycles, the wall structure consisted of more compact and thinner walls formed near the grain boundaries. At the same time, a vein structure and a diffuse wall structure were observed in the grain interior (Figure 4-10 (c,d,e)). These dislocation structures were already observed at N=50 and N=100 cycles. The strain gradient

within the active grains is clearly pointed out by cECCI. It is clear that at high strain amplitude, stress development at grain boundaries triggers dislocation slip activity in a narrow band which accommodates cyclic plasticity. This suggests that grains accommodate the strain in an individual way and that dislocation glide through grains is difficult. This leads to incompatibility effects [MUG81] producing intergranular stresses and thus intergranular strain localisation and finally intergranular crack initiation.

The Figure 4-11 illustrates the mechanisms of cyclic accommodation of the Fe-3Si steel. At low strain level ($\Delta\varepsilon_p < 0.05\%$), SRO is supposed to be present and dislocation glide is difficult. Then SRO and effective stress decreases which enables the formation of the veins and channels structure. The crack propagation is transgranular.

From $\Delta\varepsilon_p = 0.2\%$ and above, strain localisation at triple point and at grain boundaries occurs, this induces intergranular crack propagation. The high dislocation density observed even at high strain levels shows that dislocation annihilation is less favourable than dislocation creation due to high internal stress.

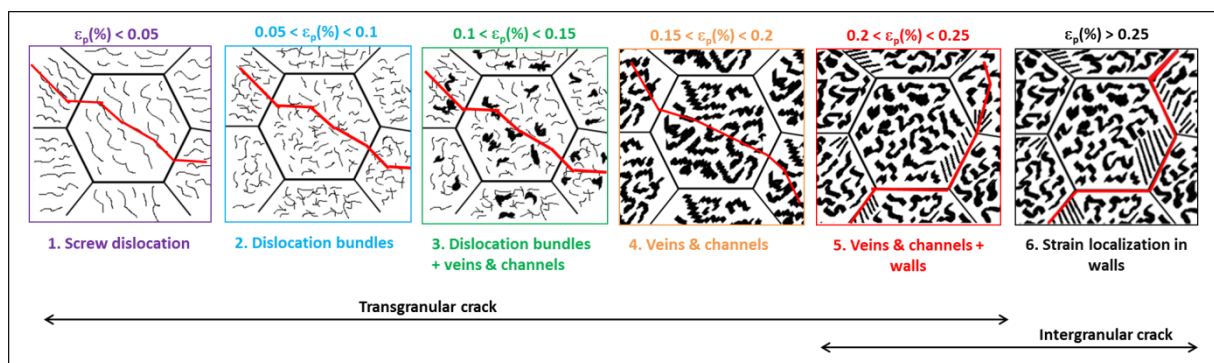


Figure 4-11: Illustration of strain accommodation in the Fe-3Si steel, the red line represents the crack propagation

4.5 Conclusion

From these microstructural investigations, it can be concluded that **M330-35A steel exhibits two different fatigue damage mechanisms which depends on the applied strain amplitude**. Based on the literature concerning the metallurgical properties of the material and based on the present observations, it is reasonable to assume that **in the as-received material, short range order between Fe and Si atoms exists which can be destroyed by cyclic plasticity**.

For **low strain amplitudes**, dislocation sources are activated within the grain and dislocation slip is planar which is encountered in short range ordered alloys [e.g. GER89]. **The dislocation glide length is restricted by the high friction effect caused by Fe-Si clusters but it is enough to accommodate the required strain in a quasi-reversible regime. Crack initiation is transgranular.**

For **high strain amplitudes**, the **plastic strain and the cumulative strain are high enough to modify the Fe-Si short range order. It decreases its effect on plasticity.** Also, there are intergranular stresses producing **strain localisation at grain boundaries** and finally **intergranular crack initiation**.

Chapter V:

Quantitative strain evaluation

1. Image quality and line segment method
2. Misorientation based analysis
3. Discussion
4. Conclusion

5 Quantitative strain evaluation

After the description of damage mechanisms of the M330-35A steel, it is proposed to estimate the strain levels and the strain localisation in a notched specimen by surface analysis at a mesoscopic scale. Therefore, EBSD technique is considered since it has proved its ability to estimate strain in a low-carbon ferritic steel subjected to cyclic loading in a previous study conducted in the group [LEA11].

For that purpose, EBSD analyses were conducted on the undeformed M330-35A steel and on ruptured samples loaded at different total strain variations $\Delta\varepsilon_t=0.4\%$, 0.5% , 0.7% , 0.9% and 1% . The scanned areas were taken randomly in the useful zone of the sample. The size of the EBSD maps was $800\mu\text{m} \times 450\mu\text{m}$, which corresponds to about 80 grains although only half of them were not on the edges because of the grain size and five maps were recorded for each strain variation for statistical purpose.

The study is conducted in term of misorientation evolution, image quality and finally with the line segment method. Only the maps corresponding to $\Delta\varepsilon_t=0.5\%$, 0.7% and 1% are shown for the qualitative analyses. Observations at $\Delta\varepsilon_t=0.4\%$ and $\Delta\varepsilon_t=0.9\%$ do not provide additional information (these maps are kept for quantitative analyses).

5.1 Image Quality (IQ) and Line Segment Method (LSM)

The Image quality (IQ) is calculated from the maximum intensity of the Hough peaks and is representative of the average intensity of the Hough peaks. It is defined by equation (5-1) with N the number of identified peaks and I_i , the intensity of peak i .

$$IQ = \frac{1}{N} \sum_{i=0}^{N-1} I_i \quad (5-1)$$

IQ maps based on a grey scale, are affected by non-indexable patterns. Hence, lower IQ patterns correspond to a lattice distortion that can be related to structures such as grain boundaries and dislocation sub-structures [PET10] [WRI11]. In addition, the presence of Geometrically Necessary Dislocations (GND) induce a change in the crystallographic orientation which can lead to the formation of sub-grain boundaries with misorientation up to 15° , they form the Low Angle Grain Boundary (LAGB). Their evolution is studied by the Line Segment Method (LSM). The inverse pole figure (IPF) maps, the IQ maps and the LSM maps are shown in Figure 5-2.

Regarding IQ maps (Figure 5-2(b)), there is no evolution of the grey scale when increasing the strain up to $\Delta\varepsilon_t=0.7\%$. This is the sign that lattice distortion is weak. Above $\Delta\varepsilon_t=0.7\%$, modifications of the

grey level can be noticed in the grain interior. When considering in details the distribution of the IQ criteria (Figure 5-1), it is observed that when:

- $\Delta\varepsilon_t < 0.7\%$, IQ is stable
- $\Delta\varepsilon_t \geq 0.7\%$, the maxima values of IQ increases and minima values of IQ decreases

This is in agreement with the literature since it is known that the lowest value corresponds to non-indexed pixel or to the presence of Statistically-Stored Dislocations (SSD) and GND which introduce lattice distortion [WRI06].

As pointed out by Buchanan *et al.* [BUC97], error in IQ is due to the contribution of inhomogeneous dislocation density. This is typically what is observed above $\Delta\varepsilon_t = 0.7\%$ in the M330-35A steel. From $\Delta\varepsilon_t = 0.7\%$, the veins and channel structure starts to form and when the total strain variation increases, the strain is localised in the vicinity of grain boundaries in the form of dislocation walls leading to an inhomogeneous dislocation structure.

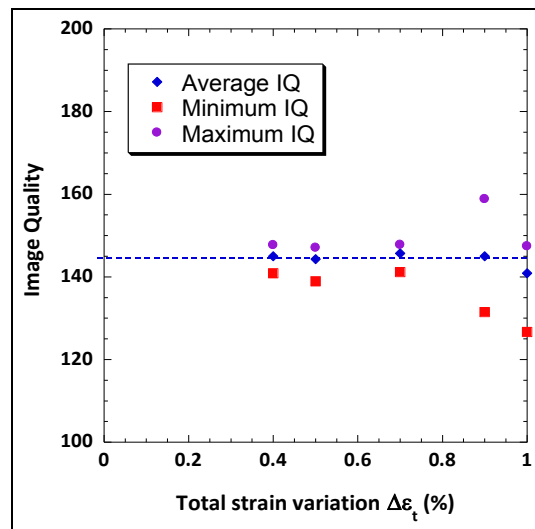


Figure 5-1: IQ distribution for the different total strain variations, the bars indicates the minima and maxima

The study of dislocation structures in Chapter 4 showed that no dislocation cells were formed when the material was subjected to cyclic loading. Therefore, the observation of sub-grain cells by the Line Segment Method is not expected. However, the evolution of High Angle Grain Boundaries (HAGB) and Low Angle Grain Boundaries (LAGB) with the total strain variation by the LSM approach has been considered. Here, High Angle Grain Boundaries (HAGB) with misorientations superior to 15° are plotted as solid black line and Low Angle Grain Boundaries (LAGB) with misorientations between 2° and 15° are plotted in colour (blue, yellow, green and red) (Figure 5-2 I). While the undeformed material exhibits few LAGBs, their fraction increases when the material is submitted to fatigue loading. At $\Delta\varepsilon_t = 0.5\%$, many LAGBs with angle superior to 5° are observed and their linear fraction

does not increase with increasing the total strain variation. It seems that these LAGBs are not a characteristic of the sub-grain boundaries created during fatigue test but to grain boundaries of grains with very close orientations as observed from IPF maps (Figure 5-2(a)). At $\Delta\varepsilon_t=1\%$, LAGBs between 2° and 3° are observed near some grain boundaries, these latter might correspond to lattice rotation induced by the cyclic strain.

Note, that except for $\Delta\varepsilon_t=1\%$, the different IQ and LSM mappings do not reveal intragranular misorientation which are known to be indicative of dislocation structures which have accumulated during deformation [BRI10] [VOG13a].

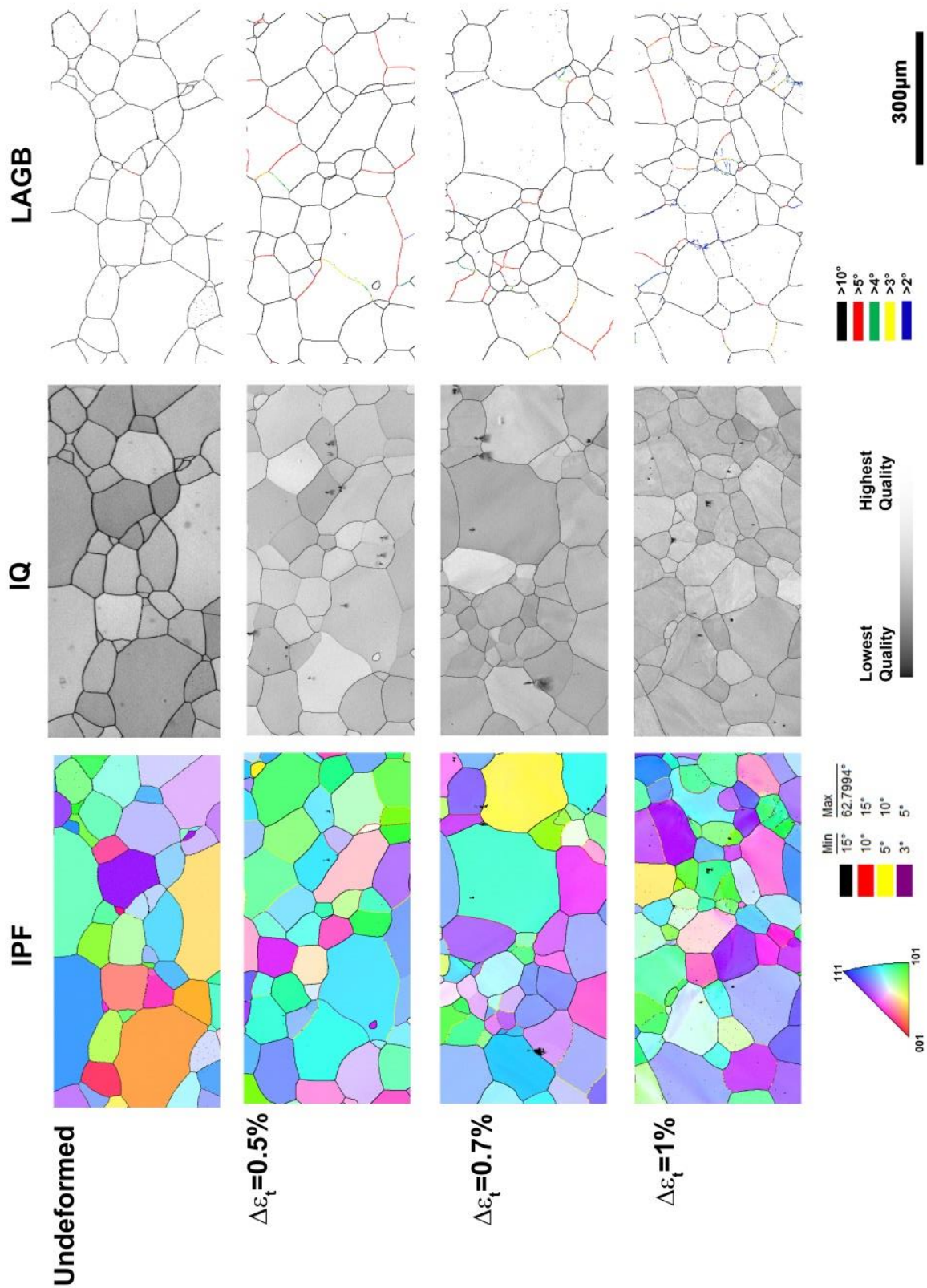


Figure 5-2: (a) Inverse Pole Figure (IPF), (b) Image Quality (IQ) and (c) Line Segment Method (LSM) maps for the different total strain variations

5.2 Misorientation based analysis

Since coupled IQ/LSM analysis is not sufficient to characterise the cyclic behaviour of the material, other misorientation based criteria have been taken into consideration.

Here, Kernel based approach (Kernel Average Misorientation – KAM maps), grain based approach (Grain Orientation Spread – GOS maps) and hybrid approaches (Grain Reference Orientation Deviation – GROD maps) are studied.

- Kernel based approach

Kernel Average Misorientation (KAM) calculates the average misorientation between a pixel I and its neighbours providing that misorientation does not exceed 5° , which corresponds to LAGB.

Hence, the local misorientation value assigned to the centre point (P_i) is the average of these misorientations as expressed by the following formula (5-2).

$$KAM_{P_i} = \frac{1}{N} \sum_{j=1}^N \Delta\theta_{ij}, \quad \Delta\theta_{ij} < 5^\circ \quad (5-2)$$

With KAM_{P_i} the value of the KAM at pixel I , $\Delta\theta_{ij}$ the misorientation angle between pixels I and j , and N the number of surrounding pixels that exhibit a misorientation $\Delta\theta_{ij}$ lower than 5° .

If plastic deformation results from dislocation glide and crystal lattice rotation [VOG13a] [GOD05] [BER09], this approach enables a quantitative evaluation of the local plastic strain gradients.

In the present work, the KAM criterion is considered for accumulated plastic strain energy. The KAM depends on factors related to the measurement conditions and more specially the grid size. To overcome this drawback, all the analyses were performed systematically with the same conditions.

- Grain based approach

Grain Reference Orientation Deviation (GROD) is based on the misorientation between a reference point of that grain and the other points. The reference point can be the mean misorientation of the grain or the point of the grain where the KAM is the lowest. It is defined by equation (5-3).

$$GROD_i = \omega_{ik} \quad (5-3)$$

With ω_{ik} the deviation angle between orientation of pixel I and reference orientation of grain k .

Grain Orientation Spread (GOS) is based on the misorientation averaged on the whole grain and is defined by equation (5-4). In this mode each point in the grain is shaded with the same colour in the maps.

$$GOS_k = \frac{1}{M} \sum_{i=1}^M GROD_i \quad (5-4)$$

With M the numbers of pixel within the grain k .

A mean GOS value over a specified area can be calculated by equation (5-5).

$$GOS_{area} = \frac{1}{n} \sum_{k=1}^n GOS_k \quad (5-5)$$

With n the number of grains within the considered area.

The resulting mappings are reported in Figure 5-5.

5.2.1 Kernel based approach

The KAM is obtained by the measure of the misorientation between a pixel and its neighbouring pixels. The KAM mapping (Figure 5-5(b)) characterises the local plastic gradient that may correspond to misorientation induced by GND [WRI11]. In this approach, the calculated misorientation is reported as a colour gradient.

The as-received state does not exhibit any gradient levels indicating that the material is almost free from deformation induced by the process. At $\Delta\varepsilon_t=0.5\%$, KAM colour gradient is homogeneous on the scanned area and KAM remains low ($KAM < 0.7^\circ$). At $\Delta\varepsilon_t=0.7\%$, the map stays globally homogeneous and light heterogeneities appear within some grains. Finally at $\Delta\varepsilon_t=1\%$, strong heterogeneities appear: grain interior remains almost free from misorientation whereas high gradient (KAM up to 3°) are observed close to grain boundaries. This means that as the strain increases, crystal lattice rotation increases also and is localised at grain boundaries. If compared with IPF maps, there is no relation between the orientation of the grain toward the loading axis and the appearance of the highest KAM at $\Delta\varepsilon_t=1\%$.

As a complement to the mapping, the statistical distribution of the KAM for the different total strain variations has been calculated and is reported in Figure 5-3. All the distributions, from the as-received material to the material fatigued up to $\Delta\varepsilon_t=0.7\%$, exhibit the same shape and a mean KAM value at about 0.4° whereas at $\Delta\varepsilon_t=0.9\%$ and $\Delta\varepsilon_t=1\%$, the KAM distribution is more widespread and dissymmetric. The widespread of the KAM curve means that the zone affected by local misorientation is wider for the highest strains.

In addition, a threshold was applied to KAM maps and the fraction number of $KAM > 0.5^\circ$ (lowest threshold value at which localisation is observed) is evaluated for the different strain variation (Figure 5-4 and Figure 5-5I).

In agreement with KAM distributions, the fraction number of $KAM > 0.5^\circ$ is constant up to $\Delta\varepsilon_t = 0.7\%$ and then increases linearly with the applied total strain variation. At $\Delta\varepsilon_t = 1\%$, KAM superior to 0.5° is localised at grain boundaries.

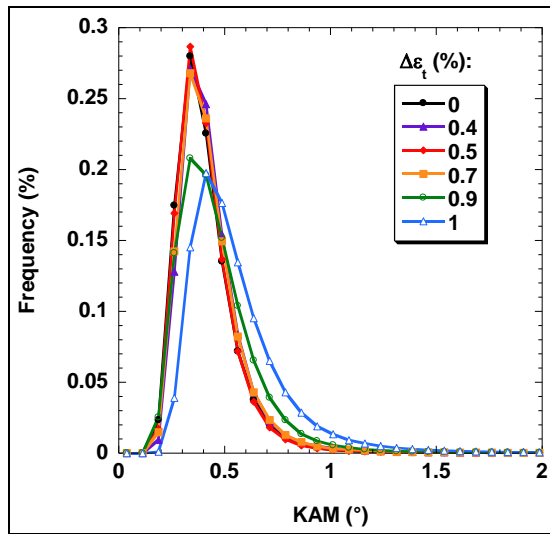


Figure 5-3: Evolution of the KAM distribution as a function of the total strain variation based on 5 EBSD maps by total strain variation

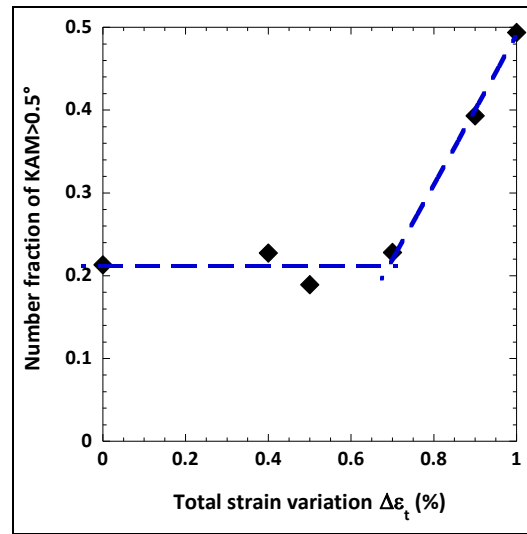


Figure 5-4: Evolution of the fraction number of $KAM > 0.5^\circ$ with the total applied strain based on 5 EBSD maps by total strain variation

These KAM analyses reveal that there is no particular evolution of the KAM value from the undeformed state to $\Delta\varepsilon_t < 0.7\%$ which is due to the uniform deformation within the grain at these strain levels. At $\Delta\varepsilon_t = 0.7\%$, strain localisation appears at some grain boundaries but is not enough to increase the mean KAM value. Above $\Delta\varepsilon_t = 0.7\%$, there is an increase of the KAM value in the vicinity of grain boundaries due to the strong strain localisation and the formation of the wall dislocations structures in these areas.

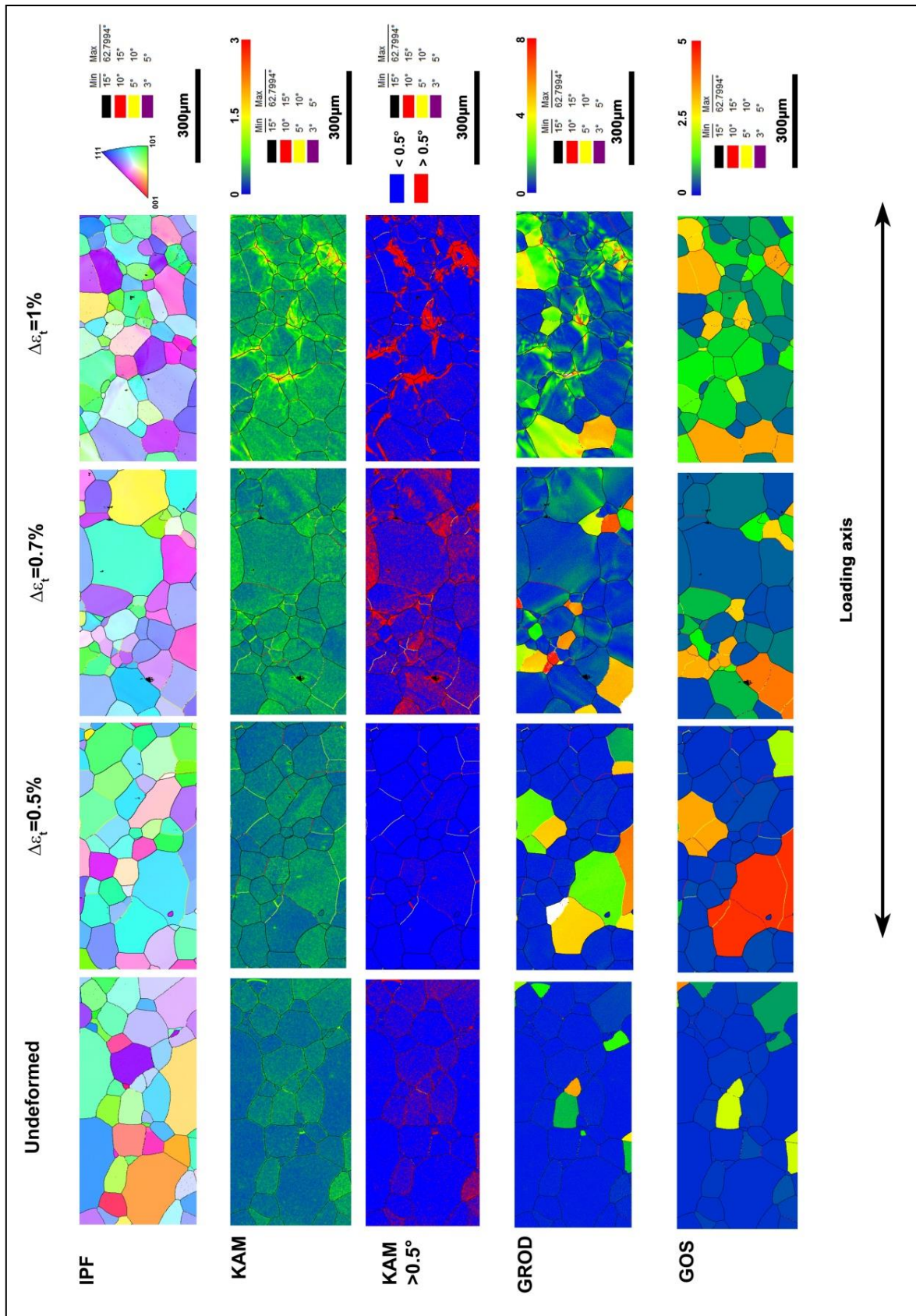


Figure 5-5: (a) Inverse Pole Figure (IPF) TD maps, (b) Kernel Average Misorientation (KAM) maps, (c) Distribution of KAM superior to 0.5° , (d) Grain Reference Orientation Deviation (GROD) maps and (e) Grain Orientation Spread (GOS) maps for samples loaded to rupture at $\Delta\epsilon_t = 0.5\%$, $\Delta\epsilon_t = 0.7\%$ and at $\Delta\epsilon_t = 1\%$ - (acquisition step = $1\mu\text{m}$)

5.2.2 Grain based approach

The grain based misorientation analysis is investigated through colour mapping of both GROD and GOS criteria (Figure 5-5 (d) and I).

5.2.2.1 Grain Reference Orientation Deviation (GROD)

The Grain Reference Orientation Deviation is obtained by measuring the misorientation between a reference orientation of the grain (the mean orientation or the point where the KAM is the lowest) and the other pixels of the grain.

The GROD investigation (Figure 5-5(d)) provides additional information. In comparison with KAM criteria, GROD data provides additional information by showing the strain distribution gradient at a larger scale.

Indeed, at $\Delta\varepsilon_t=0.5\%$ the colour is homogeneous within grains. This attests that the different grains do not present high levels of internal strain heterogeneity as revealed by the KAM maps. But at $\Delta\varepsilon_t=0.7\%$ heterogeneities are revealed within some few grains by the form of a lightly coloured band near grain boundaries or across grain starting from triple point and at about 45° to the loading axis. This was not seen or less clearly in KAM maps, this is explained hereafter with the correlation with the dislocation structure.

The number of grains affected by these bands is largely increased at $\Delta\varepsilon_t=1\%$. At high strain amplitude, the largest orientation gradients are found in the vicinity of the grain boundaries, showing the localisation of the deformation in those areas.

5.2.2.2 Grain Orientation Spread (GOS)

To complete the GROD analysis, GOS mapping (Figure 5-5I) has also been taken into account. In GOS mapping one value is attributed per grain, this value corresponds to the averaging of the GROD values in a grain.

In the GOS maps, the coldest colour means that the misorientation within the grain is low, and inversely, the warmest colours are for the grains with greater misorientation. GOS mapping shows that the number of grains with $GOS > 1^\circ$ increases with the strain amplitude. Indeed, the blue colour represents approximately 90% of the map in the undeformed state, at $\Delta\varepsilon_t=0.5\%$, it is 75% of the map, at $\Delta\varepsilon_t=0.7\%$ it is 60% and at $\Delta\varepsilon_t=1\%$ it is 25%.

In a more quantitative approach the mean GOS value averaged from five maps of the same specimen is calculated. The evolution of the mean GOS with total strain amplitude is shown in Figure 5-6. In agreement with the colour gradient evolution shown in Figure 5-5I, the GOS value increases exponentially above $\Delta\varepsilon_t=0.7\%$ (Figure 5-6), however the same mean GOS value is obtained for the undeformed state, $\Delta\varepsilon_t=0.5\%$ and $\Delta\varepsilon_t=0.7\%$.

Below $\Delta\varepsilon_t=0.7\%$, the different grains do not present high levels of internal strain heterogeneity and the dislocation structure is homogeneous in the grain, thus, no colour gradient is observed on GOS maps and constant mean GOS value is obtained. At $\Delta\varepsilon_t=0.7\%$, strain localisation appears at some grain boundaries but is not enough to increase the mean GOS value. Above $\Delta\varepsilon_t=0.7\%$, the increase of the mean GOS value arises from the strong strain localisation in the vicinity of grain boundaries and triple points due to the formation of the wall dislocations structures in these areas.

Therefore, Figure 5-6 can be used for strain estimation in the case of $\Delta\varepsilon_t$ superior to 0.7%.

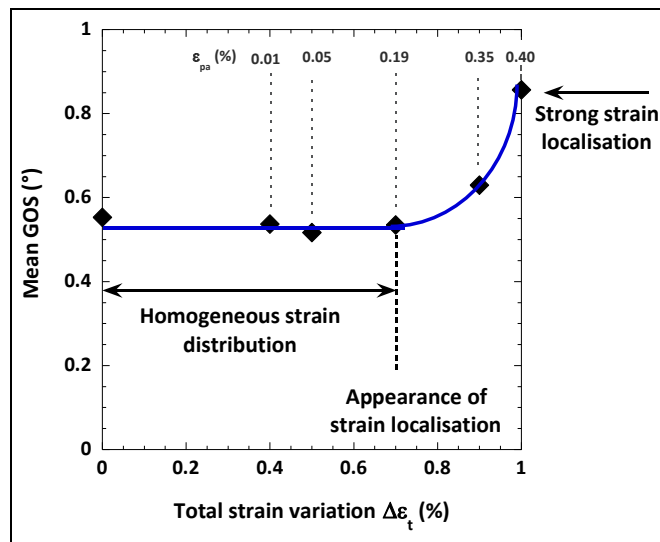


Figure 5-6: Mean GOS evolution with the total strain amplitude

5.2.3 Summary of the results

For M330-35A cycled up to $\Delta\varepsilon_t=1\%$, IQ maps are not affected by the strain but it is important to be aware that these analyses are very dependent on the acquisition conditions. The image quality is not an absolute value and it depends on material factors (lattice distortion) as well as on the sample preparation as it may induce changes in the sample surface layers from which the EBSD patterns are collected [WRI11].

The LSM approach reveals that no subgrain boundary, corresponding to geometrically necessary boundary (GNB) formed by GND, is present in the material. It was expected from the cyclic accommodation mechanisms revealed in the previous chapter. Misorientation based analyses enable the detection of local misorientation in the vicinity of grain boundary at 0.7% and above. Nevertheless, when considering the mean GOS value and the fraction number of KAM superior to 0.5° which are calculated by averaging over five different maps (of the same sample), these criteria are effective to evaluate the strain only above $\Delta\varepsilon_t=0.7\%$.

It can be concluded that the two different behaviours in the cyclic plasticity accommodation are pointed by these EBSD analyses. Indeed, there is no evolution of KAM, GROD and GOS up to

$\Delta\varepsilon_t=0.7\%$. Then, colour gradient appears in KAM and GROD maps in the vicinity of grain boundaries, the number fraction of KAM superior to 0.5° increases with the total strain variation as well as the mean GOS. The EBSD tool is thus suitable in the case of the M330-35A steel, only for the localisation and evaluation of the strain when it is superior to $\Delta\varepsilon_t=0.7\%$.

In the next paragraph, a direct correlation between the encountered dislocation structures and EBSD analyses is performed in order to highlight the effect of dislocations structure on misorientation measurements.

Then, in order to show the ability of the EBSD analyses to localise and evaluate strain, it is proposed to estimate strain in a notched specimen subjected to cyclic loadings where inhomogeneous strain distribution is encountered. Locally strain can reach values superior to $\Delta\varepsilon_t=1\%$, therefore strain distribution in the notch specimen was also measured by DIC.

Finally, it is proposed to estimate the dislocation density for samples loaded at $\Delta\varepsilon_t<0.7\%$ where homogeneous dislocation structure are encountered and where no EBSD criteria is suitable for strain estimation.

5.3 Discussion

5.3.1 Dislocation structures and EBSD analyses

The EBSD analyses performed in this work appear sensitive enough to point out the difference in dislocations arrangements according to the total strain variation. To control this statement, it appeared interesting to perform, on the same grain, EBSD maps and dislocation observations by cECCI technique.

Figure 5-7 corresponds to cECCI image and EBSD mapping of a sample loaded at $\Delta\varepsilon_t=0.5\%$. It shows the cECCI image of an entire grain, the corresponding dislocation structure is obtained at a higher magnification and is shown underneath. On the left KAM and GROD mappings of the grain are also shown. At this strain level the dislocations remained pinned in their slip planes with long straight or bowed segments. The KAM and GROD maps present a homogeneous colour within the considered grain.

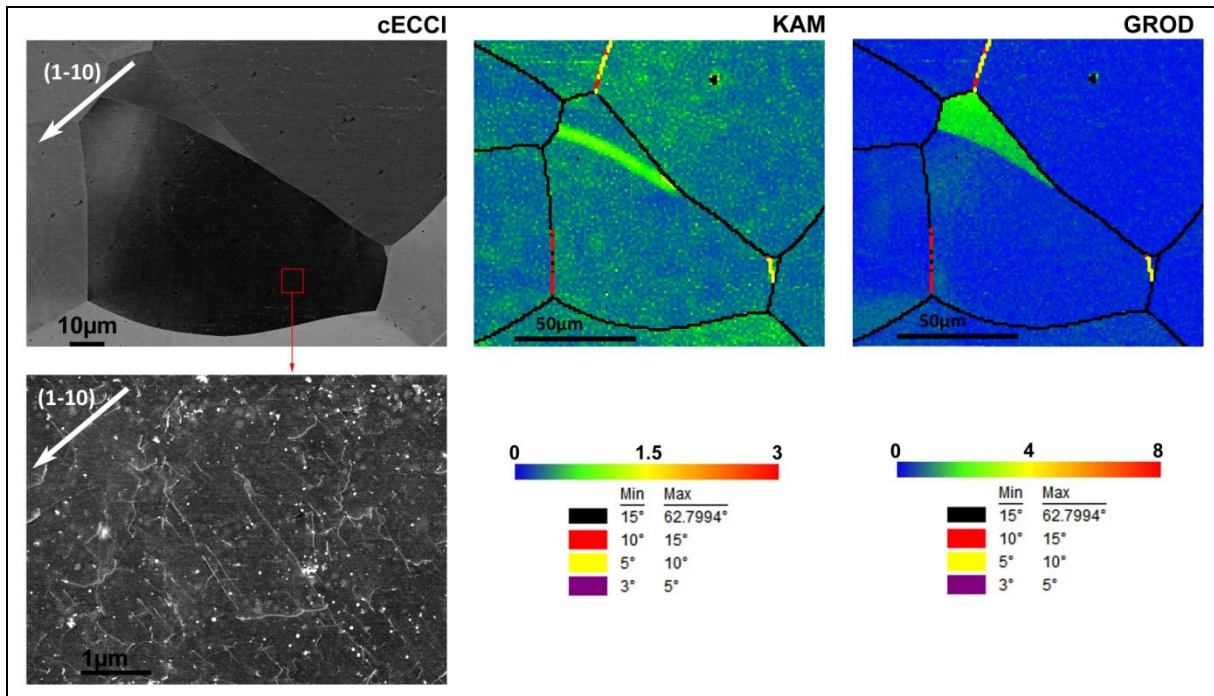


Figure 5-7: cECCI image of a sample loaded at $\Delta\epsilon_t=0.5\%$ with KAM and GROD maps of the corresponding grain

Figure 5-8 corresponds to cECCI image and EBSD mapping of a sample loaded at $\Delta\epsilon_t=0.7\%$. The first grain that is presented exhibits the vein and channel structure. The colour gradient in the KAM and GROD maps is homogeneous. In the second grain that is presented, the cECCI reveals two different dislocation structures, the vein and channel structure in the grain and the wall and channel structure near the grain boundary. The corresponding KAM and GROD maps reveal colour gradient near grain boundary highlighting higher misorientation in these zones. It is more visible with the GROD map than the KAM map.

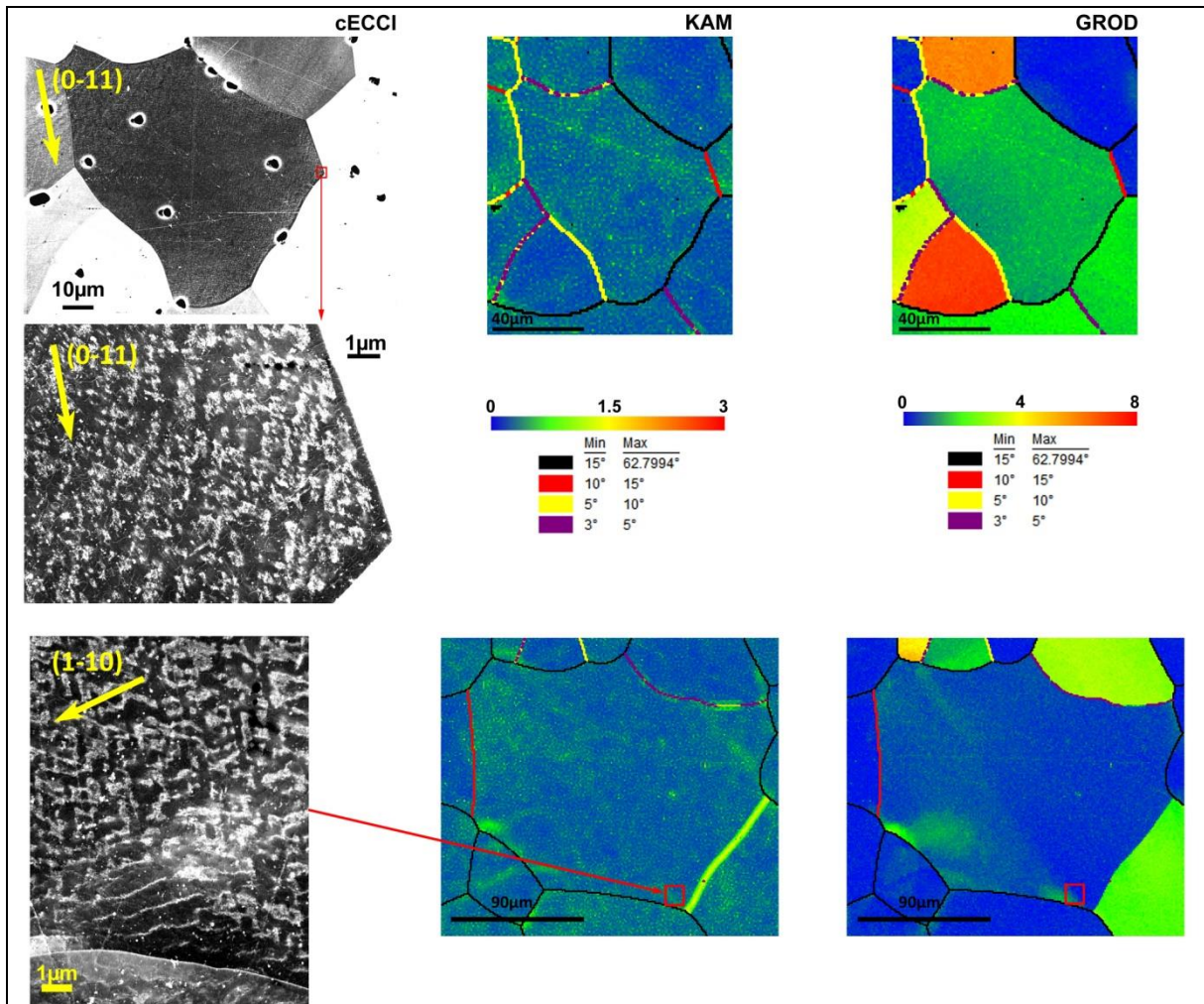


Figure 5-8: cECCL image of a sample loaded at $\Delta\epsilon_t=0.7\%$ with KAM and GROD maps of the corresponding grain

Figure 5-9 corresponds to cECCL image and EBSD mapping of a sample loaded at $\Delta\epsilon_t=1\%$. The cECCL image reveals the vein and channel structure in the grain and a band with the wall and channel structure near the grain boundary. The corresponding KAM and GROD maps reveal colour gradient near grain boundary which highlights the misorientation in these zones which corresponds to the transition between the two dislocations structures.

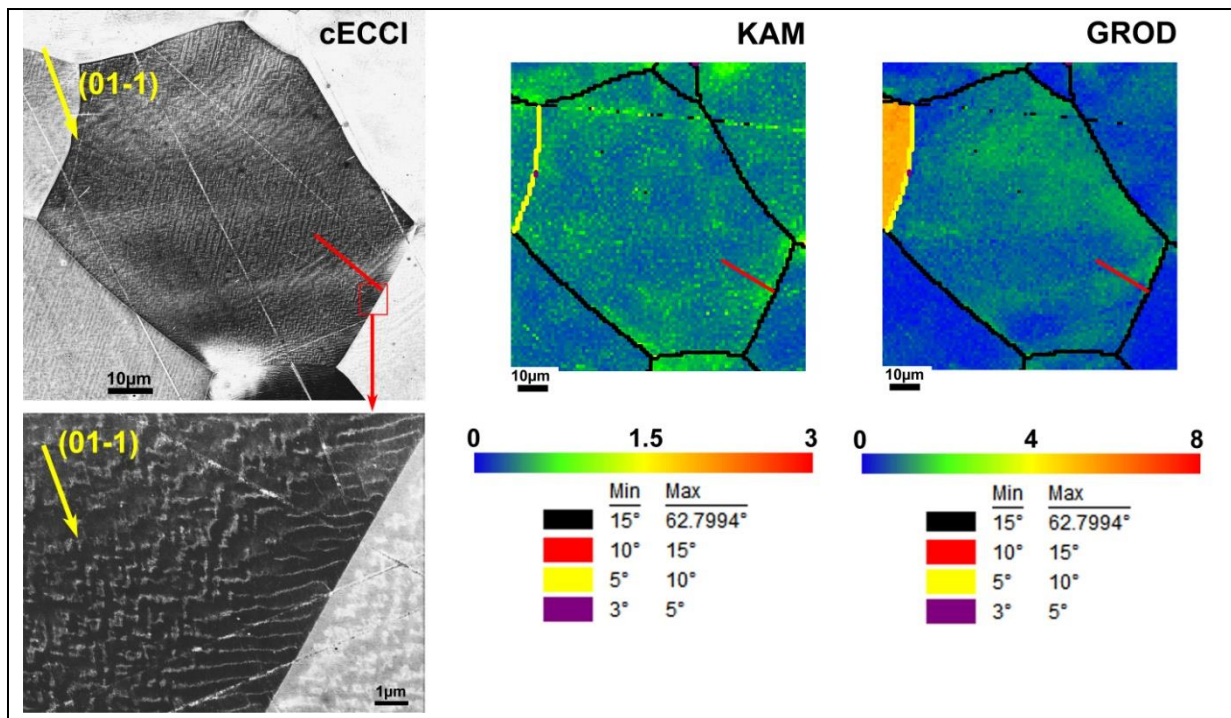


Figure 5-9: cECCI image of a sample loaded at $\Delta\varepsilon_t=1\%$ with KAM and GROD maps of the corresponding grain, the red line within the grain corresponds to the misorientation profile

At low strain level ($\Delta\varepsilon_t=0.5\%$), dislocations remained pinned in their slip planes with long straight or bowed segment (Figure 5-7). The strain accommodation occurs by planar flip-flop gliding of the dislocations which corresponds to statistically stored dislocation (SSD). Therefore, no strain accommodation signs are detected by EBSD analyses as misorientation is uniform within the grain and the lattice distortion is too weak to be detected by the EBSD system which resolution is 0.3° (Figure 5-9 and Figure 5-10). This is also not detected by IQ maps because the beam size is of 400nm which is larger than the spacing between the dislocations. At $\Delta\varepsilon_t=0.7\%$ the planar arrangements are no more observed, veins of high dislocation density and channels of low dislocation density are formed and swamp mostly the entire grain (Figure 5-8).

Very occasionally and very locally, few condensed dislocations walls reflecting strain localisation were observed near grain boundaries. The GROD maps allow a better estimation of the localisation of the walls dislocation structures than KAM maps. Indeed, the GROD criterion measures, in every grain, the misorientation between a pixel and the reference orientation (2-3). The reference is either the mean misorientation of the grain, either the point of the grain where the KAM is the lowest. If the reference is the mean misorientation of the grain, it is mainly influenced by the veins and channels structure which constitutes the major part of the grain. Consequently, the GROD at a point corresponding to the walls structure is higher than at a point corresponding to the veins and channels structure. The KAM maps measure the misorientation between neighbouring pixels. Thus to

localise the walls dislocation structure the misorientation between walls and veins and channels structures must be sharp and high enough locally to be detected. Increasing strain amplitude did not change deeply the dislocations structures which still consisted of the vein-channel structure within the grains and the wall-channel structures near grain boundaries. However, the higher mean strain amplitude and the higher cumulated plastic strain promote the expansion of the wall-channel structure toward the grain interior. In addition, the activity of secondary slip is more pronounced. The misorientation between these two regions is detected by EBSD through KAM and GROD maps in the area marked with a red line in Figure 5-9. The misorientation profile along the red line is shown in Figure 5-10. It shows that the misorientation pixel to pixel near the grain boundary is approximately 0.4° which corresponds to the wall dislocation structure then misorientation increases up to approximately 1.1° which corresponds to the vein and channel dislocation structure. The misorientation between the wall structure and the vein and channel structure is about 0.7° which is high enough to be detected.

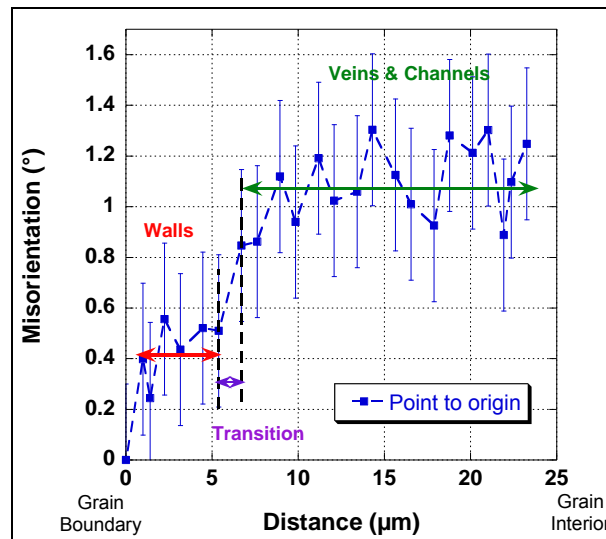


Figure 5-10: Misorientation profile within a grain of a sample loaded at $\Delta\varepsilon_t=1\%$

Additionally, the identification of strain localisation zones is very important because they can be crack initiation sites. In the present material, crack initiation is intergranular at $\Delta\varepsilon_t=1\%$ whereas it is transgranular at $\Delta\varepsilon_t=0.5\%$. This is another asset of the EBSD analyses. At high strain ranges, KAM and GROD maps reveal the localisation of deformation at grain boundaries which acts as stress concentrators and promotes crack initiation. Data processing in terms of KAM and GROD maps inferred from EBSD spectra appears as a predictive tool for fatigue crack initiation.

5.3.2 Strain estimation by EBSD analyses

To highlight the ability of the EBSD tool to localise the strain, EBSD analyses were performed on the notched sample used for the study of strain distribution by DIC (Figure 2-19). Figure 5-11 shows the

normal strain distribution (ϵ_y) measured by DIC. EBSD analyses are performed in zone 1 (behind the notch) and zone 2 (near a shear band) of the sample (Figure 5-11).

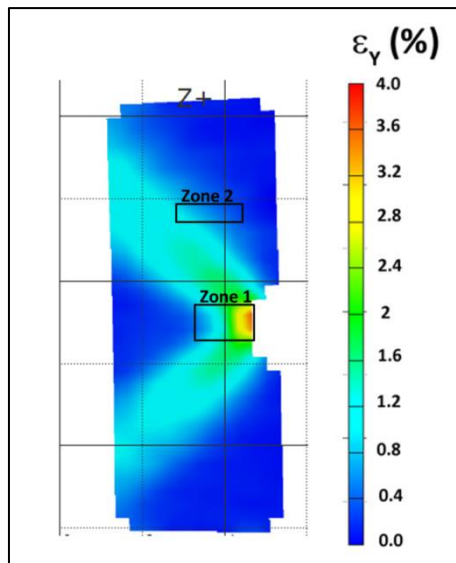


Figure 5-11: Localisation of complementary EBSD analyses

To have an overview of broad areas, several maps of $800 \times 450 \mu\text{m}$ were recorded and added to each other in order to form a global map of $1570 \times 750 \mu\text{m}^2$ (279 grains) for zone 1 and of $3000 \times 815 \mu\text{m}^2$ (483 grains) for zone 2, the DIC spatial resolution is of $210 \mu\text{m}$. IPF, GROD and GOS maps of zone 1 and 2 are shown in Figure 5-12 and Figure 5-13 respectively.

The GROD map of zone 1 (Figure 5-12) shows that close to the notch, on the right, warmer colour are obtained which is the sign of higher misorientation. Less closer to the notch, the grain colour is predominantly blue but green colour is apparent at grain boundaries, which means that misorientation is localised in grain boundary. The GOS map, which attributes one colour per grain, shows that warmer colours are obtained near the notch than in the middle of the sample. This is the sign of higher misorientation within the grains near the notch than in the grains farther from the notch. These results are consistent with the strain localisation in this area.

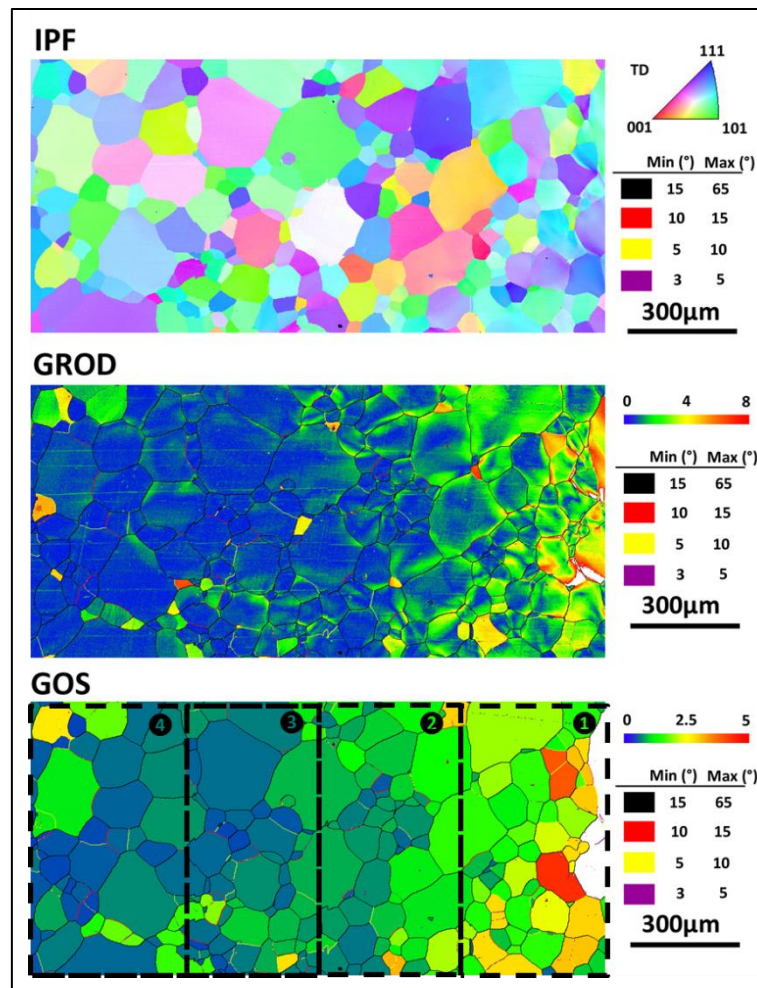


Figure 5-12: (a) IPF in TD direction, (b) GROD and (c) GOS maps of the Zone 1 of the sample (notch on the right)

The mean GOS in zone 1 (calculated from the black dot square areas of GOS map in Figure 5-12) are $GOS_{mean,1}=1.55$, $GOS_{mean,2}=0.89$, $GOS_{mean,3}=0.69$, $GOS_{mean,4}=0.6$.

The GROD map of zone 2 (Figure 5-13) shows that, on the left of the map, there is a gradient colour within grains whereas on the right, the colour is uniform within grains. The GOS maps show that the number of blue grains is higher on the left than on the right of the map. This is due to higher misorientations within grains on the left than on the right and this higher misorientations are the consequence of higher strain in this zone which is due to the presence of the shear band.

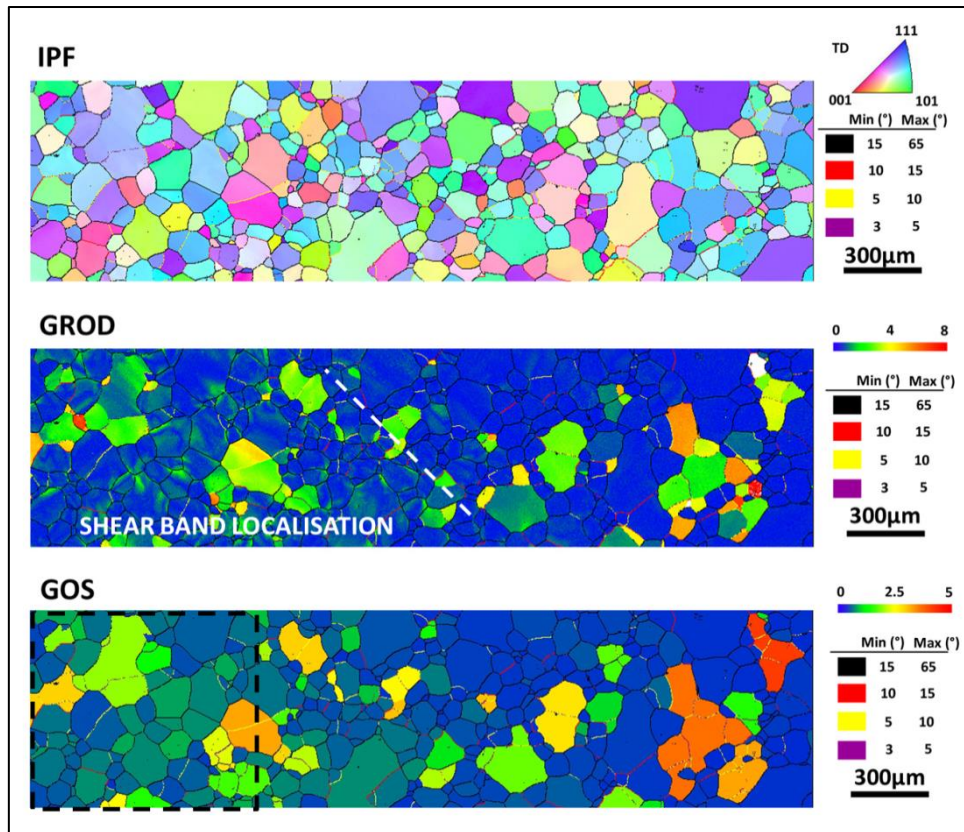


Figure 5-13: (a) IPF in TD direction, (b) GROD and (c) GOS maps of the Zone 2 of the sample

In zone 2, the mean GOS (calculated from the black dot square area of the GOS map in Figure 5-13) is 0.62.

These analyses confirm the ability of the EBSD tool and the GROD map to localise the strain.

However, the purpose is to estimate the equivalent strain undergone by the material in the different areas of zone 1 based on the relation established in Figure 5-6 in which the mean GOS value is correlated to the total strain variation.

Therefore, the mean GOS values measured on the notched specimen in zone 1 are reported in Figure 5-14 (a) and the corresponding total strain variations are deducted by graphical reading. In addition, these mean GOS values are plotted against the normal strain measured by DIC in Figure 5-14 (b). The equivalent strains and normal strain measured by DIC corresponding to the different areas of zone 1 of the notched specimen are reported in

Table 5-1

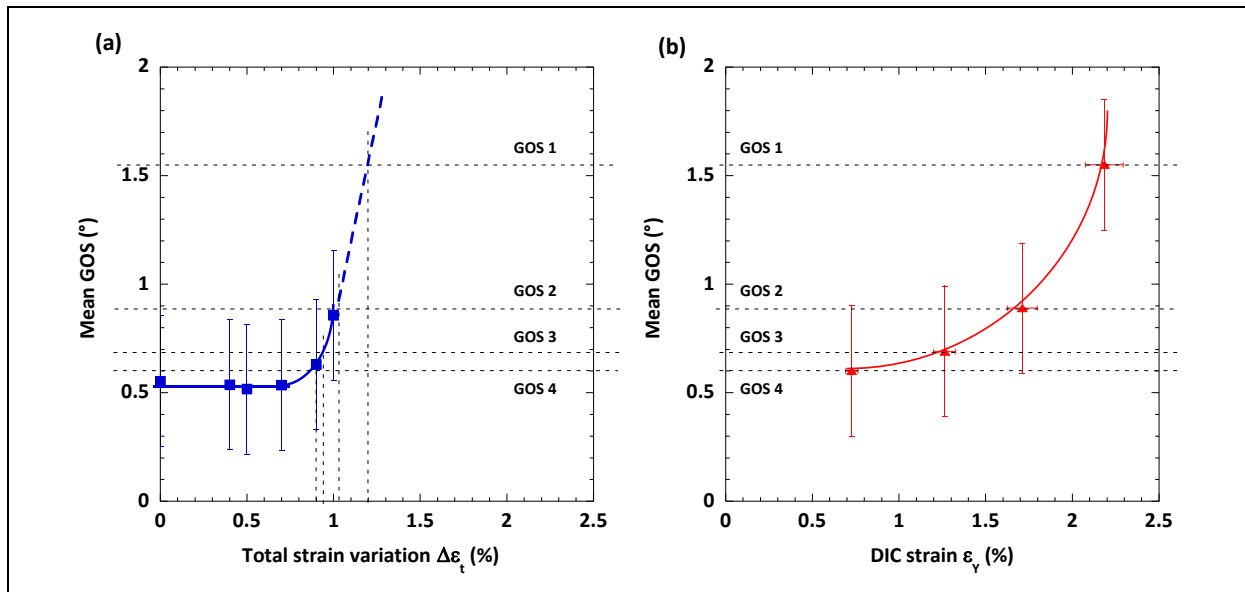


Figure 5-14: (a) Equivalent total strain estimation in the different zones of the notched specimen from the relation between GOS and total strain variation established on smooth specimen and (b) mean GOS value of the different zones of the notched specimen versus the normal strain measured by DIC

Table 5-1: Correspondence between mean GOS values of the different zones of the notched specimen, the normal strain measured by DIC ε_y and the equivalent total strain variation $\Delta\varepsilon_t$

Area	Mean GOS value	DIC ε_y (%)	$\Delta\varepsilon_t$ (%)
1	1.55	2.20	1.20
2	0.89	1.70	1.05
3	0.69	1.20	0.95
4	0.60	0.70	0.88

It can be noticed here that a direct correspondence of the normal strain calculated by DIC on notched sample with the total strain variation of smooth samples is difficult and more especially for the highest strains. Indeed, the LCF study on smooth samples was performed only up to $\Delta\varepsilon_t=1\%$. Above this deformation state, the dislocation structure and mean GOS value in the case of smooth sample are unknown. Also, a precise estimation of the strain by the GOS criteria over a small area is difficult because large grain size hinders statistical analyses and strain measurements by DIC are made on a macroscopic scale.

The observation of the dislocation structure in area 1 of zone 1 (zone where highest strains are reached) by ECCI is shown in Figure 5-15. It reveals dislocation walls transforming into dislocation cells (similar dislocation structure as already been observed in 316L steel subjected to fatigue [GER97]). The very high dislocation density underlines the fact that dislocation creation exceeds

dislocation annihilation. Dislocation glide is difficult and cross-slip is hindered by silicon atoms and jogs. In consequence high strain levels are needed to reach dislocation cells structure.

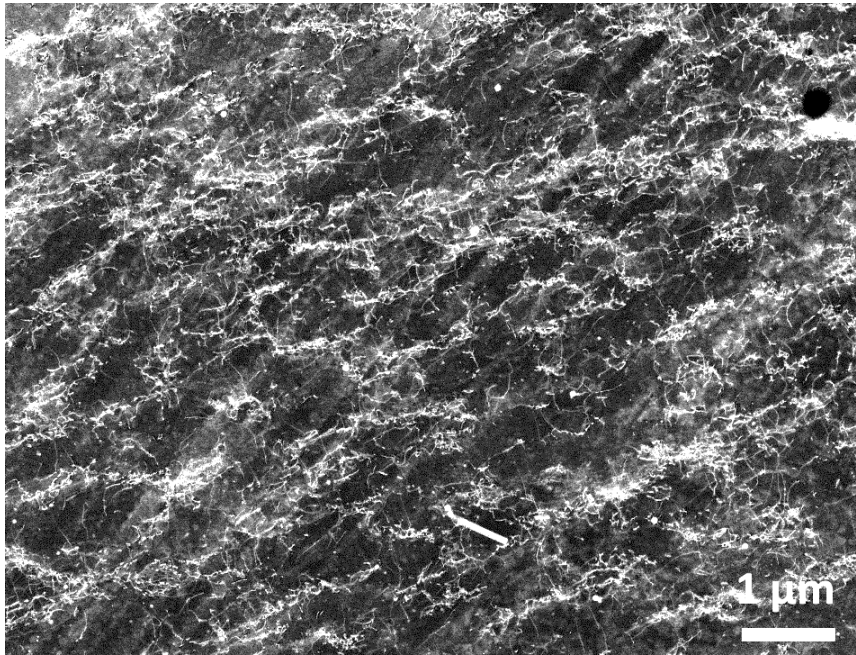


Figure 5-15: Dislocation structure near the notch

This structure corresponds to a more advanced deformation state than those observed in smooth samples loaded at $\Delta\varepsilon_t=1\%$. Therefore, it confirms that in area 1, strain superior to the equivalent total strain variation of 1% are reached.

Additional ECCI observations should be performed in areas 2, 3 and 4 of the notched sample. Thus, it would be possible to check if the dislocation structures observed in these areas are similar to those observed in smooth samples at the corresponding $\Delta\varepsilon_t$.

To estimate, with more accuracy, equivalent $\Delta\varepsilon_t$ in area 1 of zone 1 of the notch sample, it is needed to perform additional LCF test on smooth samples and higher strain. Thus, a relation between mean GOS value and $\Delta\varepsilon_t$ on a wider range of deformation would be obtained. But, due to the thickness of M330-35A which do not enable cycling above $\Delta\varepsilon_t=1\%$, LCF tests should be performed on other specimen of higher thickness.

Nevertheless, one possible mean GOS evolution is shown in Figure 5-16. In this figure, the GOS evolution with total strain variation is depicted in three stages. During the first stage, the mean GOS is constant over a wide strain range (from $\Delta\varepsilon_t=0\%$ to $\Delta\varepsilon_t=0.7\%$) because dislocation structure is homogeneous in the grain. During the second stage, the mean GOS increases rapidly with the total strain variation (from $\Delta\varepsilon_t=0.7\%$ to $\Delta\varepsilon_t=1\%$), this is due to localisation of the strain at grain boundary and higher misorientation in this zone. The third hypothetical stage corresponds to a slower increase

of the mean GOS with the total strain variation. The increase of the GOS would not be due to strain localisation at grain boundary but to the increase of misorientation within grain due to the formation of dislocation cells.

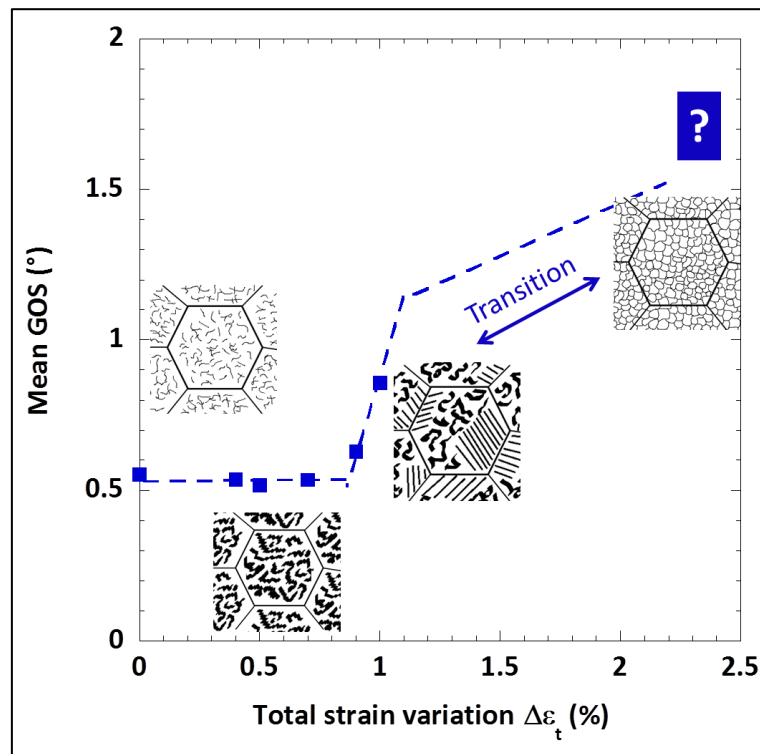


Figure 5-16: Evolution of mean GOS with total strain variation

However, to verify this idea, cycling smooth samples at higher strain variation is needed and this is only possible with thicker samples.

5.3.3 Dislocation density for low strain variation estimation

When considering the low strain amplitudes ($\Delta\epsilon_t < 0.7\%$), dislocations are not organised in well-formed structures which do not give rise to a marker. It implies that misorientation based criteria, such as KAM and GOS, are not relevant to discriminate those evolving structures. Hence, EBSD parameters do not appear as suitable markers to assess fatigue damage degree and to predict crack initiation.

Based on the previous remark, the estimation of dislocation density evolution with the fatigue life appears to be more adapted to evaluate the fatigue damage. This can be investigated by TEM but it is destructive and time consuming. Therefore an attempt using X-Ray Diffraction at Eotvos University in Budapest [GRO98] has been done but the coarse grain size acted as an obstacle in data processing. Therefore, an attempt to measure the dislocation density from cECI images was done. For that purpose, the HAM interception method was used [HAM61].

The Ham's intercept method is usually used to measure dislocation density in thin foils from TEM micrographs. To measure the dislocation density ρ , the total screen length of the dislocation lines L_p is measured in a zone of area A of a TEM micrograph. Then, the dislocation density is given by equation (5-6).

$$P = \frac{4 L_p}{\pi A \cdot t} \quad (5-6)$$

with t the thickness of the investigated zone.

To measure L_p , concentric circles are placed on the zone A , the number of intersections between the dislocations and the circles is counted, thus the estimation of L_p is obtained by (equation 5-7).

$$L_p = \frac{\pi \cdot N \cdot A}{2 \cdot L_c} \quad (5-7)$$

Then the dislocation density is given by equation (5-8).

$$P = \frac{2 \cdot N}{L_c \cdot t} \quad (5-8)$$

This method illustrated in Figure 5-17 is adapted for the measurements of homogeneous dislocation repartition within the material.

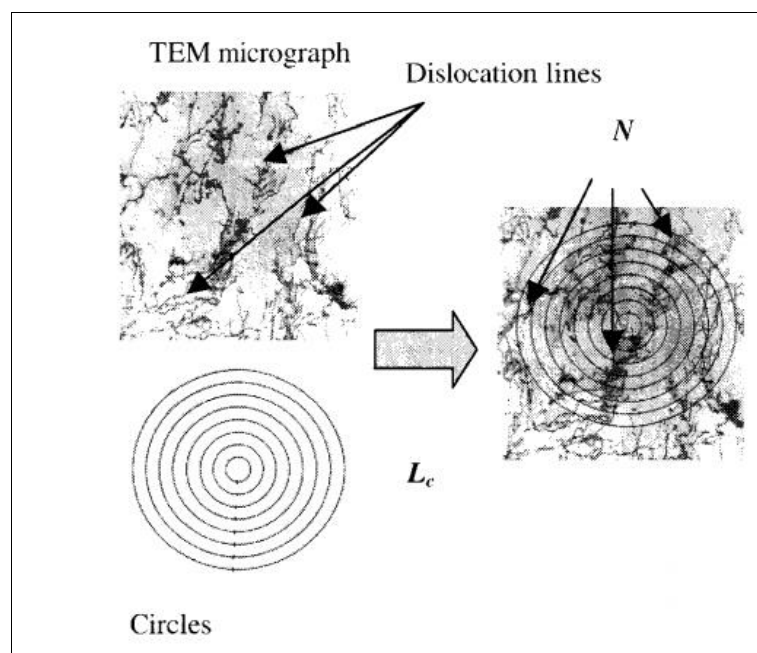


Figure 5-17: Illustration of the Ham's intercepts method [ANT03]

The main difficulty of this method is the measurement of the thickness t of the thin foils. Also, in the micrographs some dislocations are invisible; to avoid this problem different reflection should be considered.

This method was applied to evaluate the dislocation density from cECI images in a Fe-3Si steel subjected to monotonic loading [GUT12] and its accuracy was proven. Therefore, it has been applied

to the present Fe-3Si steel subjected to cyclic loading at $\Delta\epsilon_t=0.5\%$ at different number of cycles (Figure 5-18 and Figure 5-19). Below $\Delta\epsilon_t=0.7\%$, dislocations are isolated and can be distinguished from one another, which is not possible when the veins-channels or the wall-channel structure are encountered. Thus, the samples at $\Delta\epsilon_t=0.5\%$, are adequate candidate to the measurement of dislocation density by the Ham method.

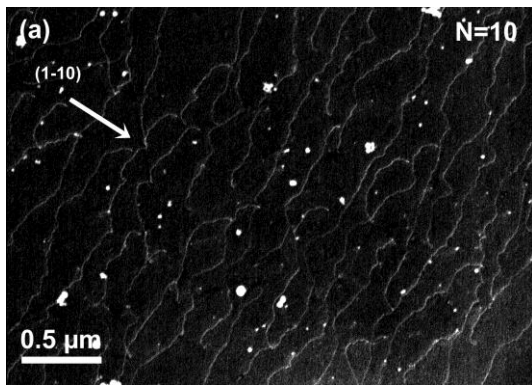


Figure 5-18: cECCL image of M330-35A loaded at $\Delta\epsilon_t=0.5\%$ for 10 cycles

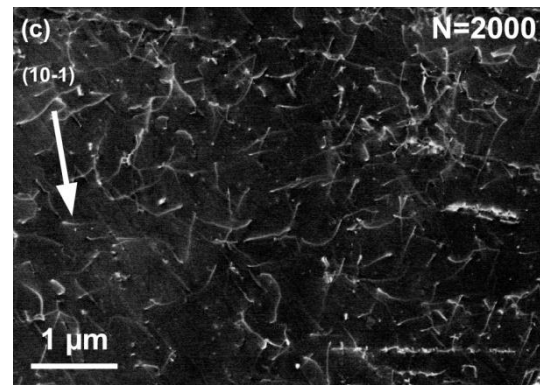


Figure 5-19: cECCL image of M330-35A loaded at $\Delta\epsilon_t=0.5\%$ for 2000 cycles

To measure the probe depth, the Monte Carlo simulation was used (Casino v2.48). At acceleration voltage of 30kV, the calculated probe depth of BSE is between 148 and 593 nm, the mean probe depth 370nm was taken for the measurement of dislocation densities. Then, with the Ham intercept's method, the dislocation densities were measured. A dislocation density of $1.4 \times 10^{13} \text{ m}^{-2}$ is obtained for the two numbers of cycles. For similar dislocation structure, Gutierrez-Urrutia *et al.* [GUT12] have measured dislocation densities of $10 \pm 4 \times 10^{13} \text{ m}^{-2}$ on a Fe-3%Si steel subjected to a monotonic load of 500MPa. Thus, the approach appears valid to measure dislocation density from cECCL images. It appears here, that the dislocation density alone cannot be a satisfactory indication of the damage state but the dislocation density added to the dislocation image can be. Indeed, at N=5 cycles, the dislocations appear as long segment with one slip direction whereas at N=2000 cycles, there are many short dislocation segments and two slip directions are activated.

5.4 Conclusion

The analyses by EBSD of the samples loaded at different total strain variations showed that this technique is adapted for strain localisation and evaluation if GNDs are present within the specimen.

Thus, **below $\Delta\epsilon_t=0.7\%$ no misorientation is detected** within the specimen **by EBSD** as **only SSDs are created**, the **misorientation is uniform** within the grain and the **lattice distortion is weak**.

When increasing the strain, GNDs are involved in the strain accommodation and **dislocation structures are formed**. The **misorientation within the sample and grains is heterogeneous**. The

lattice distortion can reach up to 1° which is well detected by EBSD and misorientation based criteria.

For M330-35A, **GROD maps are adapted for the study of strain localisation at $\Delta\epsilon_t \geq 0.7\%$** . By applying a **KAM threshold** and by calculating the **mean GOS** it is possible to **estimate the strain** from the calibration curve established in the present work.

For the lowest strain variation, the adjustment of the **Ham intercept's method to cECCI images** enables the **evaluation of the dislocation density** which, if correlated with dislocation structure state, provide **valuable information of the damage state** of the material

Chapter VI:

Rotor design optimisation

1. Introduction
2. Choice of material model
3. Validation of the model
4. Application to rotor sizing
5. Conclusion

6 Rotor design optimisation

6.1 Introduction

6.1.1 Context

This last chapter is dedicated to the finite element modelling of the strain and stress state of the rotor of the starter-alternator. The rotor geometry results from a compromise between electrotechnical, acoustic and mechanical needs. Up to know, the mechanical design is performed within Valeo R&D team and their modelling is based on the Haigh Diagram resulting from the Goodman relation (more details are given in §6.1.2). In the present case, this method induces an oversizing of the component which guarantees its integrity during use but hinder optimisation of the electromagnetic performances. The purpose of this chapter is thus to improve the machine performances by modifying the rotor geometry while staying mechanically reliable.

Therefore, it is proposed to:

- 1) Extend the material database by taking into account LCF data in a macroscopic approach.
- 2) Use the new database to modify the geometry of the rotor while staying mechanically reliable, modifications concern refinement of specific zones of the rotor (§6.4).
- 3) Estimate the machine electromagnetic performance with the new rotor geometry.

6.1.2 Methodology

To perform FEA, Ansys Structural Mechanics v.15 is used. The general methodology to perform FEA is described in Figure 6-1. The cycling sequence, the geometry and the material behaviour's law are the input data. The cycling sequence reproduces the cyclic load undergone by the component. After FEA, the local stress-strain state in the component is obtained. Then, in order to predict fatigue life of the component, the damage parameter and its corresponding fatigue resistance law are used. The material and fatigue resistance laws are obtained from experimental results. If predicted and experimental fatigue lives are similar, the methodology and the material's law are validated. In the opposite case, where experimental and predicted fatigue lives are different, the material's law is invalidated and has to be reevaluated.

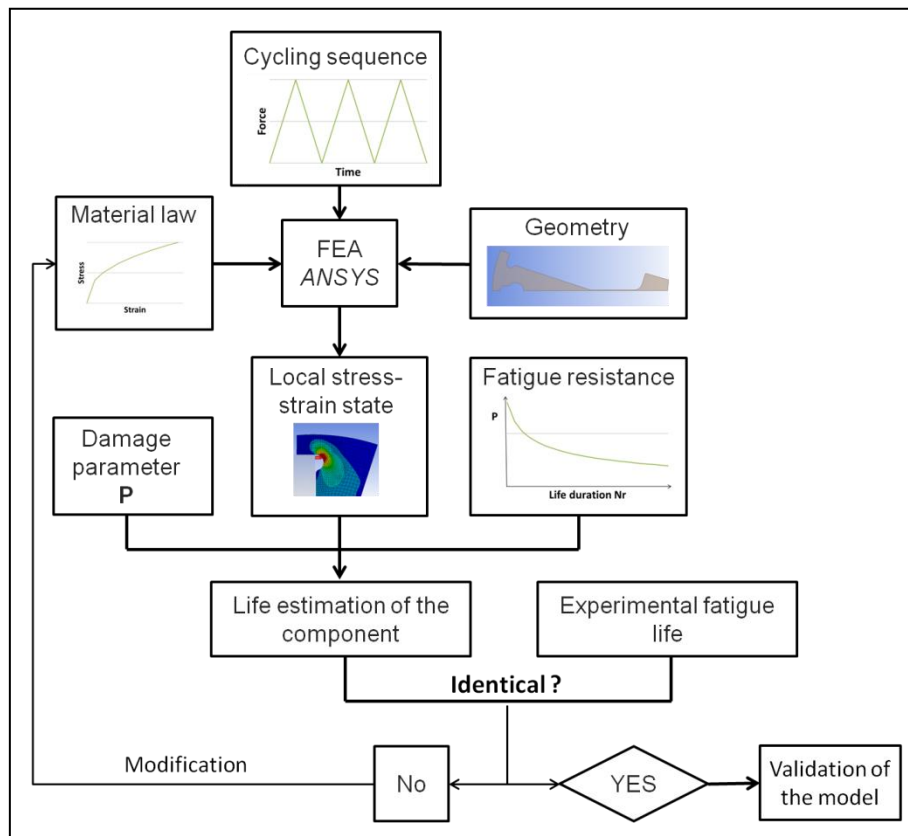


Figure 6-1: Fatigue life estimation scheme

As presented in the general introduction, up to now within Valeo, the Haigh diagram construction was used in order to validate component design subjected to cyclic loading from the mechanical point of view. This diagram is based on the Goodman relation (equation 6-1) where σ_a is the alternating stress (equation 6-2), σ_m is the mean stress (equation 6-3), σ_{fat} , the fatigue limit for completely reversed loading and UTS, the Ultimate Tensile Strength of the material.

$$\sigma_a = \sigma_{fat} \times \left(1 - \frac{\sigma_m}{UTS}\right) \quad (6-1)$$

$$\sigma_a = \left(\frac{\sigma_{max} - \sigma_{min}}{2}\right) \quad (6-2)$$

$$\sigma_m = \left(\frac{\sigma_{max} + \sigma_{min}}{2}\right) \quad (6-3)$$

This relation is used to evaluate the interaction between mean stress and alternating stress on the fatigue life of the considered material [HER97]. The trend is that increasing the mean stress for a given alternating stress decreases the fatigue life. This relation is plotted in a graph (Figure 6-2) where σ_a is plotted versus σ_m with UTS placed on the abscissa axis and σ_{fat} placed on the ordinate axis. If the coordinates given by the mean FEA stress and the alternating stress of a component lies below the line formed by the UTS and σ_{fat} , the component will handle the loading without breaking. A

safety factor can also be added. On the other hand, if the σ_a and σ_m lies above the line, the part will fail for the given cyclic load.

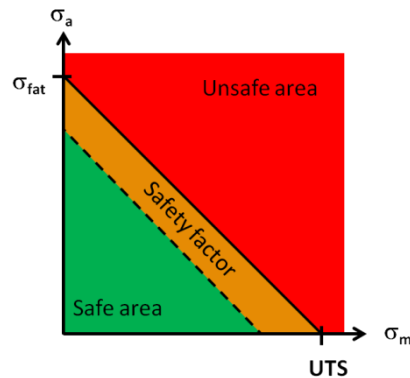


Figure 6-2: Construction of the Haigh diagram with the safety factor

This method is particularly adapted for the high-cycle fatigue regime where no plastic straining is reached. In the case of the present alternator's rotor, no failure of the component has been encountered. However, to increase the electro-technical performances of the alternator, the geometry of the rotor must be modified. The yield limit is locally exceeded and the methodology is no more adapted. In this case, the hardening properties of the material have to be taken into account. For that purpose, the elasto-plastic material behaviour has to be determined with the help of different mechanical models that are presented in the next paragraph. The different steps leading to the rotor design improvement (from mechanical point of view) are shown in Figure 6-3.



Figure 6-3: The different steps leading to the rotor design improvement

6.2 Choice of material model

To choose the material model that best describe the elasto-plastic phenomena of the material subjected to cyclic loadings, experimental and simulated stress-strain hysteresis loops from simple geometry, corresponding to the smooth specimen of the LCF testing, are compared. The material model that presents the least differences between modelled and experimental plastic strain variation, stress amplitude and hysteresis curve area is chosen. First the different regimes that can be encountered are presented followed by the different models commonly used to describe work-hardening. Then, in order to choose the most adapted model for the present material, the Fe-3Si steel, stress-strain hysteresis curves and fatigue lives are compared.

6.2.1 Cyclic accommodation regimes

Under cyclic loading with strain control, a cyclic hardening or a cyclic softening can be observed (see paragraph §1.3.1.2.1). Moreover, different regimes can be observed according to the control mode. Indeed, under force control mode, if the material stabilised, adaptation phenomena (corresponding to elastic stabilisation) or accommodation phenomena (stabilisation of hysteresis loops) can be observed (Figure 6-4 (a) and (b) respectively). If there is no stabilisation of the material, ratcheting phenomena occurs, in this case an incremental strain is added between each hysteresis loops (Figure 6-4 (c)).

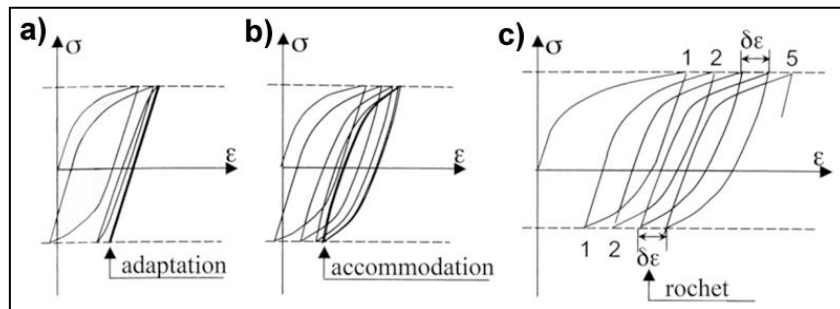


Figure 6-4: a) adaptation, b) accommodation and c) ratcheting phenomena [LEM09]

Under strain control mode, a relaxation of the mean stress can be observed during the test (Figure 6-5).

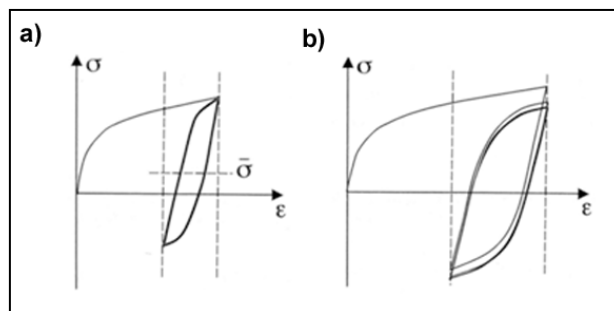


Figure 6-5: Phenomena of a) incomplete relaxation and b) total relaxation of the mean stress under strain control mode [LEM09]

6.2.2 Work-hardening laws

The reader is encouraged to refer to the reference: [LEM09] in which mechanical models are reviewed in details. There exist several methods to describe the inelastic behaviour of a material. Indeed, hardening can be isotropic or kinematic (Figure 6-6).

If elastic regimes at the beginning of the test and after plastic straining are compared, it can be noticed that:

- 1) In the case of **isotropic hardening** (§6.2.2.1), an increase of the elastic domain size can be noticed which is linked to the increase of the dislocation density.

- 2) In the case of **kinematic hardening** (§6.2.2.2), the segment of the elastic domain is displaced along the stress axis. It is linked to the microstress present within the material due to its heterogeneity. This corresponds to the Bauschinger effect (Figure 6-6).

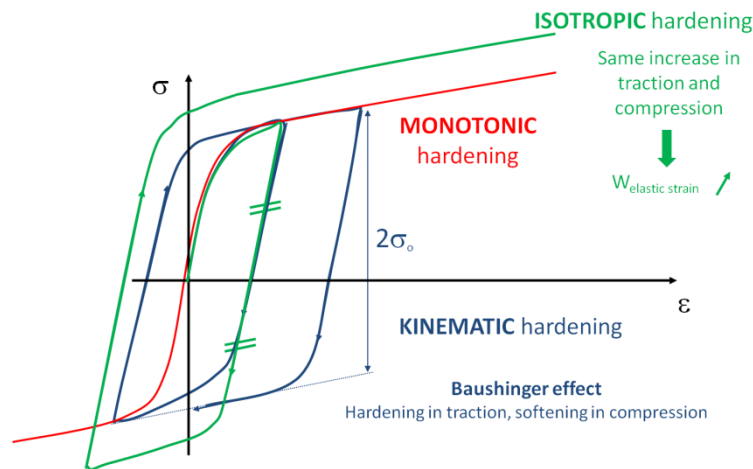


Figure 6-6: Isotropic and kinematic hardening [OUD04]

6.2.2.1 Isotropic hardening model

For isotropic hardening laws, the homothetic evolution of the elastic domain during the plastic deformation only is taken into account (Figure 6-7).

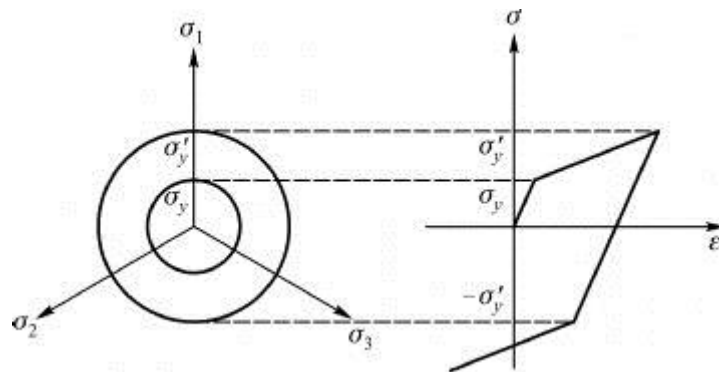


Figure 6-7: Isotropic hardening: representation in the space of principal stress and in tension-compression [LEM09]

The isotropic hardening, R , can be defined by different equation (linear equation (6-4); power law (6-5); exponential law (6-6)).

$$R = k_1 p \tag{6-4}$$

$$R = k_y p^{\frac{1}{M}} \tag{6-5}$$

$$R = R_{\infty} (1 - e^{-bp}) \tag{6-6}$$

With k_1 , k_y , M and b material constants, R_{∞} , the saturation value of the isotropic hardening and p the cumulative plastic strain.

Considering an isotropic linear law as equation (6-4), Figure 6-8 shows how to construct hysteresis curves from the equation (6-2). Indeed, it follows these steps:

- 1) At the initial stage, O , $p=0$ thus $R=0$. OA segment corresponds to the elastic load thus $d\varepsilon_p=0$.
- 2) At A , the yield limit is reached (the criteria for plastic straining to occur is reached), $\sigma=\sigma^y$.
- 3) The segment AB corresponds to plastic straining, thus $d\varepsilon_p>0$, $dp = d\varepsilon_p$ and $p = \varepsilon_p - \varepsilon_p(0)$, R can be written as $R = k\varepsilon_p$ and thus the stress is $\sigma(B) = (k\varepsilon_p + \sigma^y)$.
- 4) From B to C , there is elastic return, $d\varepsilon_p = 0$, $dR = 0$.
- 5) At C , the yield limit is reached (the criteria for plastic straining to occur is reached), $\sigma(C) = -[R(B) + \sigma^y] = -[k\varepsilon_p + \sigma^y]$
- 6) From C to D , there is plastic transformation $d\varepsilon_p<0$, $dp = -d\varepsilon_p$, with $p(D)$ the length of the plastic strain path, R can be written $R=-kp(D)$ and $\sigma(D) = -[kp(D) + \sigma^y]$.
- 7) From D to E , there is elastic return, $d\varepsilon_p = 0$, $dR = 0$.
- 8) At E , the criteria for plastic straining to occur is reached, $\sigma(E) = kp(D) + \sigma^y$.

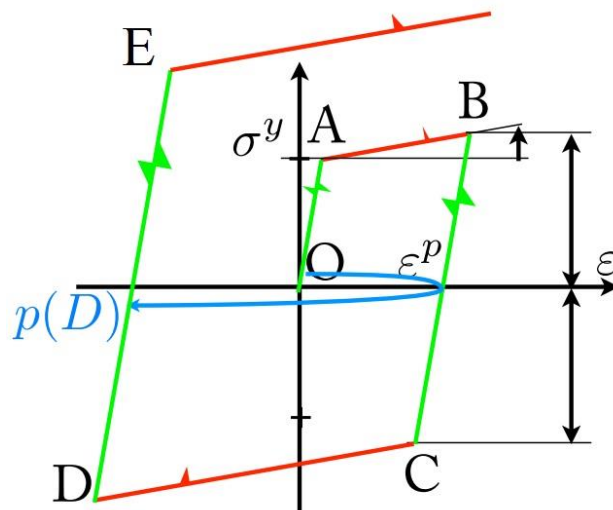


Figure 6-8: Construction of hysteresis curve with the linear isotropic law

This simple model has the advantage of limiting the calculation time. However, in the case of cyclic loadings with $R_\varepsilon=0$ and $\varepsilon_{\max}>0$, it leads to an increase of the stress during cycling and a decrease of the plastic strain which is not representative of the M330-35A behaviour.

6.2.2.2 Kinematic hardening model

The kinematic hardening model corresponds to a displacement of the load surface, but the load surface of the elastic domain remains the same during loading (Figure 6-9). This results in the fact that an increase of the elastic limit induces a corresponding decrease of the limit of elasticity in

compression; it is the Bauschinger effect. This effect refers to the evolution of the stress and deformation of the material due to the change of the distribution of microscopic stresses.

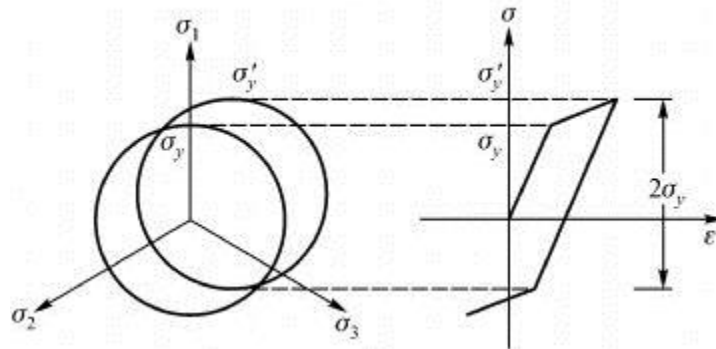


Figure 6-9: Kinematic hardening: representation in the space of principal stress and in tension-compression [LEM09]

This model can be used for all the materials that respond to Von Mises criteria (plastic straining occurs when the elastic distortion energy stored at a given time exceeds a fixed limit value).

6.2.2.2.1 Linear kinematic hardening

The simplest model is the linear kinematic hardening of Prager [PRA55], the kinematic hardening, X , is linked to the plastic strain by equation (6-7).

$$X = \frac{2}{3} C \epsilon_p \tag{6-7}$$

with C a constant of the material and ϵ_p the plastic deformation.

6.2.2.2.2 Nonlinear kinematic hardening

The nonlinear kinematic hardening of Armstrong-Frederick introduces an additional term in comparison to the linear kinematic model of Prager which is called “dynamic recovery” introducing a memory of the deformation path (Figure 6-10).

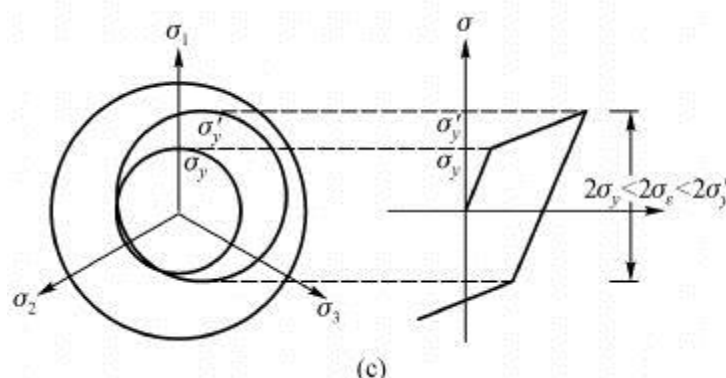


Figure 6-10: Nonlinear kinematic hardening model [LEM09]

This law is expressed by the equation (6-8) with \dot{p} , the cumulated plastic strain rate, $\dot{\epsilon}^p$, the plastic strain rate, C and γ , material parameters.

$$\dot{X} = \frac{2}{3} C \dot{\varepsilon}^p - \gamma X \dot{p} \quad (6-8)$$

The integration of this law in the uniaxial domain leads to the equation (6-9).

$$\frac{\Delta X}{2} = \frac{C}{\gamma} \tanh\left(\gamma \frac{\Delta \varepsilon_p}{2}\right) \quad (6-9)$$

C is a constant that is proportional to the hardening modulus and γ is the rate of decrease of hardening modulus and the value of C/γ corresponds to X_∞ which represents the kinematic hardening at saturation.

In the case of this study, the isotherm conditions and independent on the strain rate enable the description of $\Delta\sigma$ as $\Delta X + 2k$. Thus, in the stabilised regime, the equation (6-10) is obtained with k the stabilised yield stress.

$$\frac{\Delta\sigma}{2} - k = \frac{C}{\gamma} \tanh\left(\gamma \frac{\Delta \varepsilon_p}{2}\right) \quad (6-10)$$

Under stress control mode, the model is stabilised after one cycle, the cyclic stabilisation is possible only under symmetric load and otherwise the Rochet effect is observed.

For strain control mode, if the mean strain is different to zero, the initial dissymmetry of the load disappear progressively, there is stress relaxation.

This model describes well the Bauschinger effect but does not describe precisely the hysteresis loop shape. Improvement was obtained by Chaboche [CHA08] by creating stress hardening through superposition of M parts (equation (6-11)).

$$X = \sum_{i=1}^M X_i \quad (6-11)$$

Each kinematic hardening variable X_i follows the evolution law of the equation (6-12), in isothermal conditions.

$$\dot{X}_i = \frac{2}{3} C_i \dot{\varepsilon}^p - \gamma_i X_i \dot{p} \quad (6-12)$$

Thus, cyclic strain curve can be described by equation (6-13).

$$\frac{\Delta\sigma}{2} - k = \sum_{i=1}^M \frac{C_i}{\gamma_i} \tanh\left(\gamma_i \frac{\Delta \varepsilon_p}{2}\right) \quad (6-13)$$

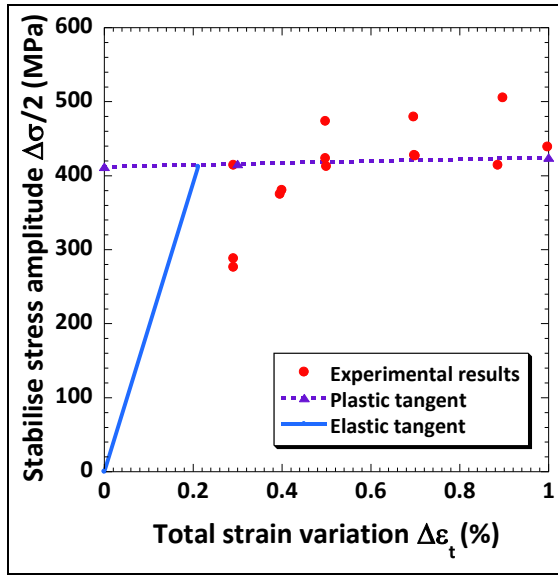


Figure 6-12: Bi-linear description

Table 6-1: Bi-linear input datas

Linear function $y=ax+b$	
a, Tangent modulus	1244
b, Yield strength	411.95 MPa

The multilinear law is represented in Figure 6-13. The stress amplitude of the experimental hysteresis curves at 70% of life duration is plotted versus the plastic strain variation (red points). The multilinear curve is then drawn to fit the best to the experimental points. Therefore, the multilinear law is obtained by four segments of different slopes (Table 6-2). The differences, calculated by the relation (6-15), are less than 15 for every point except for the points highlighted by an arrow because of the experimental dispersion.

$$\frac{1}{100} \times \left[\frac{\Delta\sigma}{2}_{experimental} - \frac{\Delta\sigma}{2}_{model} \right]^2 \tag{6-15}$$

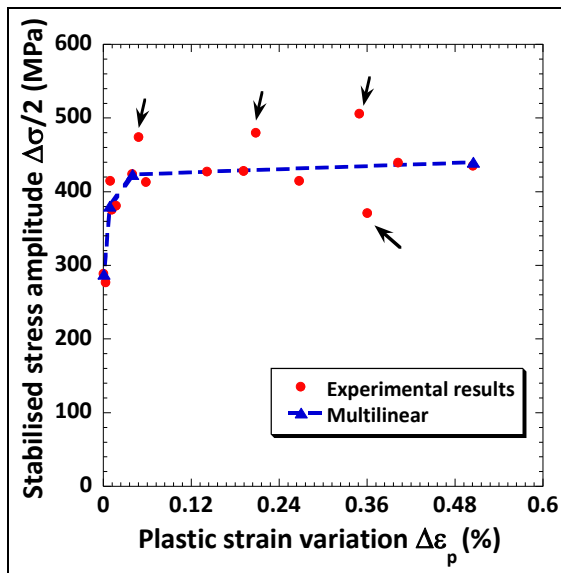


Figure 6-13: Multi-linear description

Table 6-2: Multi-linear input data

ϵ_p (mm.mm ⁻¹)	σ (MPa)
0	276.40
10^{-5}	380.18
4.10^{-4}	423.45
$5.05.10^{-3}$	440
0.01	441

Regarding the non-linear kinematic hardening, the identification of the materials parameters, k , γ_1 and γ_2 , is needed. For that purpose, hysteresis curves at 70% of life duration, corresponding to the pseudo-stabilised state, are taken for each strain variation to determine k , the stabilised yield stress. Depending on the material, k might be equal or different for every total strain. Thus, it has to be determined for each test. Figure 6-14 (a) shows how to determine k from the hysteresis curves, $2k$ is the linear part of the curve, k describes the size of the elastic domain.

Then, $\Delta\sigma/2 - k_{\text{experimental}}$ is plotted against $\Delta\varepsilon_p/2$ (in red in Figure 6-14 (b), the axis on the vertical basic is removed for confidential reason). The material parameters C_i and γ_1 (equation 6-13) are obtained by curve adjustment in order to minimise the error between $(\Delta\sigma/2 - k)_{\text{experimental}}$ and $(\Delta\sigma/2 - k)_{\text{model}}$ (in blue in Figure 6-14 (b)) as defined in equation (6-16). The parameters C_i and γ_1 are defined when an error inferior to 10 is obtained for every stress amplitude (according to equation (6-14)).

$$\frac{1}{100} \times \left[\left(\frac{\Delta\sigma}{2} - k \right)_{\text{experimental}} - \left(\frac{\Delta\sigma}{2} - k \right)_{\text{model}} \right]^2 \quad (6-16)$$

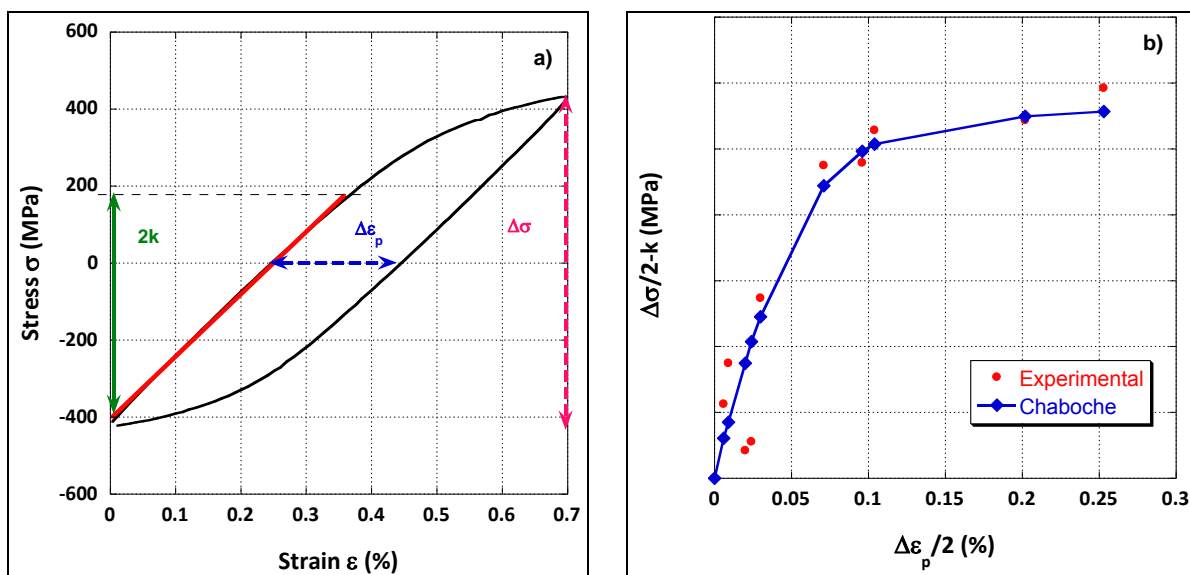


Figure 6-14: (a) Determination of k from experimental hysteresis curves taken at 70% of fatigue life ($2k$ is the size in MPa of the elastic domain) and (b) Identification of parameters C and γ . Each point is obtained from an experimental fatigue test, the blue curve is obtained by adjustment

The C_i and γ_1 parameters obtained by this method are then kept for the following FEA. FEA comparison and material hardening model choice.

To select the most suitable hardening model, the different hardening models are tested (Table 6-) by applying a cyclic load by strain control (Figure 6-15 (b)) to a component whose geometry is similar to

the useful part of the smooth specimen of the LCF test (Figure 6-15 (a)), it consists in a rectangle with symmetries on two of its edges and the load is applied on the upper side.

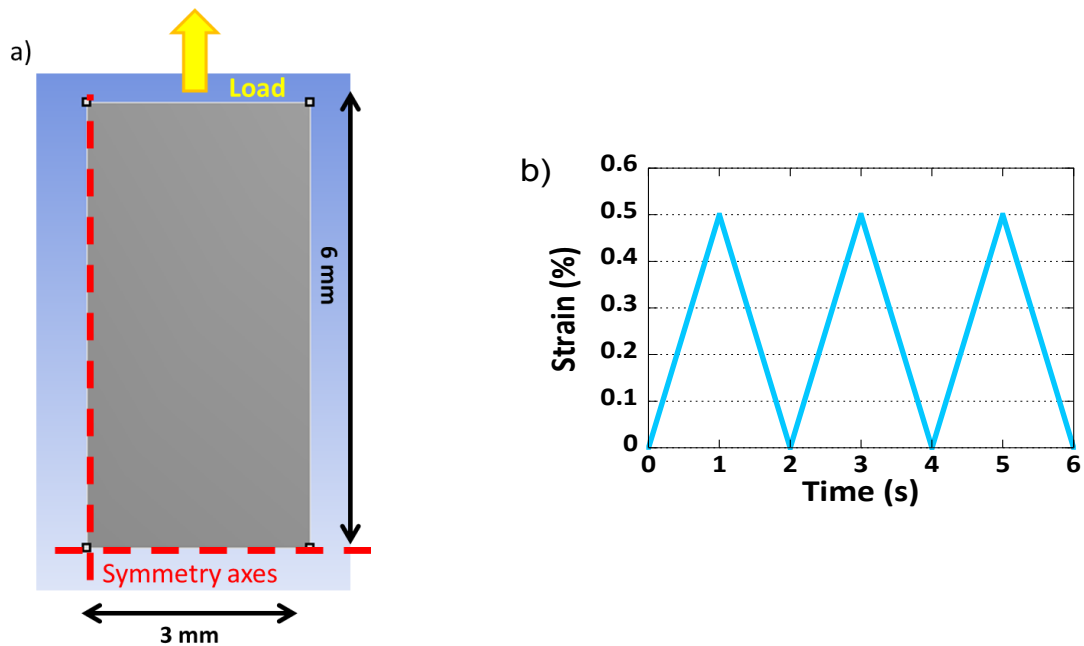


Figure 6-15: (a) Dimensions of the geometry used for FEA (two-dimensions FEA) and boundary conditions, (b) the cyclic strain load

Table 6-3: Input data for the choice of the material hardening law

Density	7850 kg.m ⁻³				
Isotropic elasticity	Young modulus, E=195 GPA				
	Poisson's ratio, $\nu=0.3$				
Hardening model	Isotropic		Kinematic		Mixed model
	Bi-linear	Multi-linear	Bi-linear	Multi-linear	Chaboche model
	See Table 6-1		See Table 6-2		See Erreur ! Source u renvoi introuvable.

Finally, the hysteresis curves obtained by modelling are compared to the experimental one taken at 70% of lifetime (pseudo-stabilised state) in Figure 6-16, Figure 6-17 and Figure 6-18 for $\Delta\varepsilon_t=0.5\%$, 0.7%, 0.9% and 1%.

In Figure 6-16, hysteresis curves obtained by the isotropic bilinear and multilinear hardening models are compared to the experimental ones. The modelled hysteresis curves shape is quadrilateral which is very different from experimental hysteresis curve. The difference is more noticeable for the highest strain variation ($\Delta\varepsilon_t=0.9\%$ and 1%). Regarding, the kinematic hardening model (Figure 6-17), modelled hysteresis curve shape is closest to experimental ones, up to $\Delta\varepsilon_t=0.7\%$, the multilinear

kinematic hardening model describes well the behaviour of the material. The hysteresis curves obtained with the Chaboche model (Figure 6-18) are very similar to the experimental ones for $\Delta\varepsilon_t=0.5\%$ and 0.7% , for $\Delta\varepsilon_t=0.9\%$ and 1% , the modelled hysteresis curve areas are superior to the experimental ones.

The error between FEA and experiments is calculated for plastic strain $\Delta\varepsilon_p$, stress variation $\Delta\sigma$ and curve area, according to equation (6-17). The model that presents the least percentage of error is the one that is most suitable to model the material behaviour.

$$Error = \frac{|Experimental\ result - Modelled\ result|}{|Experimental\ result + Modelled\ result|} \quad (6-17)$$

The results are shown in Figure 6-19. It appears that, regarding plastic strains (Figure 6-19 (a)), the Chaboche model is the closest to the experiment for all strain amplitudes. There is globally less error on stress amplitudes estimation (Figure 6-19 (b)) than plastic strain amplitude and it is the opposite concerning hysteresis curve areas (Figure 6-19 (c)). When errors of each parameter are added the model that gives the best prediction is the Chaboche model (Figure 6-19 (d)).

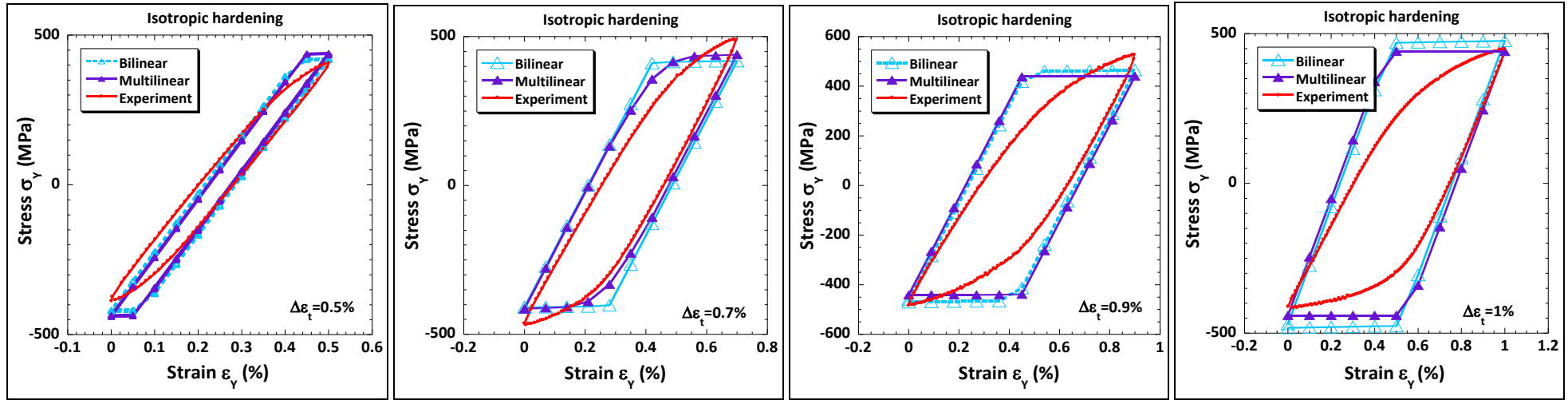


Figure 6-16: Stabilised hysteresis curve obtained at $\Delta\epsilon_t=0.5\%$, 0.7% , 0.9% and 1% by FEA with the isotropic hardening model compared to experimental results

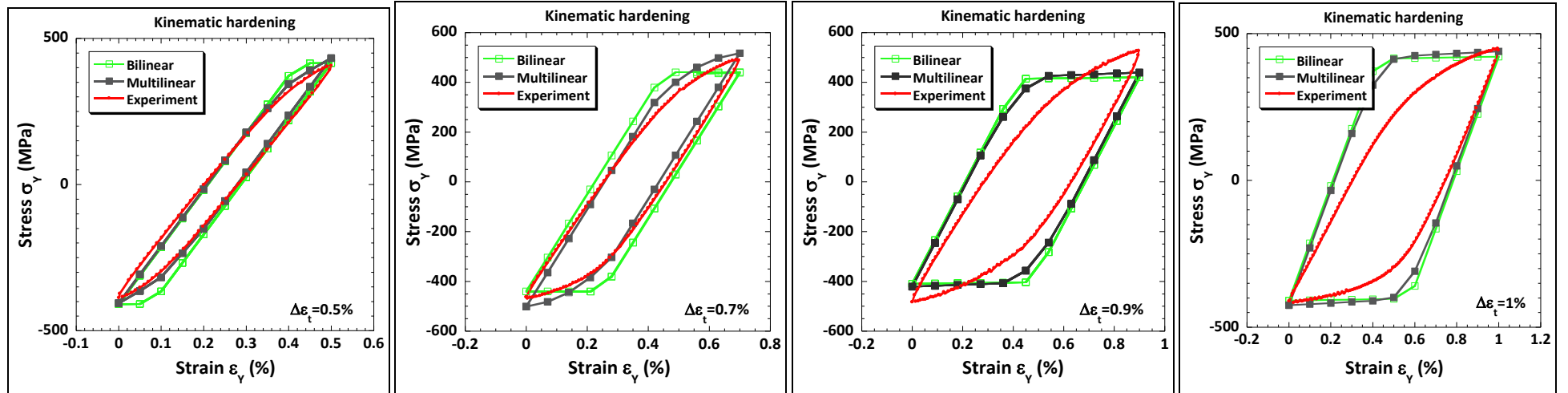


Figure 6-17: Stabilised hysteresis curve obtained at $\Delta\epsilon_t=0.5\%$, 0.7% , 0.9% and 1% by FEA with the kinematic hardening model compared to experimental results

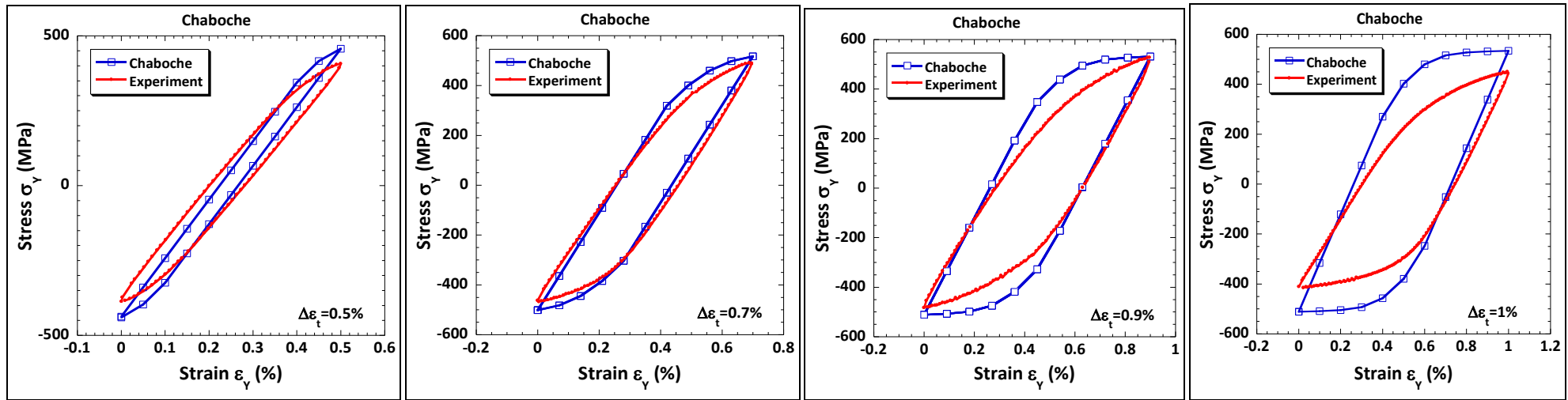


Figure 6-18: Stabilised hysteresis curve obtained at $\Delta\epsilon_t=0.5\%$, 0.7% , 0.9% and 1% by FEA with the Chaboche model compared to experimental results

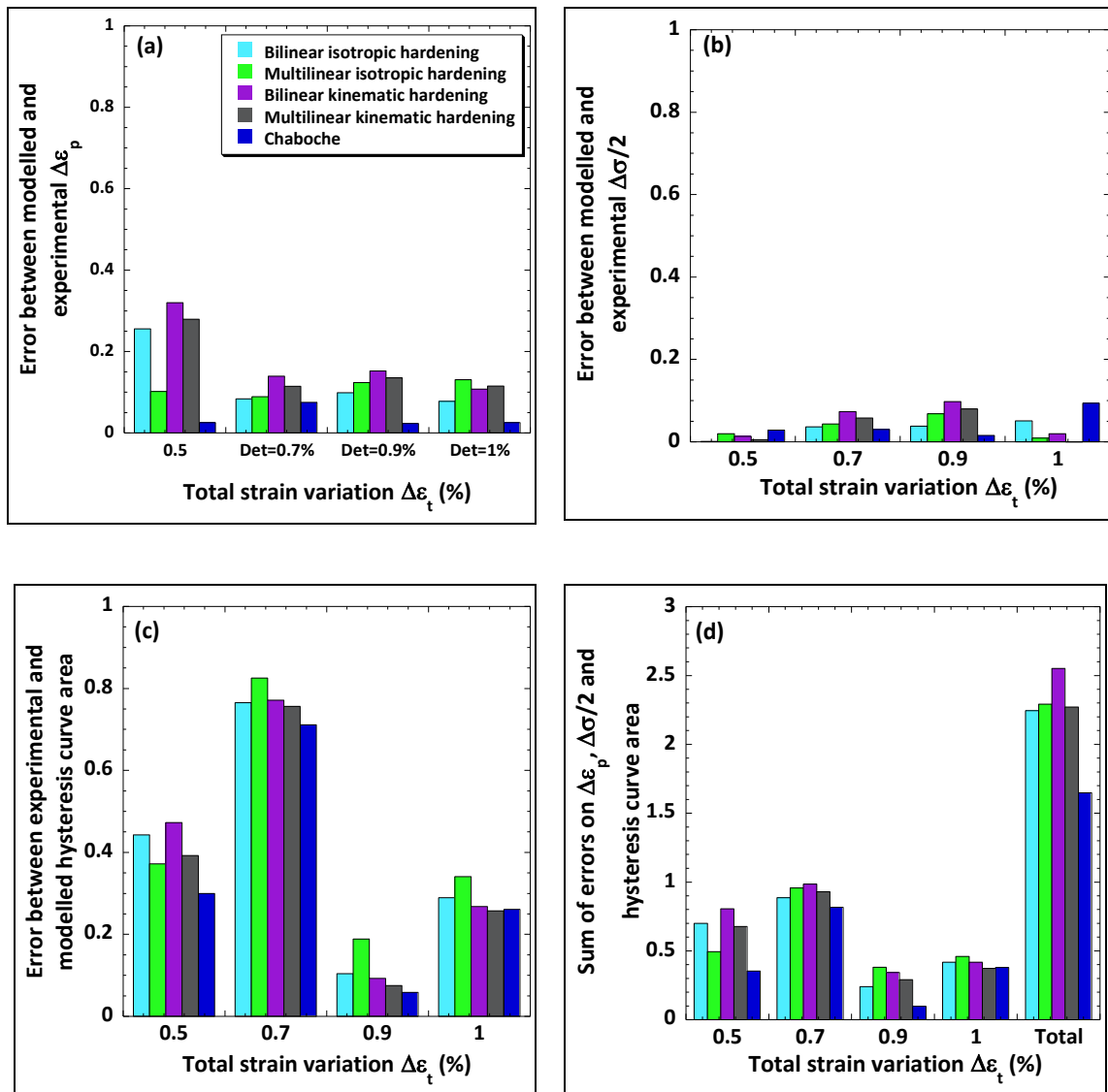


Figure 6-19: Error between modelled and experimental (a) plastic strains, (b) stress amplitudes, (c) hysteresis curve areas and (d) sum of the calculated errors according to the considered hardening model

From Figure 6-19 (a), it can be noticed that Chaboche model is the one that enables the best estimation of the plastic strain. The Manson-Coffin law is used to predict fatigue life of a component as this model is the most adapted for the present study. At high strain range, it overestimates the stress variation but such strain should not be reached in the final component. Finally, the sum of the errors is the lowest for the Chaboche model when compared to the other models.

Due to its ability to estimate precisely the plastic strain variation and hysteresis curve shape, the Chaboche model is chosen for the following FEA.

6.3 Validation of the model

The second step is the validation of the material model on a geometry having a « defect » that will introduce multiaxial stress and strain leading thereby to a more complex system. In the present case, a notch is introduced in the sample as describe in Figure 6-20. Notch samples are rarely studied in LCF; they are typically studied in the high-cycle fatigue regime and in fatigue-propagation. The notch radius is chosen from the initial schema of the rotor and corresponds to the radius of the zones circled in yellow in Figure 6-20, they maintain the magnets into the rotor.

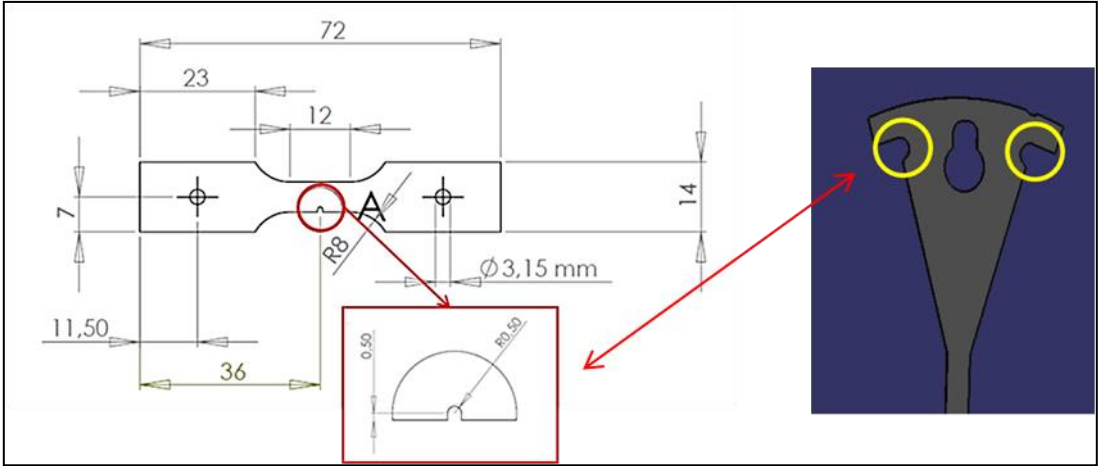


Figure 6-20: Dimensions of the notch samples obtained from the initial rotor geometry

Due to the notch, the use of an extensometer is no more possible without damaging it. Therefore, these samples are subjected to cyclic loading under force control. The testing parameters are detailed in Table 6-.

Table 6-4: Fatigue tests parameters on notch samples

Applied force	Signal	Frequency	Fatigue life
400 à 700N	Triangular	2 Hz	10^3 à 10^5

The number of cycle leading to rupture is taken for each studied step of force. The experimental results are given in Figure 6-21.

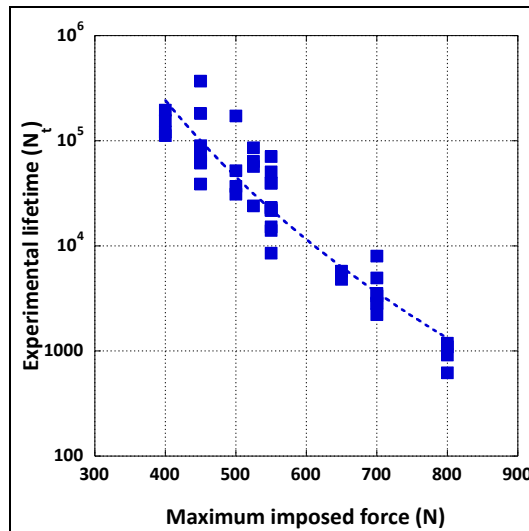


Figure 6-21: Experimental life duration of the notch samples obtained for different imposed forces

FEA were performed on a component with the same geometry than the test's specimen. The FEA component and its boundary conditions are presented in Figure 6-22.

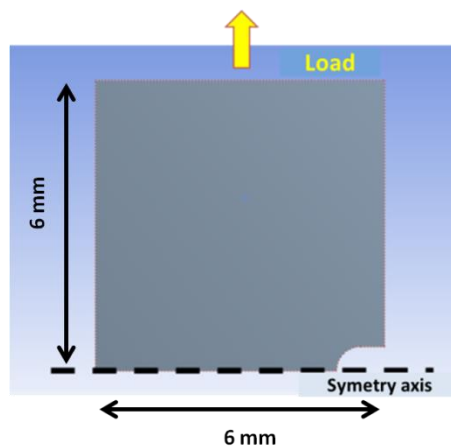


Figure 6-22: Figure of the geometry used for the FEA and corresponding boundary conditions

The presence of the notch induces localisation of the stress and strain in the notch root. Therefore, proper meshing must be done in order to describe accurately the strain localisation. This is done by mesh refining in the notch area.

There exists different type of mesh [HO88]. In two-dimensions, as it is here, mesh can be triangular or quadratic [AGA08]. Triangular mesh consists of 3 sides elements and enables fast finite element calculation but it supports only a linear variation of displacement within a single element, which means only a constant state of stress within a single element, and it is highly sensitive to element distortion [ANS13]. Quadratic mesh consists in 4 sides elements and it supports a quadratic variation of displacement in a single element which means a linear variation of stress within the element and it

is less sensitive to element distortion than triangular mesh [ANS13]. Quadratic elements are thus chosen for the meshing of the notch specimen.

Firstly, the mesh is generated automatically by the software Ansys. A cyclic positive force $F_{max}=525N$ is applied in the FEA on the sample geometry and the mesh is refined automatically step by step until a stable value of the equivalent stress (which corresponds to Von-Mises stress) is reached, that is to say when the stress value is changing less than 1% when refining the mesh (Figure 6-23).

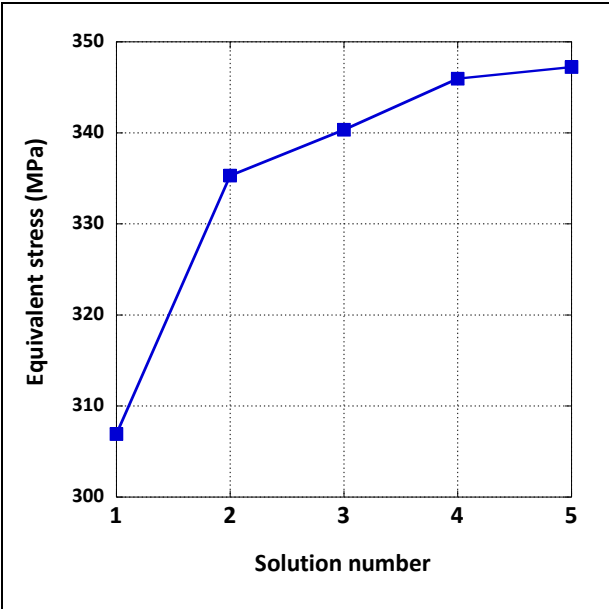


Figure 6-23: Evolution of the equivalent stress with refinement of the mesh

The last geometry solution present a fine meshing in the vicinity of the notch with element size of 0.05mm which is used for the FEA of the notch samples. Indeed, to have always the same meshing the following procedure is used: the mesh refinement is performed in the notch area by the use of the function “Body sizing”. It consists in creating a sphere of influence within which the element size is specified. A sphere of influence of a radius of 2.5mm with the same centre than the notch radius is used and element size in this sphere is specified at 0.05mm (Figure 6-24).

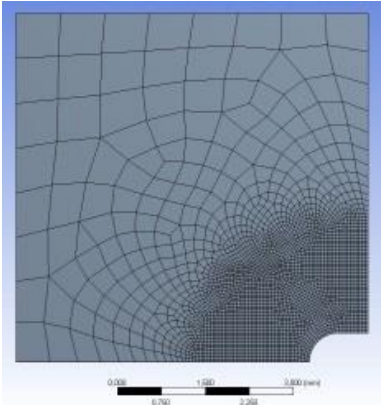


Figure 6-24: Mesh used for FEA of notched specimen

6.3.1 Fatigue lives estimation and comparison with the experiments

FEA is made using the Chaboche model with the parameters determined in §0 and the mesh shown in Figure 6-24. The cyclic load is the same than in Table 6- with $F_{min}=0N$ and $400N \leq F_{max} \leq 800N$. The Figure 6-25 shows the localisation of strain and stress in the notch root after several load at $F_{max}=525N$.

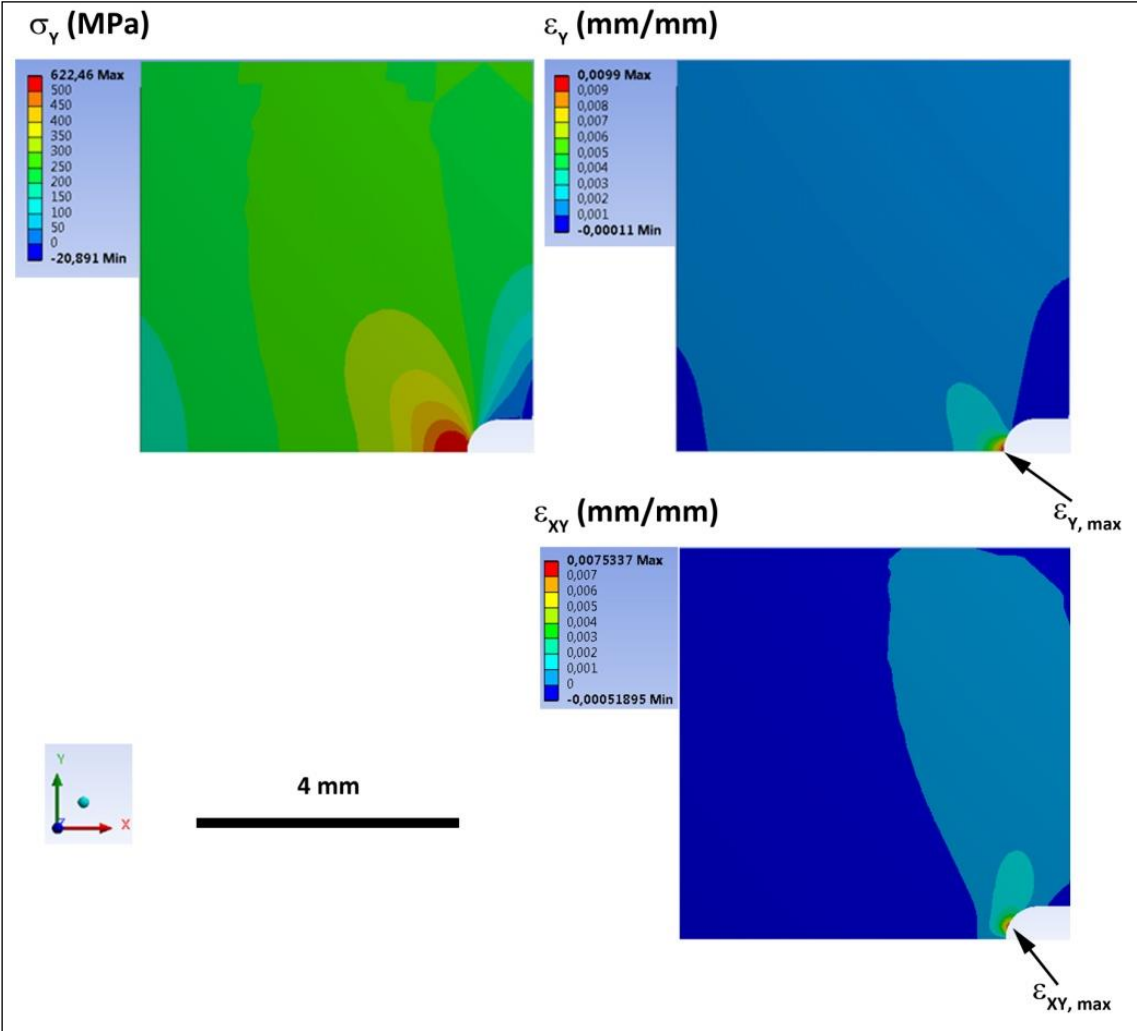


Figure 6-25: Stress and strain localisation in the notch root at $F_{max}=525N$

The point where the maximum longitudinal strain ($\epsilon_{y, max}$) is reached is first considered for fatigue life calculation.

Hysteresis curve of longitudinal stress (σ_y) versus longitudinal strain (ϵ_y) are plotted for different F_{max} which enables the measurement of plastic strain variation, $\Delta\epsilon_{p,y}$. The Manson-Coffin relation established in §3.1.3.1 from LCF tests on smooth sample is then used to estimate fatigue life as plastic strain has been chosen as damage indicator. In Figure 6-26 (a), the estimated fatigue lives are compared to the experimental ones, the black line correspond to theoretical exact coincidence between N_f^{exp} and N_f^{FEA} , the dot lines to 20% of error between N_f^{exp} and $N_f^{FEA,Y}$ and the blue point to the real relation between N_f^{exp} and N_f^{FEA} . It appears, that FEA underestimates N_f of about a factor 10

in comparison to the experimental N_f . Indeed, when considering only the point where $\varepsilon_{p,Y}$ is maximum at F_{max} (the notch root). The surroundings points are neglected, but in these points the strain is much lower. Also, the notch introduces shear strain that has not been taken into account. Therefore, $\varepsilon_{p,XY}$ is considered and fatigue lives are estimated with the same Manson-Coffin relation but based on $\Delta\varepsilon_{p,XY}$. This enables the comparison of N_f^{exp} and $N_f^{FEA,XY}$ (Figure 6-26 (b)) and better results are obtained. Indeed, the dispersion of N_f^{exp} is important but the error between $N_f^{FEA,XY}$ and N_f^{exp} is about 20%, it reaches 50% for the highest forces (e.g. the highest plastic strains).

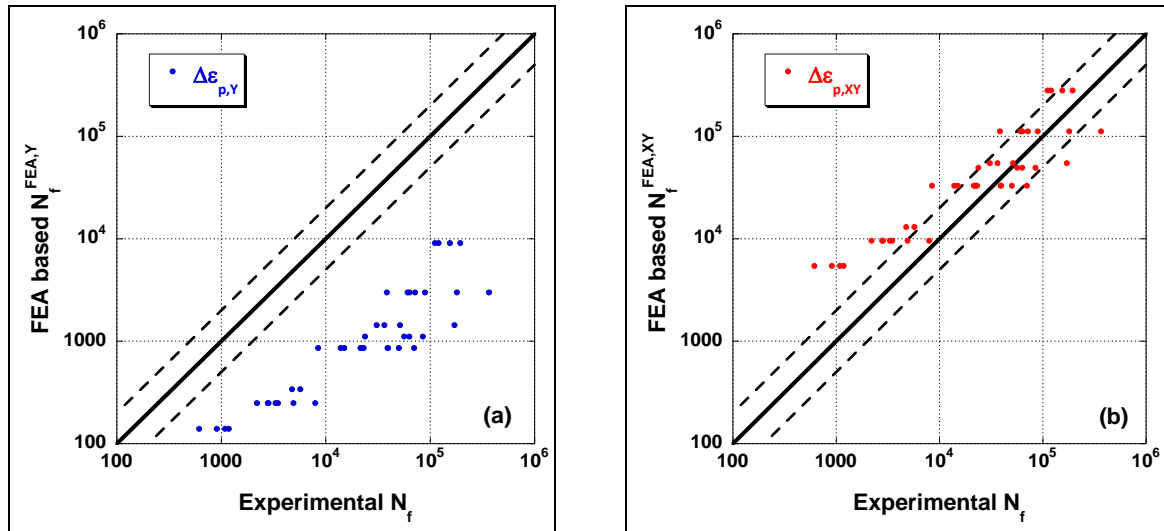


Figure 6-26: Comparison between experimental N_f and FEA based N_f considering a) $\Delta\varepsilon_{p,Y}$ and b) $\Delta\varepsilon_{p,XY}$

Thus, at this point, fatigue life in case of moderate plastic straining can be estimated with an accuracy of 20%.

6.3.2 Strain distribution validation

The comparison of DIC results with FEA is useful to validate the material model. Indeed, strain estimations are based on the material chaboche model developed in §0 and it showed that fatigue lives could be estimated from plastic shear strain variation ($\Delta\varepsilon_{p,XY}$) but were underestimated when considering plastic longitudinal strain variation ($\Delta\varepsilon_{p,Y}$). It is linked to the compression zone behind the notch.

Strains evaluated by FEA are compared to those obtained by DIC (Figure 6-27). The strains cannot be evaluated in the exact vicinity of the notch for DIC results due to the size of the facets used for strain estimation.

Nevertheless, $\varepsilon_Y^{DIC}_{max}$ is compared to $\varepsilon_Y^{FEA}_{arrow}$ (Figure 6-27). It shows that ε_Y^{FEA} is underestimated by a factor of 10 in comparison with ε_Y^{DIC} . This is in agreement with life estimation based on ε_Y^{FEA} .

$\varepsilon_{XY}^{DIC}_{max}$ is also compared to $\varepsilon_{XY}^{FEA}_{arrow}$ (Figure 6-27). It shows that the difference between ε_{XY}^{DIC} and ε_{XY}^{FEA} calculated with equation (6-13) is of 20.5%, this is the same error than between N_f^{exp} and N_f^{FEA}

shown in Figure 6-27 (b). DIC results confirm that ε_Y^{FEA} in the case of notch samples is underestimated with the Chaboche model established from smooth samples.

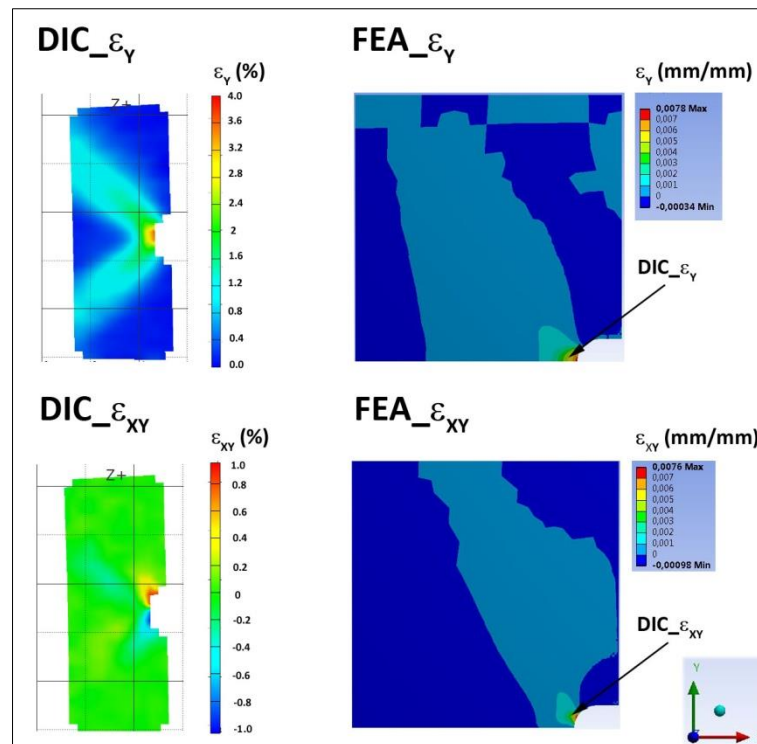


Figure 6-27: Comparison between DIC strain measurements and FEA strain prediction

Chaboche model is established from fatigue tests made with a maximum strain variation of $\Delta\varepsilon_t=1\%$ whereas in the case of notch samples, strain localise and reaches value largely superior to 1% which cannot be accurately estimated with the Chaboche model established here. This study on notch specimen highlights the limitation of the model which is linked to the limitation of the strain amplitudes that can be tested on smooth sample due to the thickness of the sheets.

6.4 Application to rotor sizing

6.4.1 Introduction

After defining the most suitable law that translate the material behaviour during fatigue, FEA on the rotor can be conducted. One of the symmetry of the rotor is schematised in Figure 6-28. The purpose here is to reduce the thickness of leakage path (TLP) (this zone corresponds to the leakage path of the magnetic flux in the rotor) and tip thickness (TT) by staying reliable from the mechanical point of view. The Figure 6-28 describes the symmetries (in red), the contact zones (in white dots) and the different parts of the rotor and the magnet which is a ferritic magnet. Vertex A, vertex B and vertex C correspond to the point that describes the corners or intersections of the rotor geometry. The airgap (short length cut in the magnetic circuit) between the rotor and the stator is of 0.3mm nominal on the diameter.

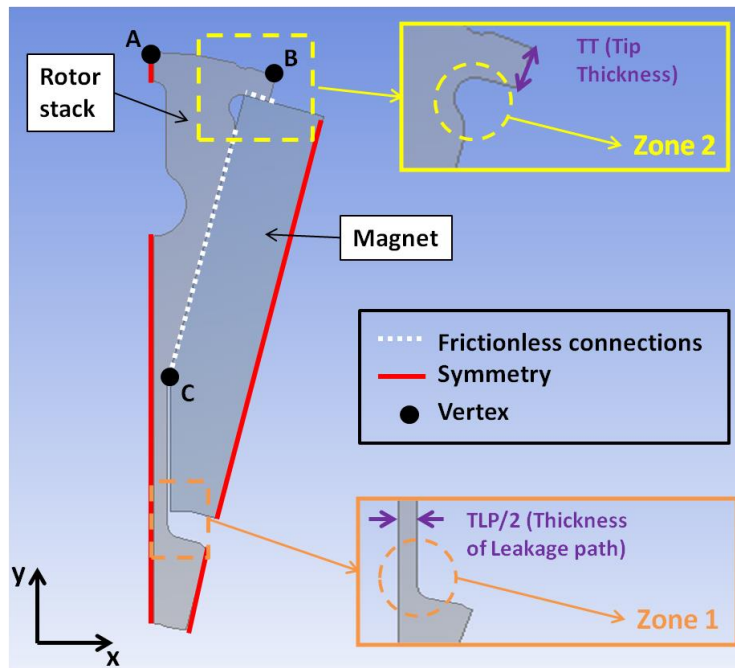


Figure 6-28: Schematic description of FEA rotor geometry

The modification of the rotor geometry is made in two steps:

- 1) refinement of TLP
- 2) refinement of TT

For both steps, the rotor is subjected to the “overspeed test” and to the “cyclic test” as defined in Figure 6-29. The overspeed test consists in the rotation of the rotor from 0 RPM to 21600 RPM only one time, monotonic properties of the material are thus considered for the FEA. The cyclic test consists in the rotation of the rotor from 0 RPM to 20000 RPM for many repetitions. The rotation speed induces rotor elongation along y axis due to the centrifugal force, the Chaboche model that has been developed in §6.2.3 is thus considered.

These FEA “overspeed test” and “cyclic test” are defined from the experimental testing conditions defined in Valeo for the validation of rotor design. Indeed, after mechanical FEA validation of these tests, a mock-up of the rotor must be tested according to Valeo reliability test specifications which consist in:

- For the overspeed test: rotation of the mock-up to 21600 RPM and holding 1h at 21600 RPM
- For the cyclic test: rotate from 0 to 20000 RPM, then hold at 20000 for 100ms decreases the rotational speed to 5000 RPM, hold at 5000 RPM for 100ms and repeat this cycle.

The mechanical design is validated if the mock-up is able to undergo the overspeed test and 100 000 cycles of the cyclic test.

The material properties used for the FEA are detailed in Table 6-5.

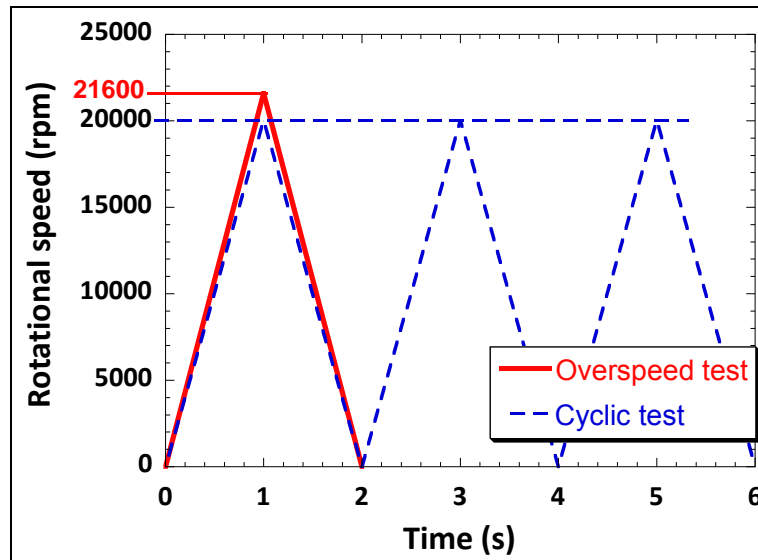


Figure 6-29: Cyclic loadings and overspeed loading for the FEM

Table 6-5: Input data for FEA of the rotor and the magnet

Ferrite magnet					
Young modulus (Gpa)		Poisson's ratio		Density (km/m ³)	
160		0.3		5150	
Rotor stack – Fe3Si – M330-35A					
Monotonic properties					
Young modulus (Gpa)	Yield strength (MPa)	Tensile Strength (MPa)	Poisson's ratio	Density (km/m ³)	Tangent modulus (MPa)
195	380	499	0.3	7850	1088
Chaboche properties					
C ₁ (MPa)	γ ₁	C ₂ (MPa)	γ ₂	C ₃ (MPa)	γ ₃
23 108	0.051927	171 390	1645.7	133 460	93 655

6.4.2 Refinement of the thickness of the leakage path (TLP)

In order to reduce losses in the magnetic circuit and thus improve the machine performances, it is priority necessary to reduce the TLP of the rotor. Therefore, the TLP is refined step by step as described in Table 6-.

Table 6-6: Dimensions of TT and TLP for TLP reduction

	TLP/2 (mm)	TT (mm)	Number of elements	Number of nodes
Initial	1.15	2.073	38295	12521
Modifications	1.1		38340	12534
	1.05		37764	12342
	1.04		37807	12355
	1.03		37877	12379
	1.02		37573	12279
	1.01		37432	12230
	1		37153	12139

To decide whether the geometry is valid or not, the stress and strain states and the elongation (as the airgap is only 0.3mm) are controlled for overspeed test and then cyclic test.

6.4.2.1 Overspeed test

For these calculations the monotonic properties of the material are considered (as defined in Table 6-). Figure 6-30 shows ϵ_y strain distribution in zone 1, ϵ_{xy} is not shown because it is negligible and ϵ_y and ϵ_{xy} strain distribution in zone 2. The point 1_Y corresponds to the maximum ϵ_y longitudinal strain in zone 1, Point 2_Y corresponds to the maximum ϵ_y longitudinal strain in zone 2 and Point 2_XY corresponds to the maximum ϵ_{xy} shear strain in zone 2.

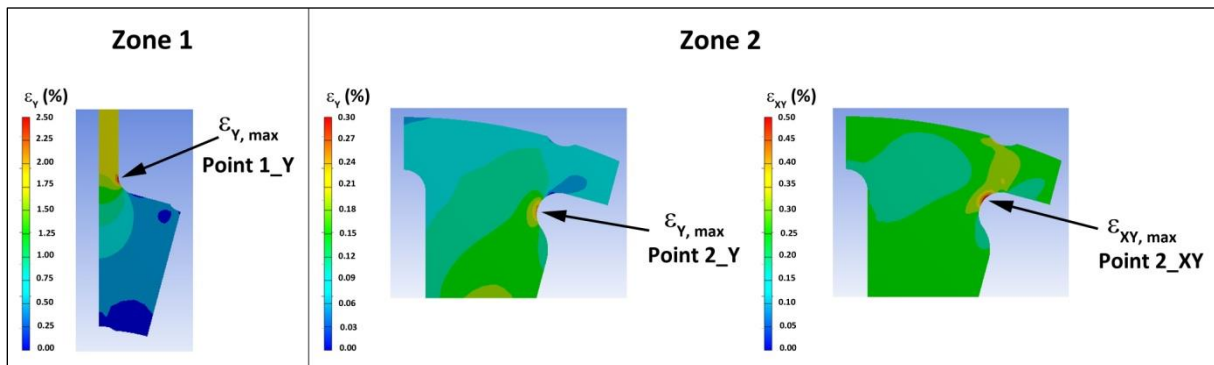


Figure 6-30: Longitudinal and shear strain distributions in zone 1 and 2

The evolution of the strain value and stress value at these points are then studied as a function of the TLP in Figure 6-31 (a) and (b) respectively.

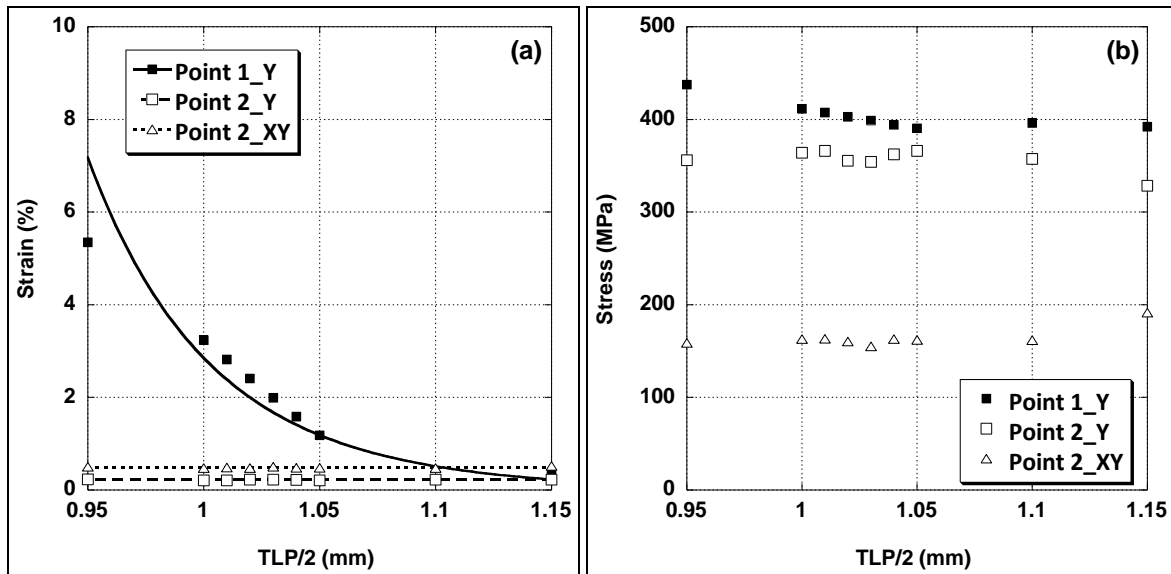


Figure 6-31: Evolution of (a) strain and (b) stress in zone 1 and zone 2 with TLP refinement

It appears that the stress is slightly increases when reducing the TLP, and the stress stays below 450MPa which is inferior to the ultimate tensile strength (UTS=499MPa). Concerning strains, the reduction of TLP has no influence on strains in zone 2 but only on ϵ_Y in zone 1. Reduction of TLP leads to the increase of the longitudinal strain.

An overspeed test can be compared to a tensile test with a monotonous load. Thus, when TLP is reduced, the elastic limit Y_S can be exceeded which leads to plastic straining.

Due to the plastic straining, elongation at vertex A, B and C (Figure 6-28) must also be verified. The Figure 6-32 shows the evolution of elongations at vertex A, B and C. Elongation at vertex B is the most important because the magnet induce a centrifugal force superior in this zone than at vertex A and C. Also, at TLP/2=1.00mm, an elongation equal to the airgap between rotor and stator is reached. This means that friction is likely to occur at TLP/2=1.00mm and is certain at TLP/2=0.95mm. For safety reasons TLP/2=1.01 mm is also isolated (elongation too close to airgap).

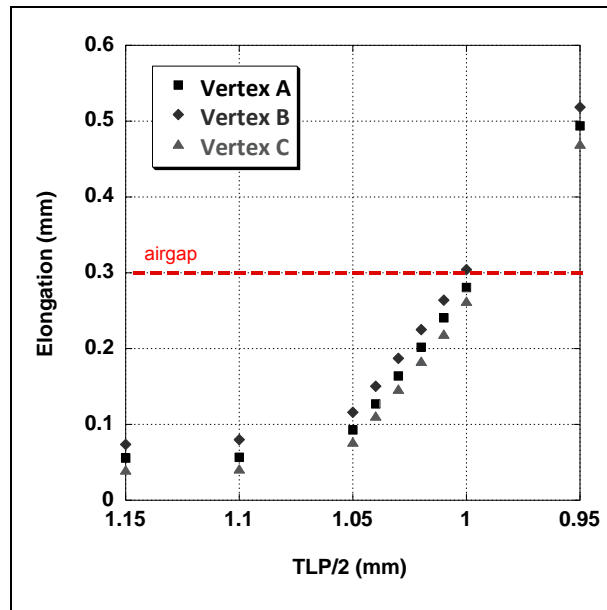


Figure 6-32: Elongation evolution with TLP refinement

The cyclic test is thus performed on different geometries with TLP/2 below 1.15 mm, down to 1.02 mm.

6.4.2.2 Cyclic test

For these calculations the Chaboche properties of the material are considered (as defined in Table 6-). The same methodology than for overspeed test is applied for cyclic test. Indeed, stress and strain states are considered and elongation is checked. Strain-stress hysteresis curves are drawn for the point where ϵ_y is maximum in zone 1 and for points where ϵ_y and ϵ_{xy} are maximum in zone 2. Hysteresis curves corresponding to TLP/2=1.02mm are shown in Figure 6-33. It shows that the fatigue behaviour is linear, there is adaptation of the material after the first load. The same behaviour is observed for all TLP dimensions. If there is adaptation of the material, it means that it is loaded in its elastic regime thus, fatigue failure will not occur during the specified life of the machine.

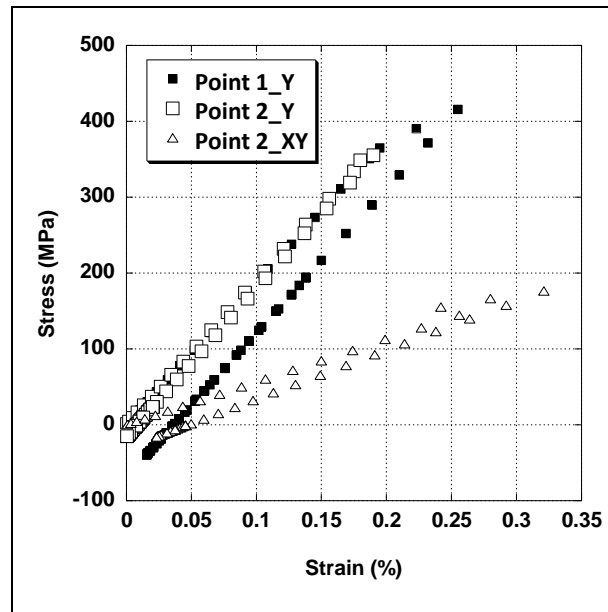


Figure 6-33: Hysteresis curves for TLP/2=1.02 mm

Moreover the elongation at vertex A, B and C are considered for the first cycle and the stabilised cycle (Figure 6-34 (a) and (b) respectively). It can be seen that elongation for the first cycle does not depend on the TLP dimensions regarding the stabilised cycle, elongation at vertex A and B follow the same trend. Moreover, all elongations at the first and stabilised cycles are both much smaller than the airgap, all these TLP dimensions can thus be used for the rotor.

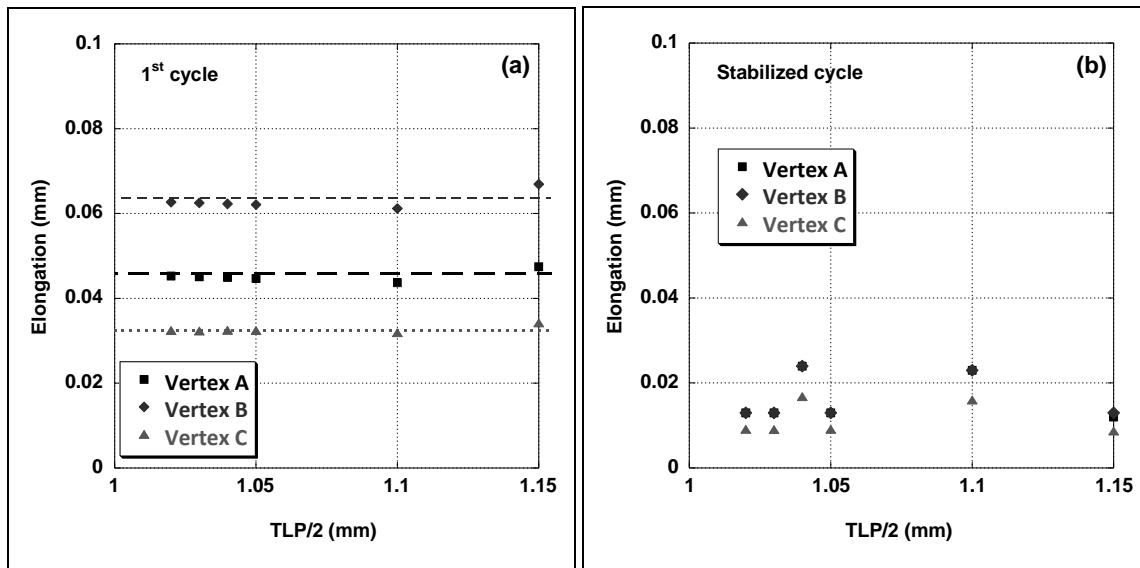


Figure 6-34: Evolution of the maximum elongation with TLP refinement for (a) the first cycle and (b) stabilised cycle

Under cyclic loadings, for the tested rotor dimensions, the material exhibits a linear behaviour which is the sign of adaption phenomena. It appears that it is the elongation due to the overspeed test that is limiting for geometry optimisation. Thus, the smallest TLP at which elongation is acceptable during

the overspeed test and for which adaptation phenomena occurs during the cyclic test can be chosen, it corresponds to $TLP/2=1.02$ mm.

The stress and strain distributions in the rotor with the $TLP/2=1.02$ mm are shown in Figure 6-35. It shows that normal stress and strain (σ_y and ϵ_y respectively) are localised in the zone of the leakage path which width has been reduced. Shear strain (ϵ_{xy}) localises near the hole, however, it does not reach damaging values and there is adaptation phenomenon of the material.

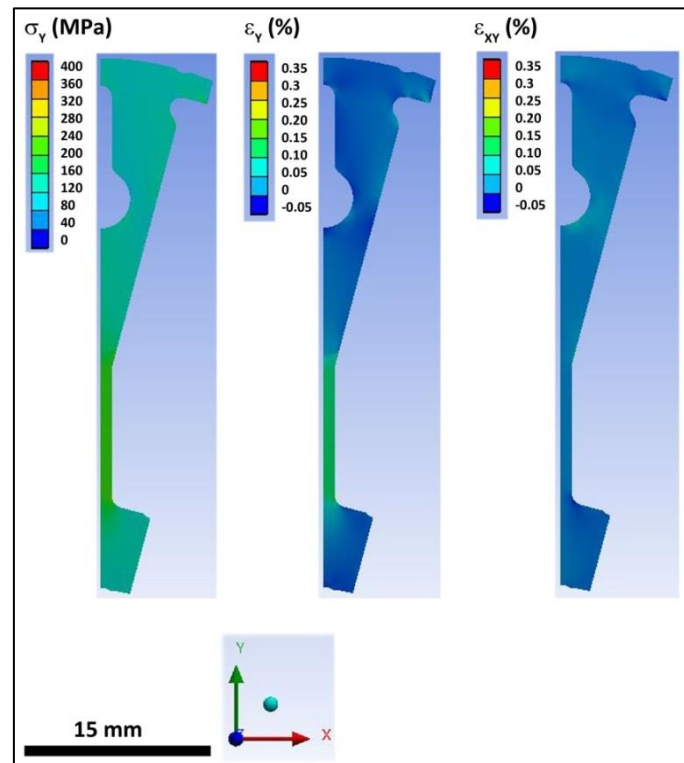


Figure 6-35: Normal stress σ_y , normal strain ϵ_y and shear strain ϵ_{xy} distributions in the rotor with $TLP/2=1.02$ mm during the cyclic test and stabilised at 20000 RPM

6.4.3 Conclusion

This study enables the reduction of the length of TLP by 11% ($TLP/2=1.02$ mm), the same methodology was applied to TT refinement (Annex 3) which enables the reduction of TT by 19% ($TT=1.473$ mm). while staying reliable from the mechanical point of view.

In order to evaluate the benefit of these geometry modifications, electro-magnetic FEA were performed with JMAG – Designer v.13, a simulation software used for electric device design which enables electromagnetic analysis, on the initial and the modified machines, calculations were made internally.

A current of 250A at 25°C and a rotational speed of 1000rpm were imposed on the machine, made of the rotor, the stator and ferritic magnets.

The obtained torque value is considered to compare the machine with the initial rotor design and the final rotor design. Indeed, as mechanical power is equal to electromagnetic power (equation (6-15)), it is possible to measure the torque value (equation (6-16)) at different currents

$$\tau \times \omega = U \times I \quad (6-15)$$

$$U = \frac{d\phi}{dt} = p \times \omega \times \Phi \Rightarrow \tau = p \times \Phi \times I \quad (6-16)$$

with τ the torque value (Nm), ω the angular velocity (rad.s^{-1}), U the voltage (V), I the current (A), p the number of pole pairs and ϕ the rotor flux (V.s^{-1}).

Figure 6-36 shows the evolution of the torque value with the current I for the initial and final rotor. The gain in torque value obtained by the rotor design modification is shown on the right ordinate axis. The torque value of the final rotor design is higher than the one of the initial design. Up to 250A, the torque gain is of 2%, then the torque gain increases in a non linear way.

At the **operating current** which is **250A**, the modification of the rotor design leads in an **increase of the torque value of 2.7%**.

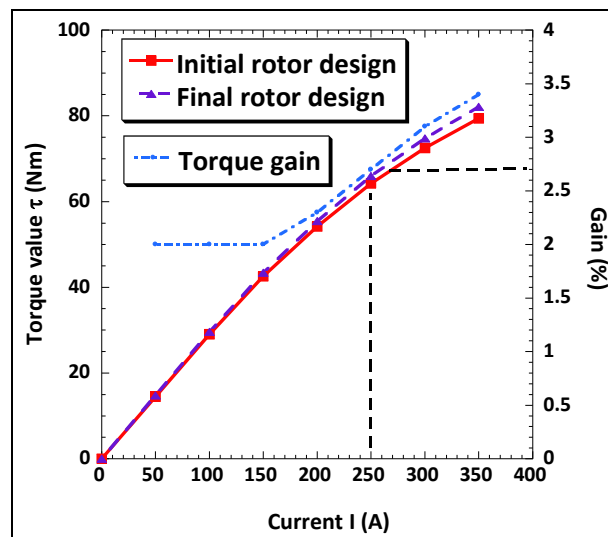


Figure 6-36: Torque vs Current for the starter-alternator with the initial and final rotor designs and the benefit in torque

The same methodology of rotor design modification was applied on a rotor working with rare earth magnets. The geometry was modified in order to decrease the magnet mass while keeping the same torque value. Between the initial and the final rotor, the magnet mass was reduced by nearly 8% which means lighter machines but more specially economic advantage as rare-earth magnet price is variable and expensive.

6.5 Conclusion

In the present chapter, the purpose was to **modify the rotor geometry** of the starter-alternator while staying reliable on the mechanical point of view. Therefore, **hardening model** has to be taken into account.

Isotropic, kinematic and Chaboche hardening models were presented. Comparison between experimental and modelled hysteresis loop enabled the choice of the model that corresponds best to the Fe-3Si steel behaviour. In the present case, **the Chaboche model is the most adapted for the estimation of plastic strain and thus for the estimation of fatigue lives**. Thus the Chaboche model is used for the FEA on the rotor.

Regarding the rotor, two zones were refined, the thickness of leakage path (TLP) was reduced by 11% and the tip thickness (TT) by 19%. **Under cyclic load, there is the adaptation phenomenon. The limiting parameter** for the refinement of these zones was thus the **elongation during the overspeed test** which must be less than the airgap to prevent friction between the rotor and the stator. Finally, the **modification of the rotor geometry increases the torque value by 2.7%** at 250A.

In addition to this work, **crystal plasticity simulation** appears as an interesting perspective. Indeed, such simulations are based on polycrystalline mechanics works with anisotropic constitutive laws of the elastic-plastic deformation of crystals and their interactions [ROT10][CHO15]. Thus, it would enable microstructure-based mechanical predictions which would be complementary to the microstructure based damage mechanisms studied in the previous chapters.

Conclusion

Conclusions and perspectives

Conclusions

This study was conducted in the frame of CO₂ emissions reduction in light weight vehicles with a goal of 95 grams of CO₂ per kilometre for 2020 imposed by the European parliament [CE09]. Therefore, Valeo innovates and produces more efficient electrical machine such as starter-alternator. In the present work, the focus is made on the rotor of these new electrical machines. Indeed, the rotor undergoes cyclic loads which induce fatigue phenomena which needed to be studied to improve the machine performances.

The rotor is made of a stack of thin iron-silicon steel sheets which were studied according to three different axes. The first concerns the understanding of low-cycle fatigue mechanisms of the iron-silicon steel by mean of mechanical testing and microstructural analysis. The second axis of the study is dedicated to the localisation and quantitative evaluation of the strain within the material by EBSD technique. Finally, the third axis concern the numerical modelling by finite element analysis of the cyclic damage of the rotor in order to modify its geometry and thus improve the machine performances.

The low-cycle study showed that the material exhibit different strain accommodation phenomena according to the total strain variation:

- For low strain amplitudes, dislocation slip is planar and homogeneous within grains and crack initiation is transgranular. The material is loaded in the low temperature regime according to the Seeger theory. Indeed, effective stress is superior to internal stress and enables strain accommodation.
- For high strain amplitudes, dislocation structures are inhomogeneous with dislocation walls near grain boundaries and dislocation veins and channels in the grain interior, crack initiation is intergranular. Internal stress is superior to effective stress and enables strain accommodation which means that the material is loaded in the high temperature regime according to the Seeger theory.

This transition from the low temperature regime to the high temperature regime is attributed to the presence of short range order in the as-received material. This short range order hinders dislocation mobility, then, when a certain amount of plastic deformation and cumulated deformation is reached, this order is removed which ease dislocations mobility. The role of grain boundaries is also important in the strain accommodation phenomena. Indeed, each grain accommodates the strain in an

individual way which induces intergranular stress and promotes strain localisation at grain boundaries.

The misorientation based analysis performed by EBSD revealed also this transition from low strain variation to high strain variation.

At low strain level, the strain accommodation is uniform within the grains, therefore no misorientation is revealed by EBSD. Above $\Delta\varepsilon_t=0.7\%$, misorientation gradient appears in the grains due to inhomogeneous strain distribution. The misorientation between veins and channels structure and walls dislocation structure is superior to 0.5° which is detected by the EBSD technique. Thus, misorientation based criteria could be established only for total strain variation superior to $\Delta\varepsilon_t=0.7\%$. Nevertheless, a link between strain variation, misorientation based criteria and dislocation structure was established and used for strain analysis of a notch sample.

For the lowest strain level, the study of dislocation density evolution was initiated by ECCI images analyses by the Ham intercept method. It gave valuable results regarding dislocation density but it showed that it has to be correlated with the image of the dislocation structure. A value of dislocation density on its own cannot be a damage criterion.

Finally, to meet the expectations of Valeo who is financially supporting this work, the LCF study enabled the extension of the mechanical material database. Indeed, the parameters of the mechanical material behaviour law of Chaboche were determined from the LCF study. After, validation of the model on samples, it was used to perform finite element analysis of the rotor damage under cyclic loadings. Then, the rotor geometry was optimised in order to improve the performances of the machine; here the torque value is increased by 3% after light modifications of the rotor geometry.

The mechanical based behaviour law established for the finite element analysis will be further validated by the realisation of a rotor mock-up and testing in real loading conditions in the next months.

Perspectives

The continuation of this work concerns the validation of the assumption that short range order is present in the as-received steel and is destroyed by cyclic plastic strain. This is possible by performing an extensive study of the evolution of short range order by Mössbauer spectroscopy. Indeed, this technique has proven its ability to link ordering phenomena to thermomechanical processing of electrical steel [RUI05]. However, the know-how of this technique requires knowledge and experiences that are becoming rare in Europe.

Also, it would be interesting to perform a statistic study on the link between dislocation structure and grain orientation. This can be performed now in the laboratory since it has just acquired a JEOL 7800F microscope equipped with an EBSD system. As there are few grains present in the sheet thickness, it would be interesting to obtain a correlation between grain orientation obtained by EBSD and dislocation structure observed by cECCI.

Moreover, these microstructural based analyses could be used in the simulations by performing crystal plasticity simulations [ROT10][CHO15]. One could then imagine that precise prediction of crack initiation localisation can be obtained from an EBSD map of the grain orientation on the virgin component.

In addition, it would be interesting for Valeo to take into account, in their electromagnetic modelling, the degradation of magnetic properties due to local plastic strain induced by cyclic loadings or also by the sheet forming process. Indeed, these aspects were not the first priority but it has already been shown by Hug [HUG93] that when plastic straining induced by the punching of the stator is taken into account in electromagnetic finite element analysis, it improves the predictions of magnetic characteristics. Moreover, a recent study conducted by Dehmani *et al.*, showed that punching process leads to a decrease of the fatigue life of Fe-3Si in the high-cycle fatigue regime [DEH15]. This aspect should not be neglected in case the rotors are processed by stamping.

References

References

- [ABB02] Abbadi M, Hähner P, Zegloul A., On the characteristics of Portevin–Le Chatelier bands in aluminum alloy 5182 under stress-controlled and strain-controlled tensile testing. *Mat Sci Eng A-Struct* 337 (2002) 194-201
- [ABE79] Abel A, Wilhelm M, Gerold V, Low-Cycle Fatigue of Single Crystals of α Cu-Al Alloys. *Mat Sci Eng* 37 (1979) 187-200
- [AGA08] Agarwal R., An Overview of the Finite Element Analysis, Introduction to FEA, Lecture Note (2008) ME273, San Jose State University
- [AHM01] Ahmed J, Wilkinson A, Roberts S, Electron Channelling contrast imaging characterization of dislocation structures associated with extrusion and intrusion systems and fatigue cracks in copper single crystals. *Philos Mag A* 81 (2001) 1473-1488
- [AHM06] Ahmed J, Roberts S, Wilkinson A, Characterizing dislocation structure evolution during cyclic deformation using electron 181etal181ling contrast imaging. *Phil Mag* 86 (2006) 4965-4981
- [AHM97] Ahmed J, Wilkinson A, Roberts S, Characterizing dislocation structures in bulk fatigued copper single crystals using electron 181etal181ling contrast imaging (ECCI). *Phil Mag Lett* 76 (1997) 237-246
- [AHM99] Ahmed J, Wilkinson A, Roberts S, Study of dislocation structures near fatigue cracks using electron Channelling contrast imaging technique (ECCI). *J Microsc* 195 (1999) 197-203
- [ALA15] Alarab F, Etude de l'influence de chargements mécaniques cycliques sur les propriétés magnétiques de l'acier Fe3Si. Master thesis (2015)
- [ANG79] Anglada M, Guiu F, Fifth International Conference on the Strength of metals and alloys. Aachen (1979) 1237-1242
- [ANS13] S. Coste, R. Lejay, G. Messenger, Qualité de la simulation mécanique : bonnes pratiques et pièges à éviter ?, Workshop, Ansys, Inc. (2013)
- [ARA84] Arato P, Boc I, Grof T, Effect of composition on the loss of non-oriented medium silicon electric steels. *J Magn Magn Mater* 41 (1984) 53-55
- [BAT99] Bathias C, There is no infinite fatigue life in metallic materials, *Fatigue Fract Engng Mater Struct* 22 (1999) 559-565
- [BAU07] Baudin T, Etter A, Penelle R, Annealing twin formation and recrystallization study of cold-drawn copper wires from EBSD measurements, *Mater Charac* 58 (2007) 947-952
- [BAV92] Bavay JC, Verdun J, Les aciers électriques pour transformateurs et machines tournantes. Situation actuelle et perspectives, *J Phys IV*, 2 (1992) 37-46
- [BER06] Berfield T A, Patel J K, Shimmin R G, Braun P V, Lambros J, Sottos N R, Fluorescent image correlation for nanoscale deformation measurements. *Small* 2 (2006) 631-635
- [BER09] Bernd-Arno B, Hans C, Pavel P, Effect of temperature and strain rate on friction factor during microforming of AW-6082AL-alloy. *Int J Mater Form* 2 (2009) 613–616
- [BOD16] Bode B, Brueckner-Foit A, Zeismann F, Quasi-static and cyclic failure behaviour of electric sheet material, *Int J Fat* 82 (2016) 350-360
- [BOU15] Bouquerel J, Diawara B, Dubar M, Dubois A, Vogt JB, Najjar D, Investigations of the microstructural response to a cold forging process of the 6082-T6 alloy, *Mater Design* 68 (2015) 245-258
- [BRI10] Britton BT, Biroasca S, Preuss M, Wilkinson AJ, Electron backscatter diffraction study of dislocation content of a macrozone in hot-rolled Ti-6Al-4V alloy. *Scripta Mater* 62 (2010) 629-642.

- [BRI80] Brissonneau P, Non-oriented Si-Fe sheets, *JMMM* 19 (1980) 52-59
- [BUC97] Buchanan P, Randle V, Flewitt P, A simple procedure for the assessment of plastic strain in electron back-scatter diffraction patterns, *Scripta Mater* 37 (1997) 1511-1518
- [BUL10] Bultel H, Vogt JB, Influence of heat treatment on fatigue behaviour of 4130 AISI steel, *Proc Eng* 2 (2010) 917-924
- [BUQ01] Buque C, Bretschneider J, Schwab A, Holste C, Dislocation structures in cyclically deformed nickel polycrystals, *Mat Sci Eng A* 300 (2001) 254-262
- [CAL07] Callister W.D., *Materials Science and Engineering: an Introduction – 7th ed.*, (2007) John Wiley & Sons, Inc.
- [CAM04a] De Campos MF, Langrad F, Takanohashi R, Chagas F, Falleiros I, Fronzaglia G, Kahn H, Effect of the Hot Band Grain Size and Intermediate Annealing on the Deformation and Recrystallization Textures in Low Silicon Electrical Steels, *ISIJ Int* 44 (2004) 591-597
- [CAM04b] De Campos MF, Landgrad M, Falleiros I, Fronzaglia G, Kahn H, Texture evolution during the processing of electrical steels with 0.5% Si and 1.25% Si, *ISIJ Int* 44 (2004) 1733-1737
- [CE09] Règlement (CE) n° 443/2009 du Parlement européen et du Conseil du 23 avril 2009 établissant des normes de performance en matière d'émissions pour les voitures particulières neuves dans le cadre de l'approche intégrée de la Communauté visant à réduire les émissions de CO₂ des véhicules légers *Journal Officiel L 140* du 5 juin 2009, p. 1–15.
- [CHA05a] Chakravarthula S, Qiao Y, Fatigue crack growth in a coarse-grained iron-silicon alloy, *International Journal of Fatigue* 27 (2005) 1210-1214
- [CHA05b] Chang S, Wang CS, Xiong CY, Fang J, Nanoscale in-plane displacement evaluation by AFM scanning and digital image correlation processing. *Nanotechnology* 16 (2005) 344-349
- [CHA08] Chaboche JL, A review of some plasticity and viscoplasticity constitutive theories, *Int J Plasticity* 24 (2008) 1642–1693
- [CHA82] Chaboche JL, Lifetime predictions and cumulative predictions and cumulative damage under high temperature conditions. *Low-Cycle fatigue and life prediction*, ASTM STP 770, C. Amzalla, B.N. Leis and P. Rabbe, Eds., American Society for Testing and Materials (1982) 81-104
- [CHE12] Chen Y, Hjelen J, Gireesh S, Roven H, Optimization of EBSD parameters for ultra-fast characterization, *J Microscopy* 245 (2012) 111-118
- [CHO74] Chopra OK, Gowda CVB, Substructural development during strain cycling of alpha-iron. *Phil Mag A* (1974) 583-591
- [CHO15] Chow W., Solas D., Puel G., Baudin T., Aubin V., Development of an in situ method for measuring elastic and total strain fields at the grain scale with an estimation of accuracy, *J Mater Sci* (2015) 1-17
- [CHU85] Chu TC, Ranson WF, Sutton MA, Peters WH, Applications of Digital-Image-Correlation Techniques to experimental mechanics. *Experimental Mechanics* (1985) 232-244
- [COA69] Coates DG, Kikuchi-like reflection patterns obtained with the scanning electron microscope. *Philos Mag* 16 (1967) 1179-1184
- [COT49] Cottrell AH, Bilby BA, Dislocation theory of yielding and strain ageing of iron. *Proc. Phys Soc A* 62 (1949) 49-62
- [CUN08] Da Cunha M, Da Costa Paolinelli S, Low core of magnetism and magnetic materials, *J Magn Magn Mater* 320 (2008) 2485-2489
- [DAL11] Dalei K, Karlsson B, Svensson LE, Stability of shot peening induced residual stresses and their influence on fatigue lifetime, *Mat Sci Eng A* 528 (2011) 1008-1015

- [DEH15] Dehmani H, Brugger C, Pallin-Luc T, Mareau C, Koechlin S, Experimental study of the impact of punching operations on the high cycle fatigue strength of Fe-Si thin sheets, *Int J Fat* (2015) *In press, corrected proof*
- [DIC84] Dickson JI, Bouton J, Handfield L, A comparison of two simple methods for measuring cyclic internal and effective stresses. *Mat. Sci. Eng* 64 (1984) L7-L11
- [DLU13] Dluhos J, Sedlacek L, Man J, Application of electron 183etal183ling contrast imaging in study of polycrystalline materials and visualization of crystal lattice defects, *Conference Metal* (2012)
- [ELL97] Ellyn F, *Fatigue damage, crack growth and life prediction*, Springer Netherlands (1997) 470
- [FUR02] Furuya Y, Matsuoka S., Abe T, Yamagushi K, Gigacycle fatigue properties for high-strength low-alloy steel at 100Hz, 600Hz and 20 kHz, *Scripta Materialia* 46 (2002) 157-162
- [GER89] Gerold V, Karnthaler HP, On the origin of planar slip in FCC alloys, *Acta* 183etal. 37 (1989) 2177-2183
- [GER97] Gerland M, Alain R, Ait Saadi B, Mendez J, Low cycle fatigue behaviour in vacuum of a 316L-type austenitic stainless steel between 20 and 600°C – Part II: dislocation structure evolution and correlation with cyclic behaviour. *Mat. Sci. & Eng. A* 229 (1997) 68-86
- [GIL62] Gilman J, Johnston W, Dislocations in lithium fluoride crystals, *Solid State Physics* (1962)
- [GOD05] Godfrey A, Cao WQ, Liu Q, Hansen N, Stored energy, microstructure, and flow stress of deformed metals. *Metall Mater Trans A* 36 (2005) 2371-2378
- [GON13] Gonzalez F, Houbaert Y, A review of ordering phenomena in iron-silicon alloys. *Revista de Metalurgia* 49 (2013) 178-199
- [GRI66] Griffiths D, Riley J, Dislocation arrangements in deformed polycrystalline 3% silicon-iron, *Acta Metall* 14 (1966) 755-773
- [GRO00] Groma I, Szekely F Analysis of the asymptotic properties of X-ray line broadening caused by dislocations, *J. Appl Crystallogr* 33 (2000) 1329-1334
- [GRO13] Asymmetric X-ray line broadening caused by dislocation polarization induced by external load, *Scripta Materialia* 68 (2013) 755-758
- [GRO98] Groma I, X-ray line broadening due to an inhomogeneous dislocation distribution, *Phys Rev B* 57 (1998) 7535-7542
- [GUT09] Gutierrez-Urrutia I, Zaefferer S, Raabe D, Electron channeling contrast imaging of twins in dislocations in twinning-induced plasticity steels under controlled diffraction conditions in a scanning electron microscope, *Scripta Mater* 61 (2009) 737-740
- [GUT12] Gutierrez-Urrutia I, Raabe D, Dislocation density measurement by electron channeling contrast imaging in a scanning electron microscope, *Scripta Mater* 66 (2012) 343-346
- [HAH62] Hahn GT, A model for yielding with special reference to the yield-point phenomena of iron and related BCC metals, *Acta Metall* 10 (1962) 727-738
- [HAL12] Halama R., Sedlak J., Sofer M., Phenomenological Modelling of cyclic plasticity, Chapter 15 of *Numerical Modelling* edited by P. Miidla (2012) 329-357
- [HAM61] Ham RK, The determination of dislocation densities in thin films, *Phil Mag* 6 (1961) 1183-1184
- [HEI01] Heino S. & Karlsson B., Cyclic deformation and fatigue behaviour of 7Mo-0.5 N superaustenitic stainless steel–stress-strain relations and fatigue life. *Acta Mater* 49 (2001) 339–351
- [HER97] Hertzberg R. W., *Deformation and Fracture Mechanics of Engineering materials*. Fourth Edition, John Wiley & Sons, INC (1997)

- [HO88] Ho-Le K., Finite element mesh generation methods: a review and classification, *Computer-aided design* 20 (1988) 27-38
- [HOE13] Van Hoecke D, Weber B, Jacobs S, Attrazic E, Bergamo S, Montaudon R, Fatigue characterization of electrical steels for designing high efficiency electrical machines for automotive traction, *JP SF2M* (2013) 18-27
- [HUB98] Hubert O, Influence des contraintes internes et de la structure des dislocations sur les couplages magnétomécaniques dans les alliages Fe-3%Si à grains non orientés, PhD thesis (1998) Compiègne, France
- [HUG93] Hug E, Etude des dégradations des propriétés magnétiques d'alliages Fe-3%Si avec les déformations plastiques. Application à la mise en œuvre de tôles utilisées dans la conception des moteurs électriques, PhD thesis (1993), Compiègne, France
- [HUM01] Humphreys F, Review Grain and subgrain characterization by electron backscatter diffraction, *J Mat Sci* 36 (2001) 3833-3854
- [IOR03] Iordache V, Suivi de l'état de contraintes appliquées et internes des alliages ferromagnétiques doux par mesure de leur propriétés magnétiques, PhD thesis (2003) Compiègne, France
- [IOR04] Iordache VE, Hug E, Effect of mechanical strains on the magnetic properties of electrical steels. *J Opt Adv Mater* 6 (2004) 1297-1303
- [ISO03] Norme ISO 12106:2003, Metallic materials – Fatigue testing – Axial-strain-controlled method
- [JED13] Jedrychowski M, Tarasiuk J, Bacroix B, Wronski S, Electron backscatter diffraction investigation of local misorientations and orientation gradients in connection with evolution of grain boundary structures in deformed and annealed zirconium. A new approach in grain boundary analysis. *J Appl Crystallogr* 46 (2013) 483-492
- [JUI11] Juijerm P, Altenberger I, Cyclic deformation behaviour and its optimization at elevated temperature, *Aluminium Alloys, Theory and applications* (2011) 183-198
- [KAM05] Kamaya M, Wilkinson A, Titchmarsh J, Measurement of plastic strain of polycrystalline material by electron backscatter diffraction 235 (2005) 713-725
- [KAM09] Kamaya M, Characterization of microstructural damage due to low-cycle fatigue by EBSD observation, *Mater Charact* 60 (2009) 1454-1462
- [KAM11] Kamaya M, Kuroda M, Fatigue damage evaluation using electron backscatter diffraction, *Mater Trans* 52 (2011) 1168-1176
- [KAN05a] Kaneko Y, Fukui K, Hashimoto S, Electron channeling contrast imaging of dislocation structures in fatigued austenitic stainless steels, *Mat Sci Eng A* 400-401 (2005) 413-417
- [KAN05b] Kang J, Jain M, Wilkinson DS, Embury JD, Microscopic strain mapping using scanning electron microscopy topography image correlation at large strain. *J. Strain Anal Eng* 40 (2005) 559-570
- [KAR12] Karuskevich M, Karuskevich O, Maslak T, Schepak S, Extrusion/intrusion structures as quantitative indicators of accumulated fatigue damage, *Int J Fatigue* 39 (2012) 116-121
- [KIR12] Kircheim R, Solid solution softening and hardening by mobile solute atoms with special focus on hydrogen, *Scripta Mater* 67 (2012) 767-770
- [LAG06] Lagattu F, Bridier F, Villechaise P, Brillaud J, In-plane strain measurements on a microscopic scale by coupling digital image correlation and an in situ SEM technique. *Mater Charact* (2006) 10-18
- [LAK74] Lakso G, Marcinkowski, Plastic deformation in Fe-Si alloys, *Metal Trans* 5 (1974) 839-845
- [LEA11] Leaux F, Relation entre microstructure et fatigue d'un acier ferritique utilisé dans l'industrie automobile : élaboration d'indicateurs d'endommagement, PhD thesis (2012) Lille, France

- [LEG11] Legranger J, Matt JC, Bouarroudj L, Palleschi F, Rotor de machine électrique tournante et machine électrique tournante comprenant un tel rotor, demande de brevet d'invention, FR 2 982 093 – A1, 2011
- [LEH00] Lehockey E, Lin YP, Lepik O, Mapping residual plastic strain in materials using electron backscatter diffraction, *Electron Backscatter Diffraction in Material Science*, Kluwer Academic/Plenum Publishers (2000) 247-264
- [LEM09] Lemaitre J, Chaboche JL, Benallal A, Desmorat R, *Mécanique des matériaux solides*. 3^{ème} ed. Dunod, Paris (2009)
- [LIT71] Littman MF, Iron and iron silicon alloys, *IEEE transactions on magnetics*, 7 (1971) 48-60
- [LOW59] Low J, Guard R, The dislocation structure of slip bands in iron, *Acta Metal* 7 (1959) 171-179
- [LOW62] Low J, Turkalo A, Slip band structure and dislocation multiplication in silicon-iron crystals, *Acta Metal* 10 (1962) 215-227
- [MAG79] Magnin T, Driver H, The influence of strain rate on the low cycle fatigue properties of single crystals and polycrystals of two ferritic alloys, *Mat Sci Eng* 39 (1979) 175-185
- [MAG82] Magnin T, Driver JH, Low cycle fatigue damage mechanisms in body-centered cubic materials, *Low cycle Fatigue and life prediction*, ASTM STP 770 (1982) 212-226
- [MAI06] Maitland T, Sitzman S, Electron backscatter diffraction (EBSD) technique and materials characterization examples, *Scanning Microscopy for Nanotechnology – Techniques and Applications*, Zhou W. & Wang Z. eds, Springer (2006) 41-76
- [MAN03] Man J, Obrtlík K, Polak J, Study of surface relief evolution in fatigued 316L austenitic stainless steel by AFM, *Mat Sci Eng A* 351 (2003) 123-132
- [MAT84] Matsumura K, Fukuda B, Recent developments of non-oriented electrical steel sheets, *IEEE transactions on magnetic*, 20 (1984) 1533-1538
- [MAY16] Mayer H, Recent developments in ultrasonic fatigue, *Fatigue Fract Engng Mater Struct* 39 (2016) 3-29
- [MEI92] Meininger JM, Gibeling JC, Low cycle fatigue of niobium and niobium-1 Pct Zirconium alloys, *Metal Trans A* 23 (1992) 3077-3084
- [MIL13] Milella PP, *Fatigue and corrosion in metals*, Springer Eds. (2013) 73-108
- [MOR79] Mori H, Tokuwame M, Miyazaki T, Cyclic deformation of silicon-iron single crystals oriented for single glide, *Phil Mag A* 40 (1979) 409-433
- [MOS90] Moses AJ, Electrical steels: past, present and future developments, *IEE Proceedings A*, 137 (1990) 233-243
- [MUG76] Mughrabi H, Herz K, Stark X, The effect of strain-rate on the cyclic deformation properties of α -iron single crystals, *Acta Metal* 24 (1976) 659-668
- [MUG78] Mughrabi H, The cyclic hardening and saturation behaviour of copper single crystals, *Mat Sci Eng* 33 (1978) 207-233
- [MUG81] Mughrabi H, Herz K, Stark X, Cyclic deformation and fatigue behaviour of α -iron mono- and polycrystals, *Int J Fracture* 17 (1981) 193-220
- [MUG83] Mughrabi H, Dislocation wall and cell structures and long-range stresses in deformed metal crystals. *Acta metal.* 31 (1983) 1367-1379
- [NEL15] Nellessen J, Sandlöbes S, Raabe D, Effects of strain amplitude, cycle number and orientation on low cycle fatigue microstructures in austenitic stainless steel studied by electron channelling contrast imaging, *Acta Mater* 87 (2015) 86-99
- [PAN09] Pan B, Qian K, Xie H, Asundi A, Two-dimensional digital image correlation for in-plane displacement and strain measurement: a review. *Measurement Science and Technology* 20 (2009) 1-17
- [PET07] Petrov R, Kestens L, Wasilkowska A, Houbaert Y, Microstructure and texture of a

- lightly deformed TRIP-assisted steel channelling by means of the EBSD technique, *Mat Sci Eng A* 447 (2007) 285-297
- [PET10] Petrovic DS, Non-oriented Electrical steel sheets, *MTAEC9*, 44 (2010) 317-325
- [PET82] Peters WH, Ranson WF, Digital imaging techniques in experimental stress analysis. *Optical Engineering* 21 (1982) 427-431
- [PIN12] Pinheiro B., Lesage J., Pasqualino I., Benseddiq N., Bemporad, E.X-ray diffraction study of microstructural changes during fatigue damage initiation in steel pipes, *Mat Sci Eng A* 532 (2012) 136-166
- [POL03] Polak J, Man J, Obrtlík K, AFM evidence of surface relief formation and models of fatigue crack nucleation. *Int J Fatigue* (2003) 1027-1036
- [POL85] Polak J, Lepistö T, Kettunen P, Surface topography and crack initiation in emerging persistent slip bands in copper single crystals. *Mat Sci Eng* 74 (1985) 85-91
- [POL91] Polak J, Cyclic plasticity and low cycle fatigue life of metals, *Materials Science monographs* 63 (1991) Elsevier
- [PRA55] Prager W., The theory of plasticity: A survey of recent achievements. *Proceedings of the institution of Mechanical Engineers* 169 (1955) 41-57
- [ROV91] Roven H, Nes E, Cyclic deformation of ferritic steel – I. stress-strain response and structure evolution, *Acta Metall Mater* 39 (1991) 1719-1733
- [RUI05] Ruiz D, Ros-Yañez T, Vandenberghe RE, Houbaert Y, Influence of ordering phenomena on the thermomechanical processing of high-Si electrical steel studied by Mössbauer spectroscopy. *AIP Proc. Conf on Industrial applications of the Mössbauer effect* 765 (2005) 331-337
- [SAB06] Sabaté N, Vogel D, Gollhardt A, Marcos J, Gracia I, Cané C, Michel B., Digital image correlation of nanoscale deformation fields for local stress measurement in thin films. *Nanotechnology* 17 (2006) 5264-5270
- [SAL08] Salazar D, Etude du partage de la plasticité cyclique d'un acier duplex par microscopie à force atomique, PhD (2008) Lille, France
- [SEE54] Seeger A, The temperature dependence of the critical shear stress and of work-hardening of metal crystals, *Phil Mag* 45 (1954) 771-773
- [SES88] Sestak B, Novak V, Libovický S, Cyclic deformation of single crystals of iron-silicon alloys oriented for single slip, *Phil Mag A* 57 (1988) 353-381
- [SHI04] Shi X, Pang HLJ, Zhang XR, Liu QJ, Ying M, In-situ micro-digital image speckle correlation technique for characterization of materials properties and verification of numerical models. *IEEE Trans Components and Packaging Technologies* 27 (2004) 659-667
- [SHI82] Shimanaka H, Ito Y, Matsumura K, Fukuda B, Recent development of non-oriented electric steel sheets, *JMMM* 26 (1982) 57-64
- [SHI89] Shiozaki M, Kurosaki Y, The effect of grain size on the magnetic properties of nonoriented electrical steel sheets, *J Mater Eng* 11 (1989) 37-43
- [SHI99] Shimojo M, Uchida Y, Turuoka S, Higo Y, Fatigue striation formation in an Fe-3%Si alloy-effects of crystallographic orientation and neighbouring grains, *Fat Fract Eng Mater Struct* 122 (1999) 153-159
- [SIN03] Sinclair C, Robaut F, Maniguet L, Mithieux JD, Schmitt JH, Brechet Y, Recrystallization and texture in a ferritic stainless steel : an EBSD study, *Adv Eng Mat* 5 (2003) 570-574
- [SMA01] Small J, Michael J, Phase identification of individual crystalline particles by electron backscatter diffraction, *J Micro* 201 (2001) 59-69
- [SOM98] Sommer C, Mughrabi H, Lochner D, Influence of temperature and carbon content on the cyclic deformation and fatigue behaviour of α -iron. Part I. Cyclic deformation and stress-behaviour, *Acta Mater* 46 (1998) 1527-1536
- [SUN97] Sun Z, Lyons JS, MnNeill SR, Measuring microscopic deformations with Digital

- Image Correlation. *Optics and Lasers in Engineering* 27 (1997) 409-428
- [SUT07a] Sutton MA, Li N, Joy DC, Reynolds AP, Li X, Scanning electron microscopy for quantitative small and large deformation measurements. Part I: SEM imaging at magnifications from 200 to 10,000. *Experimental Mechanics* (2007) 775-787
- [SUT07b] Sutton MA, Li N, Joy DC, Reynolds AP, Li X, Scanning electron microscopy for quantitative small and large deformation measurements. Part II: Experimental validation for magnifications from 200 to 10,000. *Experimental Mechanics* (2007) 798-804
- [SUT86] Sutton MA, Cheng M, Peters WH, Chao YJ, McNeill SR, Application of an optimized digital correlation method to planar deformation analysis. *Image and vision computing* (1986) 143-150
- [TAN09] Taniguchi T, Kaneko Y, Hashimoto S, ECCI observations of dislocation structures around fatigue cracks in ferritic stainless steel single crystals. *IOP Conf Ser: Mater Sci Eng* 3 (2009) 012020
- [USH09] Ushioda K, Goto S, Komatsu Y, Hoshino A, Takebayashi S, Evolution of dislocation structure and fatigue crack behavior in Fe-Si alloys during cyclic bending test, *ISIJ International* 49 (2009) 312-321
- [VAL04] Valeo. Press Release. L'alternateur développé par Valeo et PSA Peugeot Citroën récompensé par le « Prix des Ingénieurs de l'année 2004 ». Paris, France, 16/12/2004
- [VAL15] Valeo Website, visited the 01/10/2015. <http://www.valeo.com/en/our-activities/powertrain-systems/technologies/systems-stop-start-48.html>
- [VAN12] Vandebossche L, Jacobs S, Van Hoecke D, Weber B, Leunis E, Attrazic E, Improved iron loss modelling approach for advanced electric steels operating at high frequencies and high inductions in automotive machines (2012) IEEE
- [VIA 72] Viale F, Alliage fer-silicium, *Techniques de l'ingénieur D195* (1972) 1-7
- [VOG00] Vogt J-B, Argillier S, Massud J-P, Prunier V, Fatigue damage evaluation of a power plant component from analysis of the dislocation structures, *Eng Fail Ana* 7 (2000) 301-310
- [VOG01] Vogt J-B, Fatigue properties of high nitrogen steels. *Materials Processing Tehcnology* 117 (2001) 364-369
- [VOG13a] Vogt J-B, Bouquerel J, Léaux F, Palleschi F, Fatigue Damage Assessment of Alternator Fans by EBSD. *Procedia Eng* 66 (2013) 608-614
- [VOG13b] Vogt, J-B, Salazar D, Prorior Serre I, Partition of Cyclic Plasticity in the 25Cr-7Ni-0.25N Duplex Stainless Steel Investigated by Atomic Force Microscopy in Duplex Stainless Steels (2013) (eds I. Alvarez-Armas and S. Degallaix-Moreuil), John Wiley & Sons, Inc., Hoboken, NJ, USA.
- [VOG88] Vogt J-B, Degallaix S, Tissier J-C, The nature of fatigue extrusions in a 12 Cr steel. *Journal of materials science letters* 7 (1988) 700-702
- [VOG94] Vogt J-B, Bigeon C, Foct J, Combined effect of nitrogen and silicon on low cycle fatigue of 12%Cr martensitic stainless steels, *Zeit Metallkunde* 85 (1994) 92-99
- [WIL97] Wilkinson AJ, Hirsch PB. Electron diffraction based techniques in scanning electron microscopy of bulk materials. *Micron* 28 (1997) 279-308
- [WRI06] Wright SI, Nowell MM, EBSD image quality mapping, *Microsc. Microanal.* 12 (2006) 72-84
- [WRI07] Wright S, Nowell M, Bingert J, A comparison of textures measured using X-ray and electron backscatter diffraction, *Met Mat Trans A* 38 (2007) 1845-1855
- [WRI11] Wright SI, Nowell MM, Field DP, A review of strain analysis using electron backscatter diffraction., *Microsc Microanal* 17 (2011) 316-29
- [YU84] Yu W, Esaklul K, Gerberich W, Fatigue threshold studies in Fe, Fe-Si and HSLA steel: Part II. Thermally activated behaviour of the effective stress intensity at threshold,

- Met Trans A 15A (1984) 889-900
- [ZAE02] Zaefferer S, Computer-aided crystallographic analysis in TEM. *Advances in Imaging and Electron Physics* 125 (2002) 355-415
- [ZAE14] Zaefferer S, Elhami NN, Theory and application of electron channelling contrast imaging under controlled diffraction conditions. *Acta Mater* 75 (2014) 20-50
- [ZHA06] Zhang D, Luo M, Arola DD, Displacement/strain measurements using an optical microscope and digital image correlation. *Optical Engineering* 45 (2006) 033605-1-9

Annexes

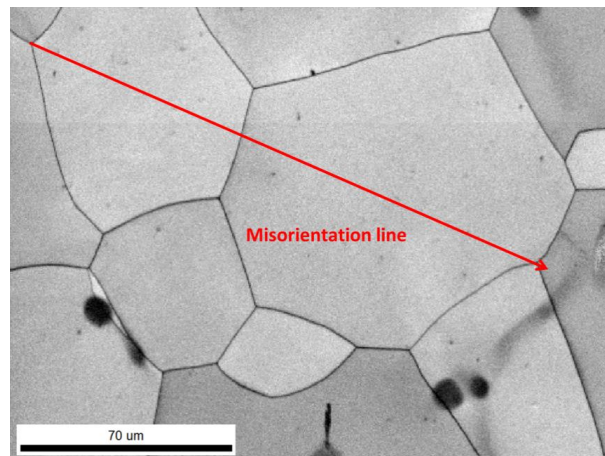
1. EBSD – acquisition step choice
2. Digital Image Correlation (DIC)
3. Rotor Tip Thickness (TT) refinement
4. Summary of fatigue tests

Annexes

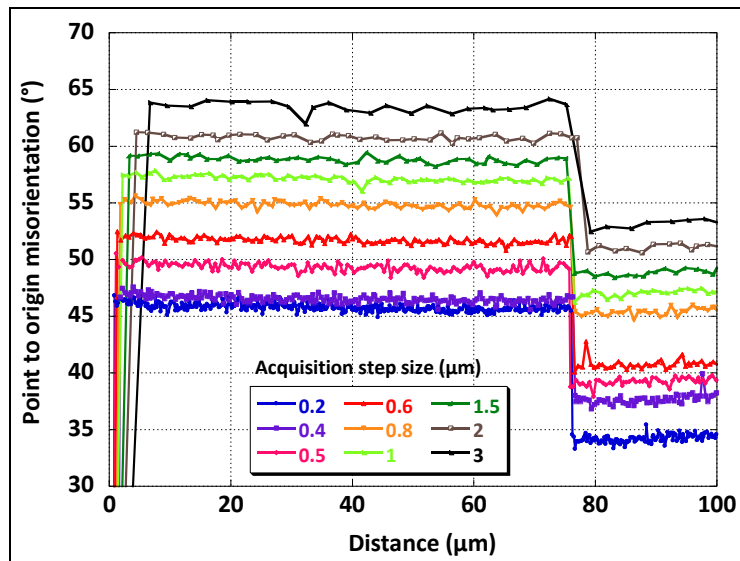
Annex 1: EBSD – acquisition step choice

The quality of the acquisitions is dependent on the acquisition step size. The step size has to be adapted to the material (grain size), the sample state (undeformed, deformed) and the equipment (SEM with tungsten filament or FEG-SEM). A large acquisition step enables fast acquisitions but induces a loss in information for localised misorientations [WRI11]. Therefore, an acquisition step inferior to the grain size is necessary to study deformation within the grain [HUM01]. The measuring error of the crystal orientation exists regardless of the acquisition step size. This induces an error on local misorientation. The misorientation angle is a positive absolute value characterising the misorientation angle between two crystals and if the misorientation is large enough, the influence of the error on the local misorientation becomes negligible. But in the case of small misorientation, the misorientation angle is smaller than the error which induces a local misorientation superior to the average misorientation. Thus, with a small step size, misorientation can be confounded with the background noise [KAM09].

Thus a study was made on a sample loaded at $\Delta\varepsilon_t=1\%$. The acquisition step size varies from $0.2\mu\text{m}$ to $3\mu\text{m}$ and its effect on several criteria is observed. First, misorientation profiles along the line shown in red in Annex 1-1 were compared in Annex 1-2.



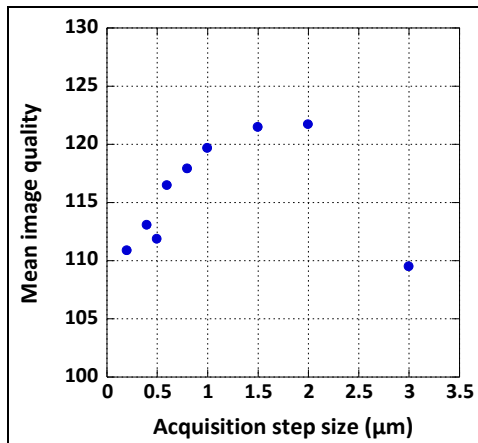
Annex 1-1: Misorientation profile analysis



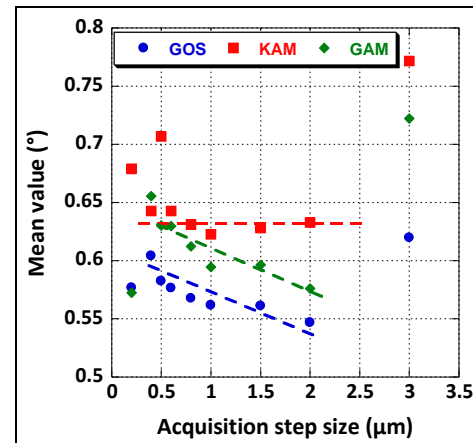
Annex 1-2: Misorientation profile lines for acquisition steps going from 0.2 to 3μm (for better readability 2° is artificially added between each acquisition steps)

It shows that at small acquisition step size (from 0.2 to 0.5μm), the misorientation is confounded with the noise. And at large acquisition step size (2 and 3 μm), the misorientation profile is too smooth and leads to a loss of local misorientation information, moreover, grain boundaries are imprecisely estimated. Thus it seems that a step size comprises between 0.6 and 1.5μm remain the best choice.

The evolution of the image quality was also checked. Annex 1-3 shows that image quality increases linearly from 0.2 to 2μm (except for the point at 0.5μm) and drops at 3μm. It confirms that acquisition step size of 3μm is not adapted for that material. The average GOS, KAM and GAM were evaluated for the same sample area for the different acquisition step size and compared (Annex 1-4). Between 0.4μm and 2μm the mean GOS decreases linearly. The same evolution is observed for the mean GAM. The mean KAM is almost stable from 0.4μm to 2μm (except for 0.5μm). This confirms that acquisition step size of 3μm is too large for local misorientation measurements and 0.2μm too small.



Annex 1-3: Average image quality evolution with acquisition step size



Annex 1-4: Average GOS, KAM and GAM evolutions with acquisition step size

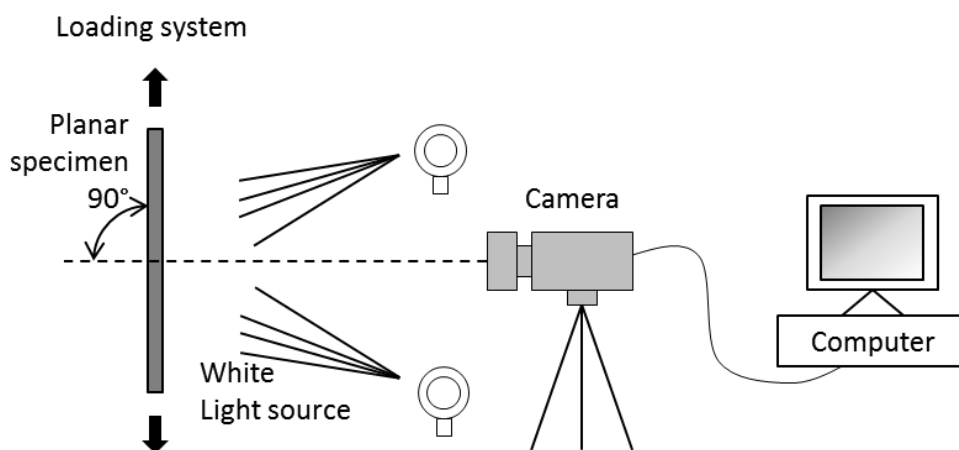
Finally, the larger acquisition step size is considered in order to reduce the acquisition time. It was shown earlier that acquisition step sizes equal and over $2\mu\text{m}$ are too large. If acquisition step size of $1.5\mu\text{m}$ is considered for the KAM, the kernel size considering the second nearest neighbours is $7.5\mu\text{m}$ which is just equal to one tenth of the average grain size of the material. It seems better to consider the $1\mu\text{m}$ step size for the KAM as the kernel size, with 2nd nearest neighbours, is $5\mu\text{m}$ and is $7\mu\text{m}$ with 3rd nearest neighbours which is inferior to one tenth of the average grain size. Thus local misorientation phenomena can be well described by the acquisition step size of $1\mu\text{m}$.

Annex 2: Digital Image Correlation (DIC)

In addition to conventional strain gauge technique, non-contact optical techniques have been developed since the 1980s [PET82][CHU85][SUT86] with the development of digital image processing and numerical computing. The DIC technique is a non-interferometric technique which records the displacement of individual points at the surface of a specimen by the comparison of the grey intensity changes of the surface before and after deformation. The evolution of the displacement field enables the calculation of the total strain. Experimental conditions are less restrictive than for interferometric methods which require coherent light source and a vibration-isolated optical platform to conduct experiment. The deformation is measured in that case by comparison of phase differences of the scattered light wave from the object surface before and after deformation. Also, DIC offers a wide range of measurement sensitivity and resolution related to the diversity of image acquisition devices. Indeed 2D-DIC can be coupled with optical microscopy [SUN97][SHI04][ZHA06], scanning electron microscope [KAN05b][BER06][LAG06][SAB06][SUT07a][SUT07b] and atomic force microscopy [CHA05b] to realise microscale to macroscale measurement. However, 2D-DIC method also suffers from disadvantages. Indeed, the sample surface must exhibit a random grey intensity distribution, the measurement depends heavily on the quality of the imaging system and strain measurement accuracy is lower than interferometric methods.

DIC method consists in the image acquisition of a specimen surface having a grey level distribution before and after deformation. Then, displacement vectors distribution is obtained by image comparison.

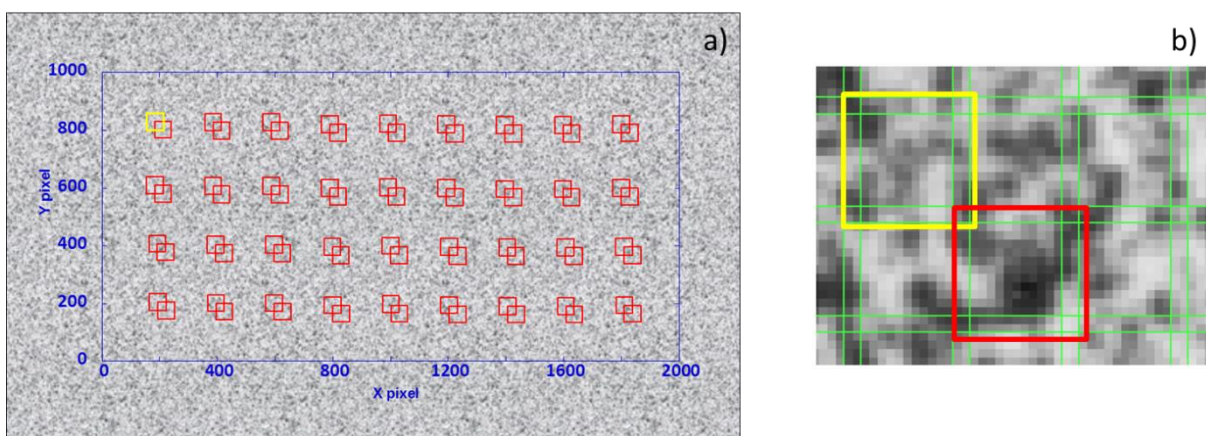
For the sample preparation, a chemical etching is made or a speckle is applied in order to obtain a distribution of the grey level on a plane surface. Then, a camera is placed in order that the optical axis is perpendicular to the sample surface. The experimental setup is shown Annex 2 - 1. Images are acquired before deformation and during or after deformation.



Annex 2 - 1: Typical optical image acquisition system for DIC

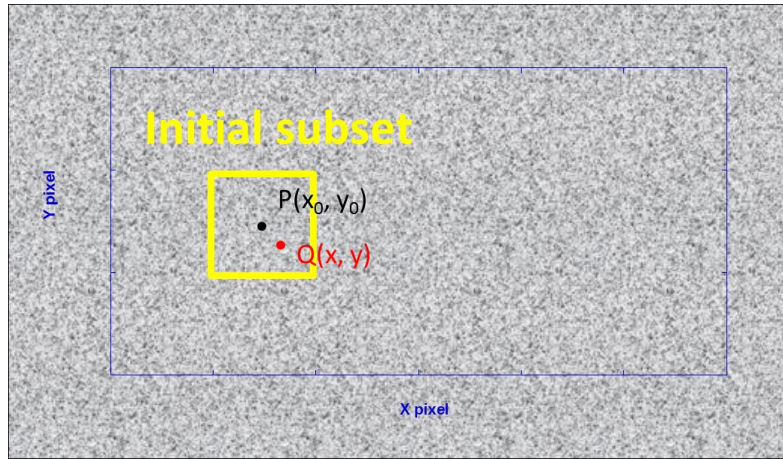
Finally, DIC computes the motion of each point of the image by comparison of the image at different steps in order to obtain strain field.

This method consists in specifying a region of interest (ROI) in the image of reference. This is the calculation area (in blue in Annex 2 - 2 (a)). The size of this zone is dependent on the optical equipment. It is then divided into square subsets of several pixels (in red in Annex 2 - 2 (b)). From each valid subset, a measuring point results after computation. Therefore, the size of the subset and of the subset step is important. Indeed, in the case of large facet, the accuracy of the resulting measuring point is improved but local effects within the facet size cannot be captured. The computation time is also increased. Increasing the facet step decreases the measuring point density and the computation time. Overlapping area of 15-20% is recommended by GOM [GOM13].



Annex 2 - 2: (a) Reference image, region of interest (ROI) in blue, red squares are the subset used to follow the movement and the yellow square is the initial subset (b) example of a 15x15 subset with 2 pixels overlapping [GOM13]

The definition of the initial subset is important as, after deformation, displacement vectors calculation starts from it. It is a square of $(2M+1) \times (2M+1)$ pixels centered at point $P(x_0, y_0)$ (Annex 2 - 3). The light intensity distribution in this subset is defined by the function $f(x_i, y_i)$ with $i, j = -M : M$. $Q(x, y)$ is a neighbouring point of $P(x_0, y_0)$ and corresponds to the point where the light intensity is the highest.



Annex 2 - 3: Initial subset $(2M+1) \times (2M+1)$ pixels of the reference image (undeformed state) with $P(x_0, y_0)$ the center point and $Q(x, y)$ the point with the highest light intensity

After deformation of the specimen, the position of this subset is sought. For that purpose, the comparison of light intensity distributions before and after deformation is made with the use of a correlation criterion. Indeed, the light intensity distribution of the subset in the deformed state is $g(x'_i, y'_i)$, with x'_i and y'_i defined by equations (A2-1) and (A2-2) respectively.

$$x'_i = x_i + \xi(x_i, y_j) \quad (\text{A2-1})$$

$$y'_j = y_j + \eta(x_i, y_j) \quad (\text{A2-2})$$

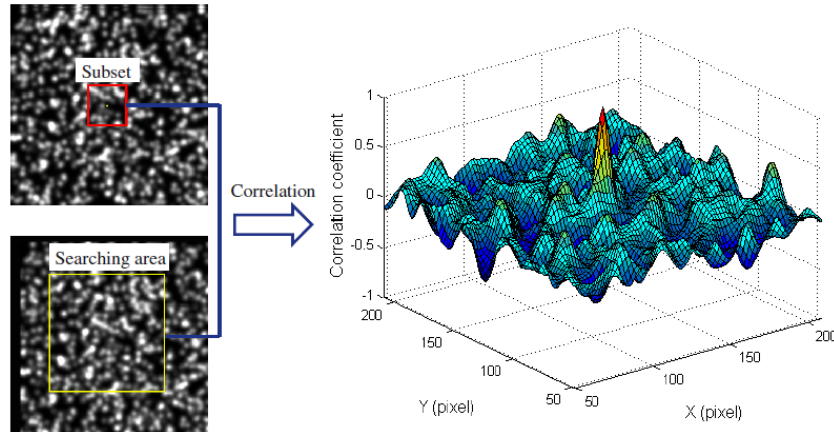
With $\xi(x_i, y_j)$ and $\eta(x_i, y_j)$, shape function or displacement mapping function.

Different correlation criteria can be found in the literature [PAN09], they can be divided into two groups: Cross-Correlation (CC) criteria (equation A2-3) and Sum of Squared Differences (SSD) criteria (equation A2-4).

$$C_{CC} = \sum_{i=-M}^M \sum_{j=-M}^M [f(x_i, y_j)g(x'_i, y'_j)] \quad (\text{A2-3})$$

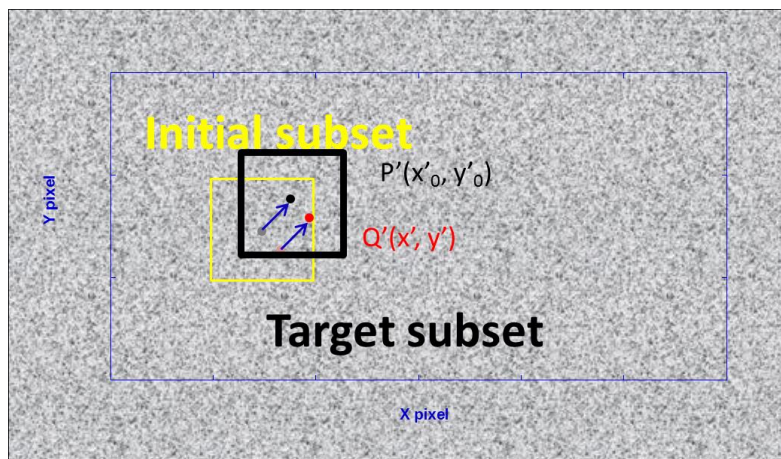
$$C_{SSD} = \sum_{i=-M}^M \sum_{j=-M}^M [f(x_i, y_j) - g(x'_i, y'_j)]^2 \quad (\text{A2-4})$$

The position of the highest intensity point in the undeformed subset $Q(x_i, y_i)$ is sought in the deformed image and corresponds to the point $Q'(x'_i, y'_i)$. The position of $Q'(x'_i, y'_i)$ is given by the peak position of the distribution of the correlation coefficient (Annex 2 - 4).



Annex 2 - 4: Cross-correlation coefficient distribution when the deformed image is subjected to rigid body translation

The difference in the position of the two points gives the displacement vector at point $Q(x_i, y_i)$ which is applied to the subset center $P(x_0, y_0)$ (Annex 2 - 5).



Annex 2 - 5: Target subset in the deformed state with, in blue, the displacement vector

If there is only rigid body translation of the subset (as presented in Annex 2 - 4 and Annex 2 - 5), the displacement of each point in the subset is the same, then a zero order shape function can be used (equations (A2-5) and (A2-6)).

$$\xi_0(x_i, y_j) = u \quad (\text{A2-5})$$

$$\eta_0(x_i, y_j) = v \quad (\text{A2-6})$$

A first-order shape function (equations (A2-7) and (A2-8)) allows translation, rotation, shear, longitudinal strains and their combinations of the subset (as illustrated in Annex 2 - 6).

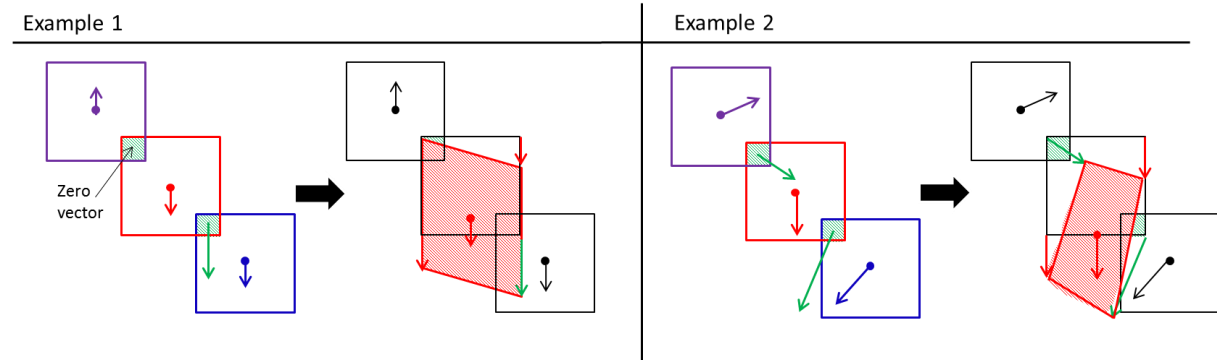
$$\xi_1(x_i, y_j) = u + u_x \Delta x + u_y \Delta y \quad (\text{A2-7})$$

$$\eta_1(x_i, y_j) = v + v_x \Delta x + v_y \Delta y \quad (\text{A2-8})$$

With $\Delta x = x_i - x_0$ and $\Delta y = y_j - y_0$.

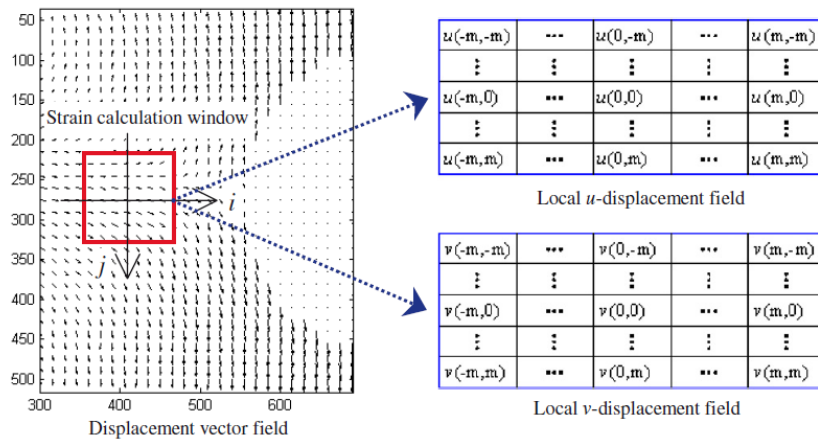
The Annex 2 - 6 highlights the importance of the overlapping areas (in dashed green). Indeed, after deformation displacement vector of each individual subset is calculated (purple, red and blue

arrows). In the overlapping area the displacement vector can be different (green arrows) thus leading to subset shape modification after deformation and complex displacement vectors distribution.



Annex 2 - 6: Illustrations of the red subset shape modification and displacement vector distribution after deformation

Strain estimation can be made by the pointwise least-square fitting technique. To measure the stain at a point, a square window containing $(2m+1) \times (2m+1)$ discrete point must be selected around it (red square in Annex 2 - 7).



Annex 2 - 7: Local strain calculation window containing $(2m+1) \times (2m+1)$ displacement data used for strain estimation

[PAN09]

With a strain calculation window small enough, the displacement distributions in it can be approximated as a linear plane. Thus the equation (A2-9) and (A2-10) can be written.

$$u(x_i, y_j) = a_0 + a_1x + a_2y \tag{A2-9}$$

$$v(x_i, y_j) = b_0 + b_1x + b_2y \tag{A2-10}$$

With $x_i, y_j = -m:m$, the local coordinates within the strain calculation window, $u(x_i, y_j)$ and $v(x_i, y_j)$, are the original displacements at location (x_i, y_j) obtained by DIC and $a_{i=0,1,2}$, $b_{i=0,1,2}$ are the unknown parameters that have to be determined. Equation (A2-9) can be rewritten as a matrix function (equation A2-11). The least square method can be used to solve the unknown polynomial coefficients.

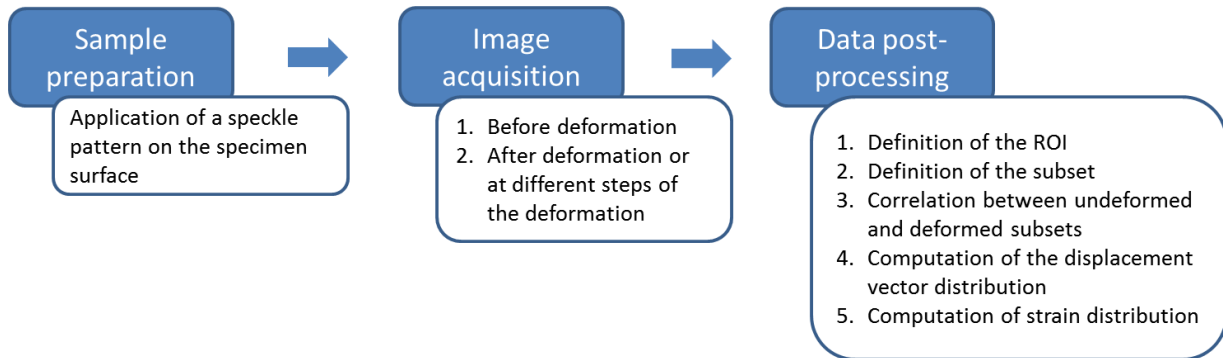
$$\begin{bmatrix} 1 & -m & -m \\ 1 & -m + 1 & -m \\ \cdot & \cdot & \cdot \\ \cdot & \cdot & \cdot \\ 0 & 0 & 0 \\ \cdot & \cdot & \cdot \\ \cdot & \cdot & \cdot \\ 1 & m - 1 & m \\ 1 & m & m \end{bmatrix} \begin{pmatrix} a_0 \\ a_1 \\ a_2 \end{pmatrix} = \begin{bmatrix} u(-m, -m) \\ u(-m + 1, -m) \\ \cdot \\ \cdot \\ u(0,0) \\ \cdot \\ \cdot \\ u(m - 1, m) \\ u(m, m) \end{bmatrix} \quad (\text{A2-11})$$

Strain is the measure of the deformation of a line element and can be defined according to equation (A2-12). Finally, strain can be estimated by the Green strain tensor [GOM13] (equation (A2-13)).

$$\lambda = \lim_{l \rightarrow 0} \left(\frac{l + \Delta l}{l} \right) \quad (\text{A2-12})$$

$$\varepsilon_G = f(\lambda) = \frac{1}{2}(\lambda^2 - 1) \quad (\text{A2-13})$$

The different steps leading to the calculation of the strain distribution in a deformed material with the DIC technique are summarised in Annex 2 - 8.



Annex 2 - 8: Process steps for strain distribution evaluation by Digital Image Correlation

Annex 3: Rotor Tip Thickness (TT) refinement

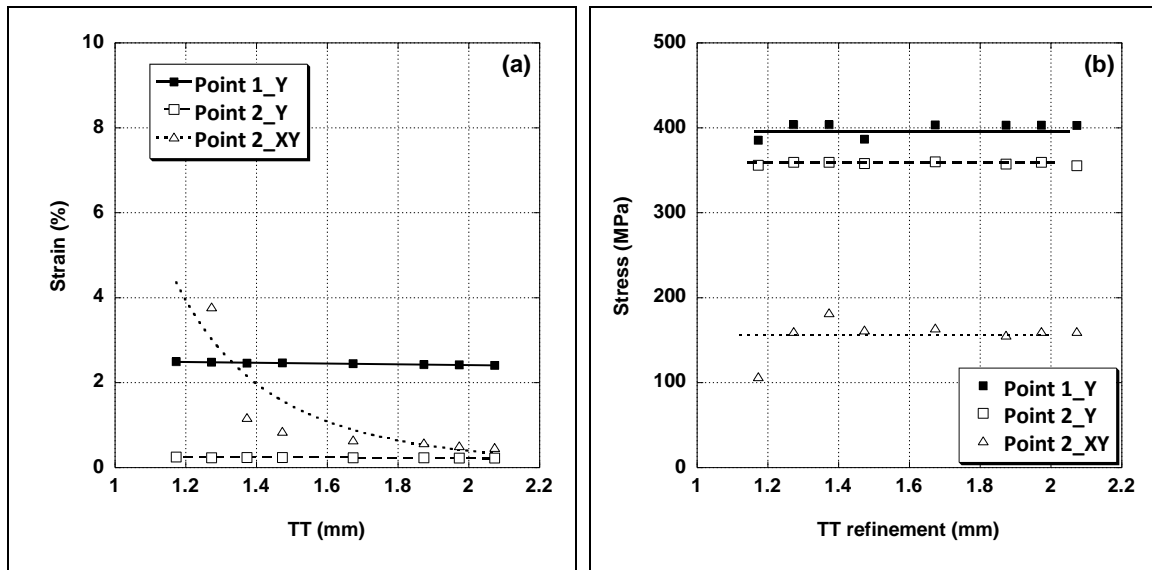
Once TLP is chosen, the TT is reduced step by step as described in Table A3-1. The same methodology than for TLP reduction is applied to decide whether the geometry is valid or not, the stress and strain states and the elongation (as the airgap is only 0.3mm) are controlled for overspeed and then cyclic tests.

Table A3-1: Dimensions of TLP and TT reductions

	TLP/2 (mm)	TT (mm)	Number of elements	Number of nodes
Initial	1.15	2.073	38295	12521
TLP refinement	1.02		37573	12279
Modifications		1.973	37172	12144
		1.873	37378	12210
		1.673	36994	12086
		1.573	36062	11776
		1.473	35997	11753
		1.373	35790	11682
		1.273	35332	11530
		1.173	35103	11455

- **Overspeed test**

For these calculations the monotonic properties of the material are considered (as defined in Table 6-). As for TLP reduction, the points where ε_Y and ε_{XY} are at their maximum in zone 1 and 2 are considered. In zone 1, ε_{XY} is negligible. Evolutions of strain and stress at these points are plotted in Annex 3-1 (a) and (b) respectively.

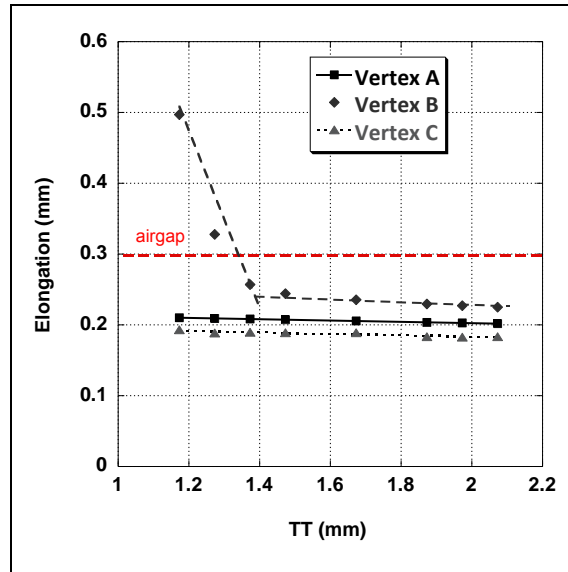


Annex 3-1: Evolution of (a) strain and (b) stress in zone 1 and zone 2 with TT refinement

It appears that the stress in zone 1 and in zone 2 (where ε_y is maximum) is almost constant and below 450MPa when reducing the TT. In zone 2 where ε_{xy} is maximum, the stress is almost constant above TT= 1.373.

Concerning strains, ε_y strains in zones 1 and 2 stay constant when reducing TT. However, ε_{xy} in zone 2 is almost constant above TT=1.673, below this value, strain increases when TT decreases.

The Annex 3-2 shows the evolution of elongations at vertex A, B and C. Elongation at vertex B is the most important. Above TT=1.673 mm, elongation is almost constant whereas under TT=1.673mm elongation increases with TT reduction. At TT=2.173 mm and below, the elongation is superior to the airgap these geometries will not be further studied. For safety reasons TT=1.373 mm is also isolated (elongation close to airgap value).



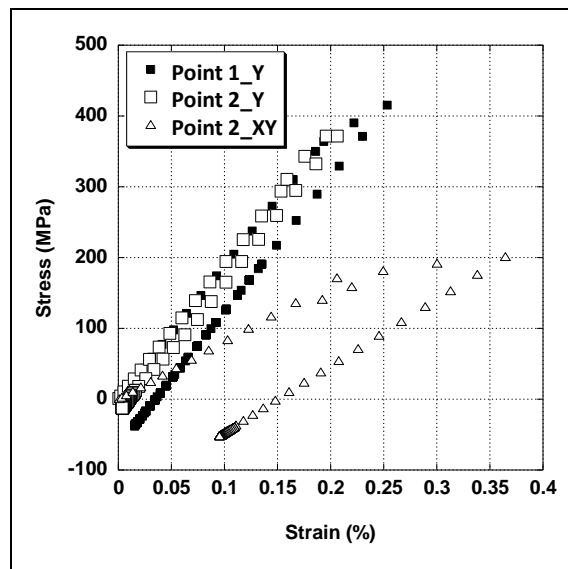
Annex 3-2: Elongation evolution with TLP refinement

The cyclic test is then performed on different geometries with TT=2.073 down to TT=1.473 mm.

- **Cyclic test**

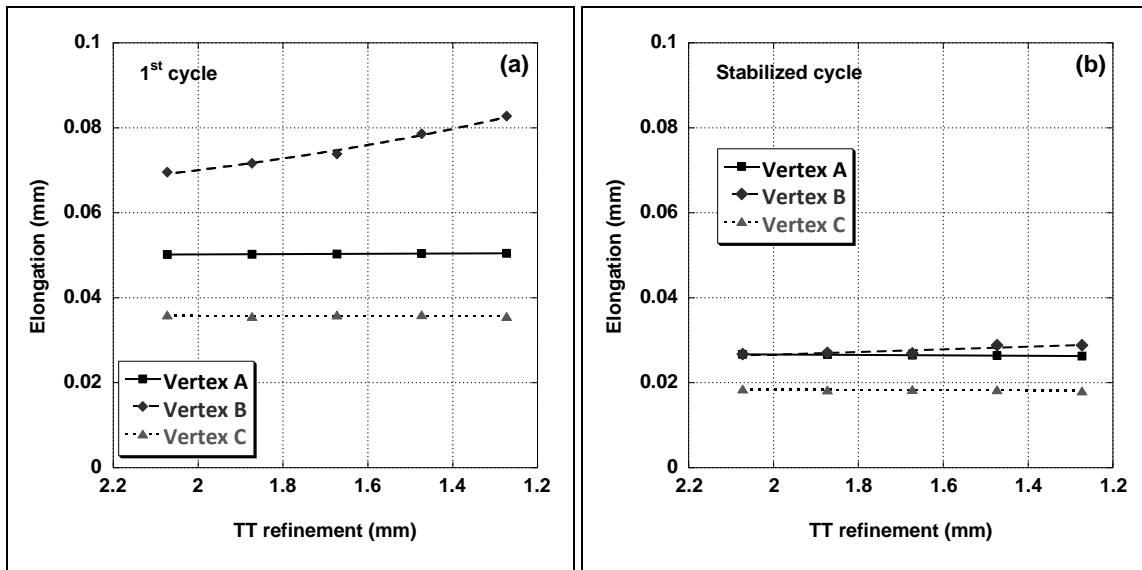
For these calculations the Chaboche properties of the material are considered (as defined in Table 6-).

The same methodology is applied for cyclic test. Indeed, stress and strain states are considered and elongation is checked. Strain-stress hysteresis curves are drawn for the point where ϵ_y is maximum in zone 1 and for points where ϵ_y and ϵ_{xy} are maximum in zone 2. The fatigue behaviour is linear in all cases (Annex 3-3).



Annex 3-3: Hysteresis curves for TT=1.273 mm

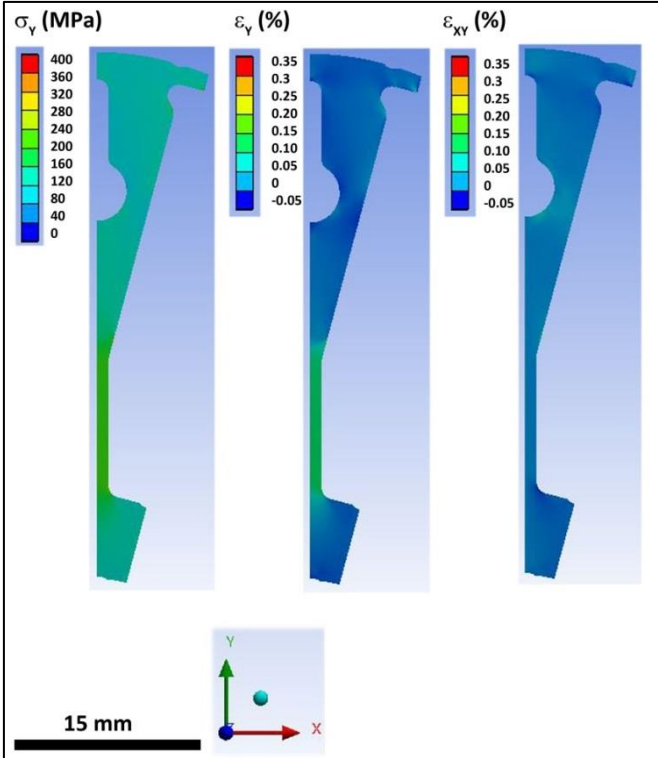
The maximum elongation at the first cycle is 0.083mm for TT=1.273 mm (Annex 3-4 (a)) and then stabilised at about 0.03mm (Annex 3-4 (b)) which is much less than the airgap.



Annex 3-4: Evolution of the maximum elongation with TT refinement for (a) the first cycle and (b) stabilized cycle

The same conclusion than for TLP refinement can be made. The material's behaviour is linear in fatigue, there is adaptation phenomena under rotational velocity. Therefore, it is elongation due to the overspeed test that is limiting for geometry optimisation. Finally, TT is reduced down to TT=1.473 mm.

The stress and strain distributions in the rotor with the TLP/2=1.02mm and TT=1.473mm are shown in Annex 3-5. It shows that normal stress and strain (σ_y and ε_y respectively) are localised in the zone of the leakage path which width has been reduced. Shear strain (ε_{xy}) localises near the hole, however, it does not reach damaging values and there is an adaptation phenomenon of the material.



Annex 3-5: Normal stress σ_y , normal strain ϵ_y and shear strain ϵ_{xy} distributions in the final rotor during the cyclic test and stabilised at 20000 RPM

Annex 4: Summary of fatigue tests

- Reference tests

Test number	$\Delta\varepsilon_t$ (%)	N_f	Interrupted test at N cycles
M13-025	0.3	185092	
M13-032	0.3	48768	
M14-058	0.3	69138	
M13-040	0.4	18100	
M13-046	0.4	21075	
M13-027	0.5	4709	
M13-035	0.5	2104	
M13-047	0.5	3720	
M14-107	0.5	-	2000
M14-108	0.5	-	10
M14-109	0.5	-	100
M14-113	0.5	-	100
M14-114	0.5	-	10
M15-001	0.5	-	100
M15-002	0.5	-	2000
M15-007	0.5	-	2000
M15-010	0.5	-	10
M13-028	0.7	1785	
M13-029	0.7	1168	
M13-048	0.7	882	
M14-103	0.7	-	10
M14-104	0.7	-	100
M14-105	0.7	-	1000
M14-056	0.9	539	
M14-094	0.9	317	
M13-030	1	279	
M13-031	1	76	
M14-100	1	-	200
M14-101	1	-	200
M14-102	1	-	200
M14-110	1	-	300
M14-039	1	-	10
M14-040	1	-	50
M14-041	1	-	100
M14-054	1	-	178
M14-055	1	-	200
M15-008	1	-	100

- 90° tests

Test number	$\Delta\varepsilon_t$ (%)	N_f
M13-58	0.5	1771
M13-61	0.5	1645
M13-60	0.7	1038
M13-78	0.7	752
M13-67	1	377
M13-79	1	317

- As received tests

Test number	$\Delta\varepsilon_t$ (%)	N_f
M13-51	0.5	3058
M13-77	0.5	3208
M13-75	0.7	1327
M13-52	1	506
M13-76	1	267

- $R_{\varepsilon}=-1$ tests

Test number	$\Delta\varepsilon_t$ (%)	N_f
M13-54	0.5	3166
M13-74	0.5	4117
M13-50	0.7	924
M13-55	0.7	925
M13-56	1	506
M13-66	1	261

- $10^{-3}s^{-1}$ tests

Test number	$\Delta\varepsilon_t$ (%)	N_f
M13-69	0.5	4505
M13-71	0.5	9080
M13-70	0.7	967
M13-72	0.7	1351
M13-81	0.7	1313
M13-63	1	84
M13-73	1	512

- Relaxation tests

Test number	$\Delta\varepsilon_t$ (%)	N_f
M14-82	0.5	-
M14-84	0.5	2312
M14-83	0.5	2388
M14-65	0.5	4186
M14-75	0.7	767
M14-80	0.7	837
M14-79	0.7	1253
M14-77	0.7	-
M14-85	1	24197
M14-74	1	173
M14-66	1	465
M14-73	1	553
M14-72	1	-

- 2-steps tests

Test number	$\Delta\varepsilon_t$ (%)	N_f
M15-021	0.3	264636
M15-028	0.3	215677
M15-024	0.5	4351
M15-025	0.5	3261
M15-022	0.7	1128
M15-023	0.7	1761

Abstract

The objective of the PhD work was to investigate the low cycle fatigue (LCF) behaviour of Fe-3Si steel employed for rotors of new starter-alternators developed by Valeo. The study took into account the relation between mechanical response and microstructure, the fatigue mechanisms, the assessment of strain at a mesoscopic scale and an optimisation of the rotor design.

Low cycle fatigue tests performed on 350 μ m thick specimen pointed out a cyclic hardening of the material. The brittle crack propagation mode underlined the low toughness of the material.

The formation of dislocations structures observed by Transmission Electron Microscopy (TEM) and controlled Electron Channelling Contrast Imaging (cECCI) was strain dependant. The total strain variation $\Delta\varepsilon_t=0.7\%$ appeared as a transition value. Below $\Delta\varepsilon_t=0.7\%$, homogeneous arrangement of dislocations and transgranular crack initiation are observed. Above $\Delta\varepsilon_t=0.7\%$, a mixture of veins-channels and wall-channels were observed inside the grains and cracking became intergranular.

An Electron Back-Scattered Diffraction (EBSD) study was then performed on the specimen fatigued above $\Delta\varepsilon_t=0.7\%$ and approached with KAM, GROD and GOS parameters. It pointed out the strain gradient within grain and highlighted the strain localisation at grain boundaries.

Finally, by taking into account LCF properties of the Fe-3Si steel in the material database of the finite element modelling, slight modifications of the rotor geometry have been performed which improves the electromagnetic performances of the machine.

Keywords: Electrical steel, Cyclic Plasticity, Electronic microscopies, Dislocation structures, Finite Element Modelling (FEM)

Résumé

L'objectif de ce travail de thèse était d'étudier le comportement en fatigue oligocyclique de l'acier Fe-3Si utilisé pour les rotors des nouveaux alterno-démarrateurs développés par Valeo. L'étude pris en compte la relation entre la réponse mécanique et la microstructure, les mécanismes de fatigue, l'évaluation de la déformation à une échelle mésoscopique et une optimisation du dimensionnement du rotor.

Les essais de fatigue, menés sur des éprouvettes d'épaisseur 350 μ m, ont montré un durcissement cyclique du matériau et le mode de propagation de la fissure, fragile, souligne sa faible ténacité.

La formation de structure de dislocations observées par Microscopie Electronique en Transmission (TEM) et par cECCI (Controlled Electron Channelling Contrast Imaging) est dépendante de la déformation et la variation de déformation totale $\Delta\varepsilon_t=0.7\%$ apparaît comme une valeur de transition. En-dessous de $\Delta\varepsilon_t=0.7\%$, des arrangements homogènes de dislocations et un amorçage de la fissure transgranulaire sont observés. Au-dessus de $\Delta\varepsilon_t=0.7\%$, des structures veines-canaux et murs-canaux sont observés et l'amorçage de fissure est intergranulaire.

Une étude EBSD (Electron Back-Scattered Diffraction) basée sur les paramètres KAM, GROD et GOS menée sur les éprouvettes fatiguées montre un gradient de déformation dans les grains et une localisation de la déformation aux joints de grain au-dessus de $\Delta\varepsilon_t=0.7\%$.

Enfin, en prenant en compte les propriétés en fatigue de l'acier Fe-3Si dans la base de données matériaux de la modélisation par éléments finis, des légères modifications de la géométrie du rotor ont été effectuées ce qui améliore les performances électromagnétiques de la machine.

Mots clés: Acier électrique, Plasticité Cyclique, Microscopies électroniques, Structures de dislocations, Modélisation par éléments finis